

2017

Novel dosimetry verification solutions for advanced radiation therapy

Shrikant Deshpande
University of Wollongong

Follow this and additional works at: <https://ro.uow.edu.au/theses1>

University of Wollongong

Copyright Warning

You may print or download ONE copy of this document for the purpose of your own research or study. The University does not authorise you to copy, communicate or otherwise make available electronically to any other person any copyright material contained on this site.

You are reminded of the following: This work is copyright. Apart from any use permitted under the Copyright Act 1968, no part of this work may be reproduced by any process, nor may any other exclusive right be exercised, without the permission of the author. Copyright owners are entitled to take legal action against persons who infringe their copyright. A reproduction of material that is protected by copyright may be a copyright infringement. A court may impose penalties and award damages in relation to offences and infringements relating to copyright material.

Higher penalties may apply, and higher damages may be awarded, for offences and infringements involving the conversion of material into digital or electronic form.

Unless otherwise indicated, the views expressed in this thesis are those of the author and do not necessarily represent the views of the University of Wollongong.

Recommended Citation

Deshpande, Shrikant, Novel dosimetry verification solutions for advanced radiation therapy, Doctor of Philosophy thesis, Centre for Medical Radiation Physics, University of Wollongong, 2017.
<https://ro.uow.edu.au/theses1/15>

Research Online is the open access institutional repository for the University of Wollongong. For further information contact the UOW Library: research-pubs@uow.edu.au

**UNIVERSITY OF
WOLLONGONG**



**NOVEL DOSIMETRY VERIFICATION SOLUTIONS
FOR ADVANCED RADIATION THERAPY**

A Dissertation Submitted in Fulfilment of
the Requirements for the Award of the Degree of

Doctor of Philosophy

from

UNIVERSITY OF WOLLONGONG

by

Shrikant Deshpande

M.Sc.(physics),Dip.R.P.

Centre for Medical Radiation Physics
Faculty of Engineering

2017

© Copyright 2017

by

Shrikant Deshpande

ALL RIGHTS RESERVED

CERTIFICATION

I, Shrikant Deshpande, declare that this thesis, submitted in fulfilment of the requirements for the award of Doctor of Philosophy, in the Centre for Medical Radiation Physics, Faculty of Engineering, University of Wollongong, is wholly my own work unless otherwise referenced or acknowledged. The document has not been submitted for qualifications at any other academic institution.

Shrikant Deshpande
April 2017

Contents

List of Tables	ix
List of Figures/Illustrations	xix
ABSTRACT	xx
Acknowledgements	xxiii
Publication List	xxv
Conference Presentations	xxvii
Invited Talks	xxix
Nomenclature	xxx
1 Introduction	1
1.1 Aims and Objectives	6
2 Literature Review	8
2.1 Cancer and the role of radiotherapy	8
2.2 History of external beam radiotherapy	8
2.3 Advanced radiotherapy techniques	10
2.4 Treatment Verification	13
2.5 Dose verification – instrumentation and methodology	15
2.5.1 Point dosimeters	15
2.5.2 2-dimensional dosimeters	16
2.5.3 EPID	18
2.5.4 Quasi 3D dosimeters	21
2.5.5 3-dimensional dosimeters (Gel dosimetry)	23
2.5.6 On board exit detector	23
3 Dose calibration of EPIDs for segmented IMRT dosimetry	25
3.1 Introduction	26
3.2 Methods and Materials	28

3.2.1	Equipment	28
3.2.2	Dose linearity for segmented fields	34
3.2.3	Inter-segment reproducibility	34
3.2.4	Clinical IMRT fields	34
3.2.5	EPID pixel-Dose calibration	35
3.3	Results	36
3.3.1	Dose linearity for segmented fields	36
3.3.2	Inter-segment reproducibility	39
3.3.3	Clinical IMRT field	42
3.3.4	EPID pixel-Dose calibration	42
3.4	Discussion	45
3.5	Conclusion	47
4	Feasibility study of a dual detector configuration concept for simultaneous mega-voltage imaging and dose verification in radiotherapy	48
4.1	Introduction	49
4.2	Methods and Materials	50
4.2.1	Equipment	50
4.2.2	Dosimetry experimental setup	51
4.2.3	Dose response evaluation	53
4.2.4	IMRT fields	55
4.2.5	Imaging experimental setup	55
4.2.6	Image quality evaluation	56
4.3	Results and Discussion	59
4.3.1	Dose response evaluation	59
4.3.2	IMRT	63
4.3.3	Image quality evaluation	66
4.3.4	Optimized dual detector design	70
4.4	Conclusion	72
4.5	Acknowledgments	72
5	Novel dual detector concept for simultaneous transit dose and image verification in radiotherapy	73
5.1	Introduction	74
5.2	Methods and Materials	76
5.2.1	Equipment	76

5.2.2	Dosimetry experimental setup	77
5.2.3	Dose response evaluation	78
5.2.4	Clinical modulated Fields	78
5.2.5	Imaging experimental setup	79
5.2.6	Image quality evaluation	80
5.3	Results and Discussion	82
5.3.1	Dosimetry evaluation	82
5.3.2	Image quality evaluation	85
5.4	Conclusion	88
6	A simple model for transit dosimetry based on a treatment planning system and a water equivalent EPID	89
6.1	Introduction	90
6.2	Methods and Materials	94
6.2.1	Equipment	94
6.2.2	EPID image corrections and dose calibration	96
6.2.3	Dose response evaluation	98
6.3	Results	100
6.3.1	Dose response evaluation	100
6.3.2	Clinical field	102
6.4	Discussion	108
6.5	Conclusion	109
6.6	Acknowledgments	109
7	Clinical significance of treatment delivery errors for helical tomotherapy nasopharyngeal plans - a dosimetric simulation study	110
7.1	Introduction	111
7.2	Methods and Materials	112
7.2.1	Patient selection and treatment planning	112
7.2.2	Simulation of delivery errors	113
7.2.3	Plan evaluation	114
7.3	Results	115
7.3.1	Evaluation of plan metrics	115
7.4	Discussion	124
7.5	Conclusion	129

8 Sensitivity evaluation of two commercial dosimeters in detecting helical Tomotherapy treatment delivery errors	130
8.1 Introduction	131
8.2 Methods and Materials	134
8.2.1 Patient selection and treatment planning	134
8.2.2 Dosimetry system	134
8.2.3 Detector sensitivity	137
8.2.4 Criteria for minimum error detection	137
8.3 Results	138
8.3.1 Detector sensitivity	138
8.3.2 Error detection by dosimeter systems	140
8.4 Discussion	140
8.5 Conclusion	144
8.6 Acknowledgements and Disclosures	144
9 Clinical implementation of an in-house Exit detector-based dose reconstruction tool for Helical Tomotherapy delivery quality assurance	145
9.1 Introduction	146
9.2 Theory	148
9.2.1 OBD Sensitivity (S)	150
9.2.2 MLC leaf Map	150
9.2.3 LSF and background signal (B)	151
9.2.4 Planned Fluence Retrieval	152
9.3 Methods and Materials	153
9.3.1 Exit detector DQA tool	155
9.3.2 Clinical validation	156
9.4 Results	158
9.4.1 Sinogram analysis sensitivity and accuracy	158
9.4.2 Reconstructed dose accuracy	160
9.4.3 Clinical assessment of Exit detector DQA tool versus ArcCHECK DQA method	161
9.4.4 DVH metrics calculation accuracy	163
9.5 Discussion	163
9.5.1 Conclusion	165
9.5.2 Acknowledgements	166

10 Discussion and Conclusion	167
10.1 General discussion	167
10.1.1 Dose characterisation and development of novel prototype hybrid EPID based dosimeters for treatment verification for a conventional linac system	169
10.1.2 Assessment of current dosimetry systems and development of an on board exit detector based tool for efficient pre-treatment verification for HT delivery	172
10.2 Implementation of this work within a clinical environment	176
10.3 Future work	176
10.3.1 Optimisation of novel prototype hybrid EPID based dosimeters	177
10.3.2 Clinical implementation of EPID based prototype for in vivo dosimetry.	178
10.3.3 Assess the clinical impact due to changes in HT delivery parameter for additional clinical sites and planning techniques	179
10.3.4 Develop the HT exit detector DQA tool for generalised use	179
10.4 Summary	179
Bibliography	216
A LSF and MTF measurement	217
B Tomotherapy error simulation for lung SABR	219
C Description of values retrieved from the patient XML in exit dosimetry DQA tool	222
D Matlab Script	226
D.1 Codes for gamma comparison	226
D.2 Codes for MTF and LSF calculations	228
D.3 Codes for CT FOV manipulation	239

List of Tables

3.1	The combinations of equipment and settings for each experiment.	29
3.2	The integrated research EPID response at CAX for both static and ‘simple’ IMRT fields with total of 20 MU exposure. The captured frames were summed as no PostBeamOff, three PostBeamOff, and ten post-beam-off frames for the same EPID image to demonstrate effect from different acquisition protocols. The percentage values in brackets indicate the relative difference in the integrated pixel values for each simple IMRT field compared the static field exposure of the same total dose	40
3.3	The percentage gamma pass rate determined using three different calibration methods for both Siemens and Elekta EPIDs for the same integrated image of an IMRT field. The IMRT fields were modified to have a fixed number of MU per segment. The Elekta EPID images were acquired with clinical setting (i.e., renormalization set to 40,000) and for two different PostBeamoff acquisition settings	44
4.1	Gamma evaluation results comparing the absolute dose map with ICA in dual detector configuration and reference dosimetry configuration for clinical IMRT fields and standard IMRT test patterns in nontransit geometry . . .	63
4.2	Gamma evaluation results comparing the ICA absolute dose map from the dual detector configuration and reference dosimetry configuration using anthropomorphic or solid water slab phantoms, and IMRT fields	65
4.3	Comparison of resolution, noise, and CNR for the dual detector configuration and reference imaging configuration. The results are quoted as mean \pm standard deviation from five repeat measurements	67

5.1	Gamma evaluation results comparing the MP absolute dose map from the dual detector configuration and reference dosimetry configuration with either an anthropomorphic phantom or 20 cm thick solid water slab placed in beam. Five clinical modulated fields were measured.	82
5.2	Comparison of resolution, noise and CNR for the dual detector configuration and reference imaging configuration. The results are quoted as mean \pm standard deviation from three repeat measurements.	85
6.1	Comparison of off-axis response measured with WE-EPID, ICA and TPS calculated with solid water thicknesses of 0 cm (i.e. no object), 10, 20, 30 and 40 cm in the beam, respectively. Data presented constitutes the mean \pm standard deviation difference in the cross-plane profiles normalised at CAX over a 12.5 cm distance from beam axis.	100
6.2	Gamma-index evaluation when comparing WE-EPID and ICA absolute dose maps with the TPS absolute IMRT fields using 3%/2 mm criteria. An anthropomorphic or solid water slab phantom was placed in the beam as a transit object. The range and mean value has presented for both gamma pass rate and average gamma value.	105
6.3	Gamma-index evaluation when comparing WE-EPID and ICA measured dose maps with TPS-calculated VMAT fields using 3%/2 mm criteria (both integrated and control point by control point). Either an anthropomorphic or solid water slab phantom was placed in the beam as a transit object. . . .	106
7.1	Description of the range of complexity among ten clinical HT plans presented in this study. All ten plans have three dose level targets (70 Gy, 63Gy and 56Gy) and extend bilaterally.	112
7.2	Five key simulated errors and the associated magnitudes simulated. All error magnitudes are defined relative to the reference clinical plan value	114
7.3	Summary of machine interlock, recommended machine QA tolerance and established using dosimetric based simulation	125
8.1	Summary of previous reported studies on detector sensitivity for commercial detectors.	132

8.2	Magnitude of change required to degrade mean gamma pass rate to below 90% with 3%/3mm gamma criteria and detector sensitivity as determined from equation 8.1 for both dosimeters. A linear fit of mean gamma pass rate versus error magnitude was used to obtain both error magnitude to degrade gamma pass rate below 90% and detector sensitivity	138
8.3	Summary of gamma pass rate with 3%/3mm tolerance criteria and error detected. The statistical Wilcoxon Signed–Rank test was used to evaluate difference in sensitivity between two dosimetry systems for detecting the delivery error	140
8.4	Comparison of minimum error detection by dosimeters, clinically relevant error magnitude based on dosimetric simulations and machine interlock . .	142
9.1	Summary of clinical plans with varying treatment characteristics for comparing two QA systems.	157
9.2	Mean MLC LOT error \pm standard deviation across all leaf events (projection) determined via sinogram analysis for both unmodified and modified ‘Tomophant’ plan. In the first column, the unmodified plan de-convolved fluence was compared to the planned sinogram. In each remaining column, the de-convolved fluence for each modification was compared to ‘ <i>a priori</i> ’ known modification to the planned fluence.	158
9.3	Gamma evaluation (2%/2mm) of original planned dose (planned) and adjusted planned dose (measured) computed from both unmodified and modified plans. In the first column, the unmodified adjusted planned dose is compared to the original planned dose. In each remaining column, the adjusted planned dose for each modification is compared to the original planned dose recalculated for the known plan modification (‘ <i>a priori</i> ’ planned dose). . .	160
9.4	Difference between the adjusted planned dose calculated by the tool and ion chamber measurement at various IEC-x positions along the cheese phantom. Measurement location X= -10.5 cm and X= -1.5 cm are in a low dose gradient region while other positions are in higher dose gradients. Each column represents different ion chamber measurement positions at different IEC-x positions along the mid-plane of the cheese phantom.	160
9.5	Comparing the clinically relevant DVH parameter from five clinical reported by exit detector based DQA tool with in-house Comp plan tool. The difference is presented as mean \pm standard deviation (from five clinical plans)	163

B.1	Comparing the dosimetrically derived QA tolerances for lung SABR, nasopharynx cases with AAPM TG-148 recommended machine QA tolerance. The nasopharynx data is taken from chapter 7.	221
C.1	Values retrieved from the patient XML for determination of the planned fluence	222
C.2	Files required for execution of the standalone dose calculator	223
C.3	Values retrieved from the patient XML for determination of the planning CT	224
C.4	Values retrieved from the patient XML for determination of the delivery parameters	225

List of Figures

1.1	Radiation therapy treatment machines a) C-arm conventional linear accelerator and b) Helical TomoTherapy	2
2.1	Timeline 1 Early landmark discoveries in radiotherapy from Thariat et al [1]	10
2.2	Timeline 2 Advances in radiotherapy technology from Thariat el al [1]. . .	12
3.1	Schematic illustration of three different frame integration methods: i) No frame PostBeamOff; ii) 3 frames PostBeamOff; and iii) 10 frames Post-BeamOff, where 0, 3, and 10 frames after the beam has stopped are included in integrated images, respectively. The beam-off trigger was estimated as the frame where the signal had fropped to approximately 50% or less of the beam-on value.	32
3.2	Experimental set-up for simultaneous EPID and ionisation chamber array measurements.	33
3.3	Relative EPID response versus MU for open static and ‘simple’ IMRT fields with fixed field size $10 \times 10 \text{ cm}^2$ for Siemens and Elekta clinical EPID systems (experimental set up 1, 2a and 3a from Table 3.1). Data points are the ratio of EPID and ICA response for both static and ‘simple’ IMRT fields. Error bars show the standard deviation from 5 repeat measurements.	37
3.4	Relative EPID response versus MU for open static and ‘simple’ IMRT fields with fixed field size $10 \times 10 \text{ cm}^2$ for research EPID measured on Siemens and Elekta linacs (experimental setup 2b and 3c from Table 3.1). Relative EPID response for clinical Elekta EPID using XIS software (experimental set up 3b from Table 3.1). Data points are the ratio of EPID and ICA response for both static and ‘simple’ IMRT fields. Error bars show the standard deviation from 5 repeat measurements.	38

3.5	The EPID response at CAX per frame for ‘simple’ IMRT fields (a and b) for 1 MU and 5 MU per segment respectively (c) static open field (20 MU).	41
3.6	Relative response per segment for 5 repeats of the ‘simple’ IMRT field for EPID (Triangle with cross-hair) and ICA (square with cross-hair) with 5 MU/segment. All the data points are normalised to non-segmented single exposure 20 MU.	41
3.7	The off-axis profiles of individual IMRT segment (frame average image) for the ‘simple’ IMRT field (4MU x 5 segments) along a) the central row (cross-plane), b) central column (in-plane) acquired with the Siemens EPID panel and c) ICA simultaneously as shown in figure 3.1	42
3.8	2D maps of the percentage standard deviation at each pixel/detector position within the field from ten repeats for a ‘clinical’ IMRT field with 5 MU per segment (a) clinical Siemens EPID (c) clinical Elekta EPID and (b) and (d) for ICA detector measured with Siemens and Elekta linac simultaneously.	43
4.1	Schematic illustration for dosimetry measurement setups (a) dual detector configuration (nontransit) (b) reference dosimetry configuration (nontransit) (c) dual detector configuration (transit) (d) reference dosimetry configuration (transit). For transit geometry measurements, either the solid water slab or anthropomorphic phantom (interchangeable) was used. For visualization purpose, only the anthropomorphic phantom image is shown ((c) and (d)) placed at isocenter.	52
4.2	Schematic of the experimental setup for image quality evaluation. Anthropomorphic phantom images were acquired for the (a) dual detector configuration and (c) reference imaging configuration. MTF measurements were performed for the (b) dual detector configuration and (d) reference imaging configuration.	57
4.3	Experimental setup for measurement of LSF. The tungsten blocks are mounted on a translating and rotating stage as close to EPID as possible.	58
4.4	Comparison of (a) nontransit geometry and (b) transit geometries, ICA measured dose profiles in reference dosimetry configuration at buildup depths of 4, 5, 6 cm (Deff), 7 and 8 cm of solid water slab with the dual detector configuration. The relative ratio between dose profiles measured at varying buildup depths in reference dosimetry configuration to the dose profile measured with dual detector configuration is also shown for (c) nontransit and (d) transit geometries, respectively.	60

4.5	Comparison of (a) nontransit geometry and (b) transit geometries, ICA measured field size output factors in reference dosimetry configuration at buildup depths of 4, 5, 6 cm (D_{eff}), and 7 and 8 cm of solid water with the dual detector configuration. The relative ratio between field size and output factors measured at varying buildup depths in reference dosimetry configuration to dual detector configuration is also shown for (c) nontransit and (d) transit geometries, respectively.	61
4.6	Comparison of relative dose profiles in the (a) nontransit and (b) transit geometries measured with the ICA in the dual detector configuration and reference dosimetry configuration for $5 \times 5 \text{ cm}^2$ and maximum achievable field sizes within the respective measurements geometries. The relative ratio between the two configurations is shown for (c) nontransit and (d) transit geometries.	62
4.7	Comparison of transmission factors measured with the dual detector configuration at buildup depths of 4, 6, 8 cm, and reference dosimetry configurations, respectively. The measurements were performed with static fields of $15 \times 15 \text{ cm}^2$ defined at the isocenter. The relative ratio of transmission factors for reference dosimetry and dual detector configurations is also shown (b).	64
4.8	Dose profile comparison for wedge IMRT test pattern measured with both reference dosimetry and dual detector configurations. The ratio of the dose profiles is displayed in the insert.	65
4.9	EPID images of the QC-3V image quality phantom taken with the (a) reference imaging configuration and (b) dual detector configuration.	67
4.10	The measured line spread function (normalized) for the reference imaging configuration and dual detector configuration.	68
4.11	The measured modulation transfer function for the reference imaging configuration and dual detector configuration.	69
4.12	Illustration of impact of backscatter in dual detector configuration: (a) Relative line profile of EPID images of an open static field for dual detector configuration (dashed–dotted line) and reference imaging configuration (solid gray line). (b) 2D pixel value relative ratio map between reference imaging configuration and dual detector configuration for static open $5 \times 5 \text{ cm}^2$ field.	69

4.13	Portal image of anthropomorphic head phantom acquired with the (a) reference imaging configuration and (b) dual detector configuration to assess the impact of the presence of the ICA on portal image visualization.	70
4.14	Schematic illustration of conceptual optimized design (RHS) for dual detector that fits within the existing standard EPID (LHS) panel dimensions. Schematics are not drawn to scale, and the gaps located between the neighboring layers are for illustrative purposes only.	71
5.1	Schematic illustration for dosimetry measurement setups (a) dual detector configuration and (b) reference dosimetry configuration. For transit geometry measurements, either the solid water slab or anthropomorphic phantom (interchangeable) was used. For visualization purpose, only the anthropomorphic phantom image is shown placed at isocenter	77
5.2	Comparison of (a) measured dual detector field size output factors at build-up depths 3 mm, 5 mm, 10 mm and 15 mm of solid water with the reference dosimetry configuration and the dual detector configuration. The relative ratio of field size output factors between reference dosimetry configuration and dual detector configuration measured at varying build-up depths is also shown (b)	81
5.3	Comparison measured dual detector off-axis profiles at build-up depths 3 mm, 5 mm, 10 mm and 15 mm of solid water with the reference dosimetry configuration and the dual detector configuration for field sizes $3 \times 3 \text{ cm}^2$, $5 \times 5 \text{ cm}^2$ and $10 \times 10 \text{ cm}^2$. The ratio of profiles between reference detector and dual detector at varying build-up depths for field size $10 \times 10 \text{ cm}^2$ is also shown in (e)	83
5.4	The gamma comparison (3% and 3mm) between measurements for one of the clinical brain IMRT fields, a) Dual detector, b) Reference detector and c) gamma map.	84
5.5	EPID images of the QC-3V image quality phantom taken with the (a) reference imaging configuration and (b) dual detector configuration (MP with no buildup) (c) dual detector configuration (MP with 10mm buildup) (d) dual detector configuration (MP with 15 mm buildup)	86
5.6	Portal image of anthropomorphic pelvis phantom acquired with the (a) reference imaging configuration and (b) dual detector configuration (MP with no buildup) (c) dual detector configuration (MP with 10mm buildup) (d) dual detector configuration (MP with 15 mm buildup).	87

6.1	Experimental setup for transit dose measurements. Two WE-EPID configurations are shown: a) Prototype EPID consisting of a plastic scintillator fibre array (15 cm x 15 cm x 3 cm) directly coupled to the EPID detector, b) Direct EPID consisting of a 30 cm x 30 cm x 3 cm solid water slab directly coupled to the EPID detector. The EPID was positioned at 150 cm and wrapped with an opaque black sheet to block any light from reaching the detector (c). The I'mRT MatriXX ion Chamber Array setup is shown in (d).	95
6.2	Representation of phantom (anthropomorphic pelvis phantom) and virtual EPID setup in the TPS.	97
6.3	Two different heterogeneous phantoms: a) an inhomogeneous slab phantom and b) an anthropomorphic breast phantom. The inhomogeneous slab phantom consists of stacked bone, lung and water equivalent solid water slab.	99
6.4	Comparison of dose measured with the WE-EPID and ICA and calculated with the TPS in the same measurement geometry: a) field size response and b) transmission factors. Only data for the direct EPID WE-EPID configuration is presented here.	101
6.5	Comparison of off-axis response (normalised half profiles) measured with a) 30 cm solid water slab and b) 40 cm solid water slab present in beam. The relative difference in off-axis response over a distance of 12.5 cm from the beam axis between the TPS-calculated or WE-EPID-measured dose when compared to the ICA-measured dose is displayed on the right axis. Only data for the direct EPID WE-EPID configuration is presented here.	101
6.6	The gamma-index comparison (3% and 2mm) between measurement (WE-EPID) and TPS calculated water-equivalent dose image for a direct beam passing through a) anthropomorphic phantom (open field) b) anthropomorphic phantom (60° wedge field) and c) inhomogeneous slab phantom (open field). The dose profiles in the rightmost panes were extracted from the planes indicated as dotted lines on corresponding EPID dose images.	103
6.7	The gamma comparison between measurement (novel WE-EPID) and calculation (TPS) for first three control points of a clinical prostate VMAT field in presence of an anthropomorphic phantom.	104

6.8	The gamma comparison (starting from left in bottom row) between the TPS-calculated versus WE-EPID measured, TPS versus ICA measured and ICA measured versus WE-EPID for integrated dose images of a clinical prostate VMAT field in presence of an anthropomorphic phantom. The integrated dose images are displayed in top row starting from left, TPS calculated, measured with WE-EPID and ICA measured.	107
7.1	Schematic describing the processes involved in creating the simulated error plans, dose recalculations for simulated error plans and the calculation of plan metrics for dosimetry comparison	114
7.2	The average percentage dose difference compared to the clinical reference (no error) plans over the ten patients for a) D_{95} of PTV70, b) D_{95} of PTV56 c) D_{1cc} for spinal cord, d) D_{1cc} for brainstem and e) mean dose to the parotid. The error bars represents one standard deviation in plan metrics from the ten patients. The red dotted line represents the set clinical tolerance	116
7.3	DVH graphs for a representative patient data set comparing the clinical reference plan with the following simulated errors a) Jaw width b) Couch speed c) Gantry period and d) Gantry start position. Other patient datasets demonstrated similar variation	117
7.4	Histogram distribution of the treatment plans from the ten patient cohort that are within the set clinical tolerances (both PTV and OAR) for varying magnitude of errors in a) Jaw width (JW) b) Couch speed (CS) c) Gantry period (GP) and d) Gantry start position (GSP). The red dashed bar shown above represents the machine interlock threshold for each error type. The jaw error has 2 levels of interlocks while the couch speed does not have a specific interlock since the couch position is monitored instead of the couch speed	118

- 7.5 The average percentage dose difference compared to the clinical reference (no error) plans over the ten patients for a) D_{95} of PTV70, b) D_{95} of PTV56, c) D_{1cc} for spinal cord and c) D_{1cc} for brainstem and d) mean dose to the parotid with simulated MLC LOT errors. Two random MLC LOT errors were considered: i) The reduction was randomly applied across all open leaves such that the mean reduction was 2% or 4% and ii) The MLC LOT random modification applies a normal random distribution to all open projections with a given standard deviation (1-10%) and a mean of 0%. The error bars represent one standard deviation in plan metrics from the ten patients. The red dotted line represents the set clinical tolerance 119
- 7.6 DVH graphs for a representative patient data set comparing the clinical reference plan with the following simulated MLC LOT errors: leaf 32 stuck open, leaf 42 stuck open and MLC LOT reduced by 2% and 4% and standard deviation of 5% and 10% with mean MLC LOT error of 0% as described in the methodology. Other patient datasets demonstrated similar variation . . . 120
- 7.7 Isodose distribution comparison between the reference clinical plan and each of the four simulated delivery error plans a) transverse view cutting through isocentre. The dose distribution example is from one selected patient dataset and shows the worst impact on the dose distribution. The simulated error magnitude were for JW was +1 mm, CS +2.5% cm per sec, GP +3sec and GSP +4⁰. The magnitude for each error type displayed here was such that the set clinical tolerance was exceeded. 121
- 7.8 Isodose distribution comparison between the reference clinical plan and each of the four simulated delivery error plans coronal view cutting through isocentre. The dose distribution example is from one selected patient dataset and shows the worst impact on the dose distribution. The simulated error magnitude were for JW was +1 mm, CS +2.5% cm per sec, GP +3sec and GSP +4⁰. The magnitude for each error type displayed here was such that the set clinical tolerance was exceeded. 122

7.9	Isodose distribution comparison between the reference clinical plan and each of the four simulated delivery error plans sagittal view cutting through isocentre. The dose distribution example is from one selected patient dataset and shows the worst impact on the dose distribution. The simulated error magnitude were for JW was +1 mm, CS +2.5% cm per sec, GP +3sec and GSP +4°. The magnitude for each error type displayed here was such that the set clinical tolerance was exceeded.	123
7.10	Comparing the expected couch position calculated based on planning parameter against the predicted couch position for simulated couch speed delivery error of $\pm 2\%$ cm per sec, $\pm 3\%$ cm per sec and $\pm 5\%$ cm per sec from planned value. The dotted red lines are the machine interlock threshold when the couch position is different from expected planned value (± 1 mm)	126
7.11	Illustration of dosimetric impact due to the gantry related delivery error i.e. gantry start position (GSP) and gantry period (GP). Error in GP or GSP will systematically offset the projection from the planned position (left) such that high fluence projections are rotated from their intended angles, affecting the delivered dose distribution	128
7.12	The transverse CT images for 3 different patients showing the spatial variation of the PTV70 contour (red colour) relative to parotid (cyan-right and purple-left side). The green contour is PTV56.	128
8.1	Comparison of mean gamma pass rate measured for intentional error plans in jaw width, couch speed and MLC LOT measured with ArcCHECK and MatriXX ^{Evolution} dosimeters. The error bar shows maximum and minimum pass rate for a given error magnitude. The dotted red line represents 90% gamma pass rate used as an action level. The mean pass rate for no error plan for both dosimeter is normalised to 100% and gamma pass rate for each plan is then scaled to no error plan	139
9.1	Exit detector response from TQA daily QA module. TQA daily QA module comprises of dynamic MLC procedure with varying MLC pattern. Each of the MLC pattern is sequenced to specific projection interval. The exit detector sensitivity (S), leaf to OBD channel, background signals (B), and leaf spread function (LSF) were determined from specific projections interval as shown.	149

9.2	Resultant superimposed even and odd leaf detector response from Daily TQA module. For projections between 5400-5699 (only the odd MLC leaves are open) and between projections 5700-5999 (only even leaves are open). This data used to define a map of MLC leaf to the OBD channel that yields the maximum signal	150
9.3	Resultant superimposed even and odd leaf detector response from Daily TQA module. For projections between 5400-5699 (only the odd MLC leaves are open) and between projections 5700-5999 (only even leaves are open). The MLC leaf map (b) was established by mapping the OBD channel that yields the maximum signal which corresponds to the known MLC leaf number(i.e. leaf held open).	151
9.4	Leaf Spread Function (left) was derived using discrete Fourier Transform (right).	152
9.5	Illustration of clinical Workflow for performing exit detector DQA tool using two commonly available methods for exporting data from the HT system. The planned fluence for the analysis was machine agnostic delivery plan which was extracted from the patient archive. The static couch DQA procedure is standard clinical DQA plan executed on treatment machine with couch retracted outside bore and couch remains static while beam is on	154
9.6	Graphical illustration of sinogram (top) extracted from original clinical plan, sinogram (middle) for the original optimised plans with ‘ <i>a priori</i> ’ known modification applied (leaf 42 stuck open) and static couch QA de-convolved measured fluence (bottom) of modified plan with leaf 42 stuck open.	159
9.7	Transverse planar doses through the target for Tomophant (plan 1) with leaf 42 held open: a) original planned dose recalculated given known plan modification (‘ <i>a priori</i> ’ planned dose), b) modified OBD based adjusted dose (‘ <i>a posteriori</i> ’ adjusted dose) by tool and c) gamma map (2% and 2mm).	161
9.8	The planning target volume (PTV) D ₉₅ dose error as a function of the mean MLC LOT error (%).	162
A.1	Comarison of measured modulation transfer function (MTF) for the reference imaging configuration versus dual detector configuration (MP placed beneath EPID) on left, reference imaging configuration versus dual detector configuration (MP placed above EPID) in middle and reference imaging configuration versus dual detector configuration (ICA placed above EPID) on right.	218

A.2	Comarison of measured line spread function (LSF) for the reference imaging configuration versus dual detector configuration (MP placed beneath EPID) on left, reference imaging configuration versus dual detector configuration (MP placed above EPID) in middle and reference imaging configuration versus dual detector configuration (ICA placed above EPID) on right.	218
B.1	Histogram distribution of the treatment plans meeting the set clinical tolerances (both PTV and OAR) for varying magnitude of errors in a) jaw width (JW) b) couch speed (CS) c) gantry period (GP) and d) gantry start position (GSP). The red dashed bar shown above represents the machine interlock threshold for each error type. The green line shown above represents the machine QA thresholds as specified by TG-148 report.	220

NOVEL DOSIMETRY VERIFICATION SOLUTIONS FOR ADVANCED RADIATION THERAPY

Shrikant Deshpande

A Thesis for Doctorate of Philosophy

Centre for Medical Radiation Physics

University of Wollongong

ABSTRACT

Improved optimisation of radiation dose delivery to tumours with improved sparing of normal tissues is an ongoing goal of radiotherapy practice. Advanced radiotherapy techniques are constantly improving to achieve this goal. However, these techniques are more complex to deliver. Hence verifying the source of dose errors is increasingly challenging. Accurate verification of treatment delivery for advanced radiotherapy becomes increasingly important in mitigating dose delivery errors which may compromise clinical outcome. This dissertation investigated treatment dosimetry verification for two different radiotherapy delivery systems i) Open gantry linear accelerator and ii) Helical TomoTherapy HI-ART[®] (HT).

Part (i) Open gantry linear accelerator - novel prototype hybrid EPID based dosimeters were developed for treatment verification to combine geometric and dosimetric verification in a single system. Initial work on dose response for standard EPIDs provided a more consistent understanding of EPID under-dose response for small monitor units (MUs).

The dose response linearity of a standard a-Si EPID was evaluated for different combinations of linac, image acquisition settings and imaging data processing methods. EPID nonlinear response was demonstrated to be primarily due to gain ghosting affects in the a-Si photodiodes. This work has resolved some of the inconsistencies in the literature regarding EPID dose response and proposes a simple yet robust pixel-to-dose calibration method for EPID-based IMRT dosimetry.

Standard EPID detectors are optimized for imaging but are suboptimal for dosimetry. Two novel prototype hybrid EPID based dosimeters also referred to as dual detector configuration were developed and characterised. First, dual detector configuration combines a conventional EPID (imager) and 2D array dosimeter ionisation chamber array (ICA) while the other dual detector combines a conventional EPID (imager) and prototype 2D silicon detec-

tor array. Excellent agreement in measured dose response ($<1.5\%$) and global gamma pass rate with 3%/3mm criteria ($>94\%$) for all clinical modulated fields was achieved for each of the prototype detectors compared to reference dosimeters in the transit geometry. The water equivalent dose response achieved overcomes a major limitation of implementing in vivo dosimetry with current EPIDs. The imaging performance of both dual detector designs was approximately the same as the standard EPID. The dual detector configuration was operated simultaneously as both imager and dosimeter without significant compromise in the performance of either device. Dual detector design decouples the imaging and dosimetry functions so that each can be optimized without compromising the other, providing more flexibility for future improvements in radiotherapy treatment verification systems. The improvement to existing standard EPID design would facilitate a superior system for simultaneous geometric and dosimetric treatment verification.

A simple model for comparing transit dosimetry with a conventional treatment planning system (TPS) was proposed and implemented. Excellent agreement was achieved in measured dose response when compared with TPS-calculated portal dose images. No additional EPID modelling was required, thereby removing the uncertainty in modelling the complex dose response of standard EPIDs. The water equivalence of the hybrid dosimeter approach provides a means of direct comparison of the plan specific treatment planning system (TPS) dose calculation and measurement.

Part (ii) Helical TomoTherapy HI-ART[®] - Potential HT delivery errors associated to the mechanical system were introduced by simulation in order to understand the potential impact of these errors on patient dosimetry. Commercial dosimetry systems sensitivity to detect delivery errors were then tested. An exit detector DQA (delivery quality assurance) tool for HT pre-treatment verification was also developed to overcome some of the limitations of phantom based verification systems.

Several potential HT delivery errors associated to the mechanical system were simulated for ten nasopharynx radiotherapy treatment plans. Plans with intentionally introduced errors were compared with the equivalent 'no error'. Results demonstrated that most of the clinically relevant errors are prevented by machine interlocks. Exceptions to this were dose differences due to couch position and the secondary interlock for jaw position. The investigation suggested that interlock thresholds for jaw position (secondary interlock) and couch speed should be monitored more precisely than monitored currently to avoid clinically rel-

evant delivery errors. This work has established a framework to characterize HT machine delivery errors and their clinical significance. This framework could be applied to any patient dataset to determine a given institutions plan specific delivery error threshold as well as validate plan robustness for a given machine QA tolerance or determine clinically relevant HT QA tolerances.

All the error plans that were determined as clinically relevant for jaw width, couch speed and MLC errors were measured with two commercial dosimetry systems (MatriXX^{Evolution} and ArcCheck). The Wilcoxon signed rank test indicated that no statistically significant differences were found in detecting the simulated delivery errors between these two dosimetry systems ($p > 0.05$, 95% confidence level). Both dosimeters were able to pick up clinically relevant delivery errors except the ArcCHECK with couch speed up to 2.5% and jaw width up to -1 mm. This work provides understanding of a widely used commercial dosimetry system's sensitivity to detect clinically relevant delivery errors as well as their inherent limitations.

An in-house exit detector DQA tool was developed and validated. Excellent agreement in global gamma pass rate with 2%/2mm criteria ($> 95\%$) between planned and reconstructed dose was achieved using this tool. The close agreement of measured ion chamber ($< 1.5\%$) to reconstructed dose computed by exit detector DQA tool on the 'cheese' phantom validated the accuracy of dose reconstruction inside the patient. The mean time for performing DQA on the 112 clinical plans was 24.7 ± 3.5 minutes using the proposed tool compared to 39.5 ± 4.5 minutes for phantom based verification system demonstrating the efficiency of exit detector DQA tool. The sensitivity to detect MLC errors was demonstrated. The exit detector DQA tool offers a direct and comprehensive solution with the opportunity to visualize the clinical significance of MLC delivery errors. This tool offers powerful advantages for supplementing existing patient specific DQA with specific utility for patient cases where field delivery geometry exceeds the size of commercial dosimetry measurement systems.

KEYWORDS: Dual detector, Waterequivalent EPID, Transit dosimetry, On board exit detector

Acknowledgements

Undertaking my PhD has been a very enjoyable and challenging experience. I would firstly like to thank my thesis supervisor Prof Peter Metcalfe, who offered me the opportunity to enrol in a PhD at the centre for Medical Radiation Physics, Engineering Physics, Faculty of Engineering, University of Wollongong. I wish to thank Prof Peter Metcalfe, for being a fantastic mentor for my clinical research. His easy-going nature and thirst for knowledge has made it a pleasure and an honour to work for him. His decades of experience and vast knowledge have provided excellent focus for my work. Thank you to Prof. Anatoly Rosenfeld, your innovative ideas and detailed knowledge and experience of dosimetric methods were invaluable during the research. I am also extremely grateful for allowing me to loan the prototype equipment for my experiments. The real inspiration for this PhD came from my local mentors Dr. Philip Vial and A/Prof. Lois Holloway. They have provided enthusiasm, support, wisdom and patience which has been of enormous benefit to me both professionally and personally. Both of them have been motivating clinical supervisors who encouraged the highest standards of research. I am very grateful for the clinical knowledge and experience I gained working with both of them whether it was late hours doing experimental work or manuscript reviewing. Phil's efforts to acquire the research EPID, prototype scintillators, his EPID dosimetry expertise and dedication to the project as a whole have been instrumental throughout. I also wish to thank to Dr Mark Geurts for his collaboration and valuable input to Tomotherapy delivery error simulation work.

I thank Dr Marco Petasecca , Dr Dean Cutajar and other CMRP members for their many hours spent on the prototype detector systems for my measurements. I also thank Dr. Aimee McNamara and Dr. Sam Blake for helping me analyse some of my data and providing some code. Thanks to all of my professional colleagues at Liverpool and Macarthur Cancer Therapy Centres for their support over the years. In particular, Dr. Aitang Xing for helping

me with software coding. I am especially grateful to Mr. Gary Goozee, director medical physics for allowing me to enrol as a PhD student and supporting to present my research work at domestic and international conferences. Dr Amy Walker for sharing her LaTeX skill and helping me in troubleshooting in the final journey of PhD write up.

My wife Pornima, and my daughter Mahi deserve the most thanks for their patience. They have made many sacrifices as I spent many hours away from home for my research and studies.

Lastly my father Mr. Ashok Deshpande and mother Alka Deshpande for having left me a seemingly endless supply of luck. To them I dedicate this thesis for teaching me to aim for excellence.

Publication List

S Deshpande, S Alhujaili , P Vial , L Holloway , M Petasecca , A Rosenfeld , P Metcalfe, *Silicon Array Dosimeter in Situ with Electronic Portal Image Device for Simultaneous Transit Dose and Image Verification in Radiotherapy*, *Physica Medica*, **(In Submission)**

S. Deshpande, A. Xing, L. Holloway, P. Metcalfe, P. Vial, "Clinical implementation of an in-house Exit detector-based dose reconstruction tool for Helical Tomotherapy delivery quality assurance" , *Medical Physics*, **(Under Review)**

S. Deshpande, A. Xing, L. Holloway, P. Metcalfe, P. Vial, "A simple model for transit dosimetry based on a treatment planning system and a water equivalent EPID" , *Medical Physics*, **(Under Review)**

S. Deshpande, M. Geurts, P. Vial, P. Metcalfe, L. Holloway, "Sensitivity evaluation of two commercial dosimeters in detecting helical Tomotherapy treatment delivery errors", *Physica Medica*, **(Accepted for publication)**

S. Deshpande, M. Geurts, P. Vial, P. Metcalfe, M. Lee, L. Holloway, "Clinical significance of treatment delivery errors for helical Tomotherapy nasopharyngeal IMRT", *Physica Medica*, 33, 159-169 (2017)

S. Deshpande, L. McNamara, L Holloway, P Metcalfe, P Vial, "Feasibility study of a dual detector configuration concept for simultaneous megavoltage imaging and dose verification in radiotherapy", *Medical Physics*, 42, (4), 1753-1764 (2015)

S Alnaghy, **S. Deshpande**, D Cutajar, A Rosenfield, P Metcalfe , "In-Vivo Endorectal

Dosimetry of Prostate TomoTherapy® Using Dual MOSkin™ Detectors", *Journal of applied clinical medical physics*, 16, (3), 107-113 (2015)

A. Xing, S Arumugam, **S. Deshpande**, A George, P Vial L Holloway, "Evaluation of 3D Gamma index calculation implemented in two commercial dosimetry", *Journal of Physics Conference Series*, 573, 012054 (2015)

A. Xing, **S. Deshpande**, S Arumugam, A George, P Vial L Holloway, "Is a quasi-3D dosimeter better than a 2D dosimeter for Tomotherapy delivery quality assurance? ", *Journal of Physics Conference Series*, 573, 012077 (2015)

A. Xing, S Arumugam, **S. Deshpande**, A George, L Holloway, G Goozee, "Streamlining EPID-based IMRT quality assurance: auto-analysis and auto-report generation", *Journal of Physics Conference Series*, 489, 012084 (2014)

S. Deshpande, A. Xing, P. Metcalfe, L. Holloway, P. Vial, "Dose calibration of EPIDs for segmented IMRT dosimetry", *Journal of applied clinical medical physics*, 15, (6), 103-118 (2014)

S J Blake, L. McNamara, **S. Deshpande**, L Holloway, P B. Greer Z Kuncic, P Vial, "Characterization of a novel EPID designed for simultaneous imaging and dose verification in radiotherapy", *Medical Physics*, 40, (9), 091902-1-11 (2013)

Conference Presentations

S Deshpande, S Alhujaili , P Vial , L Holloway , M Petasecca , A Rozenfeld , P Metcalfe, *Silicon Array Dosimeter in Situ with Electronic Portal Image Device for Simultaneous Transit Dose and Image Verification in Radiotherapy*, Oral presentation, Annual Meeting of the American Association of Physicists in Medicine, Washington DC, USA, 2016

S Deshpande, M W Geurts, C R Hansen, P Metcalfe, P Vial, D Thwaites, L Holloway, *Clinical significance of treatment delivery errors for helical TomoTherapy lung stereotactic ablative radiotherapy plans - a dosimetric simulation study*, Oral presentation, International Conference on the use of Computers in Radiation Therapy, London, UK, 2016

S Deshpande, A. Xing, P Metcalfe, L Holloway, P. Vial, *Can the water equivalent electronic portal imaging device (EPID) simplify the implementation of EPID in vivo dosimetry?*, Oral presentation, Med Phys15, Sydney, Australia, 2015

S Deshpande, P Metcalfe, L Holloway, P. Vial, *Sensitivity evaluation of two commercial dosimeters in detecting helical Tomotherapy treatment delivery errors*, Poster presentation, Annual meeting of Engineering and Physical sciences in medicine conference, Wellington, New Zealand, 2015

S Deshpande, S Blake, P Metcalfe, L Holloway, P. Vial, *Incorporating the water equivalent EPID in radiotherapy treatment planning system for In-vivo dosimetry*, Poster presentation, American Society for Radiation Oncology, San-Antonio, USA, 2015

S Deshpande, S Blake, A Xing, P Metcalfe, L Holloway, P. Vial, *Evaluation of a novel EPID design for transit dosimetry*, Poster presentation, Electronic Patient Imaging, Aarhus, Demark, 2014

S Deshpande, S Blake, A Xing, P Metcalfe, L Holloway, P. Vial, *Clinical significance of treatment delivery errors for Tomotherapy treatment- a dosimetric simulation study*, Combined Scientific Meeting, Melbourne, Australia, 2014

S Deshpande, A. George, A. Xing, L. Holloway, P Metcalfe, P Vial, M Geurts, *Sensitivity of three commercial dosimeters to delivery errors in helical TomoTherapy*, Electronic poster, 2nd ESTRO Forum, Geneva, Switzerland, 2013

S Deshpande, L. Holloway, P Metcalfe, P. Vial, *An Integrated 2-dimensional Dosimeter and Electronic Portal Imaging Device for In Vivo Dosimetry: A Feasibility Study*, Poster presentation, Annual meeting of American Society for Radiation Oncology, Boston, USA, 2012

S Deshpande, P. Vial, L. Holloway, P. Metcalfe, *Image Acquisition and Processing Characteristics of a Siemens EPID: Potential Problems for EPID Dosimetry*, Annual meeting of American Association of Medical physics, Vancouver, Canada, 2011

Invited Talks

S. Deshpande, *Clinical significance of the Tomotherapy delivery error for complex Head and Neck IMRT plans*, Presented at the Annual meeting of Association of Medical Physics in India, Loni, India, Nov 2014

Nomenclature

2D	Two Dimensional
3DCRT	Three Dimensional Conformal Radiotherapy
AC	ArcCHECK
AP	Anterior Posterior
CAX	Central Axis
CCD	Charge Coupled Device
CMRP	Centre for Medical Radiation Physics
CNR	Contrast to Noise Ratio
CP	Control Points
CSI	Cranio Spinal Irradiation
CT	Computed Tomography
DQA	Delivery Quality Assurance
EBRT	External Beam Radiotherapy
EPIDs	Electronic Portal imaging Devices
ESTRO	European Society for Radiotherapy and Oncology
FFF	Flattening Filter Free
FOV	Field Of View
GTV	Gross Tumour Volume

HT	Helical TomoTherapy
ICA	Ionisation Chamber Array
ICRP	International Commission on Radiological Protection
IGRT	Image Guided Radiotherapy
IMAT	Intensity Modulated Arc Therapy
IMRT	Intensity Modulated Radiation Therapy
kV	Kilo Voltage
linac	Linear Accelerator
LSF	Leaf Spread Function
MAT	MatriXX ^{Evolution}
MC	Monte Carlo
MLC LOT	Multi Leaf Collimator Leaf Open Time
MOSFET	Metal Oxide Semiconductor Field Effect Transistor
MP	Magic Plate
MU	Monitors Unit
MVCT	Mega Voltage Computed Tomography
NMR	Nuclear Magnetic Resonance
NTCP	Normal Tissue Complication Probabilities
NT	Normal Tissue
OAR	Organ At Risk
OBD	On Board Detector
PDI	Predicted Dose Image
PMMA	PolyMethylMethAcrylate

PRF	Pulse Repetition Frequency
PSA	Plastic Scintillator Array
PSM	Pixel Sensitivity Map
QA	Quality Assurance
QOL	Quality Of Life
RT	Radiotherapy Treatment
S&S	Step and Shoot
SDD	Source to Detector Distance
SSD	Source to Surface Distance
SW	Sliding Window
TCP	Tumour Control Probabilities
TLD	Thermo Luminescent Dosimeter
VMAT	Volumetric Modulated Arc theeapy
WE-EPID	Water Equivalent EPID
WHO	World Health Organisation
XML	eXtensible Markup Language

Chapter 1

Introduction

The main objective of effective radiotherapy treatment is to deliver high radiation doses to kill cancer cells, whilst limiting dose and hence toxicity to normal tissues (NT). Inaccurate radiotherapy can result in ineffective treatment or serious harm to the patient. Recent introduction of technology advances such as intensity modulation radiotherapy (IMRT), volumetric modulated arc therapy (VMAT) and Helical TomoTherapy HI-ART[®] (HT) have increased the achievement of these objectives [2–4]. Due to superior dosimetric conformity of these techniques, their role has further extended to hypo-fractionated treatments. These complex treatments are rapidly becoming the standard of care worldwide [1] because: i) tumour control can be increased by dose escalation, using dose distributions much more closely conformed to complex tumour shapes [5, 6]; ii) patient quality of life (QOL) is enhanced by reduced risk of treatment-related toxicities by improving normal tissue NT sparing [7, 8]; and iii) safe re-irradiation is becoming increasingly possible due to increased dose conformity of the techniques [9–11].

Many methods of achieving dose modulation have been proposed and applied to clinical practice. The IMRT technique holds the beam direction constant during irradiation and indexes the collimator shape to a fraction of the total prescribed monitors unit (MU) for that direction. In another implementation called VMAT the gantry moves during the irradiation, indexing the collimator shape and gantry angle to the delivered dose. The radiation source of the HT system is a linear accelerator (linac) mounted on a rotating gantry similar to a CT scanner (Figure 1.1 b). Radiation is delivered to the patient using helical delivery, obtained by concurrent gantry rotation and couch/patient travel. The IMRT and VMAT techniques utilise a conventional C-arm linac (Figure 1.1 a) with no couch/patient travel while radiation dose is delivered.

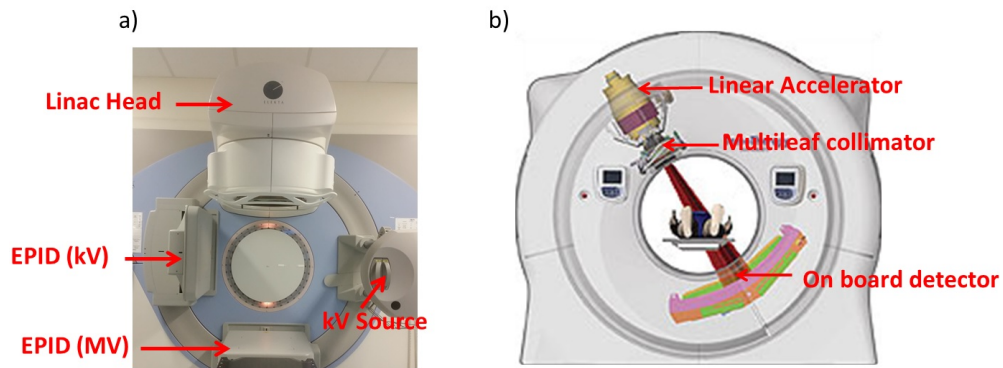


Figure 1.1: Radiation therapy treatment machines a) C-arm conventional linear accelerator and b) Helical TomoTherapy

Advanced radiotherapy technologies and methods are complex. In addition to their complexity, each of them has its own unique features that require different considerations for their clinical implementations. Misadministration of advanced radiotherapy delivery techniques are more difficult to detect and can possibly lead to poor outcomes for some patients. In response to increasing treatment complexity, quality assurance (QA) bodies throughout the world acknowledge that patient treatment verification, especially through in vivo dosimetry, is highly desirable for optimal patient safety during radiation treatment [12–15].

Recent growing interest in hypo-fractionated treatments, with steeper effective dose-response curves [16] may imply stricter dose and geometry requirements. Tumour motion during radiotherapy poses an additional challenge for accurate dose delivery [17, 18]. Development of novel techniques to compensate motion by MLC tracking [19] and couch tracking [20] are underway. Motion compensation using tracking occurs during treatment with the radiation beam on. These and other similar advances will continue to increase demands for robust dosimetric and geometrical treatment verification to ensure patient safety and treatment accuracy.

The widespread availability of integrated image guided radiotherapy (IGRT) systems has resulted in reduced geometric uncertainties prior to treatment. The kilovoltage (kV) imaging devices attached to linacs and providing superior soft tissue contrast have improved patient and target position verification prior to treatment. They do not utilise the treatment beam and therefore do not directly verify the treatment delivery in real-time. By utilising the kV imaging device, monitoring of soft tissue by tracking the implanted fiducials during treatment has been demonstrated by a few studies [21, 22]. The applicability of this tool is

currently limited to those anatomical sites where fiducial markers can be implanted safely. Electronic portal imaging devices (EPIDs) are capable of recording an x-ray image of the patient with the treatment beam, and therefore the device that can directly verify treatment delivery. This unique capability of megavoltage (MV) EPIDs recording both the patient image (i.e. geometry) and beam intensity transiting from patient (i.e. dose) during treatment has the potential to play an important role in the future development of treatment verification QA devices for linacs.

A review by van Elmpt et al [23] gives an excellent overview of the diverse applications for EPIDs in clinical dosimetry and their clinical implementations up to 2008. Despite the potential, the clinical implementation of EPIDs for dosimetry has been slow. EPID design has been optimised for imaging applications and therefore has severely limited their routine clinical use as dosimeters. This is due to mainly the energy dependent response of EPIDs [24–27]. The problem becomes worse when measurements are conducted in vivo due to the additional scatter from the patient recorded by the EPID [28]. A large body of reported research from several groups on EPID dosimetry is focused on development of methods to account for energy response either with complex algorithms or Monte Carlo computations [25, 28–34]. Current research in EPID technology is focused on developing more efficient detectors [35, 36] for imaging using very high density scintillators which are likely to be even more problematic for dosimetry.

A small body of research was focused on developing a novel EPID design. The goal of this EPID design is for the EPID to act directly as a dosimeter rather than an imager [27, 37–40]. The former scenario (i.e. dosimetry with standard EPID) typically necessitates a complex detector characterisation and calibration scheme along with custom software to convert portal images into dose images. The latter scenario has seen detector prototypes that, while capable of performing accurate patient dosimetry, suffer from decreased x-ray detection efficiency thus inhibiting their use for imaging. In both cases, proposed detectors have not been suitable for applications in both imaging and dosimetry. Therefore the focus of development work for the next generation treatment verification device should be to provide the capability to simultaneously verify both location and quantity of the dose delivered during treatment to address the demand and challenges in modern radiotherapy technique verification. Such treatment verification tools can provide a record of delivered dose that could be used to assess the effectiveness of the new techniques.

HT (Figure 1.1 b) uses a dynamic delivery in which the gantry, treatment couch, and multileaf collimator leaves are all in motion during treatment. The dosimetric impact due to variation in delivery parameters has been well studied and reported [41–46] for IMRT and VMAT delivery. However, the clinical impact due to variation of HT delivery parameters including the effect on the resulting patient dose distributions has not yet been studied. Most of the recommended HT QA procedures and tolerances in AAPM Task Group 148 [47] were adopted from the collective experience of the task group members; vendor designed QA tests and from previously published reports [48–50]. It is unclear that the recommended HT QA tolerances had any clinical relevance.

The HT clinical implementation and treatment verification is performed using either two dimensional (2D) or quasi three dimensional (3D) dosimetry systems. Most clinics perform phantom-based measurement (pre-treatment verification) as an ongoing QA with the aim to detect errors before treatment delivery and correct them at the earliest opportunity. Several studies evaluated sensitivity of commercially available dosimetry system to detect intentionally introduced potential delivery errors for IMRT and VMAT delivery [46, 51–58]. Different dosimetry systems demonstrated varying ability to reliably identify errors [58]. All of the above detector sensitivity studies focused on the MLC positional accuracy, collimator or gantry rotation and dose errors for C-arm linac based treatment and may therefore not be relevant to the different delivery mechanism of HT machines. The only study on detector sensitivity to detect HT delivery error using the ArcCHECK dosimeter was reported by Templeton et al [59]. No comprehensive comparison of different detectors for HT treatments has been undertaken. Therefore, a comprehensive error detection framework for HT includes: a systematic simulation of potential delivery errors, modeling of their clinical impact to determine clinically relevant errors, and comparison to current commercial dosimeter's ability to identify them. This will produce clear guidelines on a robust treatment verification system for clinical implementation and for the choice of the most appropriate dosimetry system for individual clinical situations.

The phantom-based verification systems are very laborious and time consuming. Clearly, there is need for a means of overcoming the increased demands on physics resources due to the additional patient specific QA typically performed using commercial phantoms [60, 61]. Another limitations of phantom-based verification systems is that they do not provide a link between QA results and its impact on patient dose. Few commercial dosimetry systems now facilitate the dose reconstruction based on dose measured in phantom to evaluate the

impact on patient dose. These algorithms contain significant approximations and their limitations have been demonstrated by recent studies [62, 63]. The unique HT delivery is often tasked with treating long or otherwise large fields such as cranio-spinal irradiation and total marrow irradiation. This large field delivery geometry exceeds the size of commercial dosimetry measurement systems. Some researchers [64, 65] proposed a QA procedure using an on board exit detector on HT. This involves applying a simple method to verify the MLC performance as a pre-treatment verification tool and demonstrated efficiency. Further development is warranted to improve the on board exit detector approach by supplementing with dose reconstruction which would overcome the current limitation of the phantom measurement based QA approach.

Testing each sub-component for sources of errors in the patient treatment pathway is becoming extremely difficult. Accurate verification of treatment delivery becomes increasingly important and challenging. Despite the rapid evolution in our ability to deliver highly conformal x-ray beams, and guide treatment using modern imaging technologies, there are still shortcomings arising in the radiotherapy process that limit the ability to predict patient outcomes. Arguably one of the largest uncertainties is the current inability to quantify the actual dose delivered to the patient. Dose verification is also a critical component of adaptive radiotherapy, as it provides a measure of delivery success.

This dissertation investigated treatment verification for two different radiotherapy delivery systems. The first part developed and characterised novel prototypes for treatment verification on a conventional linear accelerator (linac). Novel prototypes were developed to combine geometric and dosimetric verification in a single system. Also, the underlying causes of under dose response at small MU for standard EPID were investigated.

The second part investigated clinical HT treatment verification. Specifically, simulate potential HT delivery errors associated with the mechanical system to understand the impact of these errors on patient dosimetry, and understanding commercial dosimetry systems sensitivity to detect clinically relevant delivery errors as well as their inherent limitations. Also, the development and clinical implementation of an exit detector DQA (delivery quality assurance) tool for HT pre-treatment verification to overcome some of the limitations of phantom-based QA systems was investigated.

1.1 Aims and Objectives

This project aims to investigate two different components of treatment verification the first for a conventional linac and the second for HT based treatment delivery as outlined below:

1. Dose characterisation and development of novel prototype hybrid EPID based dosimeters for treatment verification for a conventional linac system

Research questions:

- (i) What are the underlying causes for EPID dose under-response at smaller monitor units?*
- (ii) Can the EPID design be improved to provide a superior system for simultaneous geometric and dosimetric treatment verification?*
- (iii) Can an EPID based hybrid novel prototype configuration overcome the current limitations of implementing a-Si EPID based dosimetry in the clinic?*

In Chapter 3, EPID dose under-response at small monitor units and its underlying causes under various combinations of linac, EPID design, image acquisition settings and different treatment delivery modes (static open and segmented beam) were investigated. This work resolved some of the inconsistencies in the literature regarding EPID dose response and also improved the understanding about consideration of the dose non-linearity effect in pixel-to-dose calibration methods for EPID-based IMRT dosimetry.

Chapters 4 and 5 outlined the development and characterisation of novel prototypes that can perform simultaneous geometric and dosimetric treatment verification. The approach of novel prototype design is based on optimisation of EPID detectors for radiotherapy applications to overcome the current challenges of the energy dependent response (problematic for dosimetry) without compromising imaging performance.

Chapters 6 discussed a simple model for implementing comprehensive transit dosimetry as a means of in vivo dose verification utilising a novel prototype (water-equivalent dosimeter) and a conventional treatment planning system (TPS). This approach removes the additional uncertainty introduced by modelling the complex dose response of standard EPIDs and the requirement of development of an additional software tool to calcu-

late the predicted dose at EPID plane which resolves current limitations of implementing a-Si EPID based dosimetry.

2. Assessment of current detector systems and development of an on board exit detector dosimetry tool for efficient pre-treatment verification for HT

Research questions:

- (i) What magnitude of changes to delivery parameters will have clinical impact on the resulting dose distributions?*
- (ii) Are the available commercial dosimeters sensitive to clinically relevant delivery errors for HT?*
- (iii) Can an on board exit detector system achieve equivalent or improved sensitivity, robustness and efficiency compared to the current standard phantom-based measurement for pre-treatment verification?*

Chapter 7 outlined a framework to characterize HT machine delivery errors and their clinical significance. This framework could be applied to any patient dataset to determine a given institutions plan specific delivery error threshold as well as validate plan robustness for a given machine QA tolerance or determine clinically relevant HT QA tolerances.

Chapter 8 assessed the sensitivity of commercially available dosimeters to intentionally introduced delivery errors that may occur based on machine malfunction or calibration errors. This improves the understanding of a widely used commercial dosimetry system's sensitivity to detect HT delivery errors.

Chapter 9 outlined the development and clinical validation of an in-house HT on board exit detector based tool supplemented with dose reconstruction. This tool has potential to overcome the limitations of phantom-based measurement QA. A comprehensive clinical evaluation is presented to assess this tool's accuracy, robustness and efficiency.

Chapter 2

Literature Review

2.1 Cancer and the role of radiotherapy

"Nothing in life is to be feared, it is only to be understood. Now is the time to understand more, so that we may fear less" Marie Curie

Cancer is a major public health problem worldwide as it accounts for a quarter of all deaths and surpasses heart disease as the leading cause of death for people under the age of 85 [66]. In Australia, it is the second most frequent cause of death in 2009, causing 29% of all deaths [67]. It is estimated that half of all cancer patients should receive radiotherapy at some point during the course of the disease if evidence-based guideline recommendations were applied to the population [68–70]. Moreover, management of cancer is a rising concern in an ageing population and is increasingly important in developing countries. The increasing rate of cancer occurrence in Australia and the need to improve the ratio of actual to optimal utilization of radiotherapy, suggests that the utilization of radiotherapy is likely to increase in the future.

2.2 History of external beam radiotherapy

The late 19th century was a prestigious period when three Nobel prizes were awarded for discoveries related to ionizing radiation. In December 1895, Röntgen discovered X rays (Figure 2.1) quickly followed, in June 1896, by Becquerel who discovered natural radioactivity and in 1898, by Curie who isolated radium [71]. These three fundamental scientific

discoveries paved the way for the two main techniques of radiotherapy: teletherapy, using long source to surface distance (SSD), and later called external beam radiotherapy (EBRT); and brachytherapy, based on a short SSD, initially delivered with radium and later with 50 kV X rays [72]. This era was also successful when considering the rapid transfer from bench to bedside. The first patients with cancer were treated with radiation in 1896, six months after Röntgen's discovery, for gastric cancer and basal-cell carcinoma in France, America and Sweden [73, 74]. The harmful effects of radiation also became apparent very quickly [75], and were taken into account to optimize the therapeutic ratio and stimulate radiation protection. By 1913, manufactured radium tubes or needles and Coolidge tubes were designed to allow the routine use of radiotherapy in the fight against cancer [76]. Since that time, the aim of radiotherapy has always been, from a physical point of view, to deliver as close as possible to 100% of the dose in the gross tumour volume (GTV) and close to no radiation to the organs at risk (OAR). A major achievement made during that period was the capacity to measure the radiation dose using ionizing chambers [77] with the first accurate dose unit (the Röntgen unit) in 1932. First, the different patterns of intrinsic radiosensitivity among cells and tissues were demonstrated by Bergonié and Tribondeau in 1906 [78]. Second, the role of fractionation to create a beneficial differential effect between cancer and normal cells was discovered [79]. In 1934, Coutard proposed a fractionation scheme of 200 Röntgen per fraction, five times per week, which was converted into the standard contemporary 2 Gy/fraction scheme and, more recently, was well fitted with the α/β model to describe its biological effect [80]. In 1928, the international Commission on Radiological Protection (ICRP) was created to address the question of radiation protection [81].

Following the discovery of artificial radioactivity, and further to Johns and Cunningham's work [82], cobalt 60 was adopted as an alternative source of high-energy γ rays for teletherapy, with a higher dose rate than could be achieved with radium. The first telecobalt unit was installed in 1948 in Hamilton, Canada (Figure 2.1) and subsequently used widely for 2 - 3 decades [83]. Linacs were developed before and during the second world war and the first electron accelerator designed for medical use was installed in the Hammersmith hospital, London in 1953 [84]. The first patient treated in North America with a 6 MV linac was at Stanford in 1956 [85]. Both telecobalt and linac based mega-voltage (MV) therapies allowed skin-sparing application of radiation dose to deep tumours in the pelvis and thorax for the first time. The first computed tomography (CT) image of a patient was acquired in 1971 [86] and in the 1980s was being implemented in radiotherapy departments. This permitted more accurate definition of the tumour and healthy tissues. Dose distributions could

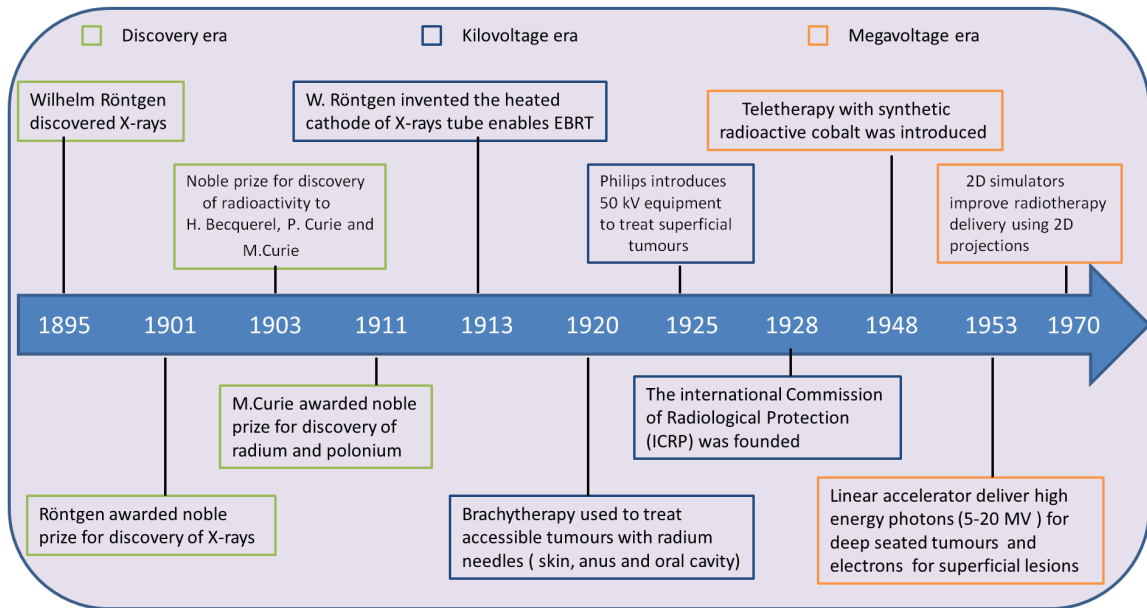


Figure 2.1: Timeline 1 | Early landmark discoveries in radiotherapy from Thariat et al [1]

now be sculpted in three dimensions (3D) using treatment planning systems (TPS) with ‘beams-eye-view’ and linacs with multileaf collimators (MLC). Three dimensional conformal radiotherapy (3DCRT) saw many tumour sites benefit from higher doses and improved OAR sparing [87].

2.3 Advanced radiotherapy techniques

Intensity modulated radiation therapy (IMRT) was proposed by Brahme [88] in 1988 and started entering clinics due to technology advances (e.g. MLC) in the late 1990s [89]. The IMRT technology provided an ability to precisely shape the dose distribution to the target while avoiding the healthy tissues [90]. There were a variety of different techniques for delivering IMRT including; beam compensators [91], and MLCs in both step and shoot [92] and sliding window mode [93], serial tomotherapy [94] and helical tomotherapy (HT) proposed by Mackie [95]. Volumetric modulated arc therapy (VMAT) first proposed by Yu [96] in 1995 also named intensity modulated arc therapy (IMAT), is a form of rotational IMRT and has become standard of care in many centres. This was later refined by Otto [97] to improve the optimisation technique required to generate a plan. It is noteworthy that these techniques also adapted to deliver simultaneous integrated boosts yielding higher

doses to the GTV without increasing the overall treatment time. There is growing interest to utilise these advanced techniques to deliver the radiation dose in a single or few fractions (< 5 fractions) often referred to as stereotactic radiotherapy commonly known as stereotactic ablative radiotherapy (SABR). SABR has shown superior and promising outcome over surgical procedures or in non-operable patients [98–100]. These complex treatments are rapidly becoming the standard of care worldwide because: i) tumour control can be increased by dose escalation, using dose distributions much more closely conformed to complex tumour shapes [5, 6] ii) patient quality of life (QOL) is enhanced by reduced risk of treatment-related toxicities by improving normal tissue (NT) sparing [7, 8]; and iii) safe re-irradiation is becoming increasingly possible due to increased dose conformity of the techniques [9–11].

Image guided radiotherapy (IGRT) is an umbrella term used to describe advanced EBRT techniques that integrate various modern imaging technologies with radiotherapy planning and delivery. Within IGRT, pre-treatment imaging is typically used to monitor patient setup with the goal of improving the accuracy of treatment delivery [101]. If using image guidance reduces the geometrical uncertainties associated with target localization, then it may be possible to reduce the margin of healthy tissue being treated around the clinical target volume [102]. Several radiation-based and non radiation-based imaging systems are currently used in IGRT [103–106]

Electronic portal imaging devices (EPIDs) are a type of radiation-based imaging system that may use either the MV therapy beam or a gantry-mounted kV x-ray source to acquire 2D planar images to verify patient set up prior to treatment. These images may then be used in real time to guide treatment delivery for a patient or may be reviewed offline at a later time [101, 102, 107, 108]. Developments in imaging technology coupled with advances in computer technology have fundamentally changed the processes of tumour targeting and radiation therapy planning. Radiation oncologists face particular problems in treating parts of the body where organs and tumours may move during treatment. Movement of the target due to respiration or for any other reason during treatment increases the risk of missing the targeted area or under-dosing the area. As the delivery of the radiation dose becomes more and more precise, movements of organs and tumour have a significant effect on the accuracy of the dose delivery. This is particularly dramatic for tumours located in the chest, since they move during breathing. However, movement is not only an issue with tumours located in the chest; tumours in the larynx, abdomen (liver), prostate and bladder and in the pelvis in

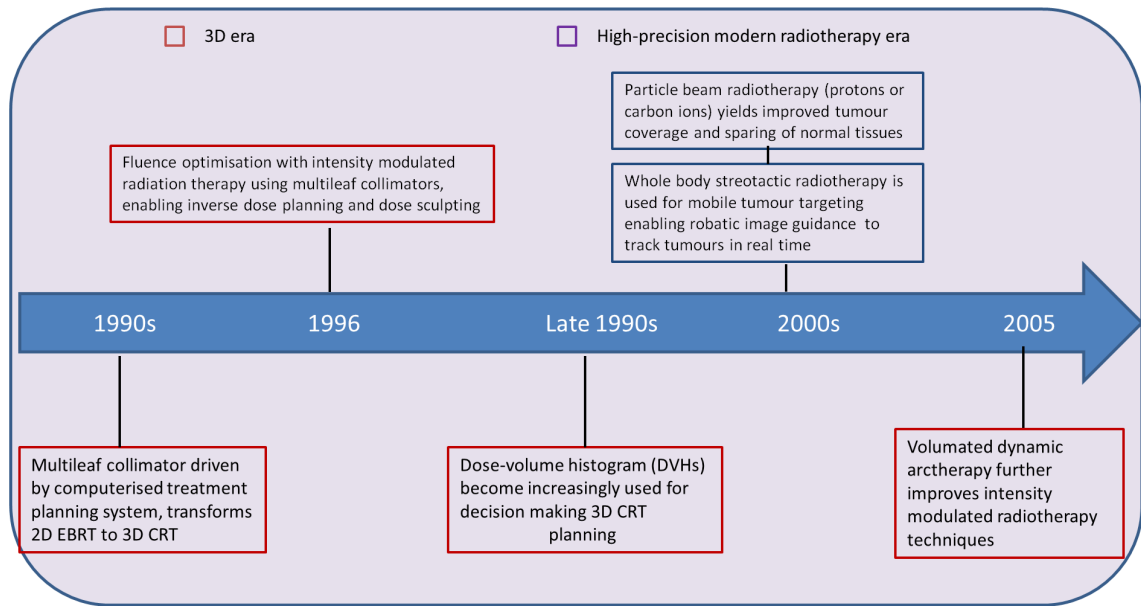


Figure 2.2: Timeline 2 | Advances in radiotherapy technology from Thariat et al [1].

general also move during and between treatment applications. The introduction of IMRT, VMAT and SABR procedures brings special physics problems. For example, calibrations have to be performed in small fields where the dosimetry is challenging, and no harmonized dosimetry protocol exists. Use of the correct type of dosimeter is critical and errors in measurement can be substantial [109]. Several new treatment machines provide radiation beams that do not comply with the reference field dimensions given in existing dosimetry protocols, thereby complicating the accurate determination of dose for small and non-standard beams. The introduction of highly precise collimators (and their use in IMRT), small fields, robotics, SABR delivery, VMAT and image guidance has brought new challenges for commissioning and quality assurance (QA). Existing QA guidelines are often inadequate for the use of some of these technologies. The new technologies are developing at a historically high rate (Figure 2.2). New commissioning and QA protocols do not follow that pace. Increasingly complex QA procedures require additional staff in adequate numbers in the radiotherapy centres that actually implement the advanced technologies. These advances do not come without a risk. IMRT, VMAT and SABR techniques are not just an add-on to the current 3DCRT process; they represent a new paradigm that requires the knowledge of multimodality imaging, setup uncertainties and internal organ motion, tumour control probabilities (TCP), normal tissue complication probabilities (NTCP), 3D dose calculation and optimization, and dynamic beam delivery of nonuniform beam intensities.

Advanced radiotherapy techniques are complex. Misadministration of advanced radiation delivery techniques is more difficult to detect and may lead to poor outcome. Therefore, their potential for improved effectiveness requires caution and a safety based approach. A robust and reliable system for treatment verification is desired to realise the potential clinical benefit.

2.4 Treatment Verification

Treatment verification has two important roles in radiotherapy: i) to mitigate mistreatments that result in adverse patient outcomes (patient safety); and ii) to optimise treatment outcomes by ensuring accuracy (treatment accuracy). Ensuring patient safety and treatment accuracy requires techniques to control both geometric and dosimetric accuracy.

Patient safety: Serious accidents due to errors do occur in radiotherapy and have resulted in fatalities [110]. A World Health Organisation (WHO) review of radiotherapy incidents between 1976 and 2007 [14] reported that the risk of injurious outcome to patients from errors was about 1500 per million treatment courses. There is considerable public concern about radiotherapy accidents. The potential dangers of implementing new radiotherapy technologies without sufficient safeguards have received wide publicity following the occurrence of several serious accidents [12, 111, 112]. Recent multicentre dosimetry studies in North America have had very poor results, with about one third of centres failing to meet the very generous global gamma criteria of 7% dose accuracy and 4 mm geometric accuracy [113]. Dosimetric errors of up to 22% were identified. The main cause of errors was identified as a combination of positional set-up errors, and incorrect configuration or implementation of MLC models in treatment planning systems (TPS) and clinical dosimetry.

Treatment accuracy: Accuracy requirements for radiotherapy are decided by compromising between what is practically achievable and what is necessary to achieve the treatment goals. There is a general consensus that the overall accuracy of radiation therapy should be within $\pm 5\%$ to the prescribed dose [114–116].

A wide variety of instrumentation and experimental methods are in use, and IMRT QA protocols continue to develop in an ad hoc manner [61] for both pre-treatment verification and in vivo dose verification. Often several different measuring devices are used in com-

bination to overcome the specific limitations of each device. Previous serious accidents [12, 111, 112], and many others, could have been avoided with accurate dose verification measurements acquired during treatment (in vivo dosimetry). It is highly likely that many more mistreatments and near misses go undetected [117–120]. The increased complexity of advanced techniques and workload may have an impact on treatment discrepancies [121]. The QA program in radiotherapy treatment (RT) diminishes uncertainties and inaccuracies in dosimetry, treatment planning, equipment performance and treatment delivery improving both dosimetric and geometric accuracy as well as precision of dose delivery. To address the increasing demands on geometric accuracy, the use of imaging for treatment verification has developed rapidly in recent years and provides submillimetre accuracy for daily patient setup and target localisation [101, 102, 122–127]. Image guided radiotherapy (IGRT) aids in tracking daily treatment setup to minimize geometric error. Verifying dose accuracy for modern treatments such as IMRT, VMAT, HT and SABR typically relies on pre-treatment dose measurements. This verification typically involves exporting the treatment fields from the patient CT scans on the TPS, and importing them onto a verification phantom CT scan. A verification phantom is usually an approximately cylindrical or cubic shaped object made from material that is approximately radiologically equivalent to water and designed to house various types of dose measuring devices within the phantom. The dose is then re-calculated for the phantom using the same treatment field. The calculated dose to a point, area, or volume within the phantom is recorded for comparison with a direct measurement of the dose obtained in the same phantom [61, 128–132]. The phantom-based verification is also performed to validate the accuracy of the TPS beam model and clinical implementation. This commissioning data is used to establish the baseline for QA tolerance and also streamline the ongoing pre-treatment verification QA program in the clinic. The pre-treatment QA process checks the correct transfer of the plan data to the linac and the accuracy of treatment plan delivery. The aim is to detect and correct errors at the earliest opportunity.

Dosimetry systems used in clinics vary widely and have varying levels of capability, sensitivity and limitations [46, 53, 133]. Moreover, pre-treatment measurements are time consuming and do not necessarily identify clinically relevant errors in dose delivery that may occur during the course of treatment. One of the limitations of phantom-based treatment verification QA is that it does not provide the connection between measurement results and how the patient dose distribution might be affected. In vivo dosimetry technique refers to measuring techniques for recording and verifying the dose actually received by patient during treatment. In vivo dosimetry helps to detect the major errors and to assess clinically

relevant differences between planned and delivered dose for each individual patient. In vivo dosimetry could help to limit the impact of a problem. In addition, it would identify and remove the systematic errors which could impact other patients. If no error is detected, in vivo dosimetry provides a confirmation record of correctly delivered dose within the expected tolerance. These factors are driving a growing demand for effective in vivo dose verification [118, 119]. Accurate in vivo dose verification will help overcome current concerns about the safety and accuracy of advanced treatment techniques.

2.5 Dose verification – instrumentation and methodology

The following sections briefly describe applications and limitations of some of the main dosimeters used for treatment verification.

2.5.1 Point dosimeters

A point detector is a dosimeter that integrates dose and reports a single dose value, often referred to as a point dose measurement. A point dose measurement has zero dimensions, but point detectors can often produce a signal as a function of time. The use of the most common types of point detectors in treatment verification is described below.

Ionisation chambers: Ionisation chambers have long been the gold standard for reference dosimetry in radiation therapy. Several IMRT guidance documents, text book chapters, and clinical studies have demonstrated an important role for ionisation chambers in patient dosimetry [60, 61, 109, 132, 134, 135]. Typically, ionisation chambers are placed in a central region of a phantom, or in a region corresponding to the uniform high dose area, which is then irradiated by all of the treatment beams. The ionisation charge reading is converted to dose with a calibration factor and the dose compared to the TPS calculation. Ionisation chambers are limited by the fact that they can only report dose to a point, or averaged over a small area.

TLDs and semiconductors: Thermo-luminescent dosimeters (TLD) and semiconductor diodes have been used in radiotherapy for many years [117, 136, 137]. The small size and solid state construction makes them well suited to in vivo dosimetry. The absence of any cables on TLDs is an added advantage for in vivo use. There is a time delay to obtain the mea-

surement results with TLDs but diodes can be read in real time. The theoretical principles and use of TLDs have been described previously [138, 139]. The theoretical principles and use of diodes for in vivo dosimetry have been described in reports [140, 141]. The use of semiconductor devices, including p-n junction diodes and Metal Oxide Semiconductor Field Effect Transistor (MOSFET) devices for dosimetry has been described by Rosenfeld [142]. MOSFETs can be made extremely small, making them suitable for high resolution measurements in brachytherapy plan verification in the in vivo setting [67, 143–146]. The *MOSkin*, a new MOSFET based detector designed by the Centre for Medical Radiation Physics (CMRP) has been shown to have promise as a real time in vivo dose monitoring device in the presence of dose gradients and modulated fields [147]. TLDs and diodes have been used for IMRT dosimetry, both in phantom measurements, and in vivo. Entrance or exit dose measurements conducted in vivo with TLDs or diodes can be used to verify individual fields but they are subject to large uncertainties due to the presence of dose gradients and modulated fields [148, 149].

2.5.2 2-dimensional dosimeters

Two dimensional (2D) detectors are able to measure dose or relative beam/fluence intensity to an entire plane. These types of detectors have become more widely used in radiotherapy because of the QA requirements of IMRT and dynamic or virtual wedge profile measurement. Some examples of two-dimensional detectors are given below.

Film: Film was one of the first types of dosimeters used in radiotherapy. The very high spatial resolution of film is an advantage for modulated treatment dosimetry. Various types of film continue to be widely used for IMRT. The two main types of film are radiographic and radiochromic. There are many challenges in obtaining accurate dose measurements with both types of film including, energy response, field size and depth sensitivity, film batch sensitivity differences, film orientation, processing and scanner variations. The future of radiographic film dosimetry is uncertain because the increased use of Electronic Portal Imaging Devices (EPIDs) and computed radiography screens in radiotherapy imaging has allowed many department to become filmless [150]. The improved coating of radiochromic films had overcome a number of issues related to dosimetry. Radiochromic films do not require chemical processing and are widely used for commissioning and for patient specific IMRT treatment verification [151] and treatment verification of SABR cases [152].

Detector arrays: Commercially available 2D detector arrays, either diode array [55, 153] or ionisation chamber arrays have been used for pre-treatment dosimetry of modulated fields [154–156]. Cilla et al. used an ionisation chamber array for a transit dosimetry phantom study using IMRT fields [157]. The use of a 2D detector as a transmission dosimetry device mounted onto the head of the linear accelerator have been demonstrated in previous studies [158, 159]. The 2D detector arrays tend to have good dose response characteristics for QA measurements but lack spatial resolution compared to other 2D dosimeters due to larger distance between detectors and also relatively large individual detector size. For example the detectors on the currently available arrays are at least 5 mm apart (centre to centre).

Alternative prototype 2D devices have been reported. A small prototype monolithic silicon segmented sensor has been manufactured and tested for radiotherapy dosimetry [160, 161]. The physical characteristics of plastic scintillating materials and their applications in radiotherapy have been extensively studied and reported in the literature [162–169]. These scintillators are manufactured using low-Z materials (i.e. low atomic number) and have been shown to respond in a nearly water-equivalent manner to both x-ray and electron beams in the energy range relevant for radiotherapy [162, 165, 166, 168, 169]. Prototype plastic scintillator sheets coupled to a Charge Coupled Device (CCD) camera have also been tested for radiotherapy and IMRT dosimetry [169–171].

The novel prototype named as ‘Magic Plate’ has been developed by Rosenfeld’s group at CMRP [172]. This prototype is a 2D semiconductor based detector specifically designed for treatment verification in transmission mode. CMRP are currently working on a miniature SRS mobile tracking version of this detector.

The potential of 2D chamber array dosimetry devices as a transit dosimeter which are typically used for pre-treatment QA have been demonstrated by a few researchers [173–175]. Prabhakar et al [126] proposed a novel approach of treatment verification in real time using a 2D MAPCHECK array attached to the treatment couch. None of the previous work used the 2D detector in series with EPIDs. In this dissertation, we investigated the novel configuration by combining dosimeter (ionisation chamber array or magic plate) and an imager (EPID) in series and used simultaneously. Chapters 4 and 5 investigated the hypothesis of dual detector concept where this configuration enabled measurement of the transit dose with (2D array dosimeter) without affecting the imaging performance of the EPID.

2.5.3 EPID

Current EPID designs contain a copper layer and a phosphor layer in combination with an amorphous silicon (a-Si) photodiode array. Optical photons are generated in the phosphor scintillator layer by incident radiation from the megavoltage photon beam and scatter from the copper plate. The optical photons create a signal in the photodiodes. This is known as the indirect EPID configuration. In this dissertation, this metal/phosphor EPID design is referred as a standard EPID.

Indirect EPIDs: EPIDs were introduced for patient position verification [176–178]. The idea of using EPIDs for dosimetry was realised in the 1980s [179]. Little was published on the topic until the mid 1990's. Since then the interest in EPIDs for dosimetry has increased rapidly [23]. The increasing research on EPID dosimetry coincided with the introduction of IMRT. EPIDs are well suited to IMRT dosimetry because they are high resolution, 2D digital detectors. EPIDs are available on most modern linear accelerators [23]. Different types of EPIDs have been clinically implemented, and these have been described in several review papers [177, 178, 180].

Dose response characteristics for a-Si EPIDs was studied and reported by a number of researchers [28, 181–185]. All these studies reported that EPIDs exhibit under response to dose at small monitor units (MU). The key studies of EPID dose response highlighted the inconsistent interpretation of EPID dose response characteristics. An under dose response correction was suggested using an empirical approach [181, 183] and applied on a pixel-by-pixel basis. These corrections are complex to implement accurately on a pixel-by-pixel basis due to the variations in time between segments and variation in dose per segment. The EPIDs under dose response is widely reported based on static open beam exposures, with little or no consideration for how accurately this behaviour translates to segmented IMRT. Chapter 3 investigates the EPID dose linearity under different combinations of linac, EPID design and acquisition system to understand the underlying causes of EPID under dose response at small MU. Also a simple pixel-to-dose calibration methodology for IMRT verification is described.

The current generation of commercially available EPIDs are indirect detection active matrix flat panel imagers, also known as amorphous silicon (a-Si) EPIDs [178, 180]. One limitation of the use of EPIDs for dosimetry purposes is the non water-equivalent response of imaging

detectors [26]. The non water-equivalent EPID response is associated with over-sensitivity to the low energy where the signal is influenced by the scatter within the bulk layers of the imager [24–27], and by patient generated low energy scatter.

A review by van Elmpt [23] gives an excellent overview of the diverse applications for EPIDs in clinical dosimetry and their clinical implementations up to 2008. Both pre-treatment and in vivo treatment verification may be performed by comparing the delivered dose distribution (measured with the EPID) to the planned distribution predicted using the TPS [29, 30, 118, 119, 186, 187]. Each of these dosimetry methods may be further categorized according to whether the detected fluence was reconstructed to give calculated dose in 2D [29, 186, 187] or 3D [30, 118, 119]

Different approaches were demonstrated to convert EPID signal to dose. The first approach applies empirical models to convert the measured grey-scale image of the EPID into a portal dose image [27, 188–192]. The second approach simulates or models the detector response, usually by Monte Carlo (MC) simulation [25, 33, 34, 193, 194] or by empirical models [192]. For accurate simulations, a detailed model of the EPID is necessary; however, accurate technical details are not always available, and often assumptions with respect to the construction and materials of the various layers are made. This requires longer dose calculation times and extra resource for development. One simple EPID dosimetry model previously demonstrated uses the ‘extended phantom’ concept to calculate a predicted dose image (PDI) at the EPID plane using the TPS dose to water model [195–199]. When used with standard EPIDs, this method still requires a separate EPID model to convert the measured EPID signal into dose to water (i.e. to model the complex dose response of the standard EPID). The potential of EPIDs for detecting various dose delivery errors has been well demonstrated in previous studies [119, 200–202]. Despite the large body of research dating back to the early 1990s and before, the reported use of clinical EPID-based in vivo dosimetry is still surprisingly limited to a small number of centres. To utilise the standard EPID as a dosimeter, requires extensive software development to integrate the various steps as outlined: i) To model dose response characteristics of a-Si EPID, ii) incorporate the dose response characteristics into a computation of predicted pixel values, or conversion from pixel values to dose in water with or without a back-projection dose reconstruction model to compute dose inside the patient, and finally iii) software tools to quantitatively compare predicted versus measurement based results.

Further, the changes in EPID technology over recent decades have not been driven by the technical demands of dosimetry, but by the need for improved imaging standards for patient positioning, such as enhancement in image quality and faster read-out [160, 161]. These efficient MV detectors generally consist of higher atomic number materials than current EPIDs, which is likely to make EPID dosimetry even less water equivalent and still more difficult to implement.

Direct EPID:

When the protective cover and all other materials covering the photodiode array, including the copper plate and the phosphor layer are removed the system is referred to as a ‘direct EPID’. The signal is produced by the interaction of the megavoltage photon beam directly within the photodiodes.

The modification of the indirect detection configuration is in an attempt to improve upon the dosimetric response of standard EPID. Several studies by Greer and his group [38, 39, 203–206] investigated modified forms of the standard indirect-detection EPID where materials above the photodiode array were replaced with water-equivalent build up material. Their hypothesis was that by removing the high-Z components and replacing them with water-equivalent material, the EPID’s response should be closer to water-equivalent, a desirable characteristic for dosimetry applications. The authors investigated applications using the modified direct-detection EPID for clinical IMRT dosimetry [39]. In doing so, they first established which configuration of buildup and backscatter material resulted in a direct-detection response that best agreed with water-equivalent measured dosimetry data. This ideal configuration was found to use a thickness of d_{\max} solid water build up without any additional backscatter. The main conclusion drawn from these studies was that it is possible to modify the standard EPID to obtain a water-equivalent dose response, however the trade off in sensitivity results in a drastic reduction in image quality, particularly for low dose imaging. Due to the absence of the metal/phosphor layer in the modified EPID design, the signal is now produced by the interaction of the megavoltage photon beam directly within the photodiodes. This results in the reduction in quantum efficiency and sensitivity. Therefore, the image quality in modified EPID design particularly for low dose imaging suffers [38]. These studies primarily focused on demonstrating how the modification of the EPID structure provides a water-equivalent dose response by comparing the modified EPIDs dose response with another established water-equivalent detector. None of these studies provided

any framework for how this configuration can be adopted in routine clinical use i.e. how the measured EPID dose information can be linked to dose received by patient and the methodology for how to obtain the predicted dose at the EPID plane for transit dosimetry verification. Chapter 6 outlines the framework for the clinical implementation of in vivo dose verification and is presented utilising a water equivalent EPID and a commercial TPS.

With the aim of improving both the quantum efficiency and water-equivalence of current EPIDs, Teymurazyan and Pang [207] proposed a modified indirect detection EPID that employs an array of plastic scintillator fibres in place of the metal plate and phosphor screen in standard EPIDs. Using MC simulations, they predicted that such an EPID could achieve a theoretical DQE of 37% for a 6 MV beam with fibers 30 cm in length. Other properties including the detection efficiency and MTF were also quantified. Unfortunately, however, the use of such thick (and consequently heavy) scintillators poses certain mechanical difficulties that may complicate their clinical practicality. Another important conclusion was that using plastic scintillator in place of the standard high-Z x-ray converter materials results in a water-equivalent dose response, which would potentially render this design suitable for portal dosimetry. A significant limitation of this study, however, is that the authors did not report any experimental data against which to validate their model.

The former scenario (standard EPID-based dosimetry) typically necessitates a complex detector characterisation and calibration scheme along with custom software to convert portal images into water- equivalent dose images. The latter scenario (direct EPID) has seen detector prototypes that, while capable of performing accurate patient dosimetry, suffer from decreased x-ray detection efficiency thus inhibiting their use for imaging. In both cases, proposed detectors have not been suitable for applications in both imaging and water-equivalent dosimetry. Chapter 4 and 5 discussed characterisation of novel EPID based prototypes that are capable of simultaneous imaging and dosimetry.

2.5.4 Quasi 3D dosimeters

Two commercial dosimeters are routinely used specifically for VMAT or other rotational therapy such as HT treatment dose verification. The Delta⁴ system (Scandidos, Uppsala, Sweden) consists of two planar dosimeter arrays mounted orthogonally. Dose reconstruction software can then generate 3D dose maps [208]. It has 1069 p-type silicon diodes on two orthogonal planes mounted within a polymethylmethacrylate (PMMA) phantom. The

diodes are cylindrical in shape with an active area 0.78 mm^2 . The diode pitch is 6 mm within the central $6 \times 6 \text{ cm}^2$ region, and 10 mm for the outer region. An inclinometer is attached to the linac gantry (providing independent measurement of the gantry rotation) in conjunction with the Delta⁴ dosimeter used for VMAT dose verification. The second dosimeter, ArcCHECK (Sun Nuclear, Melbourne, FL) consist of a cylindrical structure with 1386 diodes arranged in a helix with a diameter and length of 21 cm [51]. The device is configured with a solid PMMA insert.

Phantom-based measurement treatment verification QA process is cumbersome and limited to verify treatment length $< 25\text{-}30 \text{ cm}$. Verification of treatments exceeding the dimensions of the dosimeter is quite challenging. They can't be used for in vivo dosimetry. One of the limitations of phantom-based measurement treatment verification QA is that it does not provide the connection between measurement results and how the patient dose distribution might be affected. Software for these systems allows time dependent dose verification for VMAT delivery and calculates the delivered dose distributions in patients by perturbing the calculated dose using errors detected in fluence or planar dose measurements to correlate the gamma passing rate and the composite dose predicted with patient dose distribution. These algorithms contain significant approximations and their limitations have been demonstrated by recent studies [62, 63].

Advanced radiotherapy technologies and methods are complex; much more so than previous approaches and their treatment delivery uncertainties are not yet well studied or understood. The aim of phantom-based measurement QA is to detect and correct errors at the earliest opportunity. Therefore, the sensitivity of each dosimetry system to detect clinically relevant error must be studied and understood.

Various studies have previously been performed to assess the sensitivity to IMRT and/or VMAT simulated errors for the Delta⁴ [51, 52], ArcCHECK [51, 53, 54], MapCHECK [46, 55], MatriXX [56] and PTW 2D array [52, 57]. These studies mainly focus on C-arm linac based treatment. The general conclusion drawn from the above mentioned studies was that different dosimetry systems were able to detect particular errors. Masi et al [52] measured using four different dosimetry systems the clinical VMAT plans optimised using two TPS. Authors reported slightly lower gamma pass-rate for plans from one of the considered TPS which was attributed to a higher level of complexity of the optimised plans. The detector sensitivity to intention 3 mm translation shifts and to gantry angle offset was shown

to be strongly plan and partially detector dependent. Yet no comprehensive comparison of different detectors for key clinical sites for helical tomotherapy treatments has been undertaken. Also, no systematic study has been undertaken to determine the delivery errors that are clinically relevant.

2.5.5 3-dimensional dosimeters (Gel dosimetry)

Point detectors or 2D detectors may be used to obtain 3D measurements by combining a series of exposures. However, gel dosimetry is the only class of true 3D detectors available for radiation dose measurements. Several types of gels have been used in radiotherapy over many years. Gel dosimetry is founded mainly on the work of Gore et al [209] who demonstrated that changes due to ionising radiation in Fricke dosimetry solutions, developed in the 1920's, could be measured using nuclear magnetic resonance (NMR). Several studies have demonstrated the use of polymer gels for dose verification of IMRT treatments [210–213]. There is no consensus on the optimal formulations of gel dosimeters or the optimal evaluation techniques to be used [214]. This is a barrier to the broader implementation of gel dosimetry techniques in radiotherapy clinics.

2.5.6 On board exit detector

Helical tomotherapy (HT) was developed as an integrated system for delivering complex intensity-modulated radiation therapy (IMRT) treatments combined with mega-voltage computed tomography (MVCT) capabilities [95]. The on board exit detector is an arc-shaped CT xenon detector array located opposite the linear accelerator on a rotating slip-ring gantry. The detector array consists of cells which are small xenon gas cavities separated by thin tungsten septal plates. The detector array is designed to collect radiation exiting the patient for MVCT reconstruction. It also measures exit fluence during treatment delivery which can be used for delivery verification. The detector collects data from 640 channels and at each linear accelerator pulse (300 Hz).

The reconstruction of three-dimensional doses on HT using exit dose measurement via the in-line CT detector array is feasible. Dose verification on HT was first studied by Kapatoes [215, 216]. Methods for the verification of multi leaf collimator leaf open time (MLC LOT) have been investigated by many authors, some of whom used independent devices [217] whereas others used the MVCT detector to allow for in vivo dose calculation based on

dose reconstruction in the presence of the patient [215, 216, 218]. Some researchers [64, 65] proposed a QA procedure that involves applying a simple method to verify the MLC performance as a pre-treatment verification tool. Previously reported work on on board detector (OBD) pre-treatment verification tools has not utilised a dose reconstruction approach.

Despite the rapid evolution in our ability to deliver highly conformal x-ray beams, limitations with current detectors hinder our ability to measure dose delivery to the patient for QA and treatment plan optimization. The availability of such a detector would be extremely beneficial both to verify that the actual dose delivered matches the planned dose distribution and for identifying those patients that would benefit from treatment adaptations, thus making radiotherapy safer and more effective. The overall goal of this dissertation investigated treatment dosimetry verification for two different radiotherapy delivery systems. The first part develops and characterises a novel prototype hybrid EPID based dosimeter as a proposed solution for evaluating complex treatment techniques on a conventional linear accelerator which aims to combine both geometric and dosimetric verification in a single system. Initial work investigates the underlying causes of under dose response for standard EPIDs. The second part investigates clinical HT treatment verification. Specifically, the impact of treatment delivery parameters on clinical HT plans, sensitivity of commercially available devices to detect delivery errors and development and clinical implementation of an in-house exit detector-based dose reconstruction tool to verify dose delivery of HT treatment plans.

The proposed EPID based novel prototype configuration would improve treatment verification. Understanding the sensitivity of dosimetry systems provides information to inform support the decision of the most appropriate dosimetry system for each individual clinical situations and clinical implementations. The developed solution of exit-dosimetry would improve the efficiency of pre-treatment verification. This will facilitate a safer and more efficient implementation of other developing technologies in radiotherapy treatment delivery than is currently possible. Thus improving patient access to state-of-the-art radiotherapy will be achieved.

Chapter 3

Dose calibration of EPIDs for segmented IMRT dosimetry

Statement of joint authorship

S. Deshpande: Develop experimental design, performed experiments, analysed results, wrote manuscript

A. Xing: Matlab scripting and analysed results

P. Metcalfe: Assisted in interpreting results and writing, as supervisor he endorses the assessment

L. Holloway: Assisted with strategic implementations of the experiments and with publication submission.

P. Vial: Render advice on the experiment, interpreting results and write up

¹Part of this chapter has been published:

S. Deshpande, A. Xing, P. Metcalfe, L. Holloway, P. Vial. Dose calibration of EPIDs for segmented IMRT dosimetry. *Journal of applied clinical medical physics* 2014; 15(6):103-118

3.1 Introduction

All medical linear accelerator (linac) vendors currently provide a-Si EPID as a standard option. EPIDs are used routinely in radiotherapy for image verification of patient position. However, it has been demonstrated previously that a-Si EPIDs also have great potential for dosimetry applications [23]. Despite many studies demonstrating the potential of a-Si EPIDs for dosimetry, there remain some technical challenges to be overcome in order to realize their full potential in routine clinical practice. There are issues related to the non-water equivalence of the EPID [31, 38, 204, 219] and the detector's image acquisition process [185, 220, 221]. Previous studies of the dose response characteristics of a-Si EPIDs have reported an underresponse at small MU exposures relative to longer exposures [28, 181–184]. The resulting nonlinear EPID dose response, referred to here as gain ghosting, has been attributed to trapped charge effects [27, 181, 184, 222]. Gain ghosting is associated with variations in the quantity of trapped charge with exposure to radiation. The electric field characteristics change as the level of trapped charge increases, resulting in a change in pixel sensitivity with exposure to radiation. Image lag, defined as residual signal registered with a time delay from the original radiation induced electron-hole pair, is also attributed to trapped charge [27]. Image lag measured from the relative residual signal in image frames acquired immediately after an exposure has been reported as 2%-10%, depending upon incident exposure and EPID model [28, 181–183]. McDermott et al. [181] measured both image lag versus time elapsed (post-irradiation) and linearity of dose response (gain ghosting) for an Elekta iViewGT a-Si EPID. They proposed a correction for 'combined ghosting effects' to account for both image lag and gain ghosting using a triple exponential fitted as a function of time based on measurements with open beams. The same group quantified the nonlinear response of six EPIDs from three different vendors: Elekta iViewGT (Elekta Oncology Systems, Crawley, UK), Varian aS500 (Varian Medical Systems, Palo Alto, CA), and Siemens OptiVue (Siemens Medical Solutions, Concord, CA) [182]. The underresponse was in the order of 4%–6% at 5 MUs relative to 1000 MU for Siemens and Elekta EPIDs. Nijsten et al. [28] also reported an underresponse of up to 6% at 5 MU exposures relative to 1000 MU for a Siemens EPID, and implemented the ghosting correction factor into their EPID dosimetry calibration algorithm as proposed by McDermott et al. [181]. Similar nonlinear characteristics were measured on an Elekta EPID by Winkler et al. [183]. They proposed that the EPID dose response be a logarithmic function of dose, rather than time as proposed by McDermott et al. [181]. This research group accounted for an additional dose rate response effect during linac beam startup and demonstrated that image lag increases with the ratio of MUs

between the first and second exposure, and with reduced time interval between two subsequent exposures for IMRT fields. Recently, Warkentin et al. [223] proposed a pixel-by-pixel correction model that incorporates both image lag and nonlinearity correction for dynamic delivery with a Varian aS500 system. In the same study, they highlighted the importance of these corrections to reduce ambiguities and uncertainties in EPID-based dose verification. Van Esch et al. [192] reported a forgoing irradiation of 500 MU resulted in image lag of only 1% in the following image acquired after approximately 10 s for Varian aS500 EPIDs. They also attributed the underresponse of up to 6% at 2 MU mainly to rounding error of signal count from the acquisition software. Another factor in EPID dose response, which has not been addressed in most studies, is the importance of different image acquisition software controls and frame readout schemes. Chang and Ling [220] identified potential errors in the Varian synchronous, frame-averaging acquisition mode due to missing data between the start of irradiation and imaging, and from the last (incomplete) frame. Kavuma et al [185] also observed significant artifact in in-plane profiles at low MU exposures on Varian EPIDs with IAS2/IDU-II acquisition software, and suggested the IAS2/IDU-II acquisition system would not be suitable for step and shoot IMRT verification with low MU segments. Both of these issues were resolved in following vendor upgrades. Budgell et al. [224] investigated the intersegment EPID response reproducibility at low dose measured over a series of 20 successive segments delivered with 1 and 2 MUs. The measured inter segment variability was within 1% and consistent with ion chamber data. They also reported the acceptable reproducibility of off-axis profiles measured for 20 successive segments with 4 MU. A comprehensive investigation about the influence of the readout scheme on the dose response for all three linac vendors at small MU was carried out by Podesta et al. [221]. This research group modelled the discrepancies in dose response at low MU of up to 37% using only the incomplete integration of EPID frames acquired during irradiation. They reported no underresponse for Elekta and Varian TrueBeam systems (post-software upgrade), but reported large underresponse for Siemens, Varian TrueBeam (pre-software upgrade) and Varian Clinac systems. While difficult to compare directly, these results do not appear consistent with previous EPID dose response studies. The above review summarizes some of the key studies of EPID dose response, highlighting the inconsistent interpretation of EPID dose response characteristics. Despite the apparent successful and increasingly widespread clinical implementation of EPID dosimetry, fundamental dose response issues remain unresolved. These issues came to light during the development of an EPID dosimetry program in our department and were the motivation for this work. The specific issues we aim to address in this work include: i) the inconsistencies in the literature about the underlying

causes of nonlinear dose response of EPIDs; ii) the EPIDs nonlinear behavior is widely reported based on static open beam exposures, with little or no consideration for how accurately this behavior translates to segmented IMRT; iii) the management of these effects on a multivendor EPID dosimetry program, with particular regard to the relative importance of the EPID detector design, the linac, and the image acquisition and processing methods implemented across different systems; and iv) unexpected EPID dose response behavior observed on Siemens EPIDs. This work will contribute to a more consistent understanding and implementation of pixel-to-dose calibration methods for EPID-based IMRT dosimetry.

3.2 Methods and Materials

3.2.1 Equipment

Different combinations of linacs, EPIDs, and acquisition software were investigated in an attempt to isolate the source and relative contributions to EPID dose response behavior. Each experimental setup is described in Table 3.1. The bottom row provides a code used to refer to each experimental setup throughout this paper. In each case the standard gain (flood field) and offset (dark field) corrections were applied to EPID measurements. All IMRT fields were delivered using the segmented (step and shoot) technique with gantry angle fixed at 0° with 6 MV photons only.

3.2.1.1 Siemens EPID system

Details of EPID construction, acquisition software, and image processing implemented on the Siemens equipment (Siemens Medical Solutions, Concord, CA) can be found in a previous study [28]. The EPID images for step and shoot IMRT delivery were acquired with the multi-frame acquisition mode (experimental setup 1 and 2a from Table 3.1). This mode of acquisition saves a frame average image for each IMRT segment. According to the Siemens documentation[#], the number of frames (N_{frames}) acquired per segment or beam is determined by the following relation:

[#]Linear Accelerator System Manual, Siemens Medical Solutions

Table 3.1: The combinations of equipment and settings for each experiment.

	Linac1	Linac2			Linac3	
Linac Model	Siemens Oncor	Siemens Oncor			Elekta Synergy	
Dose Rate (MU/min)	300	300			500	
EPID model	Optivue 1000 P.E. XRD 1640 AL7	Optivue 1000ST P.E. XRD 1640 AG9	Research P.E. XRD 1640 AN CS	iViewGT P.E. XRD 1640 AL5 P	iViewGT P.E. XRD 1640 AL5 P	Research P.E. XRD 1640 AN CS
Source to Imager Dis- tance(cm)	115	115	115	160	160	160
Acquisition Software	Coherence Therapist v.2.1.24	Coherence Therapist v.2.1.24	P.E.XIS v.3.3.1.1	Elekta iViewGT v.3.4b 162-SP2	P.E.XIS v.3.2.0.7	P.E.XIS v.3.3.1.1
EPID integration time(ms)	285	143	133	433	433	433
ICA integration time(ms)	280	140	130	430	430	430
Experimental setup	1	2a	2b	3a	3b	3c

P.E. = PerkinElmer,Santa Clara,CA

ICA,IBA Dosimetry Asia Pacific,Beijing,China

$$N_{\text{frames}} = \frac{\text{Expected Dose}(MU) \cdot 60(\text{sec}/\text{min})}{\text{Dose Rate}(MU/\text{min}) \cdot \text{Integration time}(\text{sec})} \quad (3.1)$$

The integrated pixel value (IPV) for IMRT fields with n segments is given by equation 3.2:

$$\text{Integrated pixel value} = \sum_{i=1}^n (R_i \cdot N_i) \quad (3.2)$$

where, R_i denotes the EPID frame average pixel value for the i^{th} segment (i.e., EPID frame average response per segment), and N_i denotes the number of frames (N_{frames}) for the i^{th} segment.

(N_{frames}) is reported in the DICOM file header. All images were exported in DICOM format and analyzed with in-house code using MATLAB (MathWorks Inc version 7.12.0.635(R2011a); MathWorks, Natick, MA). The ‘Port during’ imaging option used for IMRT operates in ‘free running mode’. Based on personal communications[†], with other research groups and the vendor, the image acquisition is thought to be triggered by a beam-on and beam-off signal from secondary Siemens software. There is no beam pulse synchronization in ‘free running mode’.

3.2.1.2 Elekta EPID system

Details of EPID construction, acquisition software, and image processing implemented on the Elekta equipment (Elekta Oncology Systems, Crawley, UK) can be found in previous studies [181, 183]. Measurements with the Elekta EPID (experimental setup 3a and 3b from Table 3.1) were conducted using two image acquisition software systems available on the iViewGT workstation: i) iViewGT Elekta software in standard clinical mode (version 3.4b 162-SP2), and ii) XIS PerkinElmer software (version 3.2.0.7). IMRT images acquired with the iViewGT software use the ‘Single’ exposure option. This mode of acquisition saves a frame average image for each segment. The individual frame average image for each segment was exported. The integrated pixel value (IPV) for each segment or field is obtained using equation 3.3:

$$\text{Integrated pixel value} = \frac{65535 - \text{Raw Pixel Value}}{\text{PSF}} \quad (3.3)$$

where the 65535 is the 16-bit offset and PSF is the pixel scaling factor. The PSF for each segment of an IMRT field is reported by the iViewGT software. The integrated EPID image was obtained by manually adding the IPV of each segment determined using equation 3.3. The PSF includes scaling factors for the number of frames acquired and a configurable renormalization used to ensure gray-scale values are optimal for visualization of clinical images. When this renormalization is set as 0 in the iViewGT initialization file (sri.ini), the

[†]Mark Podesta, personal communication, January 23, 2013.

PSF is numerically equal to the inverse of the number of frames acquired during the image, analogous to $1/N_{\text{frames}}$ from equation 3.1. The number of frames acquired PostBeamOff (an image acquisition setting) is also configurable in the initialization file. To investigate the impact of this setting on pixel-to-dose calibration, the EPID images were collected with zero, three, and ten PostBeamOff frames with renormalization settings of 40,000 (the default clinical setting) and zero. The images and associated log files (containing the image header information) were exported using the standard export option from the iViewGT workstation for further analysis. The image data controller uses the gun pulses from the linac to synchronize the reading of the data from the panel, so that image data is read when the radiation pulse is not present. As soon as the complete frame is read from the panel, a frame synchronization pulse is sent to the data controller[‡]. The measurements with the XIS application (experimental setup 3b from Table 3.1) were conducted in continuous ‘free running mode’ with no external trigger mechanism. The acquisition was manually started immediately prior to beam-on and stopped at an arbitrary time after beam-off (at least 10 frames after beam-off). The XIS software stores the individual frames. The integrated image was obtained by summing each frame in MATLAB. The frame signal amplitude was used to indicate the start and stop of each beam and hence control the number of PostBeamOff frames used in the analysis (Figure 3.1). The two different acquisition systems (iViewGT and XIS) on the same linac enabled us to investigate the impact of software based acquisition settings on the reported dose response of the EPID.

3.2.1.3 Standalone research EPID system

A standalone PerkinElmer detector was also used in this study. This EPID was similar to the Elekta and Siemens EPIDs, with the advantage of being mobile so it could be used across the different linacs. The research EPID measurements (experimental set-up 2b and 3c from Table 3.1) were conducted on both Siemens and Elekta linacs in continuous ‘free running’ mode using XIS acquisition software. The acquisition settings were set to match the clinical acquisition settings as described Table 3.1. The integrated image was obtained by summing each frame in MATLAB as described above for the Elekta images acquired with XIS software. The beam off trigger was estimated as the frame where the signal had dropped to approximately 50% or less of the beam-on value. Figure 3.1 describes the image acquisition and triggering process. Using one EPID across different linacs provided more information on the impact of the linac on the reported dose response of the EPID. For seg-

[‡]Elekta iViewGT Corrective Maintenance Manual, Elekta, Stockholm, Sweden

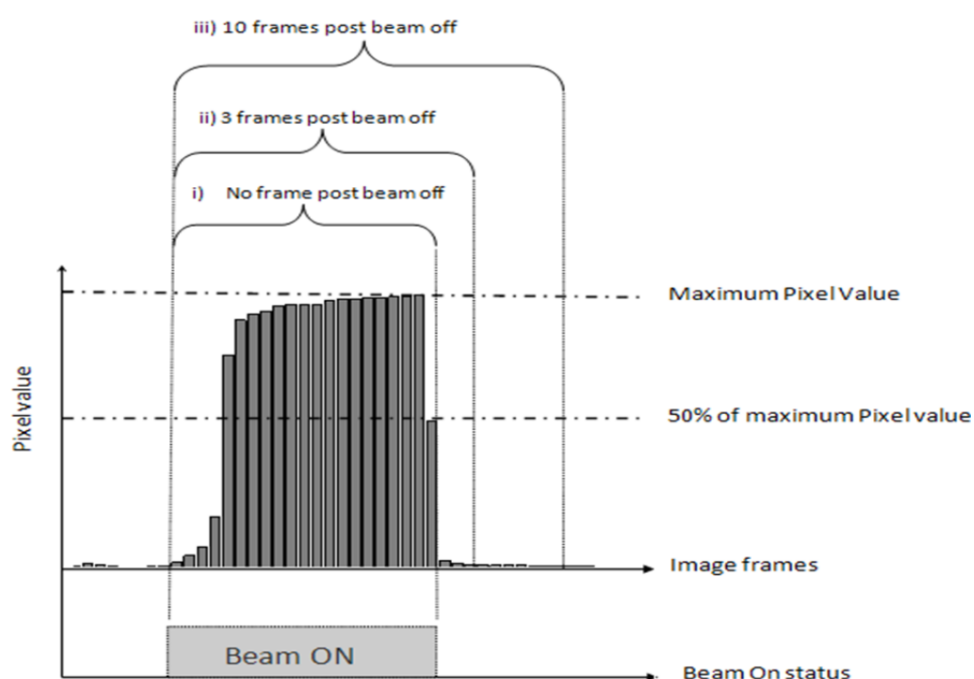


Figure 3.1: Schematic illustration of three different frame integration methods: i) No frame PostBeamOff; ii) 3 frames PostBeamOff; and iii) 10 frames PostBeamOff, where 0, 3, and 10 frames after the beam has stopped are included in integrated images, respectively. The beam-off trigger was estimated as the frame where the signal had dropped to approximately 50% or less of the beam-on value.

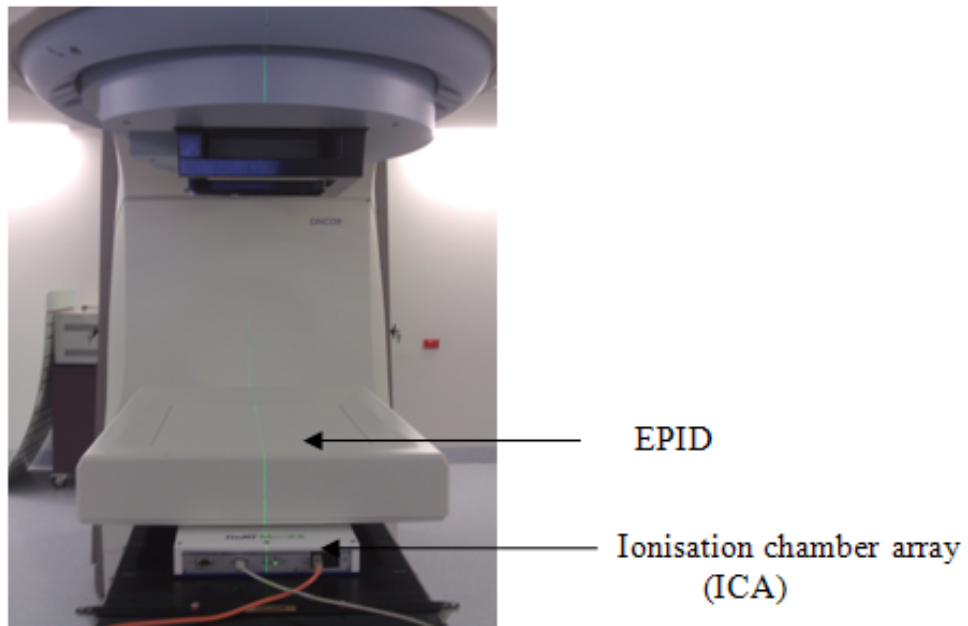


Figure 3.2: Experimental set-up for simultaneous EPID and ionisation chamber array measurements.

mented delivery, the ‘10 frames post beam off’ integrated image was obtained by summing the maximum number of post beam off frames available between two consecutive IMRT segments not strictly 10 frames. In order to isolate EPID dose response behaviour from beam characteristics, such as dose per MU linearity, each experiment was conducted with the ICA positioned beneath the EPID to acquire simultaneous reference measurements. This ICA has been previously shown to display linear dose response behaviour in both ‘movie’ mode and integrating mode [155, 225]. The ICA was operated in ‘movie’ mode at approximately the same integration time as the EPID in each experiment. The ICA software restricts integration times to multiples of ten milliseconds, therefore the ICA integration time was set to the EPID integration time rounded to the nearest 10 milliseconds (see table 3.1). The set-up for the simultaneous EPID and ICA measurements is shown in figure 3.2. Previous work verified this set-up had no effect on the EPID dose response characteristics under investigation [226].

All the measurements discussed below in sections 3.2.2 and 3.2.3 were conducted with all three equipment combinations summarised Table 3.1. All measurements were conducted with three minute intervals between each measurement unless stated otherwise to minimize image lag.

3.2.2 Dose linearity for segmented fields

The linearity of EPID response with dose was measured with static open fields for varying MU exposures (1- 100 MUs). The open beam experiment provided a baseline for comparison with EPID dose response linearity with IMRT delivery. Six IMRT fields were created specifically for this experiment. The segments of each IMRT field were fixed at 10×10 cm² field size, each field having a total of 20 MU. Field 1 consisted of 20 segments at 1 MU per segment, field 2 consisted of 10 segments at 2 MU per segment, and fields 3, 4, 5, and 6 consisted of 5, 4, 2, and 1 segments of 4, 5, 10, and 20 MU per segment respectively. The single segment at 20 MU represents a standard static open beam delivery of 20 MU. The total integrated EPID response for each IMRT field was obtained from the sum of the average of the central 20×20 pixels per frame. The integrated pixel value per segment and in total for each IMRT field was compared with the corresponding static open beam case. For the remainder of this study we refer to the IMRT fields used in this experiment as ‘simple’ IMRT fields. The ICA provided a reference of delivered dose. The integrated EPID response for total 20 MU exposure measured with single static open field and five ‘simple’ IMRT fields was compared to assess whether the under-response seen in static fields persist with segmented delivery.

3.2.3 Inter-segment reproducibility

To evaluate inter-segment variations in EPID response during segmented delivery the ‘simple IMRT fields’ described above were delivered five times consecutively. The reproducibility of EPID response at off-axis positions was also investigated from profiles along the central pixel row and column for each segment. The ICA provided a reference of delivered dose profiles.

3.2.4 Clinical IMRT fields

Four sets of ‘clinical IMRT fields’ with constant MU per segment of 2, 4, 5, and 10 MUs were created by editing the RTP file. The percentage deviation in the integrated detector response at each pixel was determined from 10 repeat measurements. This experiment was conducted on both linacs.

3.2.5 EPID pixel-Dose calibration

The integrated EPID dose for the clinical IMRT fields described in section 3.2.3 was determined using three different methods as described by Eqs. (3.4) , (3.5) and (3.6) below. The results were compared to assess the impact of calibration methodology:

Calibration method 1 (ghosting correction method):

$$Integrated\ EPID\ Dose = \sum_{i=1}^n \left[\frac{(IPV)_n}{G(t_{rad})_n} \right] \cdot (CF(100MU)) \quad (3.4)$$

Calibration method 2 (no ghosting correction):

$$Integrated\ EPID\ Dose = \left[\sum_{i=1}^n (IPV)_n \right] \cdot (CF(100MU)) \quad (3.5)$$

Calibration method 3 (small MU calibration method):

$$Integrated\ EPID\ Dose = \left[\sum_{i=1}^n (IPV)_n \right] \cdot (CF(20MU)) \quad (3.6)$$

where $(IPV)_n$ is the integrated pixel value for the n^{th} segment, $CF(100MU)$ and $CF(20MU)$ is a pixel-to-dose calibration factor determined at 100 MU and 20 MU respectively, t_{rad} is radiation beam-on time, $G(t_{rad})$ is a ghosting correction factor determined from the function of EPID dose response linearity measured with open static fields for Linac1 and Linac3 (experimental setup 1 and 3c from Table 3.1). The value of t_{rad} is determined from the product of the number of frames and frame acquisition rate for the Siemens linac and from an inverse of the product of PSF and frame acquisition rate for the Elekta linac. There is no correction for any specific ghosting or non-linearity in calibration methods 2 and 3. Method 3 uses a calibration factor determined at a MU level more closely matched to IMRT segment MU, with the aim of reducing the impact of non-linear dose response (gain-ghosting) on clinical dosimetry. A gamma evaluation, with 2% and 3% difference (global maximum) and 2 and 3 mm distance-to-agreement criterion with 10% dose threshold, is performed to quantify the difference between the integrated EPID dose map calculated from calibration

methods 1, 2 and 3 using the same EPID data. Field size correction factors and other detector scatter corrections were ignored for the EPID dose computation since they remain constant irrespective of calibration methods being investigated here.

3.3 Results

3.3.1 Dose linearity for segmented fields

The EPID dose response as a function of MU for static and ‘simple’ IMRT fields for all EPIDs are shown in figures 3.3 (a) and (b) for the Siemens Linac and figures 3.3 (c) and (d) for the Elekta linac (experimental setup 1, 2a and 3a from Table 3.1). In the case of the Elekta EPID, dose response for ‘simple’ IMRT fields versus static fields agreed to within 2.5% for $MU \geq 2$. However, for Siemens EPID, the agreement in dose response for ‘simple’ IMRT fields versus static fields was difficult to interpret due to the poor reproducibility for segmented delivery, particularly at $MU \leq 5$. Both Siemens and Elekta clinical EPIDs under responded by 9% and 8% respectively relative to ICA for 1 MU per segment (or field). At 2 MU and above the agreement between Elekta clinical EPID and ICA was within 2.5%. No significant difference was observed in dose response for the Elekta clinical EPID when measured under a different acquisition setting as described in section 3.2.1, and agreed within 1%. The renormalization for each of the three different PostBeamOff frame Elekta datasets was set to 40,000 (Figure 3.3 (c) and (d)). At 2 MU and above, the agreement between Siemens clinical EPID and ICA was within 3.5%. The reproducibility at 1 MU for clinical Siemens EPIDs was poor (7.8% and 12.7% SD for linac 1 and linac 2, respectively; 3.3 (a) and (b)), while for clinical Elekta reproducibility was clinically acceptable ($<3.0\%$ SD for all acquisition setting). The reproducibility of the ICA data remained within 0.3% in all cases.

The EPID dose response as a function of MU for static and ‘simple’ IMRT fields for the research EPID are shown in figures 3.4 (a) and (b) for the Siemens Linac and figures 3.4 (c) and (d) for the Elekta linac (experimental setup 2b and 3c from Table 3.1). In both cases the EPID dose response for ‘simple’ IMRT fields versus static fields agreed to within 1.3% for $MU \geq 2$. The research EPID under-responded by 6% and 5% relative to ICA for 1 MU per segment for Siemens and Elekta linacs respectively. At 4 MU and above the agreement between research EPID and ICA response was within 3% for both Linacs. The dose

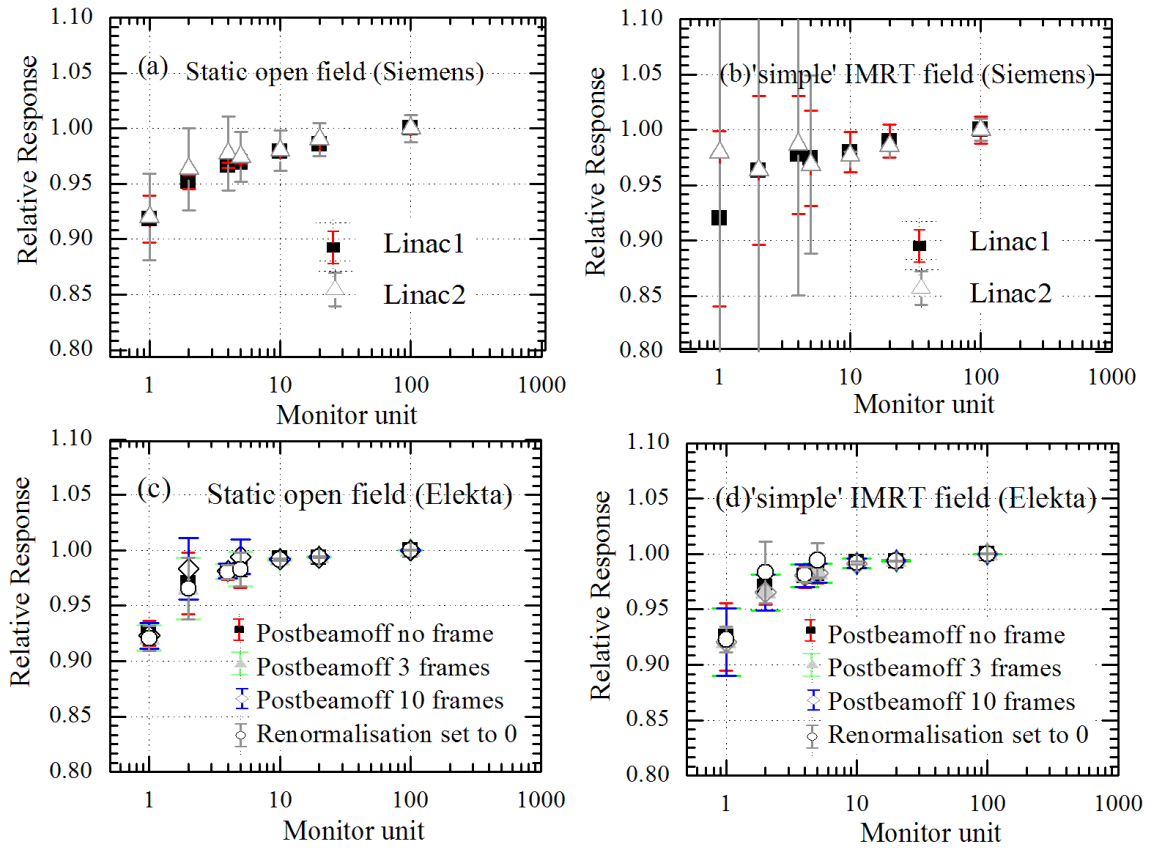


Figure 3.3: Relative EPID response versus MU for open static and ‘simple’ IMRT fields with fixed field size $10 \times 10 \text{ cm}^2$ for Siemens and Elekta clinical EPID systems (experimental set up 1, 2a and 3a from Table 3.1). Data points are the ratio of EPID and ICA response for both static and ‘simple’ IMRT fields. Error bars show the standard deviation from 5 repeat measurements.

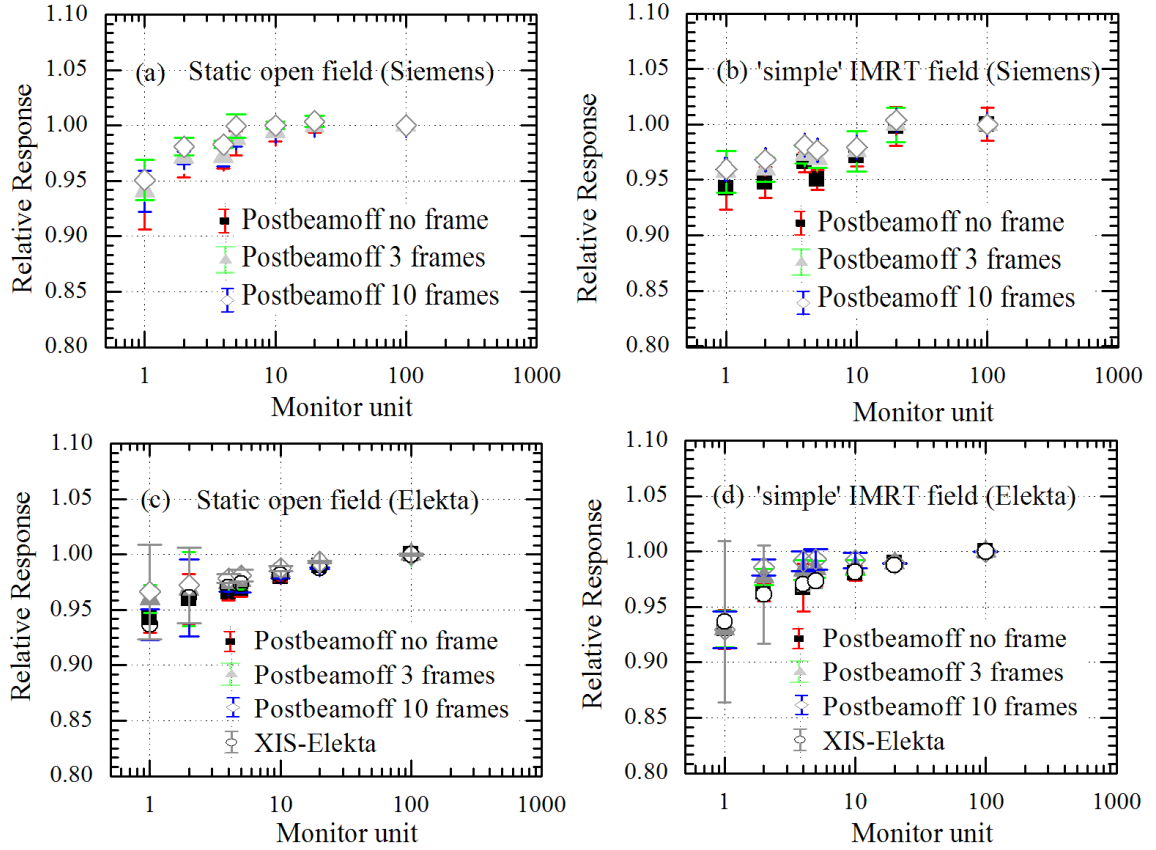


Figure 3.4: Relative EPID response versus MU for open static and ‘simple’ IMRT fields with fixed field size $10 \times 10 \text{ cm}^2$ for research EPID measured on Siemens and Elekta linacs (experimental setup 2b and 3c from Table 3.1). Relative EPID response for clinical Elekta EPID using XIS software (experimental set up 3b from Table 3.1). Data points are the ratio of EPID and ICA response for both static and ‘simple’ IMRT fields. Error bars show the standard deviation from 5 repeat measurements.

response measured with the clinical Siemens EPID agreed closest with the dose response measured with the research EPID with no PostBeamOff frame setting for static open fields. The research EPID did not show the poor reproducibility seen at small MU with the Siemens EPID (figure 3.3), confirming this was not related to the beam. The dose response measured with the clinical Elekta EPID agrees with dose response measured with the research EPID to within 1% for both static and ‘simple’ IMRT fields. The reproducibility of the ICA data remained within 0.3% in all cases. Figure 3.6 depicts the EPID pixel signal collected frame by frame at the central axis. Table 3.2 compares the integrated EPID response for single 20 MU exposure with total integrated EPID response for ‘simple’ IMRT fields for 1 MU, 2 MU, 4 MU, 5 MU and 10 MU per segments on Linac 2 and Linac 3. Table 3.2 shows the under response persists for segmental delivery with 1 MU ($\leq 4-6\%$) and 2 MU ($\leq 2-3\%$) per segment similar to static open. The under response was seen for all three post beam off frame settings.

3.3.2 Inter-segment reproducibility

a) Central axis: Figure 3.6 depicts the integrated dose response per segment at the central axis of the Siemens EPID and ICA for the ‘simple’ IMRT field with 5 MU per segment. The large variations in EPID response reflect the large errors bars in figure 3.3(b). The variation in EPID response per segment was up to $\pm 20\%$. The simultaneously measured ICA did not indicate any variation in beam delivery. Further investigation for the Siemens EPID images found inconsistencies in the value of N_{frames} . The frequency of this EPID dose response phenomenon varied depending on the MU per segment. Inter-segment reproducibility was worst at MU per segment ≤ 5 MU, at 10 MU per segment and above the phenomena was not observed at all and reproducibility was within 1%. The same variation in N_{frames} was not present for the measurements taken with the same linac, EPID and software for open static beam (non-segmented) delivery at any MU settings.

Table 3.2: The integrated research EPID response at CAX for both static and ‘simple’ IMRT fields with total of 20MU exposure. The captured frames were summed as no PostBeamOff, three PostBeamOff, and ten post-beam-off frames for the same EPID image to demonstrate the effect from different acquisition protocols. The percentage values in brackets indicate the relative difference in the integrated pixel values for each simple IMRT field compared to static field exposure of the same total dose

Linac	PostBeamOff Frames Number	Mean IPV					
		Static field 20 MU single exp.	‘simple’ IMRT fields				
			20x1MU segments	10x2MU segments	5x4MU segments	4x5MU segments	2x10MU segments
Elekta	0	765264	718307.1 (-6.14%)	736394.2 (-3.77%)	745395.4 (-2.60%)	751777.7 (-1.76%)	760431.3 (-0.63%)
	3	767489.4	723304.2 (-5.76%)	746969.1 (-2.66%)	757629.8 (-1.28%)	757975.9 (-1.24%)	764746.9 (-0.36%)
	10	769631.1	726087.9 (-5.66%)	753367.0 (-2.11%)	764005.2 (-0.73%)	764841.1 (-0.62%)	769548.7 (-0.01%)
	0	867426.2	821950.5 (-5.24%)	847584.3 (-2.29%)	860657.2 (-0.78%)	861173.2 (-0.72%)	861875.4 (-0.64%)
	3	869129.9	833360.2 (-4.12%)	858665.3 (-1.20%)	864984 (-0.48%)	865182.5 (-0.45%)	865338.6 (-0.44%)
	10	869129.9	839021.7 (-4.05%)	868133.3 (-0.72%)	870569.6 (-0.44%)	870815.8 (-0.41%)	870975.5 (-0.39%)

b) Off-axis: The off-axis profiles for each IMRT segment (frame average image) along the central row (cross-plane) and central column (in-plane) of the Siemens EPID panel and ICA were compared for the ‘simple’ IMRT fields (figure 3.7). Some EPID cross-plane profiles were tapered at the field edge while the in-plane profiles did not display this effect. By comparison the profiles in both planes (experimental set-up 1 and 2a from Table 3.1) measured simultaneously with the ICA did not show any tapering of profile shape or any variation in amplitude acquired within segments. No such artifacts in profiles were observed on the clinical Elekta EPIDs.

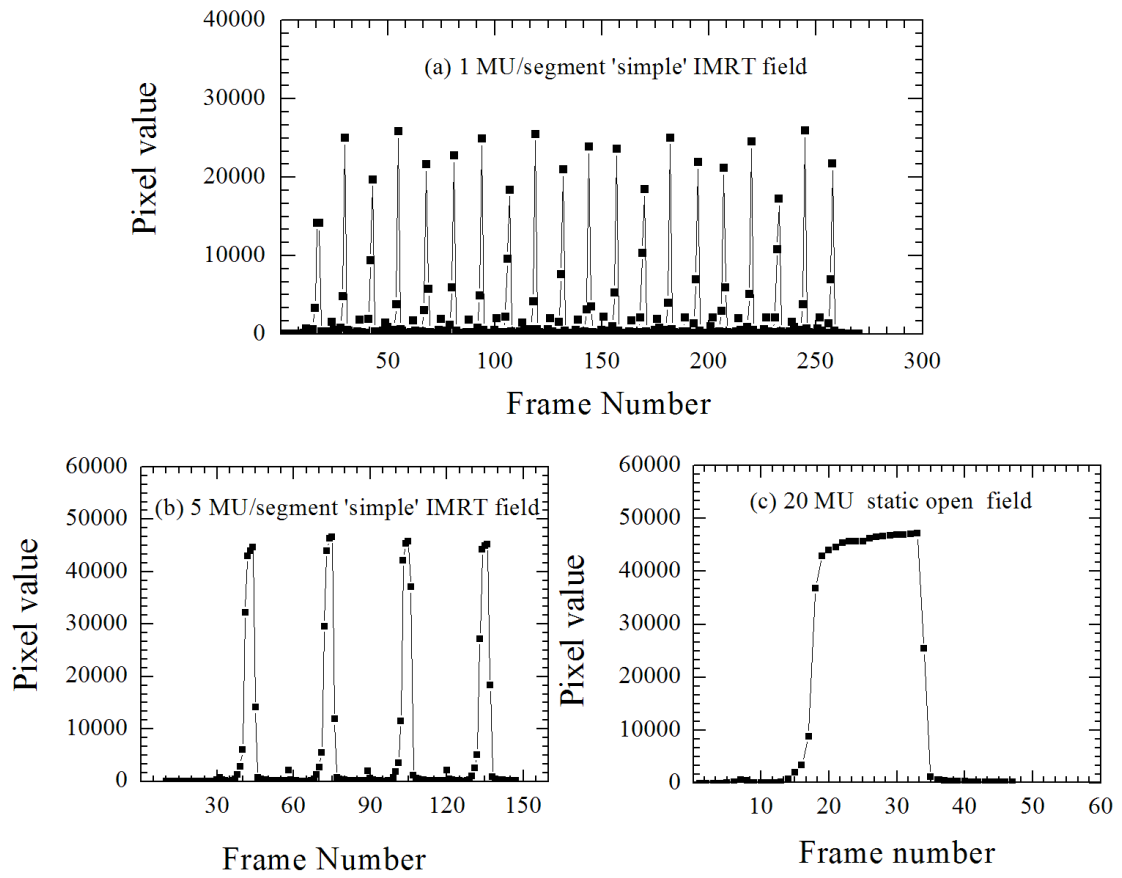


Figure 3.5: The EPID response at CAX per frame for 'simple' IMRT fields (a and b) for 1 MU and 5 MU per segment respectively (c) static open field (20 MU).

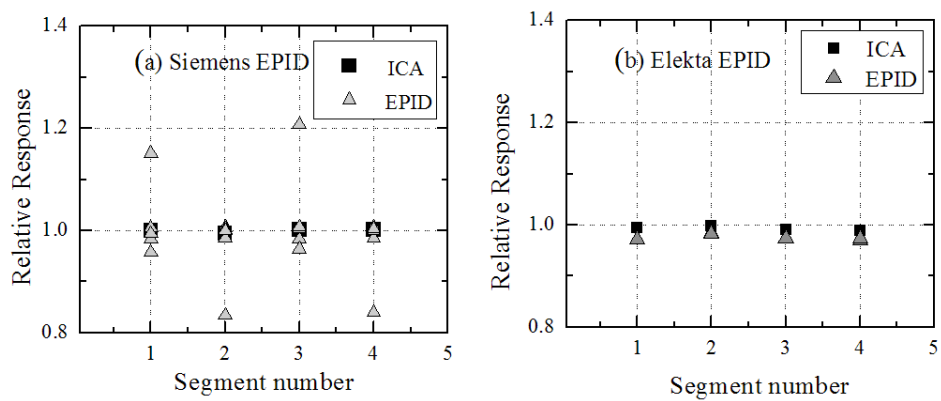


Figure 3.6: Relative response per segment for 5 repeats of the 'simple' IMRT field for EPID (Triangle with cross-hair) and ICA (square with cross-hair) with 5 MU/segment. All the data points are normalised to non-segmented single exposure 20 MU.

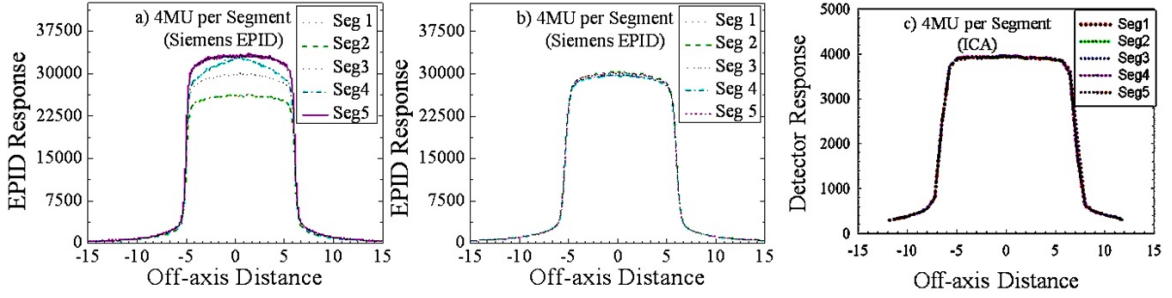


Figure 3.7: The off-axis profiles of individual IMRT segment (frame average image) for the ‘simple’ IMRT field (4MU x 5 segments) along a) the central row (cross-plane), b) central column (in-plane) acquired with the Siemens EPID panel and c) ICA simultaneously as shown in figure 3.1

3.3.3 Clinical IMRT field

Figure 3.8 shows a 2D map representing the percentage standard deviation at each pixel for both clinical EPIDs (Siemens and Elekta) and the ICA for the same ‘clinical IMRT field’ from ten sequential measurements acquired simultaneously on the two detectors (experimental setup 1 and 3a from Table 3.1). The figures have been scaled and cropped to show the same spatial extent of the IMRT field. The average percentage standard deviation of the entire region of data shown in Figs. 3.8(a) and (b) was 3.98%(0.90%), 2.94%(0.95%), 2.34%(0.68%), and 1.55%(0.17%) for the EPID (ICA) measurements with 2, 4, 5, and 10 MU per segment cases, respectively, for Siemens EPID. The average percentage standard deviation of the entire region of data shown in Figs. 3.8(c) and (d) was 1.6%(0.90%), 1.4%(0.85%), 1.3%(0.70%), and 1.05%(0.18%) for the EPID (ICA) measurements with 2, 4, 5, and 10 MU per segment cases, respectively, for Elekta EPID. The maximum percentage standard deviation of the entire region of data was 9.2%(3.5%), 8.1%(2.7%), 7.5%(2.2%), and 1.9%(1.4%) for Siemens (Elekta) EPID measurements with 2, 4, 5, and 10 MU per segment cases, respectively. The gray scale image provides a visualization of the poorer reproducibility of the Siemens EPID measurements compared to the ICA.

3.3.4 EPID pixel-Dose calibration

To determine the ghosting correction factor, $G(t_{\text{rad}})$, described in the Materials and Methods Section 3.2.5 and implemented in calibration method 1 (Eq.3.4), a curve (polynomial function) was fitted to both the Siemens and Elekta clinical EPIDs static beam exposure dose

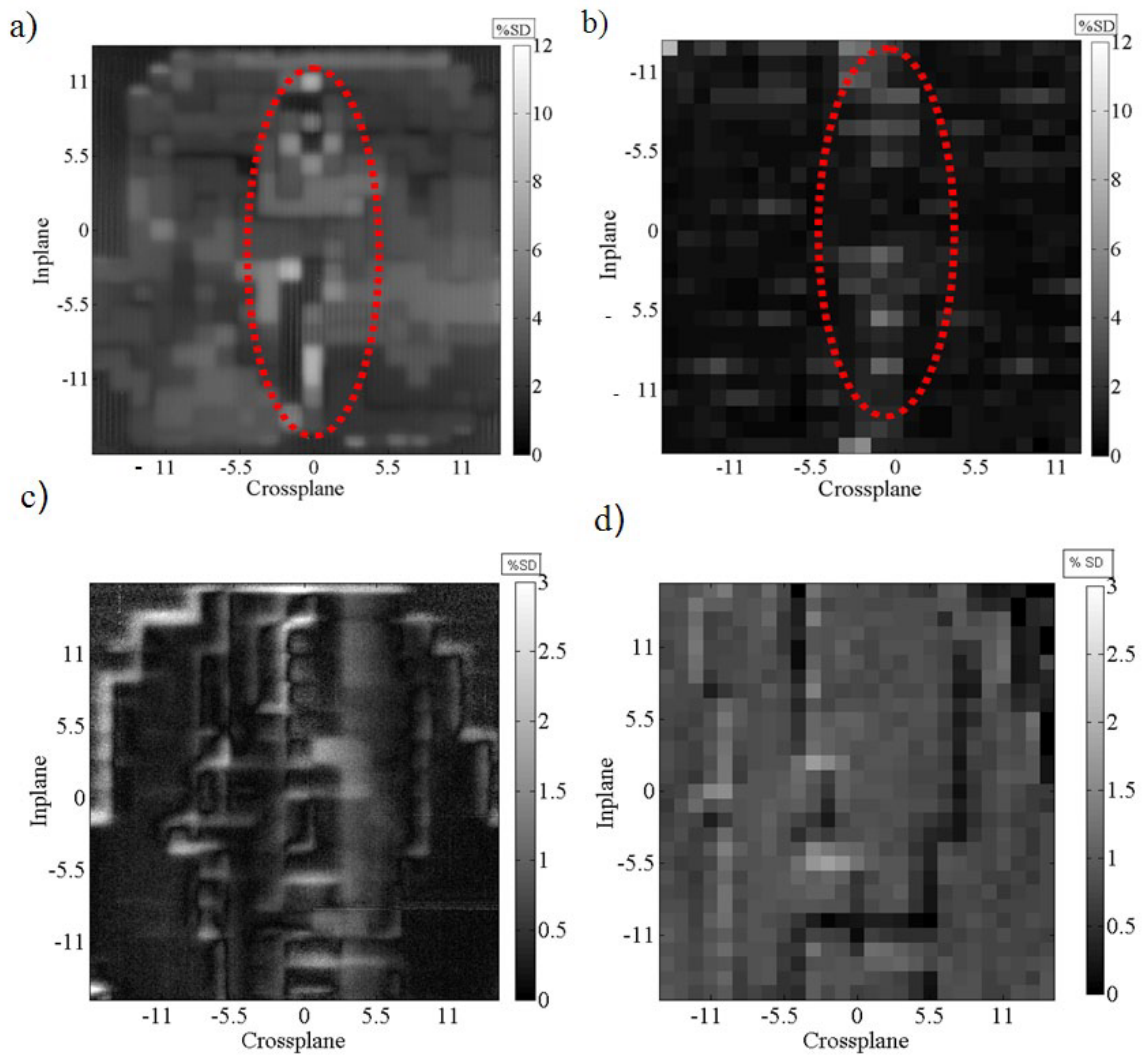


Figure 3.8: 2D maps of the percentage standard deviation at each pixel/detector position within the field from ten repeats for a 'clinical' IMRT field with 5 MU per segment (a) clinical Siemens EPID (c) clinical Elekta EPID and (b) and (d) for ICA detector measured with Siemens and Elekta linac simultaneously.

response (Fig.3.3(a) and 3.3(c)) as a function of beam-on time. The polynomial fit curve for Siemens EPID was 4th polynomial order $G(t_{\text{rad}}) = -1.02 \cdot 10^{-15} \cdot t^4 + 1.16 \cdot 10^{-11} \cdot t^3 - 4.97 \cdot 10^{-8} \cdot t^2 + 9.71 \cdot 10^{-5} \cdot t + 0.910$ where, ' $G(t_{\text{rad}})$ ' is ghosting correction and ' t ' is beam on time in milliseconds.

The polynomial curve fitted to the Elekta EPID dose response as a function of beam-on time with renormalization setting 0 and 4000 agreed within 1% and, therefore, the ghosting correction $G(t_{\text{rad}})$ for Elekta EPID was used based on EPID dose response data acquired with the renormalization value set to 0. The function fit was accurate within 0.5% to measured data for beam-on time (down to 2 MU) and given by polynomial fit equation $G(t_{\text{rad}}) = -1.06 \times 10^{-12} \cdot t^4 + 1.46 \times 10^{-9} \cdot t^3 - 6.77 \times 10^{-5} \cdot t^2 + 1.7410^{-3} \cdot t + 0.91$.

Table 3.3: The percentage gamma pass rate determined using three different calibration methods for both Siemens and Elekta EPIDs for the same integrated image of an IMRT field. The IMRT fields were modified to have a fixed number of MU per segment. The Elekta EPID images were acquired with clinical setting (i.e., renormalization set to 40,000) and for two different PostBeamoff acquisition settings

Calibration Methods	Clinical IMRT (MU/Segment)	Percentage Gamma pass rate			
		Siemens		Elekta	
		2%/2 mm	3%/3 mm	2%/2 mm	3%/3 mm
Method1 vs. Method2	2MU	64.28%	92.69%	99.83% ^a	99.98% ^a
				99.71% ^b	99.96% ^b
Method1 vs. Method3	2MU	92.25%	92.98%	99.73% ^a	99.97% ^a
				99.90% ^b	100.0% ^b
Method1 vs. Method2	4MU	85.75%	99.87%	100.0% ^a	100.0% ^a
				99.99% ^b	100.0% ^b
Method1 vs. Method3	4MU	100.0%	100.0%	100.0% ^a	100.0% ^a
				100.0% ^b	100.0% ^b

^a Three PostBeamOff frames

^b zero PostBeamOff frames

Table 3.3 depicts the percentage gamma pass rate for the 'clinical' IMRT (experimental setup 1 and 3a from Table 3.1) when the EPID dose calculated using the method 1 (Eq.3.4) against the EPID dose calculated using method 2 and 3 (Eq.3.5) and (Eq.3.6).

3.4 Discussion

The dose response linearity experiments conducted in this work confirm that the nonlinear dose response measured with static open beams at small MU persists in segmented IMRT delivery based on the MU per segment. This validates the pixel-to-dose calibration methods incorporating a ghosting correction on a segment-by-segment basis for IMRT dosimetry using corrections determined from open static beam exposures. The existence of gain ghosting was confirmed as being present and consistent across different EPIDs and linear accelerators at small MU exposure. Gain ghosting is associated with variations in the quantity of trapped charge with exposure to radiation. The rate of the accumulation of trapped charge and the rate of signal from the discharge of trapped charge slowly approaches equilibrium with increasing dose. The close agreement between segmental IMRT and static open beam delivery, and the fact that the static open beam fields had substantially longer time periods between subsequent exposures, supports the finding that gain ghosting affects dominate over image lag signal from previous exposures in terms of the EPIDs nonlinear response behavior at small MU. The nonlinearity at small MUs was relatively insensitive to acquisition settings. We have not investigated the impact of pulse repetition frequency (PRF). A method of simultaneous measurements with an ICA and EPID was demonstrated to reliably separate out the EPID dose response from beam delivery characteristics. This methodology demonstrated an irregularity in the Siemens implementation, which resulted in poor measurement reproducibility of IMRT fields at small MU per segment. It was also demonstrated that the ghosting correction is not required if the EPID is calibrated at an appropriately small MU exposure. The magnitude of underdose response reported in the present work is smaller than some previously reported studies. This may be partly due to the fact we normalized the dose response relative to 100 MU rather than 1000 MU used in other studies [28, 182]. In previous work [227] on Siemens linacs, we normalized to 800 MU and achieved larger underdose response in closer agreement with other studies [28]. At 2 MU and above, the agreement between EPID and ICA response was within 2.5% (for Elekta) and 3.5% (for Siemens). The dose response measured with clinical EPID and the default clinical software setting shown in figure 3.3 agreed with the research EPID dose response shown in figure 3.4. No significant difference ($\leq 1\%$) was observed in dose response for both the static and ‘simple’ IMRT fields measured with the clinical Elekta EPID under different PostBeamOff frame acquisition settings. This demonstrates that nonlinearity at small MUs was relatively insensitive to acquisition settings and across different EPID detectors. The poor reproducibility for the Siemens EPID in the case of ‘simple’ IMRT fields was not observed either with simulta-

neous measurement conducted with ICA or with the standalone research EPID (Fig. 3.4). There were particularly large variations in the integrated Siemens EPID response between successive segments having 2, 4, and 5 MU per segment, as shown in Fig.3.6. Intersegment reproducibility was worst at MU per segment ≤ 5 MU for Siemens EPIDs and occurs in a nondeterministic manner. This was attributed to an inconsistent number of frames per segment being recorded in the image header file. The vendor documentation indicates that the frame number is derived using Eq.3.1. This equation appears to be independent of actual delivery parameters that may affect the real number of frames acquired, such as real dose rate variations, and should therefore not vary for a given MU per segment. The variation in integrated EPID response was not seen for static beam (non-IMRT) exposures on the same linac. We also observed the tapered shape or variation in amplitude acquired within segments for ‘simple’ IMRT fields in case of Siemens EPID only. This variation in amplitude may be due to the synchronization between linac trigger pulse (beam-on and beam-off) and detector control board incorporating the real-time dose-rate variation, particularly for segment IMRT delivery. The experiment performed on both Siemens EPIDs (experimental setup 1 and 2a from Table 3.1) shows inconsistent reporting of frame number in the header file, suggesting that it is an issue with Siemens image acquisition systems for segmented delivery. Moreover, Podesta et al. [221] modeled the discrepancies in Siemens clinical EPID dose response up to 37% at 1 MU and 20% at 2 MU. The author validated that these variations are associated with acquisition readout scheme (i.e., missing frames). We have not addressed the additional scatter or spectral corrections that can be applied to account for patient transit or MLC transmission effects [28, 228]. Dynamic MLC and VMAT were not available for this study, and further work is required to determine how these results apply to that setting. The dose linearity response reported in this study is only at 6 MV. The dose linearity at 18 MV in our previous study [227] for Siemens EPID was within 2% compared to 6 MV beam at ≥ 1 MU. Winkler et. al. [183] also reported the EPID dose response for 6, 10, and 25 MV photons with an Elekta system and confirmed the dose linearity of the EPID did not depend on energy. The ghosting correction suggested by McDermott et al.[181] and Nijsten et al. [28] was designed to keep the EPID measured dose accuracy at lower MUs within approximately 1%. The ghosting correction factor was determined as a function fit to a dose-response curve that ranged from 5 MU to 1000 MU, normalized to 1000 MU. This range of MU does not reflect clinical step and shoot IMRT technique which may be delivered with fewer than 5 MU per segment and is rarely delivered with more than 30 MU per segment for conventional dose fractionation as demonstrated by previous work [229]. We selected 20 MU for calibration in our study for two reasons: i) the mode value for maximum

MU per segment in most of IMRT fields is nominally 20 MU [229]; and ii) linac output is relatively more stable after 20 MU is delivered. However based on the dose-response curve in 3.3(a) and 3.3(c), in principle, calibration value at 4 or 5 MU can be used, provided the linac output is stable. Ghosting and image lag corrections are complex to implement accurately on a pixel-by-pixel basis due to the variations in time between segments and variation in dose per segment. For step and shoot delivery, based on our results, we can conclude that adding a ghosting or image lag correction is an unnecessary complication for accurate EPID based IMRT dosimetry.

3.5 Conclusion

The EPID dose response behavior for step and shoot IMRT fields delivered by Siemens and Elekta linacs was investigated. The nonlinear EPID dose response as a function of MU measured for single open beam exposures was found to be consistent with dose response for segmented IMRT delivery. The nonlinear dose response was consistent across both clinical EPIDs and the standalone research EPID, with the exception of the poor reproducibility seen with Siemens EPID images of IMRT fields. The nonlinear dose response was relatively insensitive to acquisition settings and appears to be primarily due to gain ghosting affects in the a-Si photodiodes. When the pixel-to-dose calibration factor was determined at 20 MU, no additional ghosting correction factor was necessary for the accurate determination of dose for clinical IMRT fields.

Chapter 4

Feasibility study of a dual detector configuration concept for simultaneous megavoltage imaging and dose verification in radiotherapy

Statement of joint authorship

S. Deshpande: Develop experimental design, performed experiments, analysed results, wrote manuscript

L. McNamara: Matlab scripting and analysed results

L. Holloway: Assisted with strategic implementations of the experiments and with publication submission.

P. Metcalfe: Assisted in interpreting results and writing, as supervisor he endorses the assessment

P. Vial: Render advice on the experiment, interpreting results and write up

[‡]Part of this chapter has been published:

S. Deshpande, L. McNamara, L. Holloway P Metcalfe, P Vial. Feasibility study of a dual detector configuration concept for simultaneous megavoltage imaging and dose verification in radiotherapy. *Medical Physics* 2015; 42(4):1753-1764

4.1 Introduction

Treatment verification has two important roles in radiotherapy: (i) to mitigate mistreatments that result in adverse patient outcomes (patient safety); and (ii) to optimize treatment outcomes by ensuring accuracy (treatment accuracy). Ensuring patient safety and treatment accuracy requires techniques to verify both patient and target location (geometry) and the dose delivered. Current and emerging technologies in radiotherapy are increasingly sensitive to geometric errors, and verifying the delivered dose is increasingly challenging. To address the increasing demands on geometric accuracy, the use of imaging for treatment verification has developed rapidly in recent years [102]. Image guided radiotherapy (IGRT) aids in tracking daily treatment setup to minimize geometric error. Verifying dose accuracy for modern treatments such as intensity-modulated radiation therapy (IMRT) typically relies on pretreatment dose measurements. However, pretreatment measurements are time consuming and do not necessarily identify clinically relevant errors in dose delivery that may occur during the course of treatment. These factors are driving a growing demand for effective *in vivo* dose verification [118, 119]. All medical linear accelerator (Linac) vendors currently provide amorphous silicon (a-Si) electronic portal imaging devices (EPIDs) as a standard IGRT option [180]. Although previous studies [23, 28, 30, 118, 198] have demonstrated the EPID's potential as an *in vivo* dosimeter, the routine use of EPIDs for *in vivo* dosimetry remains generally limited to a few centers who have invested significant resources into developing in-house systems [28–30, 32, 198, 230]. The nonwater-equivalent response of EPID (optimised for imaging purpose) remains one of the limiting factor for implementing EPID as a dosimeter in routine clinical practice [26, 38]. Previous studies reported that with modifications the current commercial EPID design can be a water-equivalent dosimeter, [38–40, 206] albeit with a significant reduction in imaging performance [38]. Recently, our group introduced a new prototype EPID design that has the potential for simultaneous imaging and dose verification with a single detector [40]. More efficient detector designs have also been proposed for improved megavoltage (MV) imaging performance [36, 231]. These efficient MV detectors generally consist of higher atomic number materials than current EPIDs, which is likely to make EPID dosimetry even less water-equivalent and still more difficult to implement. Another consideration is that the increasing utilization of in-room kV imaging systems for IGRT may reduce the imaging role of MV EPIDs. Other possible approaches to *in vivo* dose verification include (i) the use of transmission dosimetry devices mounted onto the head of the linear accelerator [154, 159] (ii) the use of 2D dosimetry devices which are typically used for pretreatment QA [174, 175], and (iii) the

analysis of the delivery system computer log files [232, 233] of machine states. The linac log files do provide measured MLC positions and not the measured estimate of fluence. Previous study [234] demonstrated the discrepancy between the reported MLC position by log files and image based measured actual MLC position. This highlighted the limitations of using linac log file to reconstruct delivered dose. Point detectors that are placed onto the patient during treatment have some special applications but may be inadequate as a general solution for in vivo dosimetry in modern radiotherapy [118, 235]. In this study, we propose a new dual detector design to address the limitations in radiotherapy treatment verification described above. To the best of our knowledge, this dual detector concept has not been previously reported. The proposed dual detector combines imaging and dose detectors in series at the EPID position. The clinical application of this system requires that performance of both the dosimeter and imager is not significantly degraded in the dual detector configuration. Preliminary work indicated that a commercially available ionization chamber array (ICA) maintains accurate water-equivalent dose response when positioned directly under an EPID [226]. However, it is known that EPID response and image quality is influenced by backscatter which is dependent on the configuration of materials immediately behind the detector [236, 237]. In this study, we investigate the clinical feasibility of a dual detector configuration with a comprehensive experimental assessment. The imaging performance of the EPID and the dose response characteristics of the ICA in the dual detector configuration are compared against their respective standalone (reference) configurations.

4.2 Methods and Materials

4.2.1 Equipment

The dosimetry equipment used in this study consisted of a commercial ICA, called the I'mRT MatriXX (IBA dosimetry, Schwarzenbruck, Germany). The MatriXX ICA is a 2D array of ionization chambers with accompanying OmniPro-I'mRT software (version 1.6, IBA dosimetric, Schwarzenbruck, Germany). This device has an array of 1020 air-vented plane parallel ionization chambers (with a volume of 0.08 cm^3 each) arranged in a 32×32 grid providing a maximum field of view of $24 \times 24 \text{ cm}^2$. The ionization chambers are 4.5 mm in diameter and are spaced at 7.62 mm center-to-center. All measured ICA data were interpolated down to 1 mm resolution by applying the user selectable 'Cubic Spline' interpolation algorithm option available in the OmniPro I'mRT software. Previous work [39] validated

the accuracy of cubic spline interpolation implemented in OmniPro I'mRT software. The detector has 3.3 mm water equivalent inherent buildup. A solid water slab was used as an additional water equivalent buildup and backscatter material (Gammex RMI, Middleton, WI). The imaging detector used was an a-Si EPID (XRD 1640 AN CS PerkinElmer, Santa Clara, CA), and the imaging data were collected using XIS software V3.3.1.1 (PerkinElmer, Santa Clara, CA) using a 399 ms frame period. The EPID consists of a $40 \times 40 \text{ cm}^2$ a-Si photodiode array and comprises 1024×1024 pixels, giving a pixel pitch of approximately 0.4 mm. A QC-3V image quality phantom and Pips-Pro software (version 3.2.3a, Standard imaging, Inc., Middleton, WI) were used to assess image quality. A purpose built line spread function (LSF) apparatus was also used to determine the EPID's modulation transfer function (MTF). All experiments were conducted on an Elekta Synergy linear accelerator (Elekta Oncology Systems, Crawley, UK) with 6 MV photons at gantry 90° . All the clinical IMRT fields were planned as step and shoot IMRT fields on the Pinnacle treatment planning system (Philips Radiation Oncology Systems, Fitchburg, WI Version 9.0).

4.2.2 Dosimetry experimental setup

The dose measurements were performed in both nontransit and transit geometries. The non transit dose measurements were performed with the detector plane at the isocenter (100 cm source-to-detector distance) with no object in the beam (Figs. 4.1(a) and 4.1(b)). The transit dose measurements were performed at an extended 145 cm source-to-detector distance with sheets of solid water or an anthropomorphic phantom (ATOM[®] Dosimetry Verification phantoms, CIRS) positioned on the treatment couch and centered at the isocenter (see Figs.4.1(c) and 4.1(d)). The ICA was calibrated to dose as per the manufacturer guidelines in the reference dosimetry configuration (nontransit geometry). We assessed if a common calibration could be used for both transit and nontransit dosimetries by comparing measurements against reference ion chamber measurement (Roos[®] Plane-Parallel Ion chamber, PTW Freiburg, Germany). All the dose measurements were performed with the ICA in both reference dosimetry configuration and dual detector configuration as described below.

4.2.2.1 Reference dosimetry configuration

The reference dosimetry configuration comprised of the solid water slab equal to water equivalent reference depth (D_{eff}) as buildup placed on the ICA (Figs.4.1(b) and 4.1(d)). An additional 5 cm solid water backscatter material was added to ensure full scatter conditions.

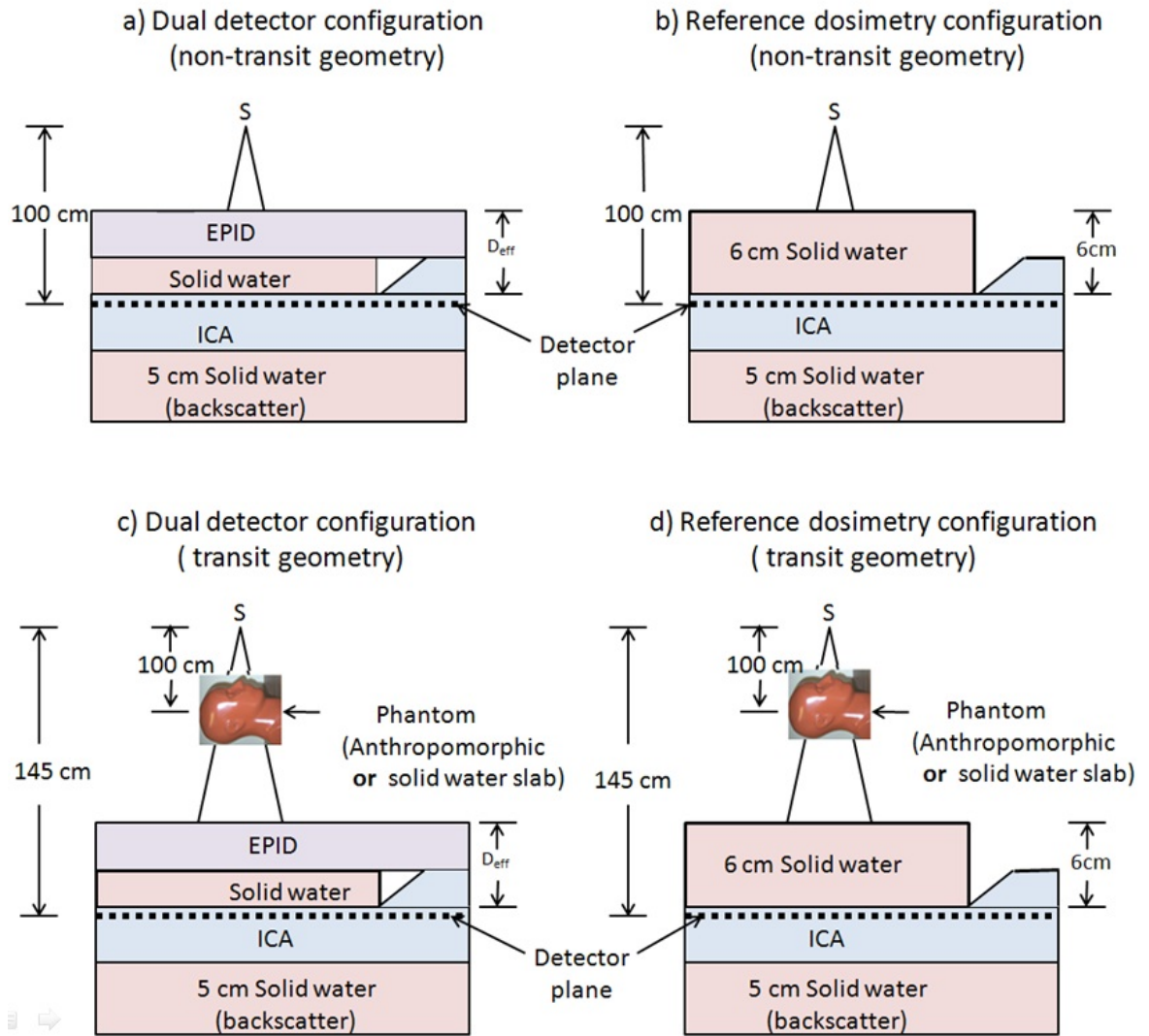


Figure 4.1: Schematic illustration for dosimetry measurement setups (a) dual detector configuration (nontransit) (b) reference dosimetry configuration (nontransit) (c) dual detector configuration (transit) (d) reference dosimetry configuration (transit). For transit geometry measurements, either the solid water slab or anthropomorphic phantom (interchangeable) was used. For visualization purpose, only the anthropomorphic phantom image is shown ((c) and (d)) placed at isocenter.

D_{eff} was determined as described in section 4.2.3.1. Measurements with the ICA in the reference dosimetry configuration were used in both the transit (Fig. 4.1(d)) and non-transit (Fig. 4.1(b)) geometries as the reference for dose response to which the dual detector configuration was compared. The water-equivalence of the ICA dose response has been extensively validated in both transit and nontransit geometries [155, 206, 238]

4.2.2.2 Dual detector configuration

The dual detector configuration consisted of an EPID (closest to the source), 2 cm solid water, the ICA, and 5 cm solid water backscatter material. The 2 cm of solid water between the EPID and ICA was necessary to fill the air gap between the two devices (see Fig.4.1(a) and 4.1(c)). Section 4.2.3 describes the experiments used to compare the dose response of the ICA in the dual detector configuration with the reference dosimetry configuration (described above).

4.2.3 Dose response evaluation

4.2.3.1 Estimation of water equivalent reference depth (D_{eff})

The water equivalent reference depth, (D_{eff}) was defined as the depth at which the measured central axis (CAX) dose and dose profiles showed the closest agreement between the reference dosimetry configuration and dual detector configuration (at the same source-to-detector distance). In other words, D_{eff} is the water equivalent thickness of the buildup material on top of the ICA in the dual detector (Fig. 4.1) configuration. The CAX dose and dose profiles were measured with $10 \times 10 \text{ cm}^2$ open fields measured with different thicknesses of solid water placed on the ICA (in 1 cm increments) in the nontransit reference dosimetry configuration (as defined in Sec. 4.2.2.1). To further validate D_{eff} , field size output factors and transmission factors were measured with varying thickness of solid water buildup in the reference dosimetry configuration and compared with dual detector configuration measurements. The value of D_{eff} was determined in the nontransit geometry and validated in the transit geometry to confirm agreement. Finally, D_{eff} was also calculated using the effective path length method described in Papanikolaou et al. [239](equ.4.1).

$$D_{\text{eff}} = \sum_{i=1}^n (\Delta d_i) \cdot (\rho_i) \quad (4.1)$$

where D_{eff} is the water equivalent reference depth (D_{eff}) and Δd_i and ρ_i are the thickness and relative electron densities of each different layer of buildup material (EPID layers plus 2 cm solid water slab), respectively, in dual detector configuration. Detailed dimensions and material compositions of the EPID were obtained from the manufacturer (PerkinElmer, Santa Clara, CA).

Subsequent clinical IMRT fields dose measurements (Sections 4.2.4.2, 4.2.4 and 4.2.4.1) undertaken using the dual detector configurations were compared to reference measurements conducted at D_{eff} . The D_{eff} depth used in reference configuration for clinical IMRT field dose verification was arrived at through basic dose response measurements (Sections 4.2.3.2 and 4.2.3.3).

4.2.3.2 Field size output factor and off-axis response

The field size output factor for square field sizes varying from 3×3 to $20 \times 20 \text{ cm}^2$ was determined from the ratio of the ICA response at CAX relative to a $10 \times 10 \text{ cm}^2$ field for nontransit and transit geometries. The dose profile and off-axis response were measured for a $5 \times 5 \text{ cm}^2$ and the maximum available field size with both dual detector configuration and reference dosimetry configuration in nontransit and transit geometries. The maximum field size of $20 \times 20 \text{ cm}^2$ in nontransit and $15 \times 15 \text{ cm}^2$ in transit geometries was used to avoid unnecessary exposure of electronics to the x-ray beam.

4.2.3.3 Transmission factors

Transmission factors measured in the transit geometry were calculated using static fields of $15 \times 15 \text{ cm}^2$ (defined at the isocenter). Sheets of solid water were positioned on the treatment couch to create a homogeneous transit object with thicknesses ranging from 0 to 25 cm in 5 cm increments and centered about the isocenter. Transmission factors were then calculated by dividing the CAX response measured with ICA to the value obtained with no solid water in the beam (for same the MUs). The transmission factors measured in the reference dosimetry configuration and dual detector configuration were compared.

4.2.4 IMRT fields

The following clinical dosimetry measurements were performed using the ICA. In-house developed MATLAB code (version: 7.10.0.499 (R2010a), Mathworks, Inc., MA) was used for data processing and comparison. The gamma evaluation technique [240] was applied to quantitatively compare the 2D dose maps measured with the calibrated ICA. Gamma criteria used was 2% dose difference (relative to the maximum dose) and 2 mm distance-to-agreement, with doses below 10% of the maximum dose excluded from the evaluation.

4.2.4.1 Nontransit geometry

A total of five step and shoot IMRT fields including, three test patterns (two wedge-shaped and one pyramid-shaped pattern) and two complex head and neck IMRT beams were measured in the nontransit geometry.

4.2.4.2 Transit geometry

Seven prostate step and shoot IMRT fields and three IMRT test patterns (as above for the nontransit geometry) were measured with a 20 cm thick solid water slabs in the beam. The 20 cm of solid water was centered symmetrically about the isocenter. In addition, seven head and neck, five brain, four lung, and seven prostate IMRT fields were measured with an anthropomorphic phantom placed in the beam at isocenter (see figs.4.1(c) and 4.1(d)).

4.2.5 Imaging experimental setup

The impact that backscatter material present in the dual detector configuration has on the imaging performance of the EPID was evaluated quantitatively and qualitatively. Similar to the dosimetry evaluation, the EPID's imaging performance was experimentally evaluated by comparison of the image quality in a reference imaging configuration and the dual detector configuration as described below. All the image quality measurements discussed in section 4.2.6 for both configurations were performed with a source to detector (imager) distance of 144 cm as shown in Fig.4.2

4.2.5.1 Reference imaging configuration

The reference imaging configuration represents the EPID in standalone mode as routinely used (i.e. without the presence of any additional buildup or backscatter material Fig 4.2(c) and 4.2(d)).

4.2.5.2 Dual detector configuration

The dual detector configuration is as described in section 4.2.2.2.

4.2.6 Image quality evaluation

4.2.6.1 QC-3V image quality phantom

The PipsPro QC-3V image quality phantom and software were used to compare the EPID spatial resolution and contrast to noise ratio (CNR) in the dual detector configuration and reference imaging configuration. The phantom was placed on its side on the treatment couch and positioned using the external alignment marks at the isocenter. EPID images of the phantom were acquired using 1 frame (4 MU, or a dose of approximately 0.6 cGy at a detector plane) in the reference imaging configuration and dual detector configurations. The low dose levels used here are similar to those typically used for pre-treatment portal imaging. Details on the algorithms used to calculate CNR, MTF and noise using PipsPro software can be found in the literature [241].

4.2.6.2 LSF and MTF

The MTF was also determined using an angled slit technique. A purpose built LSF apparatus with slit angle set to 4° was used for MV image quality experiments. Technical considerations for this method can be found in previous studies [242, 243]. The LSF apparatus employs two machine-surfaced tungsten blocks, each block having a thickness of 17.5 cm, height of 11.5 cm, and length of 8 cm, determined from previous investigations to be suitable for achieving accurate results at MV energies [242–244]. The tungsten blocks were mounted on a stage that allowed the blocks to be translated and rotated (Fig. 4.3) for alignment of the slit (approximately 80 μm wide) with the radiation beam. The tungsten blocks were positioned as close as possible to the EPID as shown in Figs. 4.2(b), 4.2(d), and 4.3.

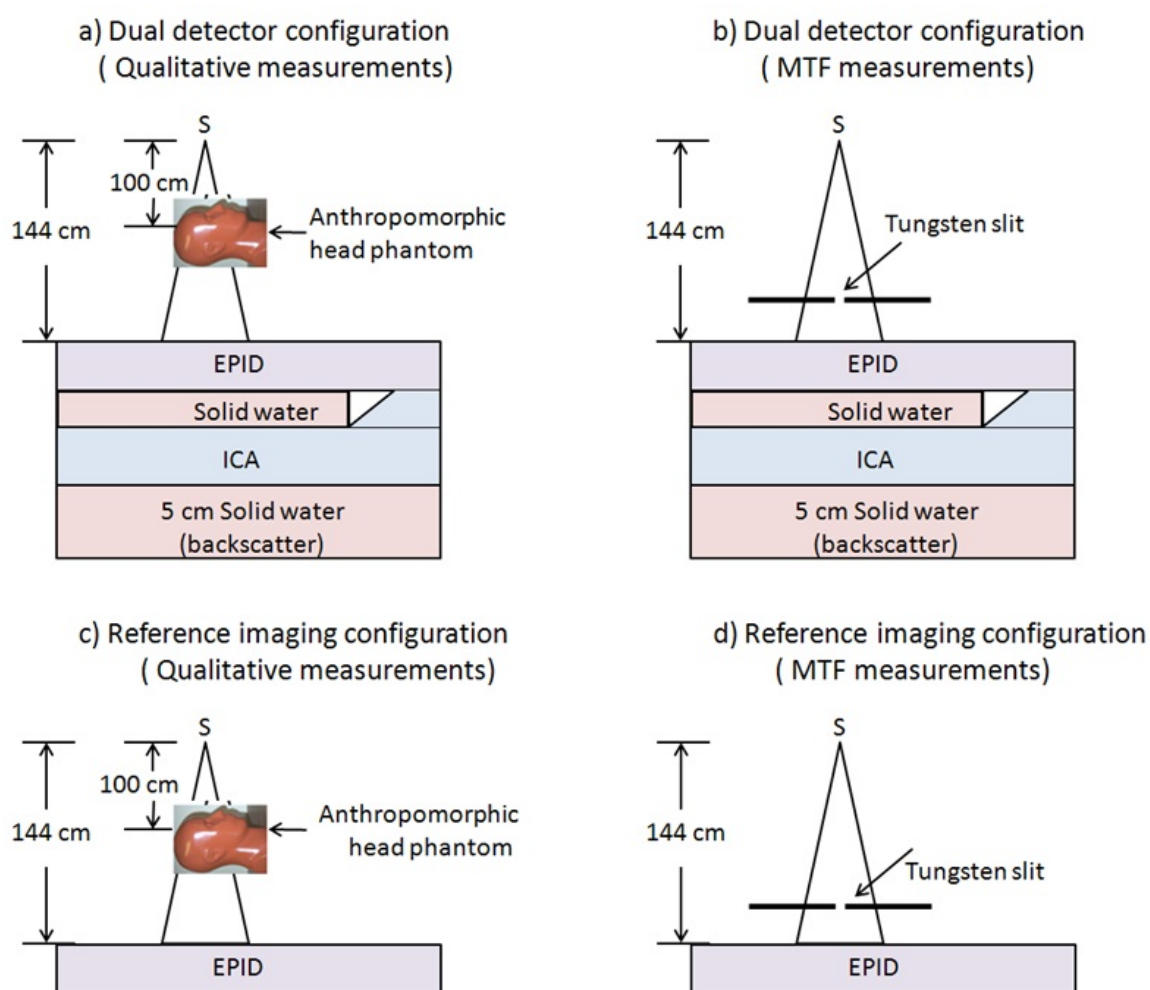


Figure 4.2: Schematic of the experimental setup for image quality evaluation. Anthropomorphic phantom images were acquired for the (a) dual detector configuration and (c) reference imaging configuration. MTF measurements were performed for the (b) dual detector configuration and (d) reference imaging configuration.

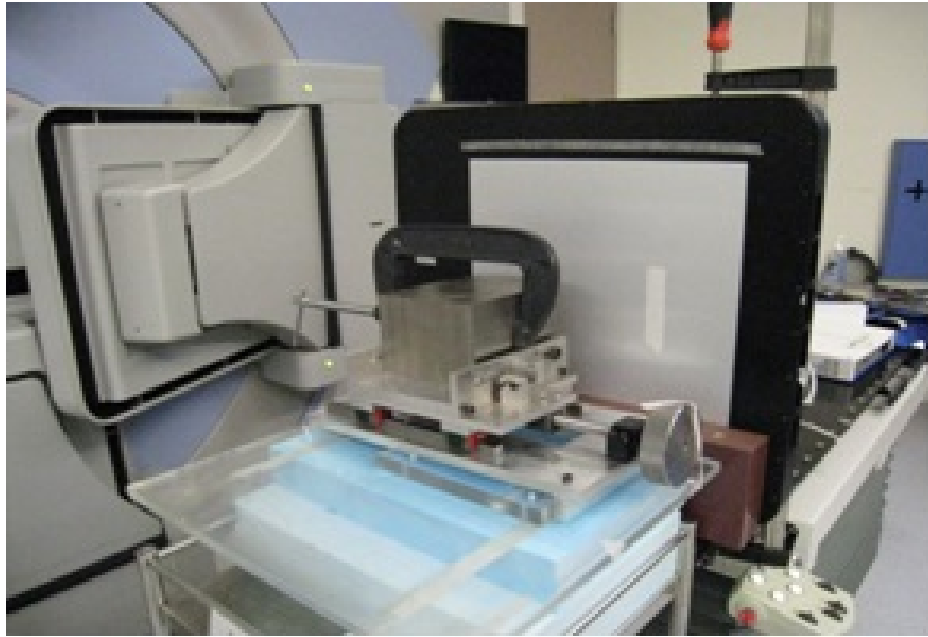


Figure 4.3: Experimental setup for measurement of LSF. The tungsten blocks are mounted on a translating and rotating stage as close to EPID as possible.

The EPID images acquired were frame averaged, each consisting of 50 frames (170 MU). The composite oversampled LSF was obtained as follows: a region of interest over the slit image was selected spanning approximately 20–30 rows. Due to the angle of the slit, each row profile is progressively shifted by a small spatial increment with respect to the previous row. Each row was shifted by the subsampling distance determined by the angle of slit, and summed over each column. For further details, the reader is referred to Fujita et al.[245]. The MTF was then calculated from the modulus of the Fourier transform of the normalized LSF, where the normalization was to the unit area under the LSF. EPID images of the slit for both reference imaging configuration and dual detector configuration were acquired.

4.2.6.3 Anthropomorphic phantom

Images of an anthropomorphic head phantom were acquired to qualitatively evaluate the performance of the EPID in the dual detector configuration and reference imaging configuration when imaging an object representative of human anatomy. With the gantry angle at 90° , the head phantom was positioned facing the source on the treatment couch and was centered at the isocenter (see Figs. 4.2(a) and 4.2(c)). For each EPID configuration, an anterior posterior (AP) image of the phantom was acquired by one frame (4MU or a dose of approximately 0.6 cGy at the detector plane).

4.3 Results and Discussion

4.3.1 Dose response evaluation

4.3.1.1 Estimation of water equivalent reference depth (D_{eff})

The calculated D_{eff} using (Eq. 4.1) was 6.05 cm. The measured $10 \times 10 \text{ cm}^2$ open field CAX dose and dose profiles with the dual detector configuration showed the best agreement with the reference dosimetry configuration measurement at solid water buildup depth of 6.0 cm (Fig. 4.4). This result was consistent in both the transit and nontransit geometries and agreed with calculation (Eq. 4.1) to within 0.5 mm. Therefore, D_{eff} was determined to be 6.0 cm for all configurations. The sensitivity of CAX dose versus depth at D_{eff} was approximately 0.3%/mm.

4.3.1.2 Field size output factor and off-axis response

Figures 4.5(a) and 4.5(b) show the field size output factor measured with the dual detector configuration and reference dosimetry configuration at varying buildup depths, in nontransit and transit geometries, respectively. Field size output factors measured with the dual detector match within 0.8% to those measured with the reference dosimetry configuration at buildup depth 6 cm (D_{eff}). Consistent with results described in Section 4.3.1.1, the best agreement with dual detector field size output factors was achieved with 6 cm buildup. The detector response at positions away from the central axis of the x-ray beam is shown in Fig. 4.6 for the dual detector configuration and reference dosimetry configuration in nontransit and transit geometries. The maximum percentage difference in beam profiles between the dual detector configuration and reference dosimetry configuration was $\leq 2.5\%$ in both nontransit and transit geometries (inside the radiation field). The noise for field size $5 \times 5 \text{ cm}^2$ seen in figure 4.6(b) could be associated to slight offset of the detector position from central axis while changing the setup.

4.3.1.3 Transmission factors

Transmission factors measured with both the dual detector configuration and reference dosimetry configuration in transit geometry are shown in Fig. 4.7. Transmission factors measured with the dual detector configuration match within $\leq 0.5\%$ to those measured with the refer-

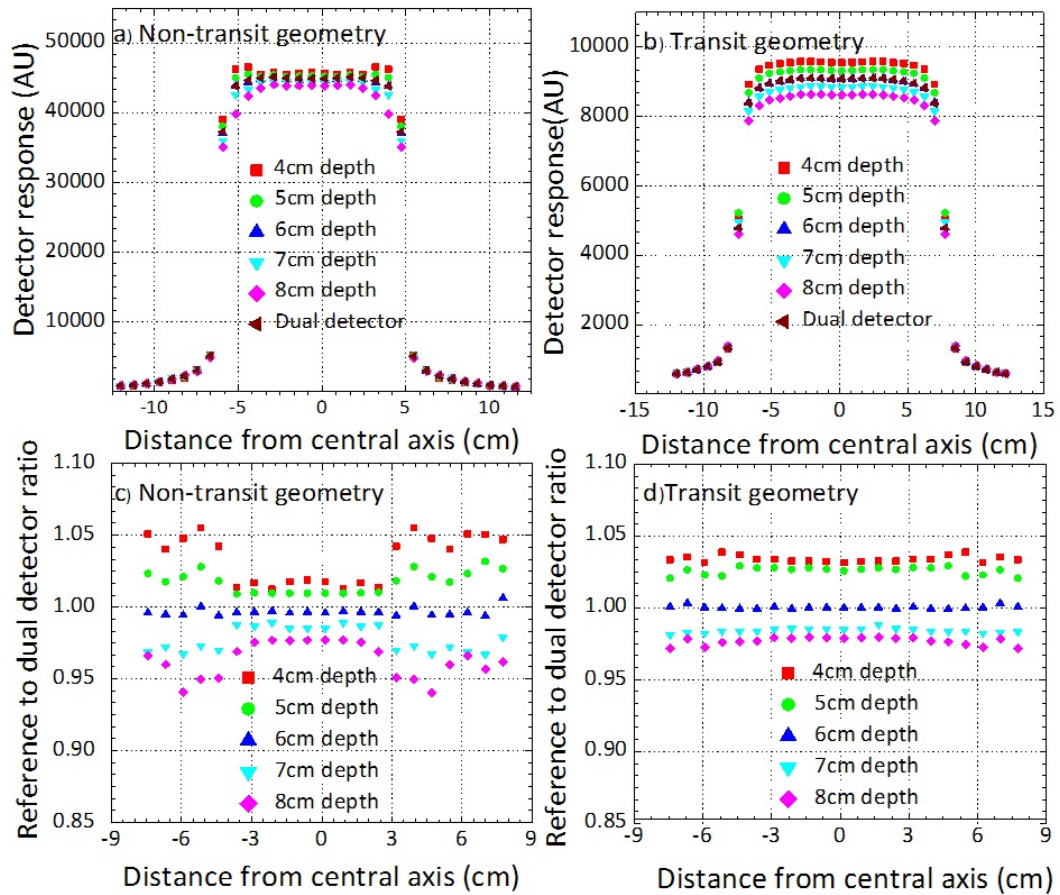


Figure 4.4: Comparison of (a) nontransit geometry and (b) transit geometries, ICA measured dose profiles in reference dosimetry configuration at buildup depths of 4, 5, 6 cm (D_{eff}), 7 and 8 cm of solid water slab with the dual detector configuration. The relative ratio between dose profiles measured at varying buildup depths in reference dosimetry configuration to the dose profile measured with dual detector configuration is also shown for (c) nontransit and (d) transit geometries, respectively.

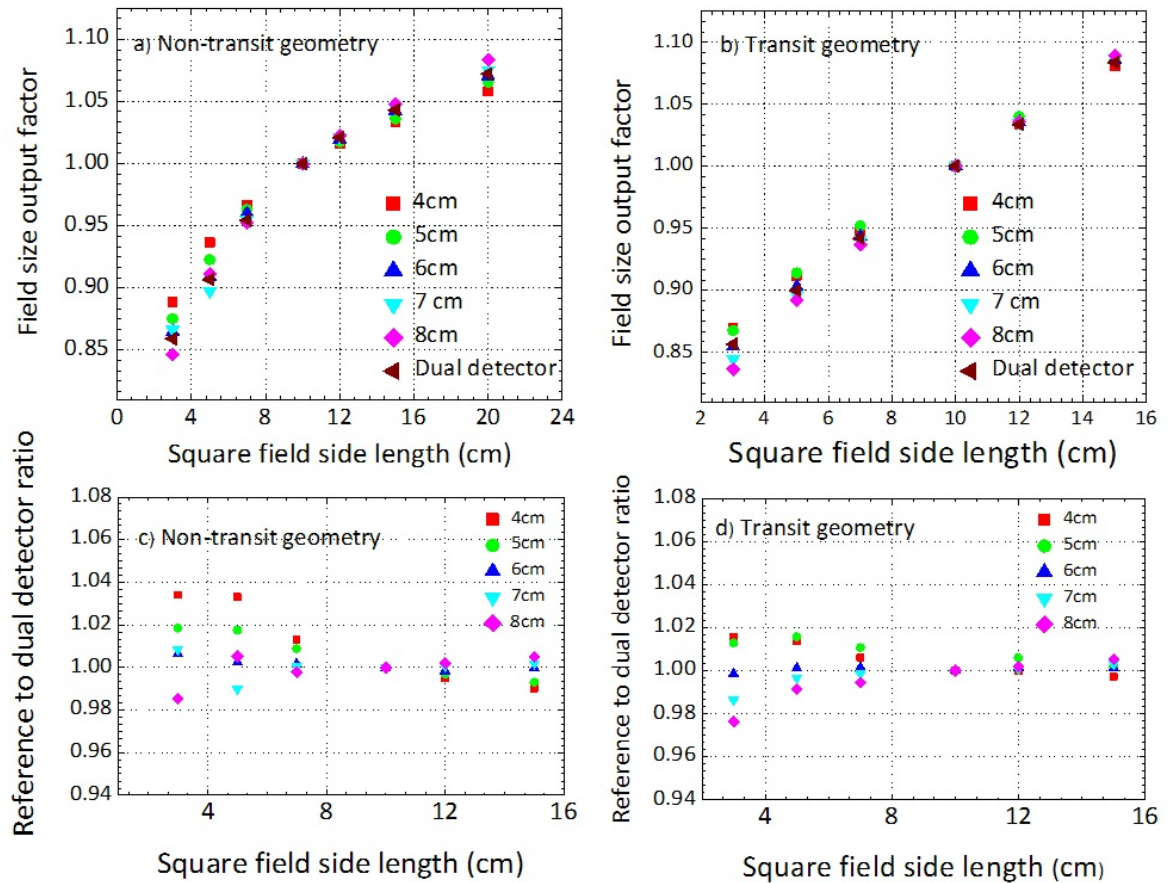


Figure 4.5: Comparison of (a) nontransit geometry and (b) transit geometries, ICA measured field size output factors in reference dosimetry configuration at buildup depths of 4, 5, 6 cm (D_{eff}), and 7 and 8 cm of solid water with the dual detector configuration. The relative ratio between field size and output factors measured at varying buildup depths in reference dosimetry configuration to dual detector configuration is also shown for (c) nontransit and (d) transit geometries, respectively.

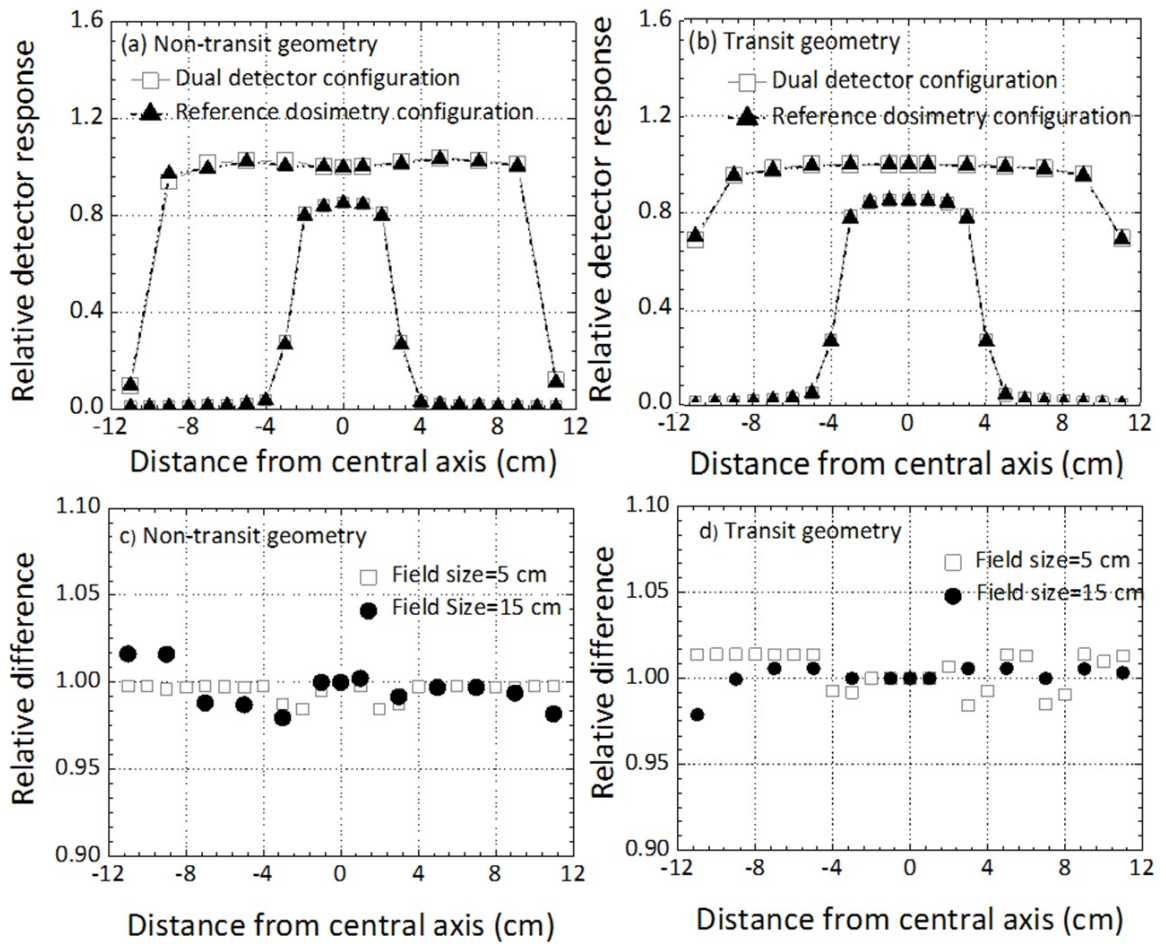


Figure 4.6: Comparison of relative dose profiles in the (a) nontransit and (b) transit geometries measured with the ICA in the dual detector configuration and reference dosimetry configuration for $5 \times 5 \text{ cm}^2$ and maximum achievable field sizes within the respective measurements geometries. The relative ratio between the two configurations is shown for (c) nontransit and (d) transit geometries.

ence dosimetry configuration at 6 cm (D_{eff}).

4.3.2 IMRT

4.3.2.1 Non-transit geometry

The gamma evaluation results for the absolute dose maps of IMRT fields measured with ICA in the dual detector configuration and reference dosimetry configuration in the nontransit geometry are presented in Table 4.1. In all cases, the pass rates were greater than 99%, indicating a very close agreement between detector configurations. Figure 4.8 shows the almost indistinguishable dose profiles of a wedge IMRT pattern measured with the ICA in the dual detector configuration and reference dosimetry configuration.

Table 4.1: Gamma evaluation results comparing the absolute dose map with ICA in dual detector configuration and reference dosimetry configuration for clinical IMRT fields and standard IMRT test patterns in nontransit geometry

IMRT fields	Percentage gamma pass rate (2%/2 mm)
Y1-step wedge	99.1
X2-step wedge	99.4
Complex pyramid	100.0
Clinical IMRT-1	99.7
Clinical IMRT-2	100.0

4.3.2.2 Transit geometry

The Gamma evaluation results for the ICA absolute dose map with the dual detector configuration and reference dosimetry configuration in head and neck, brain, lung, and prostate IMRT fields with anthropomorphic phantoms and solid water slab phantom placed in the beam are presented in Table 4.2. The mean pass rates, averaged over all fields in the individual plans were greater than 98% including IMRT standard test patterns (data not shown), indicating a very close agreement between detector configurations in the transit geometry.

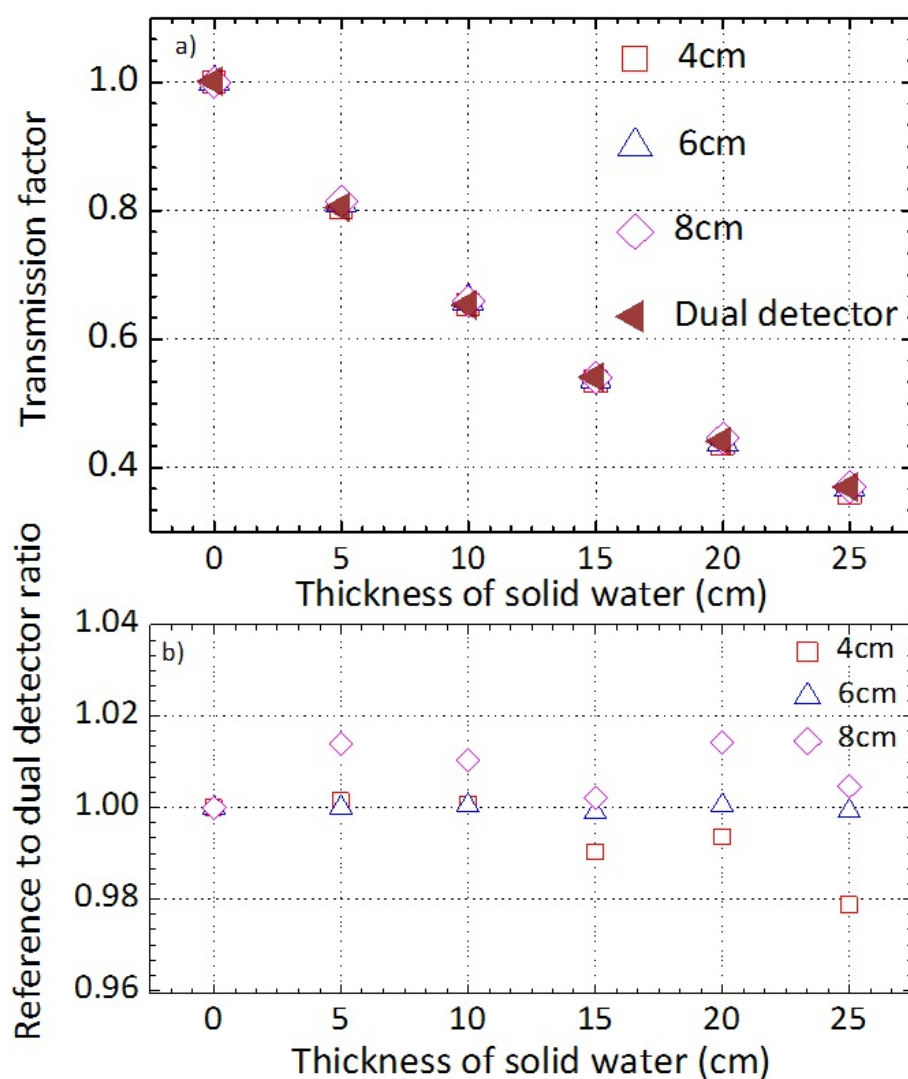


Figure 4.7: Comparison of transmission factors measured with the dual detector configuration at buildup depths of 4, 6, 8 cm, and reference dosimetry configurations, respectively. The measurements were performed with static fields of $15 \times 15 \text{ cm}^2$ defined at the isocenter. The relative ratio of transmission factors for reference dosimetry and dual detector configurations is also shown (b).

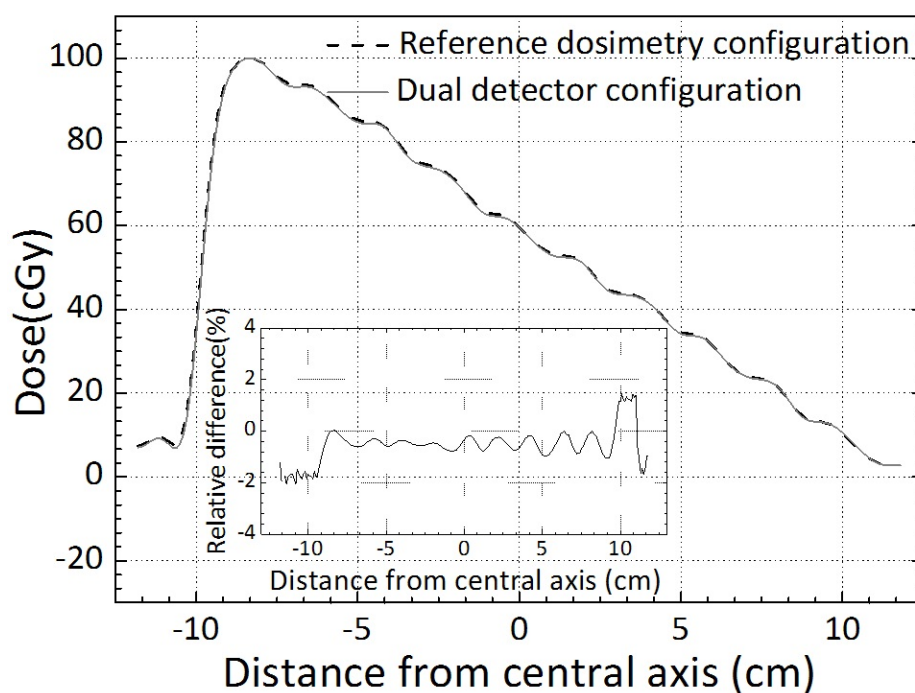


Figure 4.8: Dose profile comparison for wedge IMRT test pattern measured with both reference dosimetry and dual detector configurations. The ratio of the dose profiles is displayed in the insert.

Table 4.2: Gamma evaluation results comparing the ICA absolute dose map from the dual detector configuration and reference dosimetry configuration using anthropomorphic or solid water slab phantoms, and IMRT fields

	Head and Neck ^a	Brain ^a	Lung ^a	Prostate ^a	Prostate ^b
Field	Percentage gamma pass rate (2% and 2 mm criteria)				
1	98.1	97.66	100	97.95	99.5
2	100	100	97.6	100	99.2
3	96.5	99.5	100	100	99.8
4	100	100	100	98.2	100
5	100	100	98.2	99.3	
6	100			100	99.1
7	97.6		96.32		
Mean	98.8	99.43	99.39	98.59	99.5

^a Measurement with anthropomorphic phantom in the beam.

^b Measurement with solid water slab phantom in the beam.

The above dose response evaluation demonstrates that integrating the ICA with the EPID in the dual detector configuration had no significant impact on dose response over a wide range of clinically relevant conditions once the equivalent depth is accounted for. The dose response of the ICA was not sensitive to the non-water equivalent layers of material of the EPID (e.g., the thin metal screen that sits on top of the phosphor scintillator). The EPID is known to be materially homogeneous in the direction perpendicular to the beam, and this is an important requirement for the dosimetry aspect of the dual detector concept. As the ICA can acquire and report data frame by frame in real-time, it could, in principle, be used for time resolved dose verification during IMRT or volumetric modulated arc therapy (VMAT) [201, 246] in the dual detector configuration. The development of a clinical dosimetry model is beyond the scope of this work. Many models for implementing the transit in vivo dosimetry with EPIDs have been demonstrated and continue to be developed. It is anticipated that any of these published EPID based models could be adapted for use with a water equivalent dosimeter and implemented with more reliable dosimetry based on standard dose in water models.

4.3.3 Image quality evaluation

4.3.3.1 QC-3V image quality phantom

The spatial resolution (determined by the spatial frequency at half the maximum MTF (f_{50})), noise, and CNR measured using the PipsPro QC-3V image quality phantom and software in the reference imaging configuration and dual detector configuration are shown Table 4.3. The presence of additional backscatter material decreases CNR in the dual detector configuration. Figure 4.9 shows the images of the QC-3V image quality phantom taken with the EPID in the reference imaging configuration and dual detector configuration. While the resolution and CNR reported by the PipsPro software was better for the reference imaging configuration, there is no appreciable difference in the visual perception of high or low contrast detail between the two configurations.

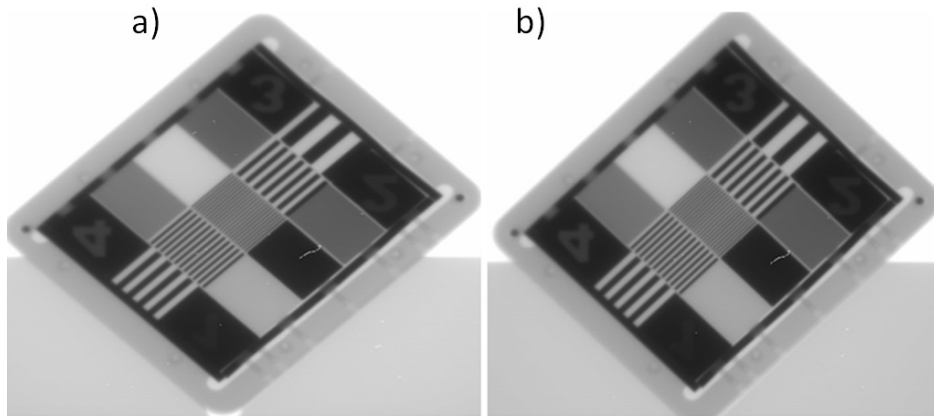


Figure 4.9: EPID images of the QC-3V image quality phantom taken with the (a) reference imaging configuration and (b) dual detector configuration.

Table 4.3: Comparison of resolution, noise, and CNR for the dual detector configuration and reference imaging configuration. The results are quoted as mean \pm standard deviation from five repeat measurements

EPID configuration	Resolution(f_{50})(lp/mm)	Noise	CNR
Dual detector configuration	$0.40 \pm 1.25 \times 10^{-3}$	14.94 ± 3.34	263.23 ± 24.85
Reference configuration	$0.41 \pm 1.14 \times 10^{-3}$	7.81 ± 1.57	324.01 ± 26.65

4.3.3.2 LSF and MTF

Figure 4.10 compares LSFs measured in the dual detector configuration and reference imaging configuration as described in section 4.2.6.2. The FWHM for the reference imaging configuration and dual detector configuration matches very closely (0.075 mm difference). The LSF for the dual detector configuration becomes increasingly wider compared to the reference imaging configuration below approximately 10% of the peak signal. This is consistent with signal blurring from the additional broad angle backscatter, due to the presence of the solid water and ICA in the dual detector configuration. Figure 4.11 compares the MTFs derived from the measured LSFs in Fig. 4.10. The measured spatial frequency at half the maximum MTF (f_{50}) was 0.14 mm^{-1} and 0.12 mm^{-1} for the reference imaging configuration and dual detector configuration, respectively. The kink in MTF curve at approximately 0.8 mm^{-1} which could be the combination of both analysis approach and slight setup variation while switching from reference configuration to dual detector configuration measurement.

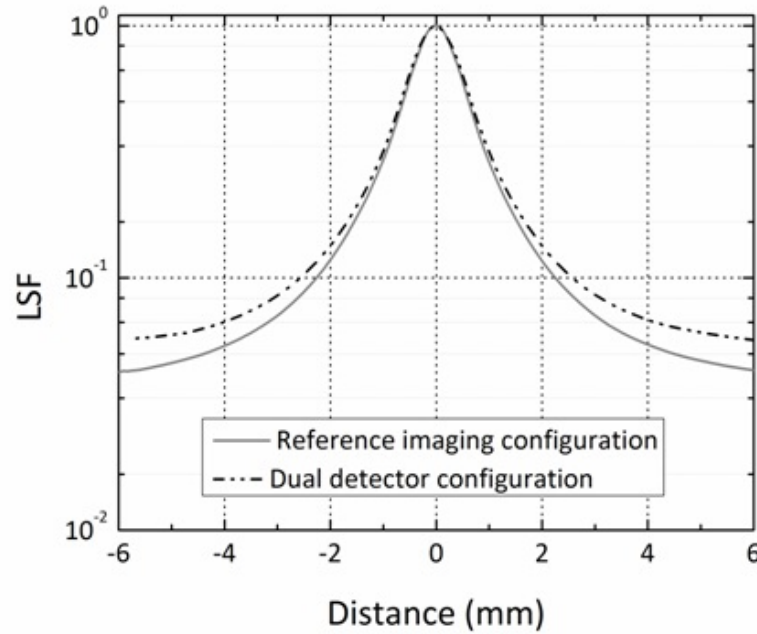


Figure 4.10: The measured line spread function (normalized) for the reference imaging configuration and dual detector configuration.

Figure 4.12 compares the relative pixel sensitivity for an open static $5 \times 5 \text{ cm}^2$ field acquired in both configurations. The increase in EPID signal with the dual detector configuration is an approximately uniform 2%–3% across the image due to the contribution of additional backscatter signal from the solid water and ICA. The characteristics of the backscatter effect on EPID signal seen here are consistent with that reported previously [204]

4.3.3.3 Anthropomorphic phantom

AP projection images of an anthropomorphic head phantom acquired using the reference imaging configuration and dual detector configuration are shown in Fig. 4.13. The images from the two configurations show no discernible difference in the visualization of anatomical details. The qualitative and quantitative imaging results reported above demonstrate that while the presence of the additional backscatter material had a measurable effect on EPID imaging performance (see Table 4.3), the effect was not visible in qualitative image comparisons (see Figs. 4.9 and 4.13) and is considered negligible for clinical purposes. Further study is required to assess the dual detector imaging performance comprehensively in a clinical setting.

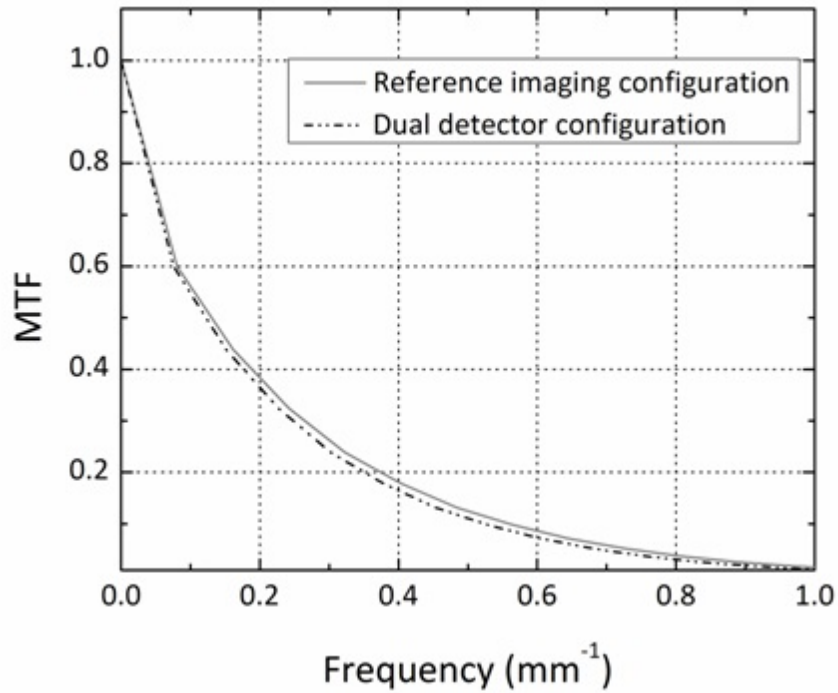


Figure 4.11: The measured modulation transfer function for the reference imaging configuration and dual detector configuration.

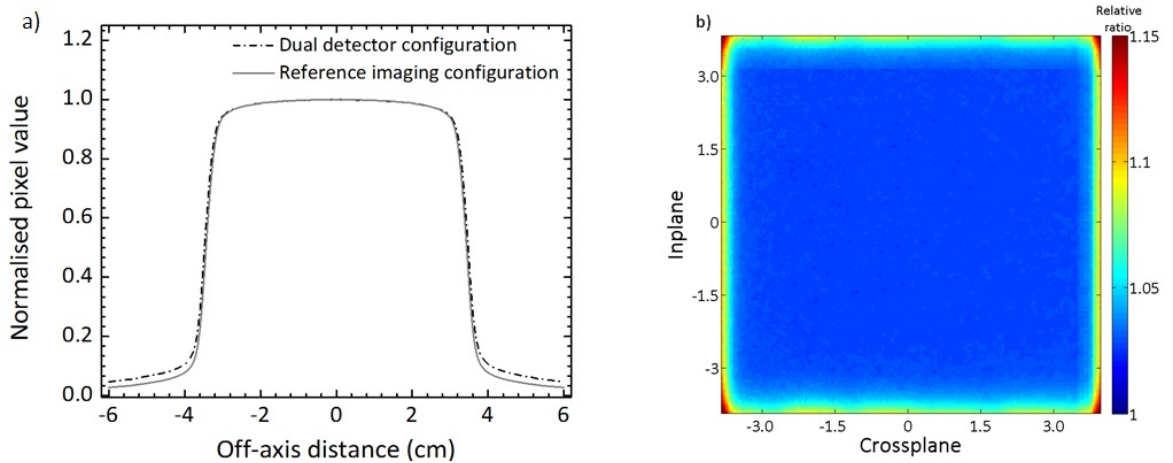


Figure 4.12: Illustration of impact of backscatter in dual detector configuration: (a) Relative line profile of EPID images of an open static field for dual detector configuration (dashed-dotted line) and reference imaging configuration (solid gray line). (b) 2D pixel value relative ratio map between reference imaging configuration and dual detector configuration for static open $5 \times 5 \text{ cm}^2$ field.

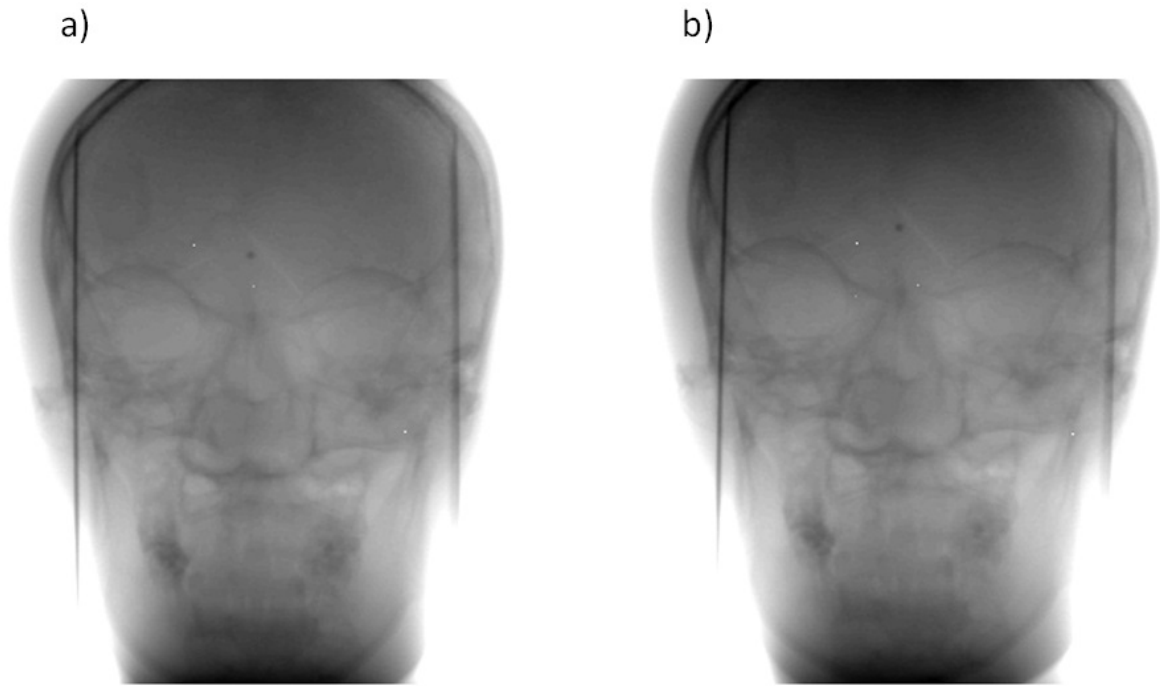


Figure 4.13: Portal image of anthropomorphic head phantom acquired with the (a) reference imaging configuration and (b) dual detector configuration to assess the impact of the presence of the ICA on portal image visualization.

4.3.4 Optimized dual detector design

In this study, we used readily available equipment to demonstrate the feasibility of the dual detector concept. The measured dose was offset by 1.3% at CAX and both the field size and transmission factor by $<0.5\%$ when 5 cm backscatter was removed in the dual detector configuration. This suggests the required backscatter material thickness could be further optimized for dosimetric purposes. Figures 4.10 and 4.11 compares the measured LSF and MTF for dual detector configuration (5 cm solid water plus ICA) and reference imaging configuration (without backscatter material). It is demonstrated that the difference is due to the presence of backscatter material. These are two extreme scenarios. The backscatter material thickness optimized for dosimetric purpose will further improve the imaging performance. It is envisaged that a more elegant design could be easily achieved based on the same concept but with a purpose built configuration to optimize performance. An optimized dual detector may incorporate different imaging or dosimetry detectors to those used in this study. For example, a more efficient imager consisting of high atomic number segmented crystalline scintillators [35, 36, 231, 247] could be incorporated without compromising dose verification capability as long as the sensitive detector of the overlying EPID is materially

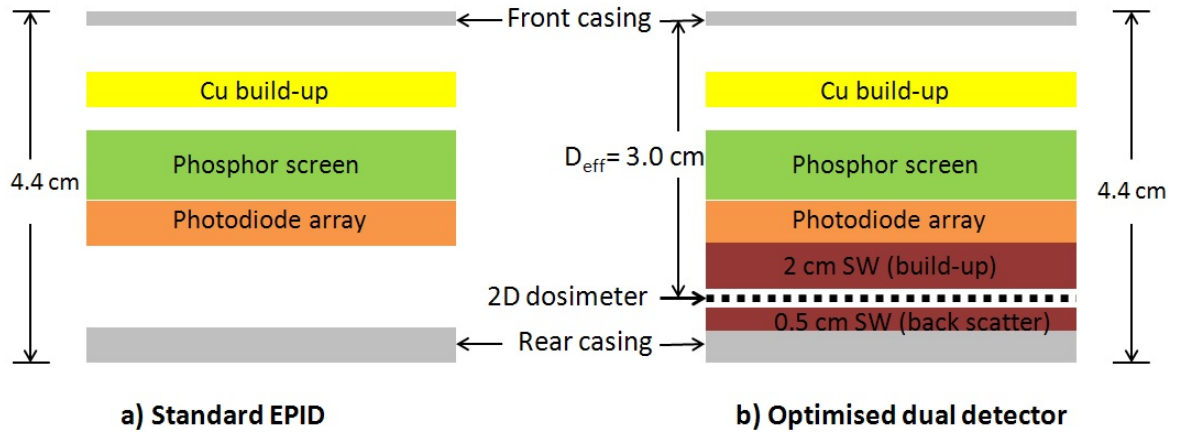


Figure 4.14: Schematic illustration of conceptual optimized design (RHS) for dual detector that fits within the existing standard EPID (LHS) panel dimensions. Schematics are not drawn to scale, and the gaps located between the neighboring layers are for illustrative purposes only.

homogeneous in a direction perpendicular to the beam. A smaller detector spacing on the dose detector for higher resolution dosimetry with higher signal to noise ratio would also be desirable for modulated fields and improved characterization of high dose gradient regions. Figure 4.14 shows a schematic diagram of a possible dual detector design that fits within the size of existing EPID panels. A water-equivalent depth equal to the depth of dose maximum for the highest photon energy being used would be adequate for dosimetry with all photon energies. The dimensions shown in Fig. 4.14 would be suitable for a Linac delivering up to 18 MV photons. The total dimensions of the dual detector in Fig. 4.14 are compatible with existing Perkin Elmer EPID panels and should, therefore, be compatible with existing Linac EPID housings. Additional considerations not investigated in this study include the engineering requirements of the mechanical support and the configuration of electronics and data readout schemes required to implement the proposed dual detector configuration.

This study demonstrates proof-of-concept of a novel dual detector for radiotherapy treatment verification. Current EPID detectors are optimized for imaging but are suboptimal for dosimetry. The proposed dual detector concept decouples the imaging and dosimetry functions so that each can be optimized without significantly compromising the other, providing more flexibility for future improvements in radiotherapy treatment verification systems.

4.4 Conclusion

The proposed dual detector configuration, combining a conventional EPID and 2D array dosimeter, can be operated simultaneously as both imager and dosimeter without significant compromise in the performance of either device. This study demonstrates the feasibility of a dual detector configuration device for simultaneous imaging and in vivo dosimetry in radiation therapy.

4.5 Acknowledgments

The authors report no conflicts of interest in conducting the research. The authors would like to acknowledge the funding support from the Cancer Institute NSW Australia (Research Equipment Grant 10/REG/1-20) and Cancer Council NSW (Grant ID RG 1-06).

Chapter 5

Novel dual detector concept for simultaneous transit dose and image verification in radiotherapy

Statement of joint authorship

S. Deshpande: Develop experimental design, performed experiments, analysed results, wrote manuscript

S. Alhujaili and O. Brace: Assisted with experiments

P. Vial and L. Holloway: Render advice on the experiment, interpreting results and write up

M. Petasecca M.Lerch: Assisted with experiments and interpreting results

A. Rosenfeld and P. Metcalfe: Assisted in interpreting results and writing, as supervisors both of them endorse the assessment

[‡]Part of this chapter has been submitted for publication:

S. Deshpande, S. Alhujaili, O Brace, P. Vial, L. Holloway, M, Petasecca, M.Lerch, A. Rosenfeld, P. Metcalfe, Silicon array dosimeter in situ with electronic portal image device for simultaneous transit dose and image verification in radiotherapy *Physica Medica*, (**In Submission**)

5.1 Introduction

Currently, radiation therapy (RT) is trending toward more precise and accurate dose delivery, which employs radiation beam intensity modulation and image guidance for target positioning either on-line or in real time. Emerging techniques are increasingly sensitive to geometric errors and verifying the delivered dose is increasingly challenging. Therefore, a comprehensive treatment verification system should have the capability of verifying both geometric (i.e. location of target in real time) as well as dosimetric accuracy (i.e. correct quantity of dose delivered) to ensure the delivered dose matches the prescribed dose. To address the increasing demands on geometric accuracy the use of imaging for treatment verification has developed rapidly in recent years [102]. Image-guided radiotherapy (IGRT) aids in tracking daily treatment setup to minimize geometric error.

The kilovoltage (kV) imaging devices attached to the linac providing a superior soft tissue contrast have improved patient and target position verification prior to treatment. They do not utilise the treatment beam and therefore do not directly verify the treatment delivery in real-time or/and may not be done routinely. Verifying dose accuracy for modern treatments such as intensity-modulated radiation therapy (IMRT) typically relies on pre-treatment dose measurements. However, pre-treatment measurements are time consuming and do not necessarily identify clinically relevant errors in dose delivery that may occur during the course of treatment. These factors are driving a growing demand for effective in- vivo dose verification [61, 119]. All medical linear accelerator (linac) vendors currently provide amorphous silicon (a-Si) electronic portal imaging devices (EPIDs) as a standard IGRT option [23]. These standard EPIDs are optimised for imaging but are suboptimal for dosimetry due non-linear energy dependence [25–27, 189, 248]. Several groups have developed methods to account for energy response, either with complex algorithms or Monte Carlo computations [25, 28–34] to utilise the standard EPID as a dosimeter. Despite the demonstrated potential, the clinical implementation of EPID dosimetry still limited to a relatively small number of centres.

Further, the changes in EPID technology over recent decades have not been driven by the technical demands of dosimetry, but by the need for improved imaging standards for patient positioning, such as enhancement in image quality and faster read-out. More sensitive detector designs have also been proposed for improved megavoltage (MV) imaging performance [35, 36]. These efficient MV detectors generally consist of higher atomic number materi-

als than current EPIDs, which is likely to make EPID dosimetry even less water equivalent and still more difficult to implement. A small body of research explores novel EPID design specifically to act as dosimeters rather than imagers [27, 37–39]. The former scenario i.e. dosimetry with standard EPID typically necessitates a complex detector characterisation and calibration scheme along with custom software to convert portal images into water-equivalent dose images, an approach undertaken in majority of previously reported studies on EPID dosimetry [23]. The latter scenario has seen detector prototypes that, while capable of performing accurate patient dosimetry, suffer from decreased x-ray detection efficiency thus inhibiting their use for imaging [38, 40]. In both cases, proposed detectors have not been suitable for applications in both imaging and dosimetry.

Our research group is engaged in developing a system which is capable of verifying both delivered dose (dosimetry) and geometric (location of target) accuracy without compromising each other. First approach was to replace the metal/phosphor screen by plastic scintillator array referred as a novel prototype EPID configuration [40]. Although demonstrated to be a water equivalent dosimeter, further improvement is required to match the imaging performance of this configuration to commercially available a-Si EPIDs. Another approach was a dual detector concept [249] that combined the dosimeter (2D ionization array) with imager (standard EPID), as described in Chapter 4 of this thesis. The configuration utilized a bulky 2D ionization chamber array dosimeter (ICA). This posed engineering challenges to combine both imager and dosimeter into a clinical system. An important requirement for the dosimetry aspect of the dual detector concept is that the overlying EPID imager structure should be materially homogeneous in a direction perpendicular to the beam [249]. It is unclear whether the next generation of more efficient EPID imager e.g. [247], will meet this requirement. The initial assessment of imaging performance demonstrated that placing the ICA either above EPID (Appendix A) or underneath the EPID as shown in previous chapter 4 degrades the EPID imaging performance.

In this study, we proposed an alternate dual detector design which different from our previously reported design [249]. The main design differences of the alternative dual detector were: (i) Radiation transparent prototype 2D silicon array ('Magic Plate') [250, 251] was utilised as the dosimeter, (ii) Magic Plate was placed above the EPID (imager). Apart from being radiation transparent, the Magic Plate also possess several favourable characteristics to be used as an in vivo dosimeter including; compact design, high temporal resolution (time resolved dosimetry) and high signal-to-noise ratio. The dose response characterisation of the

Magic Plate as a 2D transmission detector [250, 252] and as a 2D detector when sandwiched in solid water for pre-treatment verification [250] had been reported previously. The clinical application of the dual detector system requires that performance of both the dosimeter and imager is not significantly degraded due to the presence of either device. In this study we investigate the clinical feasibility of a new dual detector configuration with a comprehensive experimental assessment. The imaging performance of the EPID and the dose response characteristics of the Magic Plate in the dual detector configuration as an in vivo dosimeter were compared against their respective standalone (reference) configurations.

5.2 Methods and Materials

5.2.1 Equipment

The dosimetry equipment used in this study consisted of a prototype 2D silicon diode array dosimeter with 11 x 11 epitaxial silicon diodes (figure 5.1a) , hereafter referred as Magic Plate (MP). The silicon detectors are spaced at 10 mm centre-to-centre. The physical size of each diode in MP is 1.5 x 1.5 x 0.425 mm³ with field of view of 11 x 11 cm². Details regarding MP detector construction and data acquisition system are reported in previous work [250, 252]. The commercial 2D ion chamber array (ICA), I^mRT MatriXX (IBA Dosimetry, Schwarzenbruck, Germany) was used as the 2D reference dosimeter. This device has an array of 1020 air-vented plane parallel ionization chambers (with a volume of 0.08 cm³ each) arranged in a 32 × 32 grid of dimensions 24 × 24 cm². The ionization chambers are spaced at 7.62 mm centre-to-centre. A solid water slab was used as water equivalent build-up material (Gammex RMI, Middleton, WI, USA). The imaging detector used was an a-Si EPID (XRD 1640 AN CS PerkinElmer, Santa Clara, CA) and the imaging data was collected using XIS software V3.3.1.1 (PerkinElmer, Santa Clara, CA) using a 399 ms frame period. The EPID consists of a 40 × 40 cm² a-Si photodiode array and comprises 1024 × 1024 pixels, giving a pixel pitch of approximately 0.4 mm. A QC-3V image quality phantom and Pips-Pro software (version 3.2.3a, Standard imaging, Inc., Middleton, WI, USA) were used to assess image quality. All the clinical modulated fields were planned on the Pinnacle treatment planning system (Philips Radiation Oncology Systems, Fitchburg, WI Version 9.0).

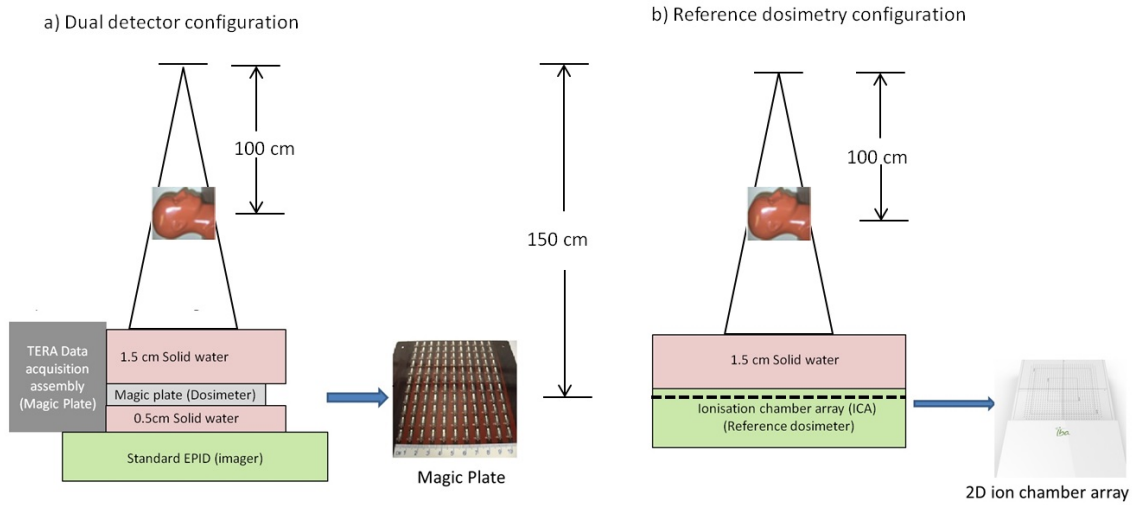


Figure 5.1: Schematic illustration for dosimetry measurement setups (a) dual detector configuration and (b) reference dosimetry configuration. For transit geometry measurements, either the solid water slab or anthropomorphic phantom (interchangeable) was used. For visualization purpose, only the anthropomorphic phantom image is shown placed at isocenter

5.2.2 Dosimetry experimental setup

Transit dose measurements were performed at an extended 150 cm source-to-detector distance with a slab of solid water (Gammex RMI, Middleton, WI) or an anthropomorphic phantom (ATOM[®] Dosimetry Verification phantoms, CIRS)) positioned on the treatment couch and centred at the isocenter. The equalization factor to account for detectors sensitivity differences within the MP was obtained by the method proposed by Kwan et al [253] and applied. The MP was calibrated to dose by cross calibration with the ICA at a 10×10 cm² field size, source to detector distance (SDD) of 150 cm, with no object present in the beam.

5.2.2.1 Reference dosimetry configuration

The reference dosimetry configuration comprised of a small solid water buildup placed on the ICA (figure 5.1b) to ensure electronic equilibrium at the detector array. All dosimetry measurements with the ICA in the reference dosimetry configuration were used to compare with the dose response of the dual detector configuration. The water equivalence of the ICA dose response has been validated in both transit and non-transit geometries [155, 206, 238].

5.2.2.2 Dual detector configuration

The dual detector configuration consisted of an MP (closest to the source), 0.5 cm solid water slab and EPID. The 0.5 cm of solid water slab between MP and EPID was necessary to fill the air gap between the two devices (see figure 5.1a). Sections 5.2.3.2 and 5.2.4 describe the experiments used to compare the dose response of the MP in the dual detector configuration with the reference dosimetry configuration (described above in Section 5.2.2.1).

5.2.3 Dose response evaluation

5.2.3.1 Estimation of optimal build-up thickness for dosimetry

There is a trade-off between increasing the buildup thickness required for reliable dosimetry and decreasing the imaging performance due to associated blurring. The optimal buildup thickness for dosimetry was determined as the minimum build up thickness at which the measured field size output factor and off-axis response (as described in section 5.2.3.2) showed the closest agreement between the reference dosimetry configuration and dual detector configuration. Measurements were performed with 3, 5, 10 and 15 mm solid water build-up for both reference dosimetry configuration and dual detector configuration.

5.2.3.2 Field size output factor and off-axis response

The field size output factor for square field sizes varying from 3 x 3 to 15 x 15 cm² was determined from the ratio of the detector response at CAX relative to a 10 x 10 cm² field. The measured profiles for field sizes 3 x 3 cm², 5 x 5 cm² and 10 x 10 cm² with both dual detector configuration and reference dosimetry configuration were compared.

5.2.4 Clinical modulated Fields

Several clinical dosimetry measurements were performed for absolute dose comparison. Four brain, step and shoot IMRT fields and a VMAT prostate field (single arc plan) were measured (integrated acquisition mode) using both the dual detector configuration and the reference dosimetry configuration. Either a 20 cm thick solid water slab or an anthropomorphic phantom was placed at isocentre as a transit object. All measurements employed the optimal build up thickness on the detectors (as described in Sections 5.2.3.1 and 5.2.3.2). These transit dose measurements were performed at a source-to-detector distance (SDD) of

150 cm with sheets of solid water or an anthropomorphic phantom positioned on the treatment couch and centered at the isocenter. All experiments were conducted on an Elekta Synergy linear accelerator (Elekta Oncology Systems, Crawley, UK) with 6 MV photons at gantry 0° only. The MP plate has a 1 cm², 2D spatial resolution. For an accurate dose verification of modulated treatment field, a higher spatial resolution detector is recommended [109]. To improve the spatial resolution, we delivered the same clinical plans to the MP five times with the MP shifted relative to the radiation beam by 0.5 cm orthogonally between measurements (central position, 5 mm in positive X-direction, 5 mm in negative X-direction, 5 mm in positive Y-direction and 5 mm in negative Y-direction from beam axis). Data from the five measured dose distributions were merged. The gamma evaluation technique [240] was applied to quantitatively compare the 2D dose maps measured of the dual detector and reference dosimetry detectors. The gamma criteria used was 3% dose difference (relative to the maximum dose) and 3 mm distance-to-agreement, with doses below 10% of the maximum dose excluded from the evaluation.

5.2.5 Imaging experimental setup

The impact from additional build up material and MP used in the dual detector configuration on the imaging performance of the EPID was evaluated quantitatively and qualitatively. For both quantitative and qualitative assessment of the dual detector imaging performance, images were acquired for three different experimental setups: i) MP with no buildup, ii) MP with 10 mm thick solid water and iii) MP with 15 mm thick solid water. Similar to the dosimetry evaluation, the EPID's imaging performance was experimentally evaluated by comparing the image quality in a reference imaging configuration with the dual detector configuration. The reference imaging configuration represents the EPID as routinely used in a clinical setting without the presence of any additional material on the EPID structure. All the image quality measurements were performed (as discussed in section 5.2.2.2) at a fixed source to detector (imager) distance of approximately 151.2 cm.

5.2.5.1 Reference imaging configuration

The reference imaging configuration represents the standard EPID as routinely used in a clinical setting without the presence of any additional material on EPID structure.

5.2.5.2 Dual detector configuration

The dual detector configuration is the MP with the added solid water slab placed above the standard EPID as described in section 5.2.2.2

5.2.6 Image quality evaluation

5.2.6.1 QC-3V image quality phantom

The PipsPro QC-3V image quality phantom and software were used to compare the EPID spatial resolution, noise and contrast-to-noise ratio (CNR) in the dual detector configuration and reference imaging configuration. The phantom was placed on its side on the treatment couch and positioned using the external alignment marks at the isocenter. EPID images of the phantom were acquired using an average of 1 frame (4 MU, or a dose of approximately 0.6 cGy at the detector plane) in the reference imaging configuration and dual detector configurations. The low dose levels used here are similar to those typically used for pre-treatment portal imaging. Details on the algorithms used to calculate CNR and MTF using PipsPro software can be found in the literature [241].

5.2.6.2 Anthropomorphic phantom

Images of an anthropomorphic pelvis phantom were acquired to qualitatively evaluate the performance of the EPID in the dual detector configuration and reference imaging configuration, when imaging an object representative of human anatomy. With the gantry angle at 0° , the pelvis phantom was positioned facing the source on the treatment couch and was centred at the isocenter. For each EPID configuration, an anterior-posterior (A-P) image of the phantom was acquired by averaging 1 individual frame (4 MU or a dose of approximately 0.6 cGy at detector plane).

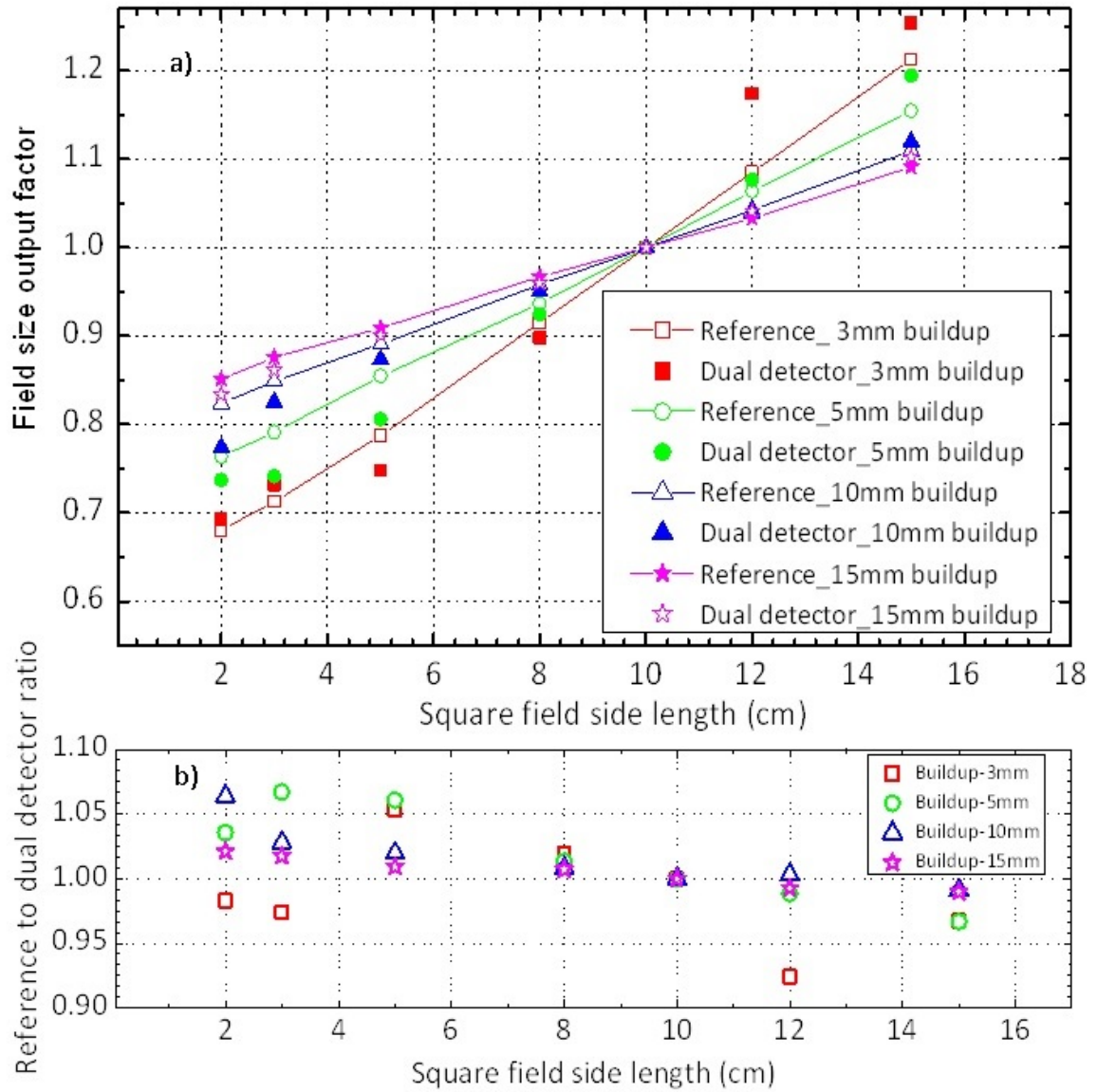


Figure 5.2: Comparison of (a) measured dual detector field size output factors at build-up depths 3 mm, 5 mm, 10 mm and 15 mm of solid water with the reference dosimetry configuration and the dual detector configuration. The relative ratio of field size output factors between reference dosimetry configuration and dual detector configuration measured at varying build-up depths is also shown (b)

5.3 Results and Discussion

5.3.1 Dosimetry evaluation

5.3.1.1 Field size output factor and Off-axis response

Figure 5.2 displays the comparison of field size output factor measured with the dual detector configuration and reference dosimetry configuration at 3 mm, 5 mm, 10 mm and 15 mm build-up depths. Field size output factors measured with the dual detector match within 1.5% to those measured with the reference dosimetry configuration at build-up depth 1.5 cm. Figure 5.3 displays the comparison of off axis profiles measured with the dual detector configuration and reference dosimetry configuration at 3 mm, 5 mm, 10 mm and 15 mm build-up depths. Off-axis profile measured with the dual detector agreed within 1.0% to that measured with the reference dosimetry configuration at build-up depth 1.5 cm and is the closest agreement among build up thicknesses considered here.

5.3.1.2 Clinical IMRT fields

The gamma evaluation results comparing the MP dose map in the dual detector configuration with reference dosimetry configuration for one prostate and four brain modulated fields with either anthropomorphic phantoms or 20 cm of solid water slab phantom placed in the beam are presented in Table 5.1.

Table 5.1: Gamma evaluation results comparing the MP absolute dose map from the dual detector configuration and reference dosimetry configuration with either an anthropomorphic phantom or 20 cm thick solid water slab placed in beam. Five clinical modulated fields were measured.

Clinical site	Field no.	Treatment technique	Gamma pass rate	3%/3mm	Mean Gamma	
Brain	1	IMRT	97.4 ^a	96.1 ^b	0.34 ^a	0.38 ^b
Brain	2	IMRT	96.8 ^a	95.8 ^b	0.39 ^a	0.41 ^b
Brain	3	IMRT	95.5 ^a	94.9 ^b	0.42 ^a	0.46 ^b
Brain	4	IMRT	96.4 ^a	95.7 ^b	0.38 ^a	0.40 ^b
Prostate	1	VMAT	95.8 ^a	95.1 ^b	0.41 ^a	0.44 ^b

^aMeasurement with solid water slab phantom in the beam

^bMeasurement with anthropomorphic phantom in the beam

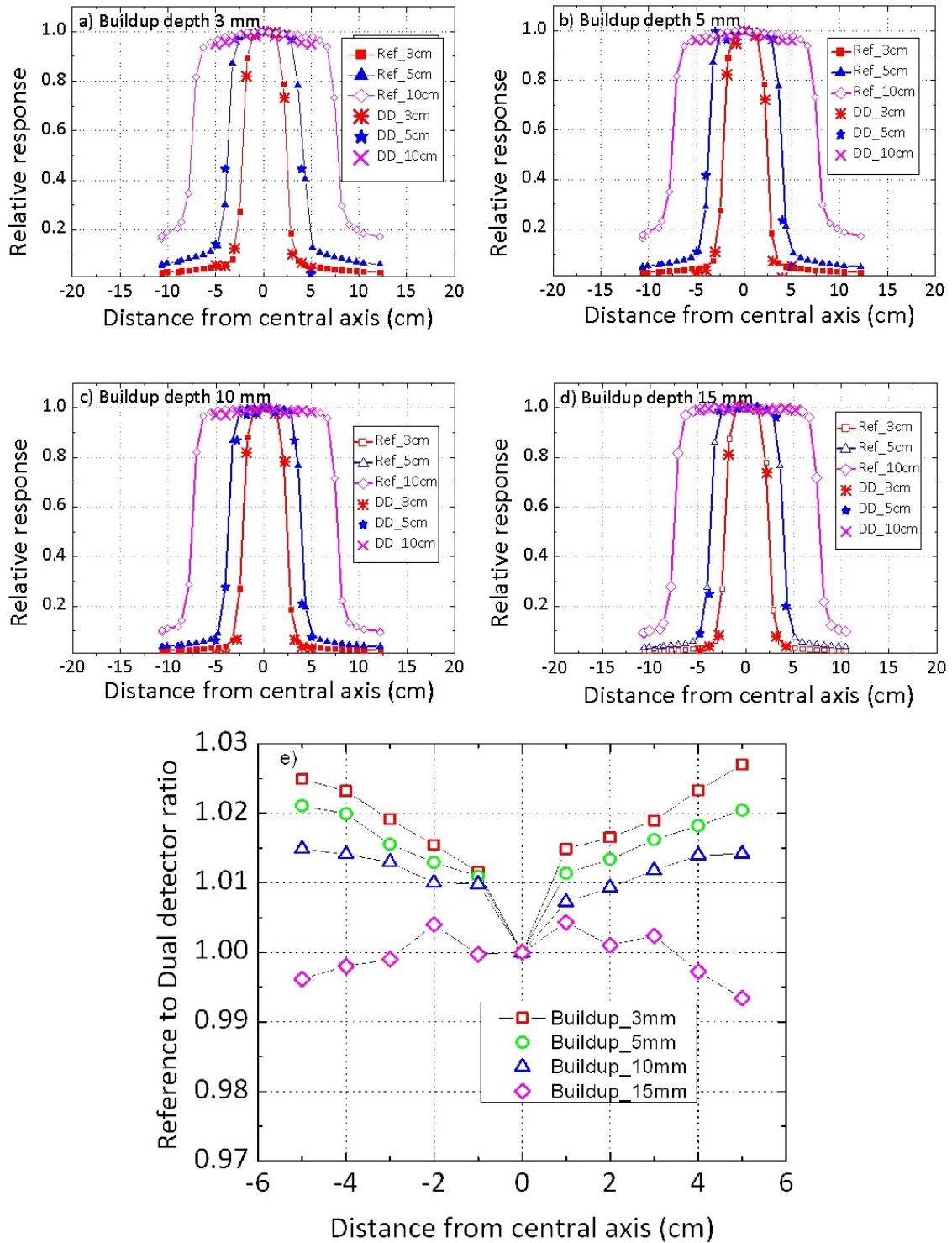


Figure 5.3: Comparison measured dual detector off-axis profiles at build-up depths 3 mm, 5 mm, 10 mm and 15 mm of solid water with the reference dosimetry configuration and the dual detector configuration for field sizes 3 x 3 cm², 5 x 5 cm² and 10 x 10 cm². The ratio of profiles between reference detector and dual detector at varying build-up depths for field size 10 x 10 cm² is also shown in (e)

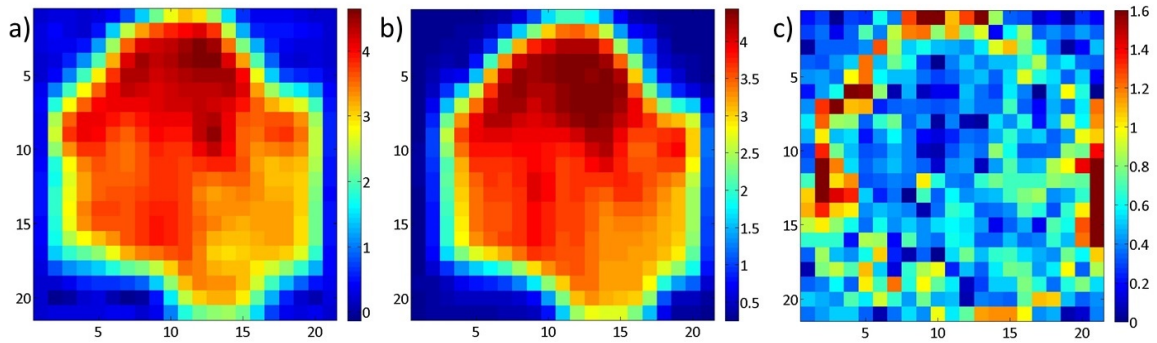


Figure 5.4: The gamma comparison (3% and 3mm) between measurements for one of the clinical brain IMRT fields, a) Dual detector, b) Reference detector and c) gamma map.

Figure 5.4 displays the gamma agreement of one of the clinical brain IMRT fields. The gamma pass rates for all clinical modulated fields were greater than 95% indicating a very close agreement between the two detector configurations in the transit geometry.

The dose response evaluation (figures 5.3 and 5.4, Table 5.1) demonstrates that integrating the MP with the EPID in the dual detector configuration has no significant impact on dose response for the five clinical modulated fields investigated here. As the MP can acquire and report data frame by frame in real-time with very high temporal resolution compared to the currently available commercially 2D detector, it could, in principle, be used for time resolved dose verification during IMRT or volumetric modulated arc therapy (VMAT) [201, 246] in the dual detector configuration. The dose discrepancy at the field edge may be due to an error in manual shift of 5 mm performed during the measurement with the dual detector. Future work is underway to investigate the dose response for a flattening filter free (FFF) 10 MV and a 18 MV beam. The development of a clinical dosimetry model is beyond the scope of this work. The majority of previously reported EPID dosimetry approaches employed a dose in water based model and require additional corrections to convert the measured EPID signal into a dose in water image. The proposed dual detector configuration directly provides a water equivalent dose image and hence, removes any of the uncertainty which could contribute to the modelling dose response of the detector particularly in the case of standard EPIDs. By eliminating this middle step of dose characterisation of the detector response, measured dose with dual detector configuration can be directly compared with predicted the dose image calculated using any of the previously reported EPID dosimetry models. Therefore, having the dual detector configuration would simplify the implementation of in vivo treatment verification.

5.3.2 Image quality evaluation

The spatial resolution determined by the spatial frequency at half the maximum MTF (f_{50}), noise and CNR measured using the PipsPro QC-3V image quality phantom and software in the reference imaging configuration and dual detector configuration are shown in Table 5.2. Although, the quantitative analysis (Table 5.2) had shown the presence of solid water build up material and the MP used in the dual detector configuration had impact on both CNR and resolution. Figure 5.5 shows the images of the QC-3V image quality phantom taken with the EPID in the reference imaging configuration and dual detector configuration. There is no appreciable difference in the visual perception of high or low contrast detail between the two configurations (Figure 5.5).

5.3.2.1 Anthropomorphic phantom

Anterior-posterior projection images of an anthropomorphic pelvis phantom acquired using the reference imaging configuration and dual detector configuration are shown in Figure 5.6.

Table 5.2: Comparison of resolution, noise and CNR for the dual detector configuration and reference imaging configuration. The results are quoted as mean \pm standard deviation from three repeat measurements.

EPID configuration	Spatial resolution f_{50} (lp/mm)	noise	CNR
Standard EPID	$0.414 \pm 1.151 \times 10^{-3}$	12.80 ± 1.57	643.96 ± 28.85
MP with no buildup	$0.412 \pm 1.222 \times 10^{-3}$	13.1 ± 1.37	590.40 ± 26.65
MP with 10mm buildup	$0.405 \pm 1.245 \times 10^{-3}$	22.80 ± 1.47	370.96 ± 31.25
MP with 15mm buildup	$0.402 \pm 1.274 \times 10^{-3}$	26.80 ± 2.07	314.40 ± 32.15

The images from the two configurations show no discernible difference in the visualization of anatomical details. These qualitative results and the quantitative imaging results reported above demonstrate that while the presence of the additional MP detector and solid water build up had a measurable effect on EPID imaging performance (see Table 5.2), the effect was not visible in qualitative image comparisons (see Figs. 5.5 and 5.6) and is considered

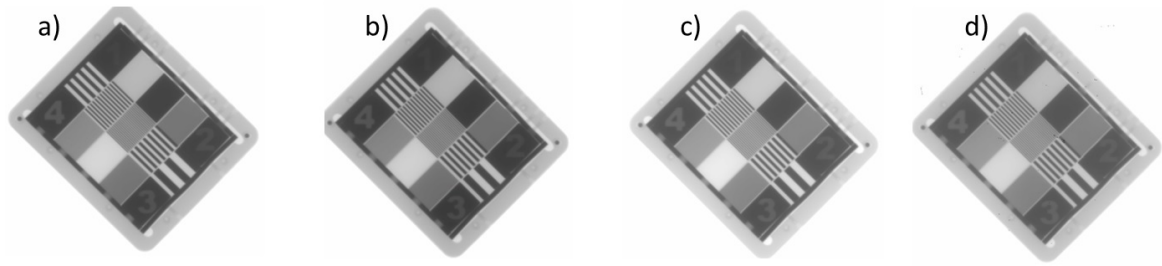


Figure 5.5: EPID images of the QC-3V image quality phantom taken with the (a) reference imaging configuration and (b) dual detector configuration (MP with no buildup) (c) dual detector configuration (MP with 10mm buildup) (d) dual detector configuration (MP with 15 mm buildup)

negligible for clinical purposes.

In this study, we used readily available equipment to demonstrate the feasibility of the dual detector concept. The proposed dual detector configuration has overcome some limitations of the previously reported dual detector configuration [249]. The current focus of EPID technology development is to improve the imaging standards by employing more sensitive detectors [35, 36]. The success of the previously reported dual detector for dosimetry purposes depends on the overlying EPID imager structure and its composition which should be materially homogenous perpendicular to the beam. Any structural modification as a part of a future EPID design development would not impact the dosimetry performance of the proposed dual detector configuration. Also, the compact design of MP detector used in the proposed dual detector would resolve some of the engineering challenges such as integration of the MP detector inside the EPID structure. Additional considerations not investigated in this study include the engineering requirements of the mechanical support and the configuration of electronics and data readout schemes required to implement the proposed dual detector configuration. This study demonstrates a proof-of-concept of a novel dual detector for radiotherapy treatment verification. Current EPID detectors are optimized for imaging but are suboptimal for dosimetry. The proposed dual detector concept decouples the imaging and dosimetry functions so that each can be optimized without compromising the other, providing more flexibility for future improvements in radiotherapy treatment verification systems.

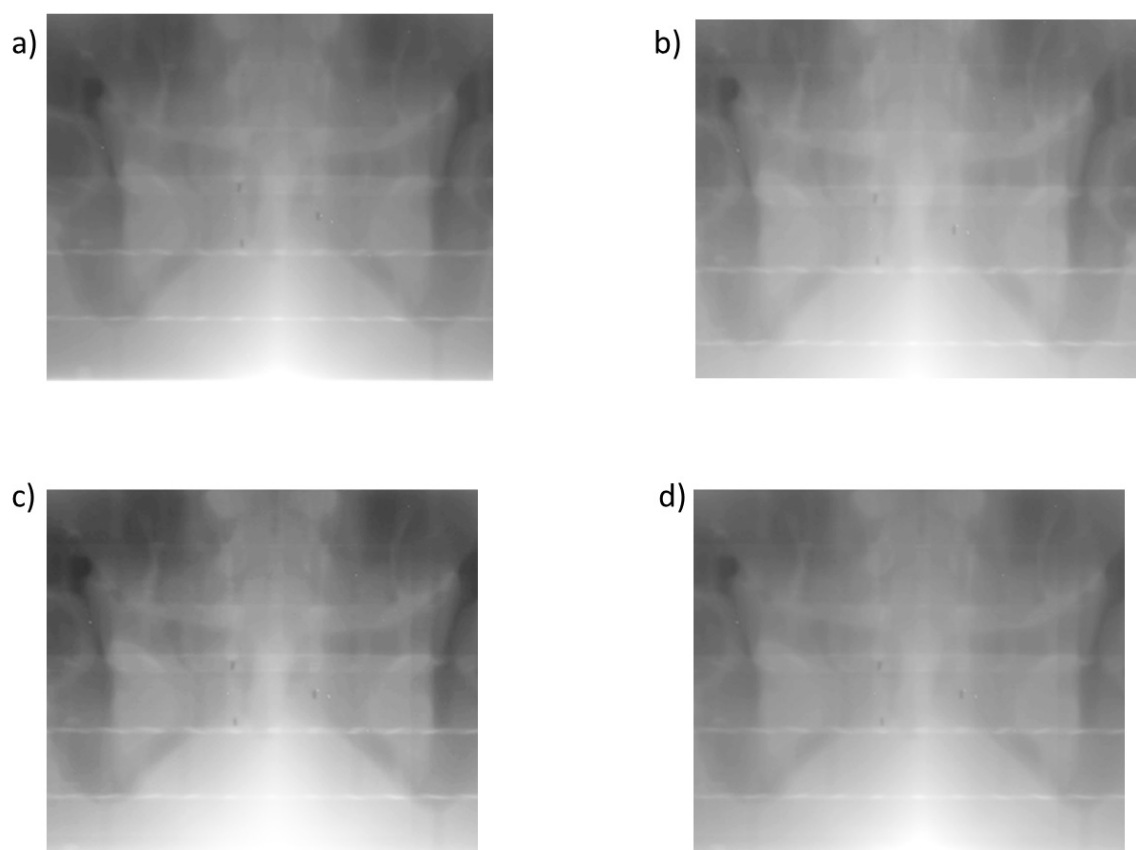


Figure 5.6: Portal image of anthropomorphic pelvis phantom acquired with the (a) reference imaging configuration and (b) dual detector configuration (MP with no buildup) (c) dual detector configuration (MP with 10mm buildup) (d) dual detector configuration (MP with 15 mm buildup).

5.4 Conclusion

The proposed dual detector configuration, combining a conventional EPID and a prototype Magic Plate 2D array dosimeter, can be operated simultaneously as both imager and dosimeter without significant compromise in the performance of either device. The prototype tested requires higher spatial resolution and a larger detection area for clinical implementation. This is being addressed with a new higher resolution system which is currently in design phase. This work shows a proof of concept.

Chapter 6

A simple model for transit dosimetry based on a treatment planning system and a water equivalent EPID

Statement of joint authorship

S. Deshpande: Develop experimental design, performed experiments, analysed results, wrote manuscript

A. Xing: Matlab scripting and analysed results

P. Metcalfe: Assisted in interpreting results and writing, as supervisor he endorses the assessment

S. Blake and L. Holloway: Assisted with strategic implementations of the experiments and with publication submission.

P. Vial: Render advice on the experiment, interpreting results and write up

[‡]Part of this chapter has been submitted for publication:

S. Deshpande, S. Blake, A.Xing, P.Metcalfe, L.Holloway, P. Vial, Clinical implementation of water equivalent EPID utilising the commercial treatment planning system for in vivo dose verification *Medical Physics*, (Under Review)

6.1 Introduction

The current trend of radiation therapy (RT) is moving toward increasingly precise and accurate dose delivery, which employs radiation beam intensity-modulation for dose sculpting and image guidance for target positioning. Modulated beams often contain complex fluence maps with large dose gradients that are tailored to each individual patient and bear little resemblance to standard fields used for commissioning beam models. Factors that could lead to differences between the delivered and planned dose distributions include i) anatomical changes (e.g. changes in tumour size and shape, patient weight and organ motion [254, 255]), ii) treatment delivery issues (e.g. MLC calibration offsets [256, 257]) and iii) limitations in TPS beam model accuracy [258]. In response to increasing treatment complexity, quality assurance (QA) bodies throughout the world acknowledge that patient treatment verification using in vivo dosimetry is highly desirable for optimal patient safety during radiation treatment [12, 14, 110].

Commercial a-Si EPIDs have been shown to be suitable for in vivo dosimetry and offer several advantages over other common dosimeters [23]. However, the effective use of standard EPIDs for dosimetry necessitates comprehensive models of both the linac's treatment beam and the EPID's dose response characteristics, both of which vary on a per-patient basis [23]. Regardless of the prediction method used, current portal dosimetry methods are based on a completely different algorithm or model of linear accelerator than which is used for dose calculation. Therefore, the strategy of comparing measured dose versus dose estimated at the EPID plane only verify the machine delivery error and not necessarily verify the TPS dose model and dose algorithm accuracy. This would potentially undermine the robustness of the link between EPID dosimetry results and the real agreement in delivered dose versus prescribed treatment. Considering the complexity of EPID dosimetry algorithms, extensive commissioning that must be performed in order to optimise EPID utility and minimise the risk of masking errors as well as patient safety.

The potential of EPIDs for detecting various dose delivery errors has been well demonstrated in previous studies [119, 200]. Bojecho et al [200] quantified the effectiveness of EPID-based dosimetry in detecting clinical incidents such as changes in the machine output, corrupted plans and patient positioning errors occurring during setup. The authors reported that 74% of 229 high severity incidents reported over a 2.5 year period could be detected by using in vivo first fraction EPID dosimetry, compared to just 6% when using pre-treatment

EPID dosimetry. The three most common error modes reported by the authors were wrong isocenter information, patient misalignment during treatment and error in CT scan data. Access to EPID based in vivo dosimetry solutions has improved recently with the introduction of commercially available systems [259–261]. However, despite the large body of research dating back to the early 1990s and before, the reported use of clinical EPID based in vivo dosimetry is still limited to a relatively small number of centres. Nelms et al pointed out the advantages of using measured EPID images for IMRT QA over predicted portal images generated independently of the TPS dose calculation algorithm, as the latter approach may mask TPS modelling errors [262]. Current EPID dosimetry models use various corrections in both the predicted and measurement derived data that are unrelated to the TPS dose calculation. The reliability and robustness of such systems requires independent validation that captures the range of clinical scenarios for which it is used, a process that is difficult to achieve comprehensively without additional specialised tools and resources. The degree to which these issues may undermine the reliability of EPID dosimetry to ensure patient safety is not well understood.

One simple EPID dosimetry model that has previously been demonstrated uses the ‘extended phantom’ concept to calculate a predicted dose image (PDI) at the EPID plane using the TPS dose in water model [195, 196, 199]. When used with standard EPIDs, this method still requires a separate EPID model to convert the measured EPID signal into dose in water. Despite being demonstrated two decades ago, this approach has not been widely adopted in EPID dosimetry models. More recently, Ortega et al [263] proposed a method to compute PDIs using a clinical dose in water beam model in a commercial TPS. The authors utilised the actual CT images of a commercial EPID as a quality assurance phantom. After calibrating the EPID according to vendor guidelines, the authors demonstrated that the PDIs computed using the commercial TPS agreed well with measured EPID dose images ($> 95\%$ gamma-index pass rate with 3%/3mm criteria) in a non-transit geometry. Yohannes et al [264] have written in-house scripts in the Pinnacle³ TPS that can create the structures and define them as virtual planes. These virtual planes can be generated for any arbitrary gantry and couch angles, as well as source to planar distance, so that the planar dose maps at these planes can be computed. Authors verified the planar dose distributions computed using the scripts for limited clinical fields (three open fields and one IMRT field) with films and ionisation chamber array and have showed good agreement. Baek et al [175] reported the feasibility of EPID based transit dosimetry utilising a commercial TPS (Eclipse, Varian Medical Systems, Salt Lake City, UT, USA). In their work, the EPID was calibrated using

vendor guidelines. Authors reported that the gamma pass rate (using relative gamma criteria) for transit dose measurements with clinical modulated fields was lower with an anthropomorphic phantom ($86.8 \pm 3.8\%$) compared to a homogeneous phantom ($94.2 \pm 1\%$) and concluded that the reduction in gamma pass rate was partially due to the inaccuracy of TPS calculations for inhomogeneity. Millin et al [265] also reported the feasibility of EPID based transit dosimetry utilising a commercial TPS (iPLAN[®], BrainLAB, Feldkirchen, Germany). Their work compared the measured EPID dose, calculated using an analytical model, with predicted dose calculated by TPS and Monte Carlo (MC) simulations. To facilitate the dose calculations at the EPID plane, a slab of water equivalent material identical in dimensions to the EPID was added to the TPS as an RT structure. The authors utilised a separate correction to account for the differences in TPS-calculated dose to water and the measured dose to the EPID imager. The authors demonstrated that the MC-simulated dose showed better agreement with the measured EPID dose compared to the TPS-calculated dose when 3%/3mm relative gamma criteria were used. The dose verification in their study was validated for a maximum field size of only $5 \times 5 \text{ cm}^2$ with no intensity modulation. Another issue in this work is that it used small field sizes that limits the amount of the patient scatter created and incident on EPID, which will simplify the EPID dosimetry model. Both these studies [175, 265] recommended that the EPID model refinement is necessary in order to convert the EPID signal to absorbed dose to water for clinical dosimetry. Standard EPIDs were originally designed and optimised for imaging applications and therefore employ high density and high atomic number materials to ensure high detection efficiency of the megavoltage photon beam.

Alternative EPID designs that are better suited for dosimetry applications relative to standard a-Si EPIDs include several water equivalent EPIDs (WE-EPID) developed and proposed by our group [38–40, 206]. In these detectors, the high atomic number materials above the photodiode array are replaced with water equivalent build up material such as solid water or segmented plastic scintillator array. A prototype a-Si direct detector dosimeter has demonstrated dosimetric properties that were more water equivalent than standard EPIDs [40, 266]. More recently, a standard commercial EPID was modified to operate as a direct detection dosimeter (direct EPID) and its performance under modulated fields was evaluated by directly comparing the measured dose with ionisation chamber measurements [38, 39, 206]. However, the demonstrated benefits of a more water-equivalent dose response have come at a cost of lower sensitivity and reduced overall imaging performance. The direct EPID exhibits only about 10% of the signal measured with the standard EPID, which means

that higher doses are needed to achieve comparable image quality. Our group is currently working to optimise the imaging performance of our plastic scintillator prototype EPID for this precise reason [267, 268]. In our previous work [40], we characterised the dosimetric response of a physical plastic scintillator fibre array EPID prototype and demonstrated its near water-equivalent response in both non-transit and transit configurations using standard square fields. In this study, we report for the first time the dosimetric characterisation of our WE-EPID prototype using intensity-modulated fields including dynamic treatments such as VMAT. This prototype offers improvements in sensitivity compared to the direct detection EPIDs because of the signal gain introduced when using the scintillator to convert incident x-rays into optical photons.

The ‘extended phantom’ concept employing in TPS provides water equivalent dose image at EPID plane and does not requires any additional modelling of the clinical beam or an independent image prediction algorithm. The main advantage of this method is that portal dose prediction is calculated with the same algorithm and beam model used for patient dose distribution calculation. Unlike the standard a-Si EPIDs, WE-EPIDs do not require any additional dose response corrections and therefore the measured WE-EPIDs dose may be compared directly to TPS dose calculations. The present study combines the WE-EPID and the ‘extended phantom’ TPS concepts to propose a new model for transit dosimetry as a means of in vivo dosimetry and demonstrates for the first time the application of the ‘extended phantom’ concept for dosimetry applications using two different WE-EPID configurations. The dosimetric response of both WE-EPIDs was characterised with respect to a reference ionization chamber array dosimeter using standard open and wedged fields, as well as intensity-modulated fields (IMRT and VMAT). This new concept removes some of the limitations of current EPID dosimetry models by allowing for a more direct comparison of TPS calculated dose with the delivered dose.

6.2 Methods and Materials

6.2.1 Equipment

6.2.1.1 Water equivalent EPID

The EPID device used was based on a standard a-Si EPID (XRD 1640 AN CS PerkinElmer, Santa Clara, CA) and the imaging data was collected using XIS software V3.3.1.1 (PerkinElmer, Santa Clara, CA). The EPID was used in either of two prototype WE-EPID configurations: novel EPID configuration [40] or the direct EPID configuration [38]. Both configurations have 3 cm of water equivalent build-up material in place of the copper sheet and gadolinium oxysulfide phosphor screen components of standard clinical EPIDs (see figure 6.1 a) to c)). The novel EPID design incorporates a custom-made segmented 2D plastic scintillator array (PSA) device, which measures 3 cm in thickness and 15 x 15 cm² in area and has previously been demonstrated for simultaneous imaging and dosimetry applications in radiotherapy [40, 266]. The direct EPID configuration uses either 30 x 30 x 3 cm³ (Gammex RMI, Middleton, WI) or 40 x 40 x 3 cm³ (CIRS, Norfolk, VA, USA) of solid water build-up. Both configurations have been demonstrated to be water equivalent to within 1.5% [38, 40, 266]. Hereafter, both configurations are referred to as water equivalent EPIDs (WE-EPIDs) unless stated otherwise. Since the PSA used in the novel EPID configuration is limited to 15 x 15 cm² in area, the dosimetric validation measurements with this novel EPID configuration (described in Section 6.2.3) were limited for treatment field dimensions up to 10 x 10 cm² defined at isocentre. To validate the ‘extended phantom’ concept comprehensively over a wide range of clinical scenarios, all treatment fields as described in Section 6.2.3 including those measured with novel EPID configuration were measured with the direct EPID.

6.2.1.2 Reference 2D transit dosimeter

The I^mRT MatriXX two dimensional ionisation chamber array (ICA) and accompanying OmniPro-I^mRT software (version 1.6, IBA Dosimetry, Schwarzenbruck, Germany) was used as a reference 2D transit dosimeter (Figure 6.1 d). All the ICA measurements were performed at 3 cm depth to match the WE-EPID setup.

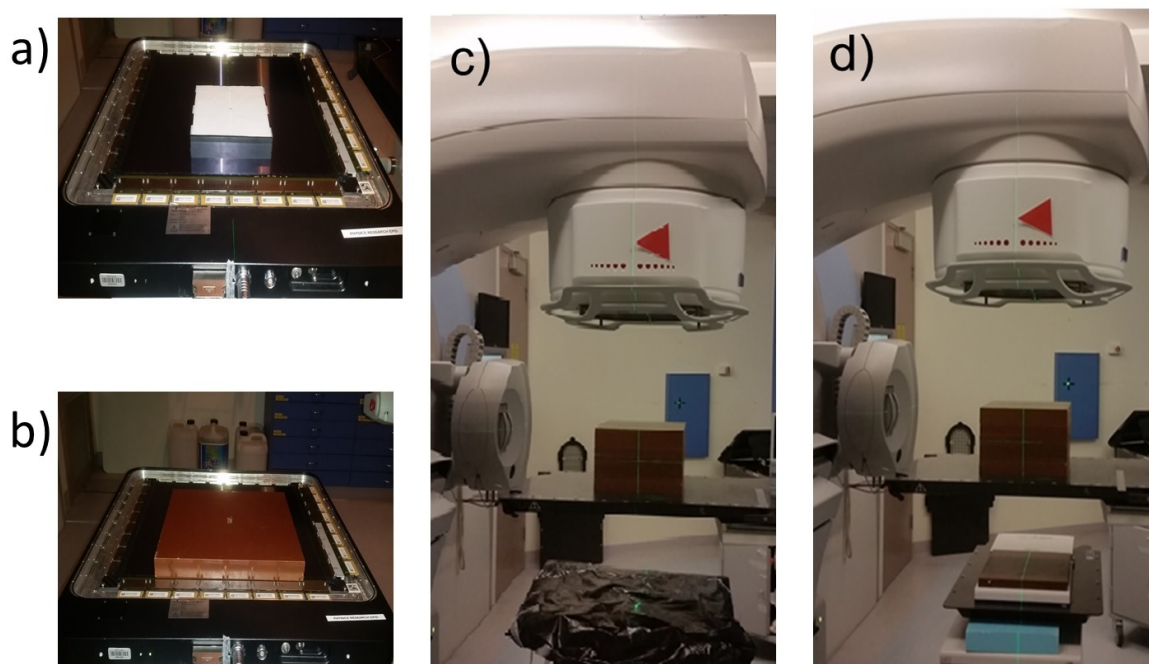


Figure 6.1: Experimental setup for transit dose measurements. Two WE-EPID configurations are shown: a) Prototype EPID consisting of a plastic scintillator fibre array (15 cm x 15 cm x 3 cm) directly coupled to the EPID detector, b) Direct EPID consisting of a 30 cm x 30 cm x 3 cm solid water slab directly coupled to the EPID detector. The EPID was positioned at 150 cm and wrapped with an opaque black sheet to block any light from reaching the detector (c). The I'mRT MatriXX ion Chamber Array setup is shown in (d).

6.2.1.3 Treatment planning system

All radiation fields described in Sections 6.2.3.1, 6.2.3.2 and 6.2.3.3 were planned using a clinical Pinnacle TPS (Pinnacle, v9.10, Philips Medical Systems, Fitchburg, WI) and calculated using the adaptive convolution/superposition dose algorithm [269]. We adapted a similar ‘extended phantom’ approach as described in previous studies [195, 196] to modify the image field of view (FOV) (Figure 6.2). The CT images were processed to extend the image FOV from 512 x 512 pixels to 1024 x 1024 pixels using in-house software written in Matlab (version: 7.10.0.499 (R2010a), Mathworks Inc., MA) before importing them into the TPS. The size of individual pixels was not altered. The padded image pixels were assigned CT numbers corresponding to air. Extending the FOV was required to incorporate the EPID as an RT structure with dimensions 4 x 30 x 30 cm³ at 150 cm source to detector distance (SDD). The EPID structure was assigned a uniform density of 1.0 g cc⁻¹ to match that of water (Figure 6.2). This allowed the TPS to perform dose calculations outside of the scanned CT FOV. The TPS dose at EPID plane was calculated using a dose grid of 2 mm x 2 mm x 2 mm at a depth of 3 cm inside EPID RT structure for all water equivalent detector configurations. The planner dose calculated at EPID plane was exported using standard DICOM export option in TPS.

6.2.2 EPID image corrections and dose calibration

All acquired EPID images were dark field and flood field corrected. The flood field correction removes the variation in pixel-to-pixel sensitivity as well as the beam intensity profile information from the image. In order to restore the beam profile, a pixel sensitivity map (PSM) was measured using a multiple field calibration method described previously [270]. The PSM contains only the inherent differences in sensitivity of the individual pixels in the imaging matrix, specified relative to the central pixel. Each EPID image was processed using in house MATLAB code to restore beam profile information using a similar methodology to that described in a previous study [248]. The corrected WE-EPID pixel values were calibrated to dose by cross calibration with Farmer chamber. The reference conditions used for cross calibration were 10 × 10 cm² field size, 150 cm SDD and 20 cm of solid water positioned on the treatment couch centred at the isocenter. A pixel-to-dose calibration factor and PSM was applied to each EPID image to convert it to a dose image. The same principle of calibration was applied to the ICA, with a dose calibration established from a calibrated Farmer chamber and a vendor supplied pixel sensitivity map.

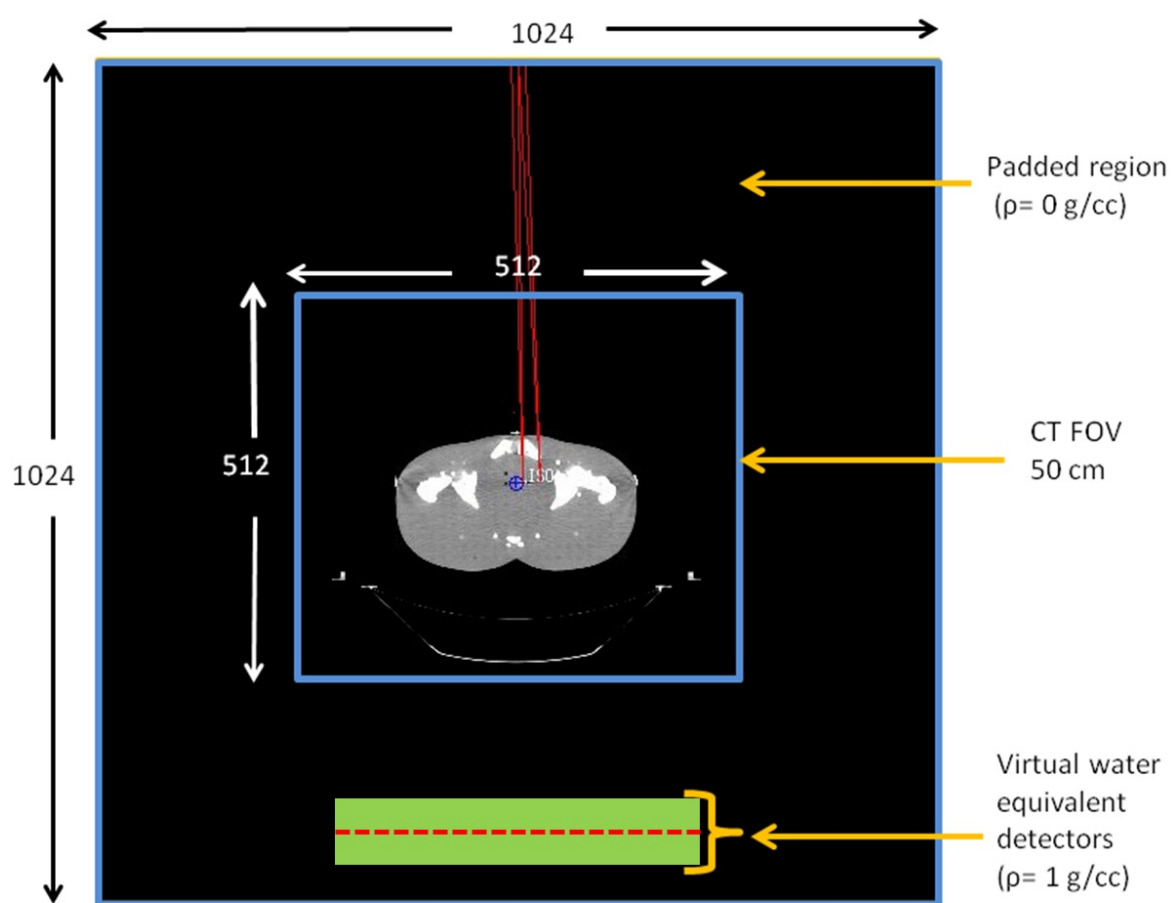


Figure 6.2: Representation of phantom (anthropomorphic pelvis phantom) and virtual EPID setup in the TPS.

6.2.3 Dose response evaluation

Basic dose response tests for different field sizes, off axis ratios and transmission factors were performed. The measured dose response with the both WE-EPIDs and ICA was compared to the TPS-calculated dose at the WE-EPID plane to verify the accuracy of the clinical TPS beam model under transit dosimetry conditions. For field sizes and transmission factors dose response analysis of WE-EPIDs, the pixel value averaged over central 10 x 10 pixels of the exposed field size. In case of an ICA detector the dose value averaged over central four detectors was used. The TPS model used was a standard clinical model commissioned according to standard guidelines [271, 272]. We also compared beam profiles for the largest field size of 25 x 25 cm² with varying thickness of object in the beam (0, 10, 20, 30 and 40 cm solid water slab). All the field size dimensions reported in this work describe the field width as defined at the isocentre, unless stated otherwise.

6.2.3.1 Open and Wedged fields with heterogeneous phantoms

Three individual fields were measured: i) a single direct 12 x 12 cm² open field transit through an inhomogeneous slab phantom, ii) an open breast tangent field and iii) a wedged breast tangent field transit through an anthropomorphic phantom (ATOM[®] Dosimetry Verification phantoms, CIRS) to mimic the traditional tangential breast treatment setup. Figure 6.3 displays the two heterogeneous phantoms and beam arrangements used for these experiments.

6.2.3.2 IMRT fields

Twenty clinical IMRT cases were measured with either 20 cm or 40 cm thick solid water slab or an anthropomorphic phantom in the beam. The clinical IMRT cases consisted of four modulated fields from brain plans and sixteen modulated fields from prostate cases (out of sixteen clinical fields, seven were from intact prostate plans having low modulation while nine clinical fields were from prostate plans with involved pelvic nodes covering treatment areas at least 20 cm in width). All these plans were planned using step and shoot delivery only.

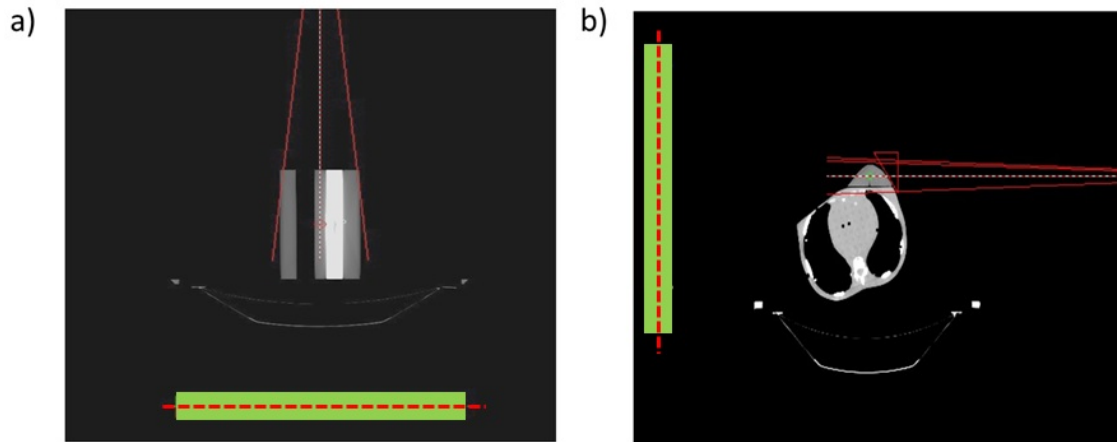


Figure 6.3: Two different heterogeneous phantoms: a) an inhomogeneous slab phantom and b) an anthropomorphic breast phantom. The inhomogeneous slab phantom consists of stacked bone, lung and water equivalent solid water slab.

6.2.3.3 VMAT field

Three clinical VMAT cases were measured with either 20 cm thick solid water slab or an anthropomorphic phantom in the beam. The clinical VMAT cases included one intact prostate plan (single full arc with low modulation) and two head and neck plans (planned with two arcs covering a treatment area approximately 23 cm in width).

The measured and calculated doses were evaluated with all control points (CP) collapsed to gantry zero. To compare time-resolved measurements to predicted dose, the measured dose was sampled at the correct frequency to match the TPS-calculated dose per control point. The EPID data was acquired in free running mode unsynchronised with linac gun pulses. Using a priori knowledge of monitor units and dose rate from the DICOM RTPLAN for each control point, the number of expected EPID frames per control point can be determined. The EPID frames were then resampled into integrated CP images. This approach is based on the method described by Podesta et al [273].

The treatment couch was modelled in the TPS. All experiments were conducted on an Elekta Synergy linear accelerator (Elekta Oncology Systems, Crawley, UK) with Agility MLC and 6 MV photons at gantry 0° or 90° only. The gamma evaluation technique [240] was applied to compare the 2D dose maps measured with both WE-EPID detectors and calculated with the TPS. The gamma criteria used was 3% dose difference (relative to the maximum dose)

and 2 mm distance-to-agreement, with doses below 10% of the maximum dose excluded from the evaluation.

6.3 Results

Table 6.1: Comparison of off-axis response measured with WE-EPID, ICA and TPS calculated with solid water thicknesses of 0 cm (i.e. no object), 10, 20, 30 and 40 cm in the beam, respectively. Data presented constitutes the mean \pm standard deviation difference in the cross-plane profiles normalised at CAX over a 12.5 cm distance from beam axis.

Equipment/ detector	Relative ratio in off-axis response for varying solid water thickness (cm) placed in beam				
	0 [†]	10 [†]	20 [†]	30 [‡]	40 [‡]
WE-EPID vs ICA	0.992 \pm 0.007	0.989 \pm 0.006	0.988 \pm 0.004	0.993 \pm 0.004	0.991 \pm 0.004
TPS vs ICA	0.999 \pm 0.002	1.003 \pm 0.004	1.008 \pm 0.007	1.008 \pm 0.006	1.006 \pm 0.007
WE-EPID vs TPS	0.991 \pm 0.006	0.987 \pm 0.006	0.984 \pm 0.007	0.989 \pm 0.005	0.988 \pm 0.006

[†] Measurement with 30 x 30 x 3 cm³ solid water build up for 20 x 20 cm² open field size

[‡] Measurement with 40 x 40 x 3 cm³ solid water build up for 25 x 25 cm² open field size

6.3.1 Dose response evaluation

Figure 6.4 compares the WE-EPID and ICA measured dose response with TPS-calculated dose response for varying square field sizes and transmission through solid water slabs of varying thickness. The measured dose response for all tests agreed with the TPS-calculated dose response to within 2%, suggesting the clinical beam model predicts transit dose accurately at the EPID plane. Figure 6.5 compares the measured beam profiles with 30 cm and 40 cm of solid water thickness for open 25 x 25 cm² fields with TPS-calculated profiles. The relative profile agreements are also summarised in Table 6.1. We have presented the data for prototype WE-EPID configurations with direct EPID only since the novel WE-EPID configuration results were the same (< 0.5%).

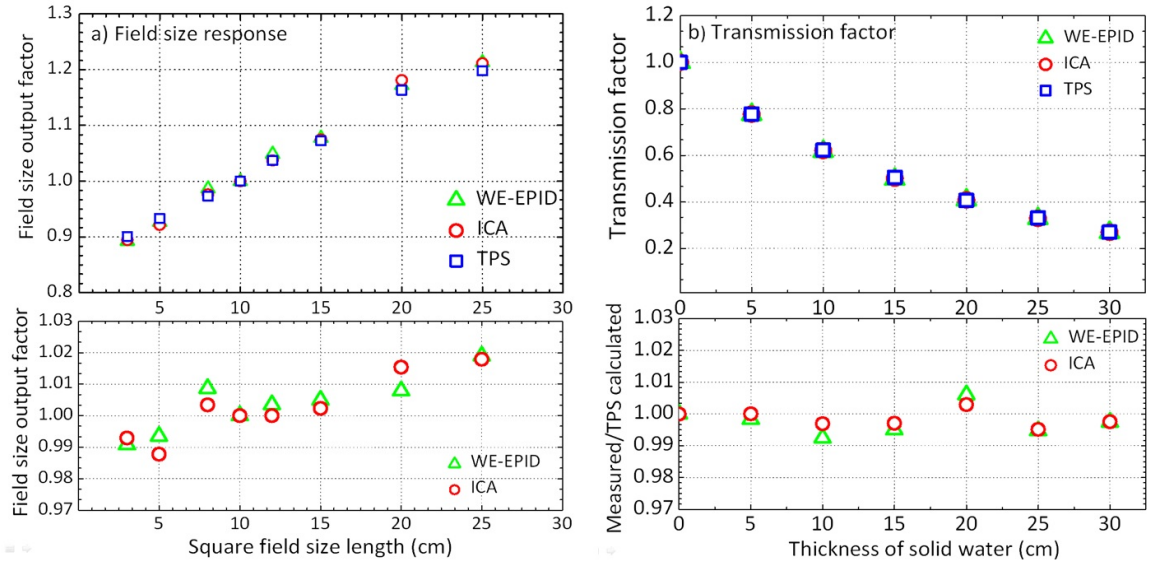


Figure 6.4: Comparison of dose measured with the WE-EPID and ICA and calculated with the TPS in the same measurement geometry: a) field size response and b) transmission factors. Only data for the direct EPID WE-EPID configuration is presented here.

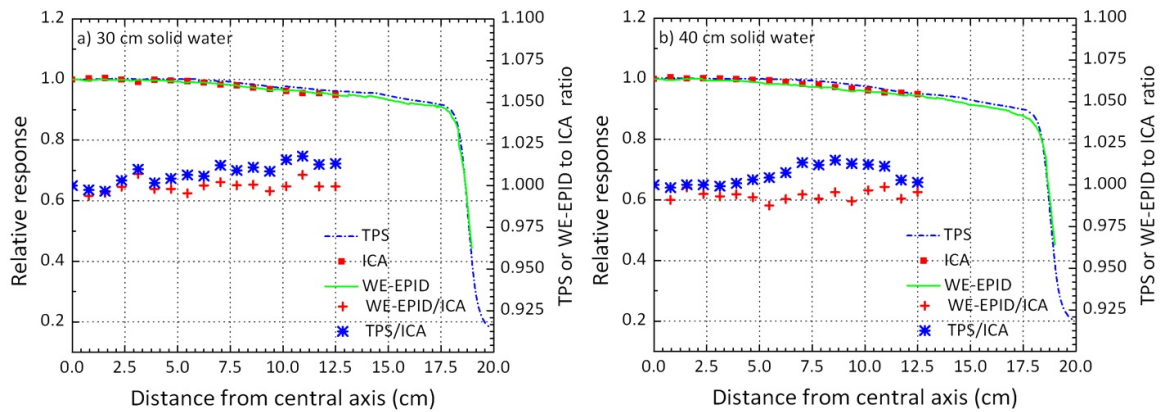


Figure 6.5: Comparison of off-axis response (normalised half profiles) measured with a) 30 cm solid water slab and b) 40 cm solid water slab present in beam. The relative difference in off-axis response over a distance of 12.5 cm from the beam axis between the TPS-calculated or WE-EPID-measured dose when compared to the ICA-measured dose is displayed on the right axis. Only data for the direct EPID WE-EPID configuration is presented here.

6.3.2 Clinical field

6.3.2.1 Open and Wedged fields with heterogeneous phantoms

The transit dose images measured with the WE-EPID and calculated with the TPS for direct single field (described in Section 6.2.3.1), using an anthropomorphic phantom (open or wedged) and an inhomogeneous slab phantom (open field) are displayed in Figure 6.6. The gamma evaluation of the dose images acquired with the WE-EPID versus those measured with the TPS for all fields showed at least 93.6% agreement with average gamma-index values between 0.33 and 0.41. Dose profiles in the WE-EPID and TPS-calculated dose images have also been extracted and compared in Figure 6.6. The measured data presented in Figure 6.6 was acquired with the direct WE-EPID configuration only since measured fields were larger compared to physical dimensions of the novel WE-EPID detector.

6.3.2.2 IMRT fields

A summary of the gamma-index pass rates for all modulated fields measured with a 20 cm and 40 cm solid water slab (homogeneous phantom) and an anthropomorphic phantom placed in the beam is shown in Table 6.2. The gamma-index evaluation of the dose images acquired by the WE-EPID and ICA when compared to those calculated with the TPS for all clinical IMRT fields showed at least 91% agreement with average gamma-index values between 0.35 and 0.55.

6.3.2.3 VMAT field

The gamma evaluation of the integrated VMAT dose images acquired by WE-EPID and ICA versus TPS showed greater than 90% agreement with gamma index < 1 . A summary of the gamma index pass rates for VMAT fields measured with either 20 cm solid water slab (homogeneous phantom) or an anthropomorphic phantom placed in the beam is shown in Table 6.3.

Figure 6.7 displays the 2D gamma evaluation between the TPS-calculated and measured dose images per control point for the first three control points for prostate case. The gamma pass rate was $95.7 \pm 2.4\%$ for all the control points (Table 6.3). The gamma pass rate for both WE-EPID configuration when compared with ICA and TPS was similar ($< 0.6\%$) and data presented (Table 6.3) was acquired with the novel EPID and direct EPID configura-

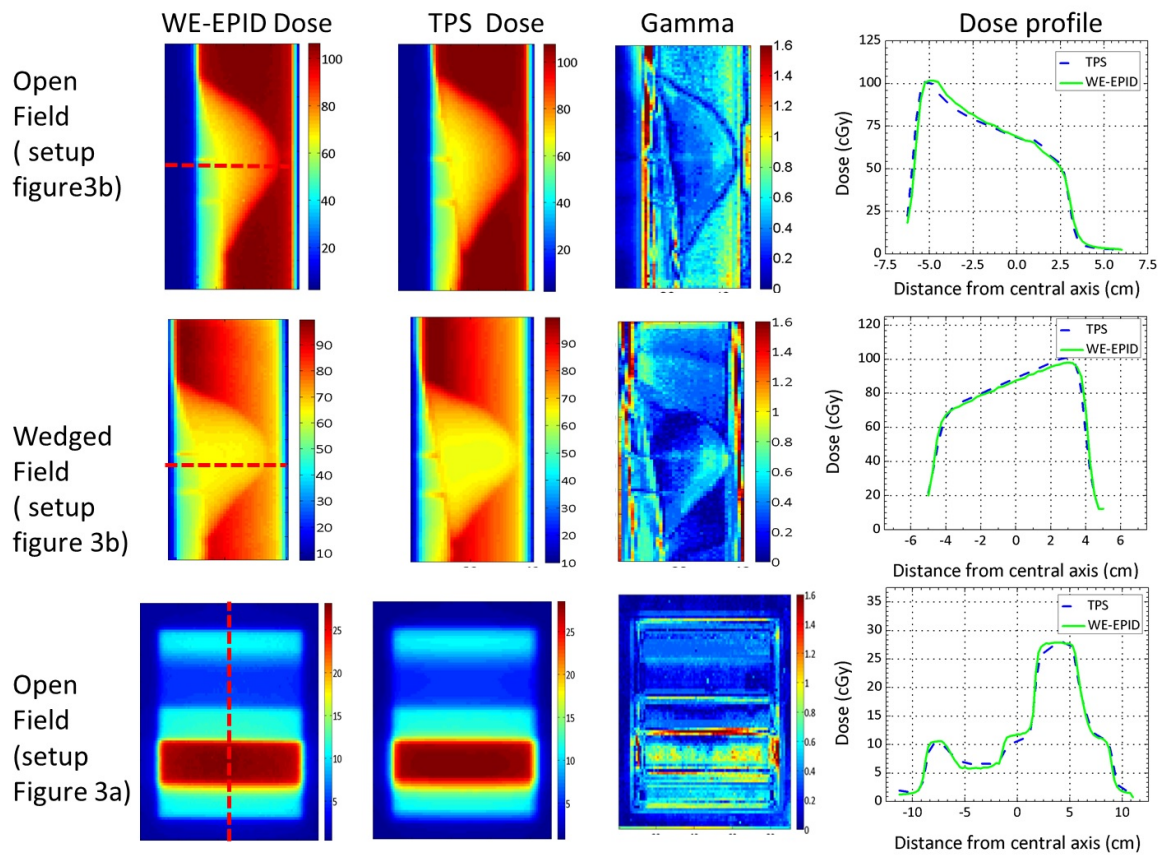


Figure 6.6: The gamma-index comparison (3% and 2mm) between measurement (WE-EPID) and TPS calculated water-equivalent dose image for a direct beam passing through a) anthropomorphic phantom (open field) b) anthropomorphic phantom (60° wedge field) and c) inhomogeneous slab phantom (open field). The dose profiles in the rightmost panes were extracted from the planes indicated as dotted lines on corresponding EPID dose images.

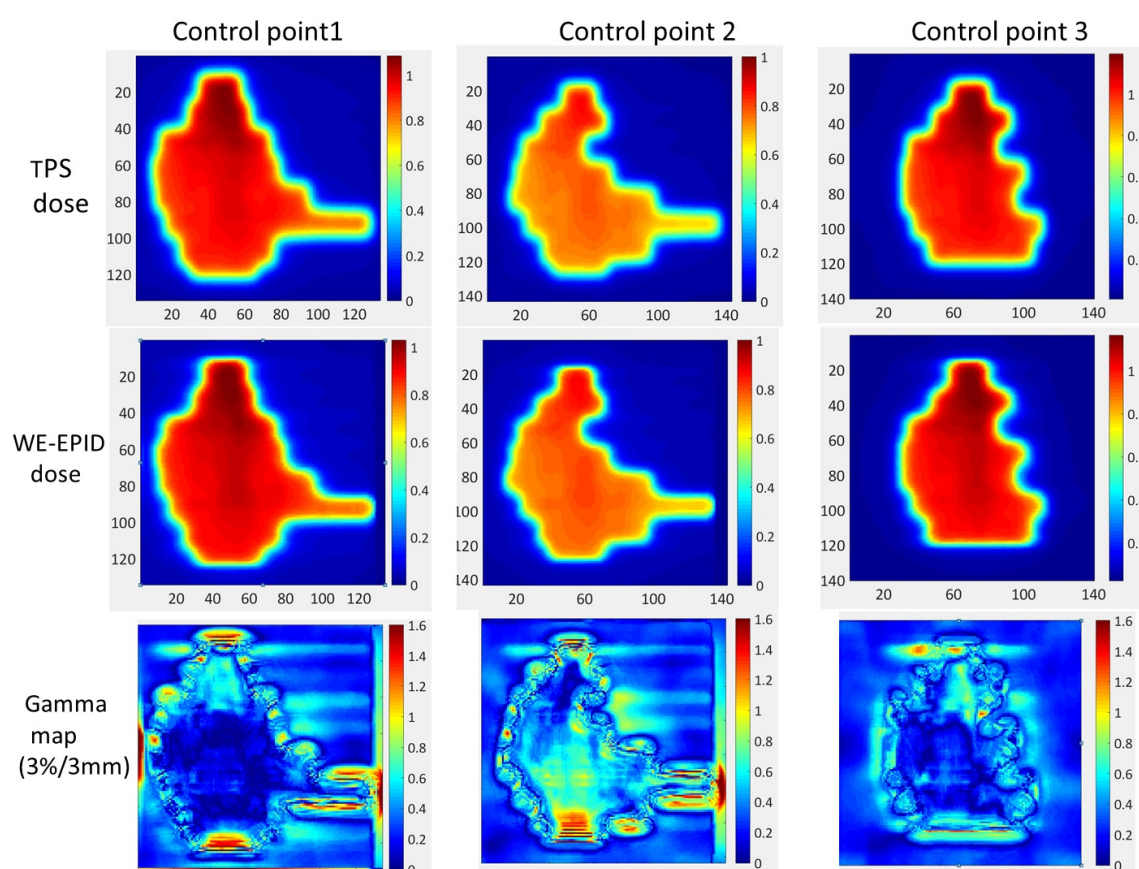


Figure 6.7: The gamma comparison between measurement (novel WE-EPID) and calculation (TPS) for first three control points of a clinical prostate VMAT field in presence of an anthropomorphic phantom.

tion for prostate and head and neck cases respectively. Figure 6.7 displays the 2D gamma evaluation between the TPS-calculated and measured dose for integrated images.

Table 6.2: Gamma-index evaluation when comparing WE-EPID and ICA absolute dose maps with the TPS absolute IMRT fields using 3%/2 mm criteria. An anthropomorphic or solid water slab phantom was placed in the beam as a transit object. The range and mean value has presented for both gamma pass rate and average gamma value.

		Prostate [‡]	Prostate [#]	Prostate [#]	Brain	Brain
		SW [‡]	SW [‡]	AP	SW [‡]	AP
WE-EPID Vs TPS	γ	91.5-94.5	92.5-96.5	92.2-96.7	93.2-97.7	93.2-98.1
	pass rate	(92.5)	(93.5)	(93.4)	(94.5)	(94.4)
	Avg.	0.47-0.61	0.43-0.59	0.44-0.60	0.40-0.50	0.42-0.52
	γ value	(0.55)	(0.47)	(0.48)	(0.44)	(0.48)
ICA Vs TPS	γ	92.4-94.6	93.5-96.5	93.4-97.7	94.1-97.4	94.2-98.2
	pass rate	(92.7)	(94.2)	(94.4)	(94.6)	(94.7)
	Avg.	0.48-0.57	0.42-0.54	0.43-0.56	0.42-0.46	0.43-0.50
	γ value	(0.53)	(0.44)	(0.45)	(0.43)	(0.46)
WE-EPID Vs ICA	γ	91.2-94.6	92.5-96.8	92.4-96.8	94.2-97.8	94.5-98.2
	pass rate	(92.5)	(93.5)	(93.4)	(94.9)	(94.6)
	Avg.	0.47-0.61	0.41-0.52	0.47-0.61	0.38-0.44	0.39-0.49
	γ value	(0.52)	(0.44)	(0.52)	(0.35)	(0.36)

Prostate[‡]-Clinical intact prostate plan

Prostate[#]-Clinical prostate with pelvic nodes plan

SW[‡]: 40 cm solid water as a transit object in beam

SW[‡]: 20 cm solid water as a transit object in beam

AP: Anthropomorphic phantom as a transit object in beam

Table 6.3: Gamma-index evaluation when comparing WE-EPID and ICA measured dose maps with TPS-calculated VMAT fields using 3%/2 mm criteria (both integrated and control point by control point). Either an anthropomorphic or solid water slab phantom was placed in the beam as a transit object.

Percentage and mean gamma pass rate with 3%/2mm criteria				
	Integrated			Control point by control point
	Prostate [†]	Head and Neck1 [‡]	Head and Neck2 [‡]	Prostate [†]
WE-EPID	92.9	91.5	92.3	92.7±2.4
Vs	0.46	0.56	0.53	
TPS				
WE-EPID	91.5	92.4	92.6	92.9±2.1
Vs	0.44	0.53	0.51	
ICA				

[†] Anthropomorphic phantom as a transit object

[‡] 20 cm solid water slab as a transit object

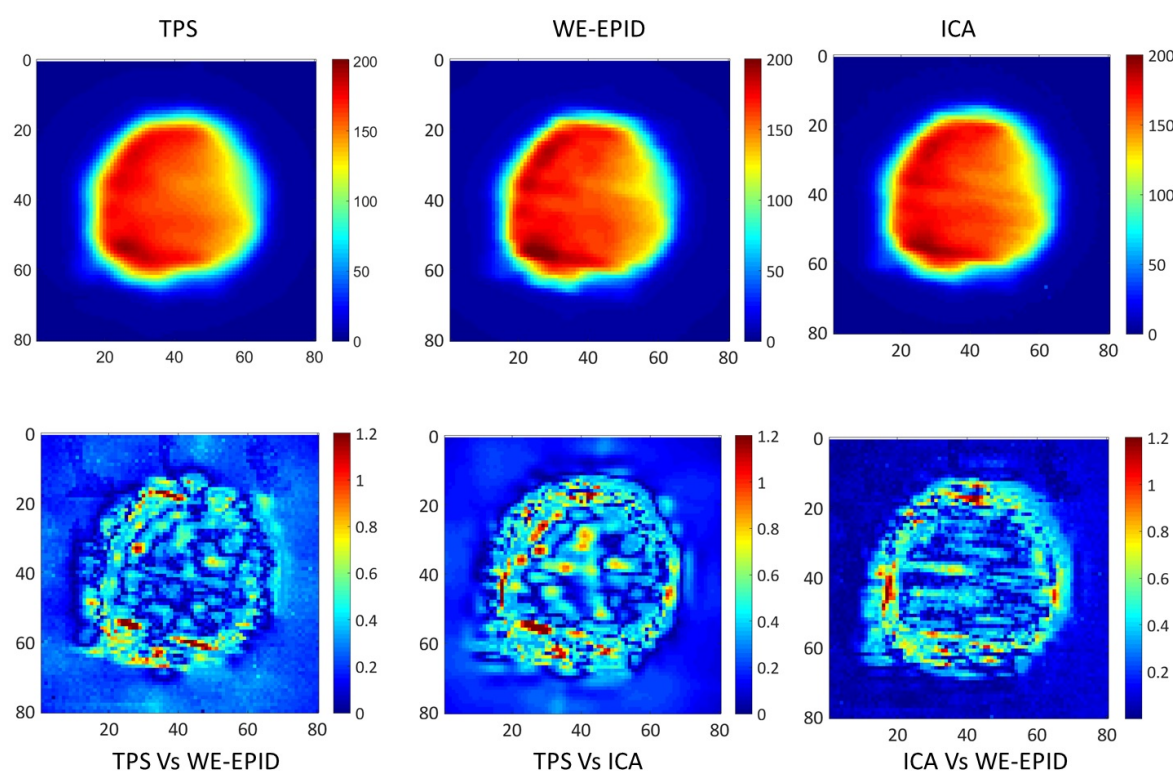


Figure 6.8: The gamma comparison (starting from left in bottom row) between the TPS-calculated versus WE-EPID measured, TPS versus ICA measured and ICA measured versus WE-EPID for integrated dose images of a clinical prostate VMAT field in presence of an anthropomorphic phantom. The integrated dose images are displayed in top row starting from left, TPS calculated, measured with WE-EPID and ICA measured.

6.4 Discussion

A simple model for implementing transit dose verification with a WE-EPID as a means of in vivo dosimetry has been demonstrated. The dose measured with a WE-EPID can be directly compared to the dose calculated by the TPS in a clinical treatment plan, replacing the need for a separate EPID model.

The TPS dose calculated at the EPID plane showed good agreement with the dose measured by two different dosimetry systems. The gamma-index agreement between measurement with ICA and both WE-EPIDs for clinical modulated IMRT fields were similar to the previously reported work [39, 206]. This study reports for the first time VMAT dosimetry measurement with both WE-EPIDs. Hence, the VMAT dosimetry results presented in this work cannot be directly compared with previous work. The water equivalence of both these devices has been demonstrated in several studies [39, 40, 206, 266]. Although, the previous work [199, 264] presented the approach to calculate dose at EPID plane using TPS, none of the previous work verified comprehensively the accuracy dose prediction at the EPID plane against water equivalent dose measurements for wide range of clinical scenario. This study demonstrates that a TPS model commissioned according to conventional radiotherapy guidelines [274] may be sufficiently accurate for transit EPID dose calculations for a wide range of clinical scenarios, including open, wedged, modulated and dynamic beams. We validated the ability of the Pinnacle TPS using the ‘adaptive convolve’ dose calculation algorithm, which is based on the collapsed cone convolution [269]. Accurate dose in water algorithms implemented in other modern radiotherapy treatment planning systems can be expected to have similar success [275, 276].

The issue of imaging performance with a WE-EPID is not addressed in this study but is the topic of ongoing studies into optimal detector designs [267, 268]. The focus of this work was to demonstrate a simple yet powerful approach to in vivo dosimetry that becomes available with access to a WE-EPID.

Since current TPSs are not designed for the in vivo dosimetry applications presented in this study there are several limitations to be addressed before the full potential of our system can be realised. For example we have only included beams at orthogonal gantry angles similar to proposed by Yohannes et al [264]. Further work is therefore required to develop a process for extracting TPS-calculated doses at the EPID plane for beams and control points

at all gantry angles. It would also be possible for a conventional TPS to incorporate a back-projection dose calculation method to facilitate in vivo dose verification in the future similar to presented in previous work [198].

The same approach presented in this study could be implemented using a dose in water algorithm on a separate software platform independent of the TPS, similar to currently available EPID dosimetry systems, but without the need to model the standard EPID dose response. Any EPID-based dosimetry system that has been proposed using standard EPIDs could be implemented with a WE-EPID, without the added uncertainty and limitations of modelling the complex dose response of standard EPIDs. With this increased confidence in dosimetry, EPID-based dosimetry could maintain tighter tolerances under a wider range of clinical conditions and maintain high levels of confidence in the delivered dose as delivery techniques become increasingly more complex.

6.5 Conclusion

An approach to transit dose verification is presented utilising a water equivalent EPID and a commercial TPS. The accuracy of dose calculations at the EPID plane using a commercial TPS beam model was experimentally confirmed. The model proposed in this study provides an accurate method to directly verify doses delivered during treatment without the additional uncertainties inherent in modelling the complex dose response of standard EPIDs.

6.6 Acknowledgments

The authors report no conflicts of interest in conducting the research. The authors would like to acknowledge the funding support from the Cancer Institute NSW Australia (Research Equipment Grant 10/REG/1-20) and Cancer Council NSW (Grant ID RG 1-06).

Chapter 7

Clinical significance of treatment delivery errors for helical tomotherapy nasopharyngeal plans - a dosimetric simulation study

Statement of joint authorship

S. Deshpande: Develop experimental design, performed experiments, analysed results, wrote manuscript

M. Geurts: Automation the simulation process and interpreting results and write up

P. Metcalfe: Assisted in interpreting results and writing, as supervisor he endorses the assessment

M. Lee and P. Vial: Render advice on the experiment, interpreting results and write up

L. Holloway: Render advice on the experiment, interpreting results and write up

[‡]Part of this chapter has been published:

S. Deshpande, M. Geurts, P. Vial, P. Metcalfe, M. Lee, L.Holloway Clinical significance of treatment delivery errors for helical tomotherapy nasopharyngeal plans - a dosimetric simulation study *Physica Medica* 2017; 33:159-169

7.1 Introduction

High radiation dose delivery to tumours with improved sparing of normal tissues is an ongoing goal of radiotherapy practice. Advanced radiation therapy techniques such as fixed beam intensity-modulated radiation therapy (IMRT), volumetric modulated arc therapy (VMAT) and helical tomotherapy (HT) have improved our ability to achieve this goal [277]. However, these techniques are also more complex to deliver. As such, an understanding of delivery uncertainties within these advanced planning and delivery techniques is required to ensure the potential for improved effectiveness from these techniques is actually being achieved. Margalit et al.[278] outlined the different errors associated with either IMRT or 3D/conventional treatment techniques and highlighted how the occurrence of error types differs between treatment techniques. The dosimetric impact of multileaf collimator (MLC) leaf position errors has been thoroughly studied and reported [41–46] for IMRT and VMAT delivery. Further, Tatsumi et al.[279] demonstrated that the sensitivity to MLC errors depends upon the treatment planning system (TPS) type, implementation of inverse optimization, and MLC segmentation algorithm within the TPS. The dosimetric impact from simulated delivery errors from other mechanical parameters such as gantry angle, collimator angle and table position in IMRT and VMAT delivery has also been studied [42, 280, 281]. Betzel et al.[133] reported that RapidArc™ (Varian Medical Systems, Palo Alto, CA) deliveries were found to be more tolerant to variations in dose rate, gantry position, and MLC leaf position compared to IMRT delivery. All of the above reported studies on the sensitivity to treatment delivery errors were based on a C-arm gantry linac. The information is therefore not relevant to HT machines as the mechanics of HT treatment delivery are different from other forms of external beam RT. As opposed to the work discussed above for IMRT and VMAT, few researchers have conducted a similar analysis for HT plan delivery. Fenwick et al [282] studied the link between machine characteristics and the delivered dose for HT by modelling the dose distribution delivered to an on-axis target with a cylindrical phantom aligned co-axially using a simple unmodulated beam. They characterised the impact on the on-axis target dose distribution from the angular variation in gantry rotation speed and output per linac pulses.

Most of the recommended HT QA procedures and tolerances in AAPM Task Group 148 [47] were adopted from the collective experience of the task group members, vendor designed QA tests and from previously published reports [48–50]. It is unclear whether suggested QA tolerances have any clinical significance. This is the first study to demonstrate the potential

clinical impact of variation in delivery parameters on actual HT clinical plans. The goal of this study was to simulate several potential HT delivery errors associated with the mechanical system, considering nasopharynx plans with common plan parameters and to understand the impact of these errors on patient dosimetry. We assessed the errors resulting in clinical impact against the current machine interlock values. This work provides a framework to establish QA tolerances that are clinically significant for specific anatomical sites and for relevant planning techniques.

7.2 Methods and Materials

7.2.1 Patient selection and treatment planning

Table 7.1: Description of the range of complexity among ten clinical HT plans presented in this study. All ten plans have three dose level targets (70 Gy, 63Gy and 56Gy) and extend bilaterally.

Patient	Parotid sparing intent	OAR overlap with Target	Maximum off-axis distance from bore centre (cm) [†]	Treatment length (cm)	Treatment time (sec)
1	Bilateral	Partial overlap with both parotid	11	22.6	273.8
2	Ipsilateral	RT Partial and Brainstem	10.5	22.5	271.7
2	Bilateral	Partial overlap with both parotid	12	23.5	394.1
4	Ipsilateral	LT Partial and Brainstem	12.3	25.3	305.6
5	Ipsilateral	RT parotid	10.9	23.3	346.7
6	Bilateral	Brainstem	13.3	25.1	373.6
7	Ipsilateral	Both parotid	9.5	24.7	275.8
8	Bilateral	None	11.4	20	220
9	Ipsilateral	Both parotid and Brainstem	10.6	24.6	408.7
10	Ipsilateral	Both parotid	10.5	21.6	260.8

[†] Maximum distance of any pixel within PTV56 or parotid from the bore centre.

Ten retrospective clinical nasopharynx HT plans with varying complexity (Table 7.1) were selected randomly for this study. All ten clinical plans were optimised using a fixed 2.5 cm jaw width, 0.287 or 0.403 pitch and 2.2-2.4 modulation factor with the clinical TomoTherapy TPS version 4.2, hereafter referred as the clinical TPS. The approved dose distributions were used as a baseline for dosimetry comparison. It was decided to use a single plan type for this study to focus the investigation on planning methods and error introduction.

7.2.2 Simulation of delivery errors

All dose calculations were performed using a TomoTherapy version 5.0 standalone GPU dose calculator; hereafter referred as the research TPS. Use of the research TPS was necessary for two reasons: i) this version of software is capable of interpolating between the jaw penumbra data at different jaw positions, essential for simulating the jaw errors and ii) introducing the error and then recalculating dose without re-optimization is not possible in the clinical TPS. Figure 7.1 is a schematic describing the multiple steps involved in simulating HT delivery errors, error plan dose re-calculations and plan metric, and calculations using Comp Plan [283] which is an in-house software application to extract the dose volume histogram (DVH) from DICOM RT dose and RT structure files and calculate various radiobiological plan metrics. Simulated error plans were generated by converting the optimized clinical plan into an XML-defined calibration procedure and then modifying either the XML or binary MLC sinogram to introduce simulated errors. Five key mechanical errors were simulated: couch speed (CS), gantry start position (GSP), gantry period (GP), jaw width (JW) and MLC leaf open time (MLC LOT).

Each error type was simulated independently for a range of magnitudes as described in table 7.2 The JW error in this study is the error in individual jaw position (either front or back jaws). In the case of MLC LOT errors, the optimized clinical plan sinogram was edited using MATLAB (version: 7.10.0.499 (R2010a), Mathworks Inc., MA). Three different MLC LOT errors were simulated: (1) leaf 32, 42 or 52 stuck open, (2) random errors using a normal distribution with a mean and standard deviation of -2% and then with a mean and standard deviation of -4%. The leaf open times greater than 100% are not possible to deliver, so were truncated and (3) a normal distribution with mean of 0% and standard deviation ranging 1-10%. As demonstrated in previous work, the MLC LOT random error with mean and standard deviation of -2% can occur when suboptimal pitch is used during plan optimisation [284].

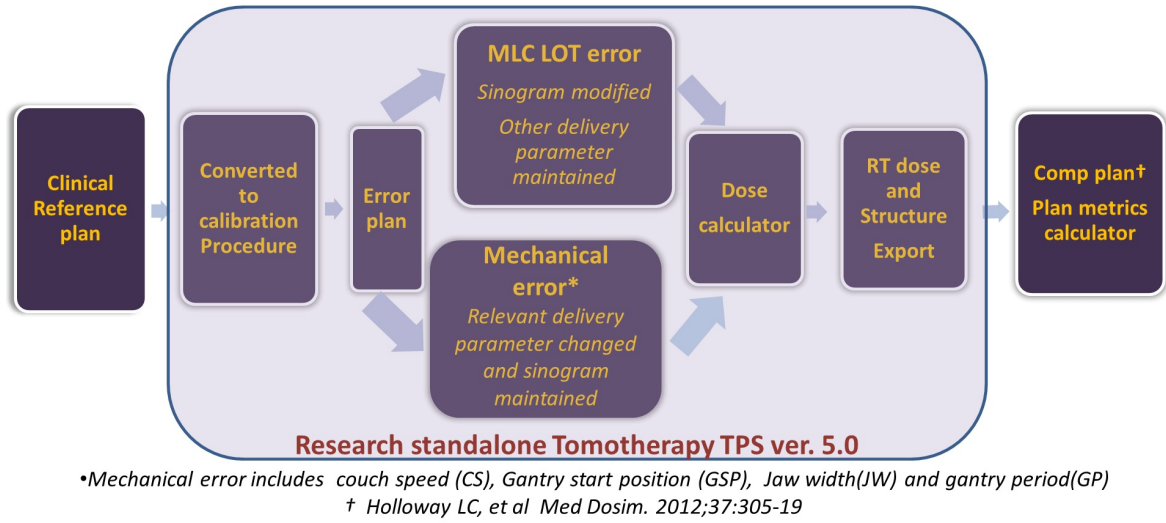


Figure 7.1: Schematic describing the processes involved in creating the simulated error plans, dose recalculations for simulated error plans and the calculation of plan metrics for dosimetry comparison

Table 7.2: Five key simulated errors and the associated magnitudes simulated. All error magnitudes are defined relative to the reference clinical plan value

Machine delivery parameter	Number of simulated error plans	Magnitude of simulated error
Couch speed [†] (cm per sec)	24	$\pm 0.1, \pm 0.3, \pm 0.5, \pm 1, \pm 1.5, \pm 2, \pm 2.5, \pm 3, \pm 3.5, \pm 4, \pm 4.5$ and ± 5
Gantry Start Position [‡] (deg)	24	$\pm 0.1, \pm 0.3, \pm 0.5, \pm 1, \pm 1.5, \pm 2, \pm 2.5, \pm 3, \pm 3.5, \pm 4, \pm 4.5$ and ± 5
Gantry period [‡] (sec)	24	$\pm 0.1, \pm 0.2, \pm 0.4, \pm 0.5, \pm 0.6, \pm 0.8, \pm 1, \pm 1.5, \pm 2, \pm 2.5, \pm 3, \pm 4$
Jaw width [‡] (mm)	12	$\pm 0.1, \pm 0.3, \pm 0.5, \pm 1, \pm 1.5, \pm 2$
MLC LOT	3	Leaf 32 stuck open, Leaf 42 stuck open Leaf 52 stuck open
	2	[†] Mean random error of -2% and -4%
	2	[‡] standard deviation of error of 1-10%

[†] Percentage difference relative to planned value

[‡] absolute difference relative to planned value

7.2.3 Plan evaluation

The plan metrics considered for quantitative analysis were D_{95} for PTV70 and PTV56, D_{1cc} for spinal cord, D_{1cc} for brainstem and mean dose for parotid similar to those used by a previous study [285]. The percentage dose difference was calculated using equation 7.1 similar to work [285]. It has been suggested that a percentage dose difference of 3–5% can affect the tumour response and outcome of treatment [286, 287].

In this paper, we used a percentage dose difference of 5% as a clinical tolerance for D_{95} of PTV70 and D_{95} PTV56, D_{1cc} of the spinal cord and D_{1cc} of the brainstem [285]. Hunter et al [288] demonstrated that a mean parotid dose difference of less than 3.6 Gy was not clinically important as radiobiological models do not change below this difference. For the parotid gland, a percentage dose difference of 10% in the mean dose to the parotid was used as the clinical tolerance; however, if a difference of greater than 3.6 Gy in the mean dose to parotid was seen this was also noted for comparison as suggested in previous studies [285, 288].

$$\text{Percentage dose difference} = \left(\frac{D_{\text{error}} - D_{\text{clinical}}}{D_{\text{clinical}}} \right) \cdot 100 \quad (7.1)$$

7.3 Results

7.3.1 Evaluation of plan metrics

Figure 7.2 displays the average percentage dose difference over ten patients in D_{95} of PTV70, D_{95} of PTV56, D_{1cc} for spinal cord, D_{1cc} for brainstem and the mean dose to the parotid (for parotid that was spared during optimisation) for simulated JW, CS, GP and GSP errors. The overall impact on the dose distribution from each error type varies both with the magnitude and direction of the errors from the planned values as well as between patients as indicated by error bars (Figure 7.2). The patient dose distribution was compromised either by under dose to the target or overdose to the OAR based on the set clinical tolerance when simulated delivery errors of $JW \geq 1\text{mm}$, $CS \geq 2.5\% \text{ cm per sec}$ and $GP \geq \pm 2 \text{ sec}$ were reached. A difference of greater than 3.6 Gy in the mean dose to parotid was seen in 5 patients out of 10 for simulated errors of JW of 1.5 mm, CS of -3% cm per sec, GP of -3 sec and MLC42 stuck open. For the JW, CS and GP systematic errors, noticeable dosimetric variations from the clinical reference plan DVH are seen in figure 7.3 for one representative patient dataset. Overall, the impact of GSP error up to 4° on patient dosimetry particularly PTV70 was small, as demonstrated by only small changes in percentage dose difference (figure 7.2) and by small shifts in the dose volume histograms (DVHs) for all structures (figure 7.3).

Figure 7.4 displays the distribution of the ten patient datasets for which the dose variation are within the set clinical tolerance. From the patient cohort data considered here to ensure

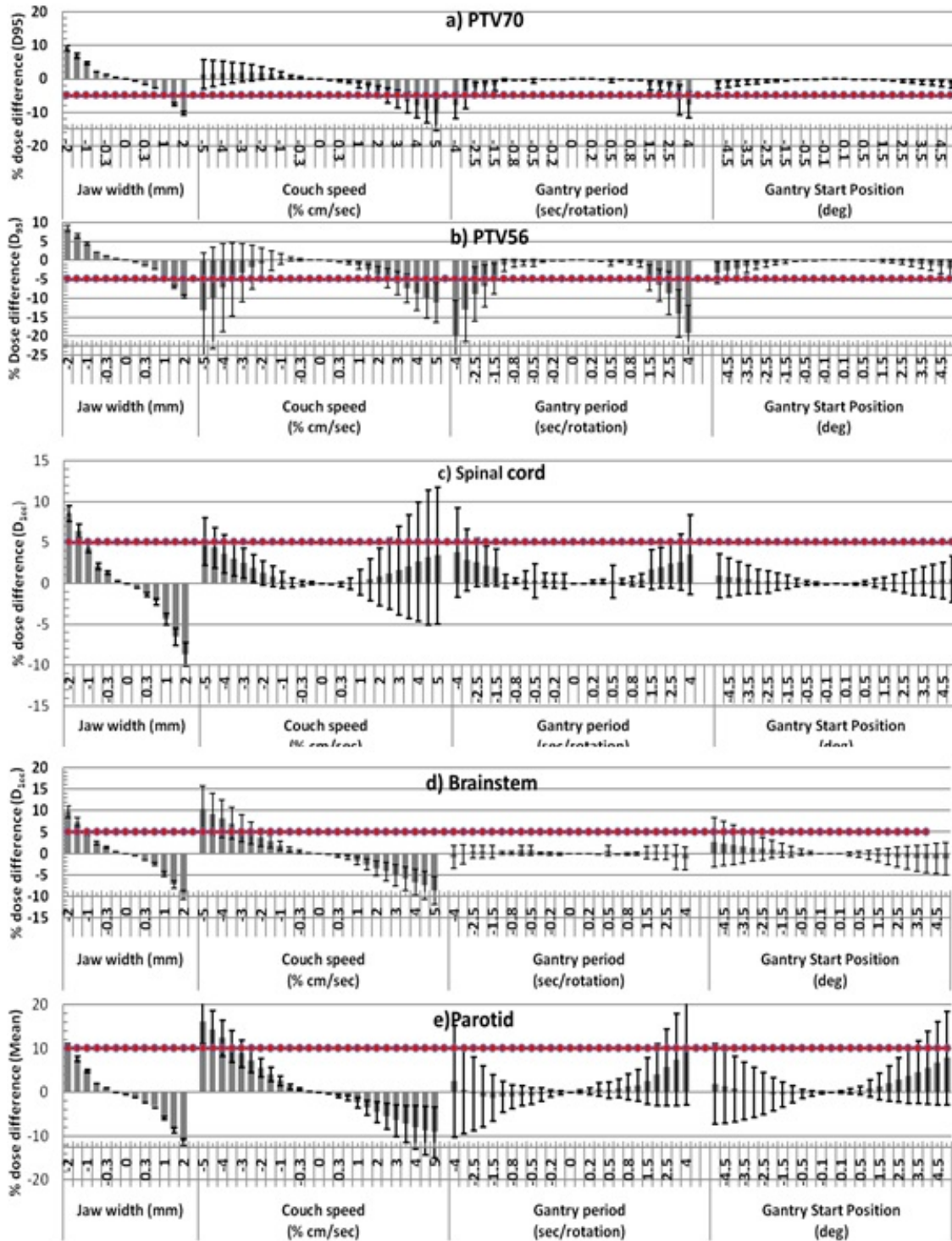


Figure 7.2: The average percentage dose difference compared to the clinical reference (no error) plans over the ten patients for a) D_{95} of PTV70, b) D_{95} of PTV56 c) D_{1cc} for spinal cord, d) D_{1cc} for brainstem and e) mean dose to the parotid. The error bars represents one standard deviation in plan metrics from the ten patients. The red dotted line represents the set clinical tolerance

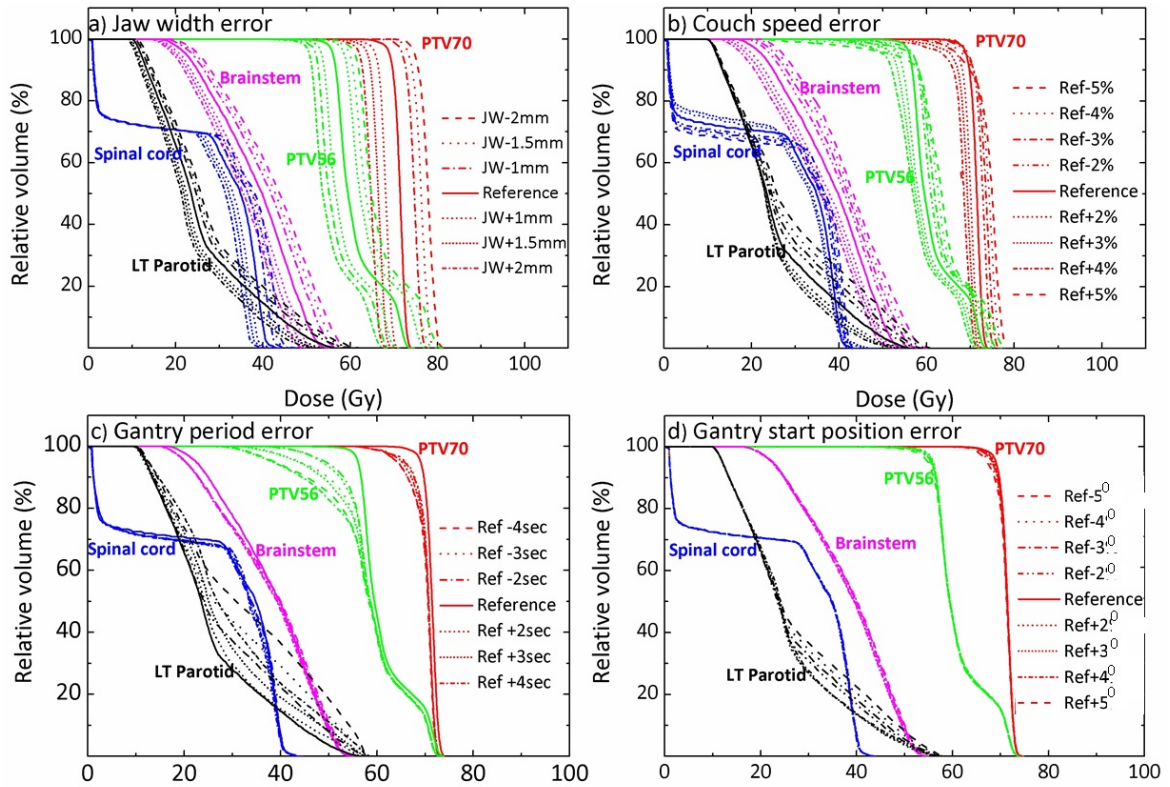


Figure 7.3: DVH graphs for a representative patient data set comparing the clinical reference plan with the following simulated errors a) Jaw width b) Couch speed c) Gantry period and d) Gantry start position. Other patient datasets demonstrated similar variation

dose variation is within the set clinical tolerance, the machine QA tolerance should be set to JW 0.5 mm, CS 1.5% cm per sec, GP 1 sec and GSP 2°.

The average percentage dose difference with simulated MLC LOT errors is presented in figure 7.5. For the MLC LOT error with MLC stuck open and a MLC LOT random reduction of 4%, noticeable dosimetric variations from the clinical reference plan DVH are seen (figure 7.6). The MLC LOT random error up to 10% with mean MLC LOT error of 0% did not display any effect on the dose distribution.

Figure 7.7, 7.8 and 7.9 shows example of degradation in the dose distribution from four different simulated delivery error types for a same patient with error magnitudes that were found to be clinically relevant.

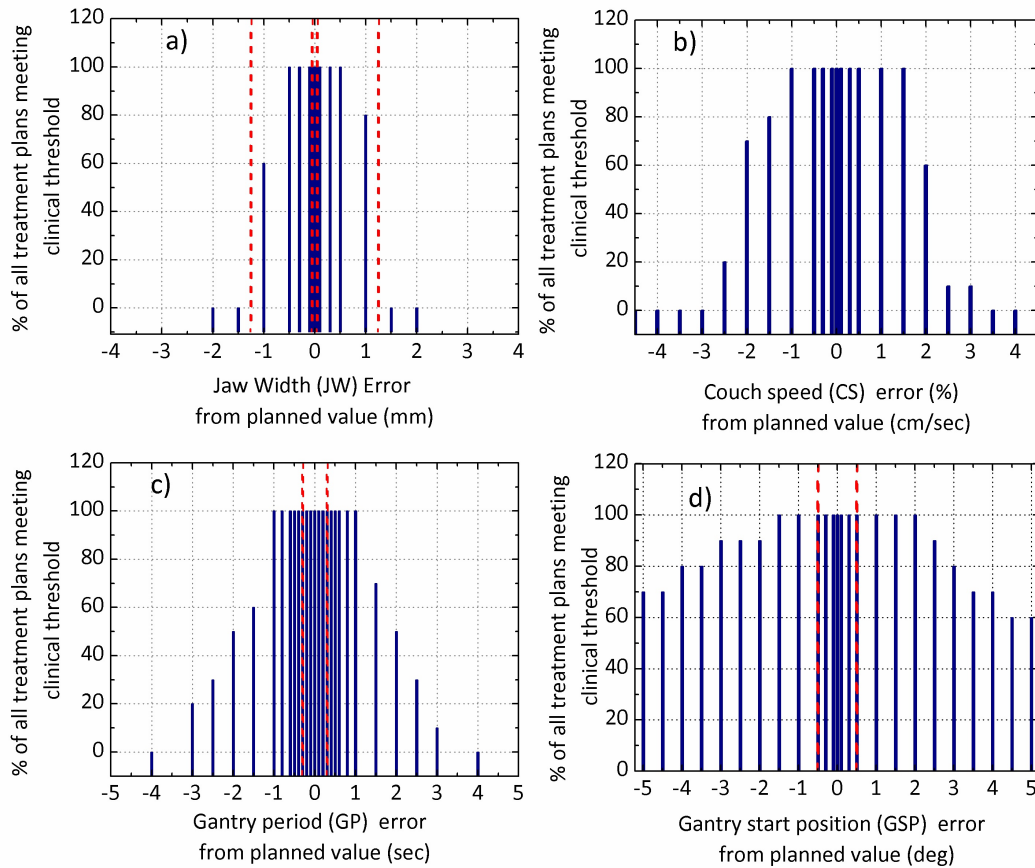


Figure 7.4: Histogram distribution of the treatment plans from the ten patient cohort that are within the set clinical tolerances (both PTV and OAR) for varying magnitude of errors in a) Jaw width (JW) b) Couch speed (CS) c) Gantry period (GP) and d) Gantry start position (GSP). The red dashed bar shown above represents the machine interlock threshold for each error type. The jaw error has 2 levels of interlocks while the couch speed does not have a specific interlock since the couch position is monitored instead of the couch speed

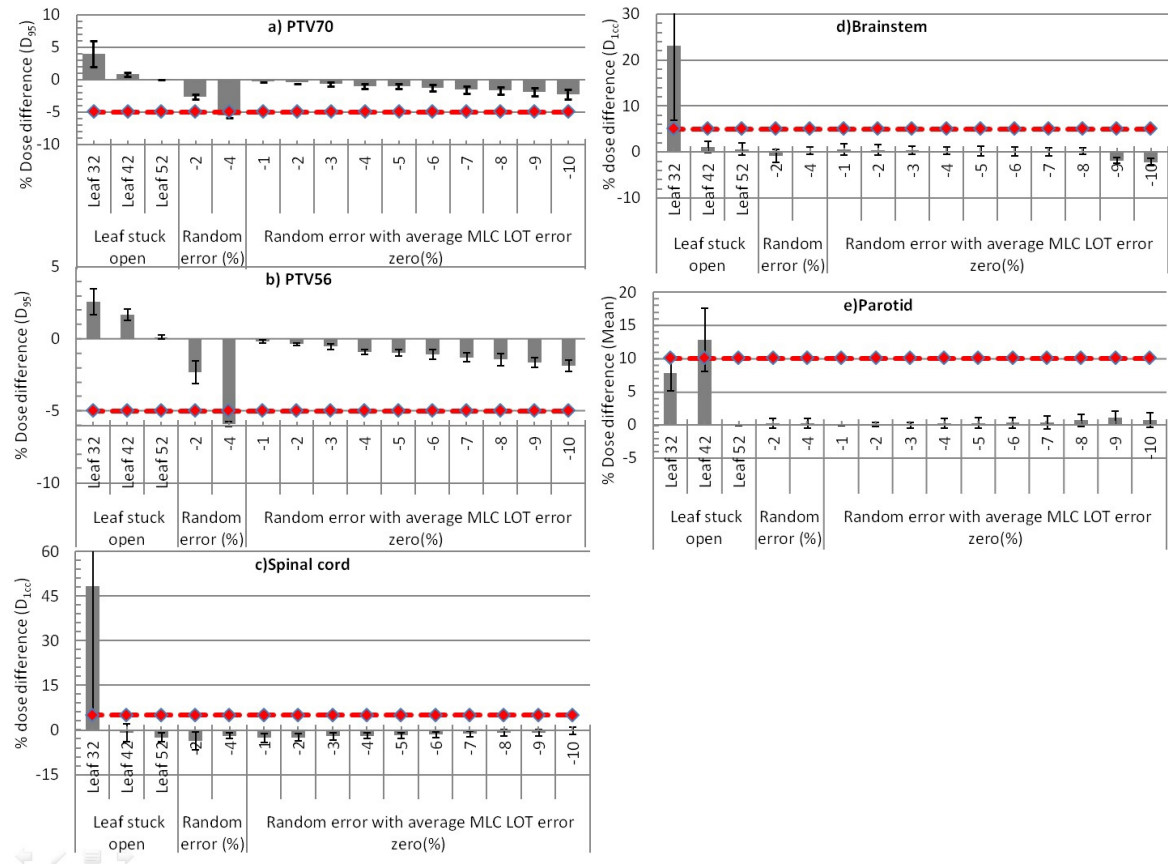


Figure 7.5: The average percentage dose difference compared to the clinical reference (no error) plans over the ten patients for a) D_{95} of PTV70, b) D_{95} of PTV56, c) D_{1cc} for spinal cord and c) D_{1cc} for brainstem and d) mean dose to the parotid with simulated MLC LOT errors. Two random MLC LOT errors were considered: i) The reduction was randomly applied across all open leaves such that the mean reduction was 2% or 4% and ii) The MLC LOT random modification applies a normal random distribution to all open projections with a given standard deviation (1-10%) and a mean of 0%. The error bars represent one standard deviation in plan metrics from the ten patients. The red dotted line represents the set clinical tolerance

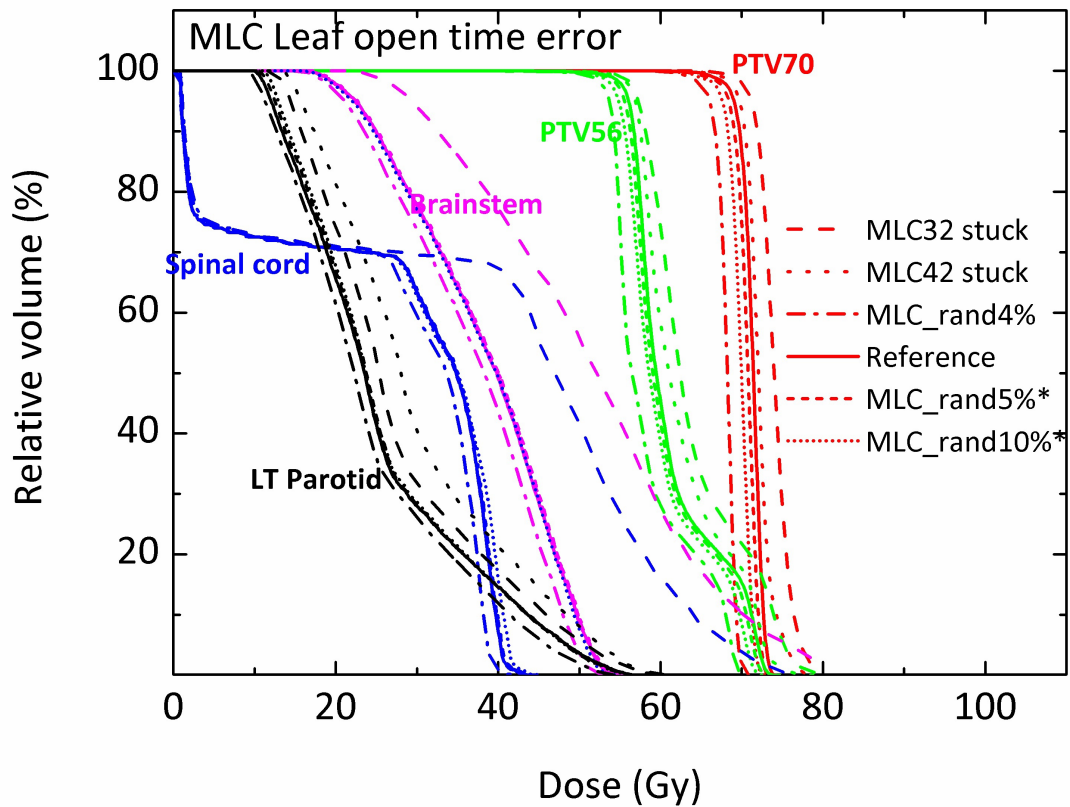


Figure 7.6: DVH graphs for a representative patient data set comparing the clinical reference plan with the following simulated MLC LOT errors: leaf 32 stuck open, leaf 42 stuck open and MLC LOT reduced by 2% and 4% and standard deviation of 5% and 10% with mean MLC LOT error of 0% as described in the methodology. Other patient datasets demonstrated similar variation

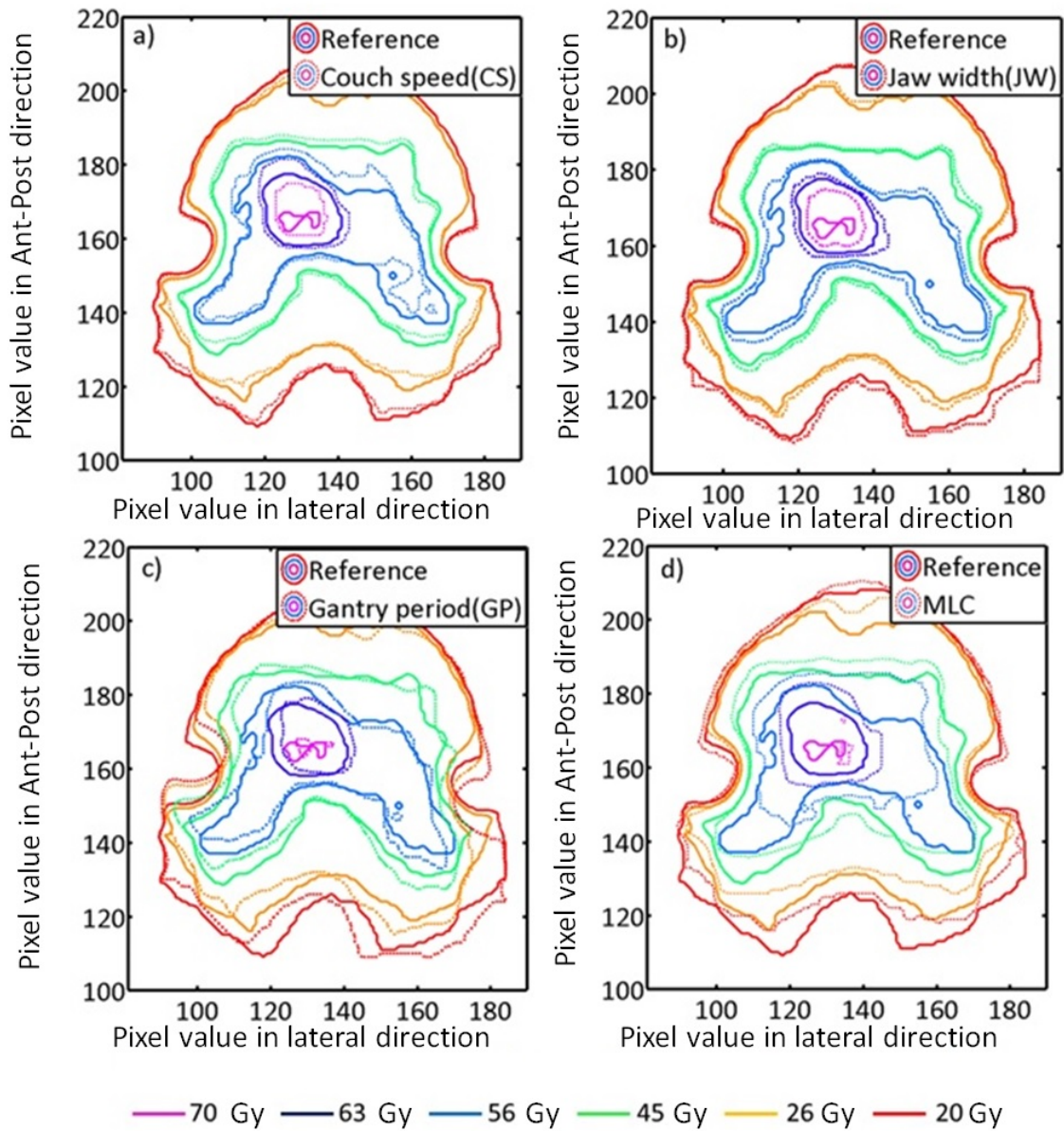


Figure 7.7: Isodose distribution comparison between the reference clinical plan and each of the four simulated delivery error plans a) transverse view cutting through isocentre. The dose distribution example is from one selected patient dataset and shows the worst impact on the dose distribution. The simulated error magnitude were for JW was +1 mm, CS +2.5% cm per sec, GP +3sec and GSP +4°. The magnitude for each error type displayed here was such that the set clinical tolerance was exceeded.

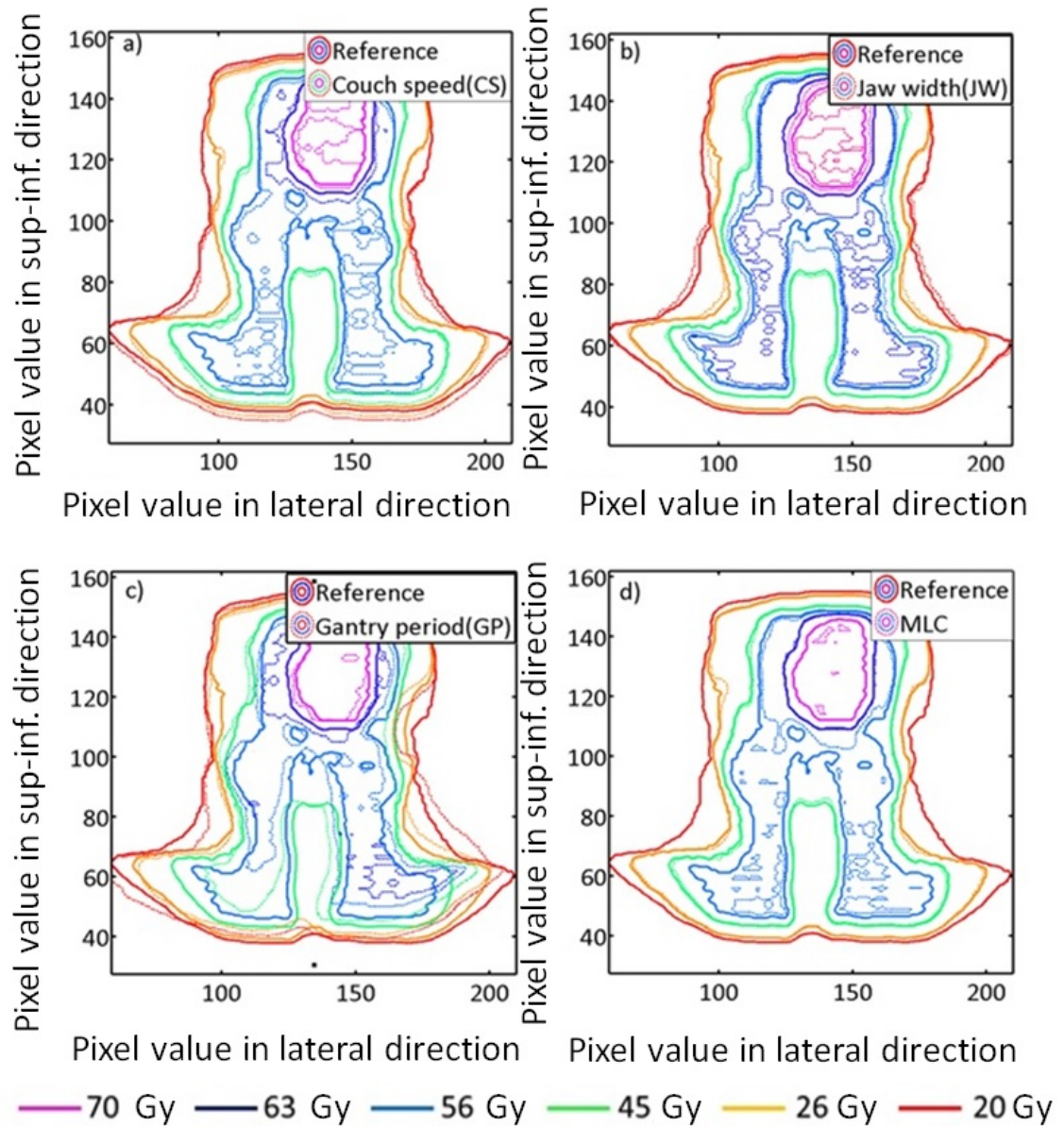


Figure 7.8: Isodose distribution comparison between the reference clinical plan and each of the four simulated delivery error plans coronal view cutting through isocentre. The dose distribution example is from one selected patient dataset and shows the worst impact on the dose distribution. The simulated error magnitude were for JW was +1 mm, CS +2.5% cm per sec, GP +3sec and GSP +4⁰. The magnitude for each error type displayed here was such that the set clinical tolerance was exceeded.

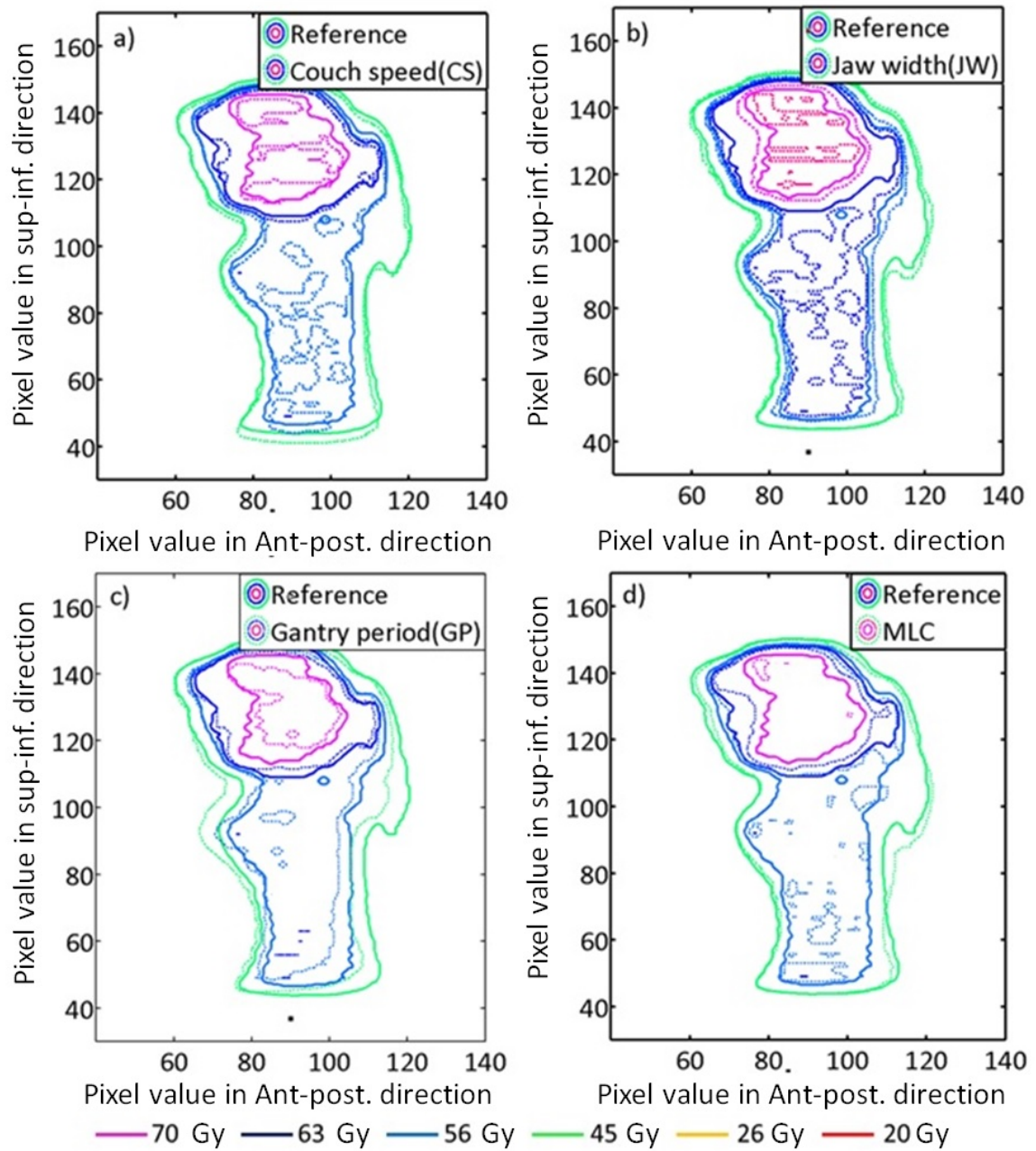


Figure 7.9: Isodose distribution comparison between the reference clinical plan and each of the four simulated delivery error plans sagittal view cutting through isocentre. The dose distribution example is from one selected patient dataset and shows the worst impact on the dose distribution. The simulated error magnitude were for JW was +1 mm, CS +2.5% cm per sec, GP +3sec and GSP +4⁰. The magnitude for each error type displayed here was such that the set clinical tolerance was exceeded.

7.4 Discussion

In this study, we present a framework to simulate several HT mechanical errors and assess the clinical impact on HT plans typical of nasopharynx treatments in our clinic. Furthermore, we demonstrate how clinically meaningful HT QA tolerances can be developed and provide examples of how to evaluate the sensitivity to errors of several delivery parameters for individual treatment sites. We also assess the effectiveness of the machine interlock settings in preventing the simulated parameter errors that were found to be clinically relevant.

The dose variation due to simulated errors exceeds the set clinical tolerance in patient cohorts for the following simulated errors: in JW ± 0.5 mm, CS ranges between -1% cm per sec to 1.5% cm per sec, GP ranges ± 1 sec, GSP ranges between -1.5° to 2° and MLC LOT random error up to 2% from the planned value. The sensitivity of all the simulated delivery errors reported in this study are applicable to nasopharynx treatments planned with similar planning parameters used and dose fractionation (2-2.4 Gy). As seen in Table 7.3 and figure 7.4, for the plans considered the current machine interlocks will prevent delivery errors resulting in a clinical impact with a few exceptions. In the case that the primary interlock for JW fails, the secondary interlock of 1.25 mm may not prevent clinical impact as this work demonstrated that a JW error > 1 mm would affect the patient dosimetry. A tighter tolerance on this interlock should be considered for 2.5 cm JW. The suggested QA tolerance by AAPM Task Group 148 [47, 50] for JW is FWHM within 1% (i.e. 0.25 mm for 2.5 cm JW) and GSP within 1° .

In addition, our study demonstrates that MLC LOT and GP errors can lead to unacceptable dose distribution. While the MLC LOT and GP performance is stringently monitored during treatment, no specific recommended QA test frequency and tolerance to monitor the performance for MLC LOT and GP is suggested in the AAPM TG-148 report [47]. We recommend that routine QA tests be implemented to monitor MLC and GP performance. Although couch speed itself is not monitored, a matrix of couch position versus time based on pitch is created by planning system and the interlock will trigger when the instantaneous position of the couch deviates by more than 1 mm during couch travel at specific time. We created a similar matrix of table position versus time for the first five gantry rotations using a pitch value and jaw width for the planned couch speed as well as for simulated errors in couch speed of $\pm 2\%$ cm per sec, $\pm 3\%$ cm per sec and $\pm 5\%$ cm per sec to determine the interlock threshold for couch speed. As shown in figure 7.10, even couch speed errors of

2% cm per sec and 5% cm per sec from planned values which is demonstrated as clinically relevant would be undetected by machine interlocks for an initial couch travel of 50 mm and 22 mm respectively. This suggests that the couch position should be monitored with improved precision. Fortunately, an internal review of patient logs files from actual patient treatments at our centre suggest that the average error value in couch position was observed to be 0.20 ± 0.05 mm from the expected position.

Table 7.3: Summary of machine interlock, recommended machine QA tolerance and established using dosimetric based simulation

Machine parameter	Machine interlock	TG-148 tolerance or Previously published reports	QA	Dosimetric based QA tolerance
Jaw width	Primary interlock 500 microns Secondary interlock 1.25mm	1% of JW (0.25 mm for 2.5 cm JW)		0.5 mm for 2.5 cm JW
Couch speed	Couch position at any point of delivery is differing by 1mm from the planned value	2%		< 1.5% from planned value
Gantry period	2% of planned value	No specific tolerance		< 1 sec of planned value
Gantry position	$\pm 0.1^\circ$ from planned value (Tomo-Direct capable machine)	1°		1.5°
MLC LOT	Leaf does not begin to move in about 40ms from the time when a leaf does not reach its destination in about 70ms when a leaf moves past its intended destination Leaf reaches its destination in the allotted time, but then transitions back to the transit state before settling at its destination	No specific tolerance		Random error 2and mechanical fault (individual stuck open or closed)

A simulated error in GSP, similar to patient rotation setup error (roll), up to $\pm 3^\circ$ did not show any clinical impact on the planned dose distribution (in 8 out of 10 patients) indicating that this error is less sensitive compared to other delivery errors simulated in this study. Although not directly comparable, simulated GSP error $< 3^\circ$ also did not show any clinical impact

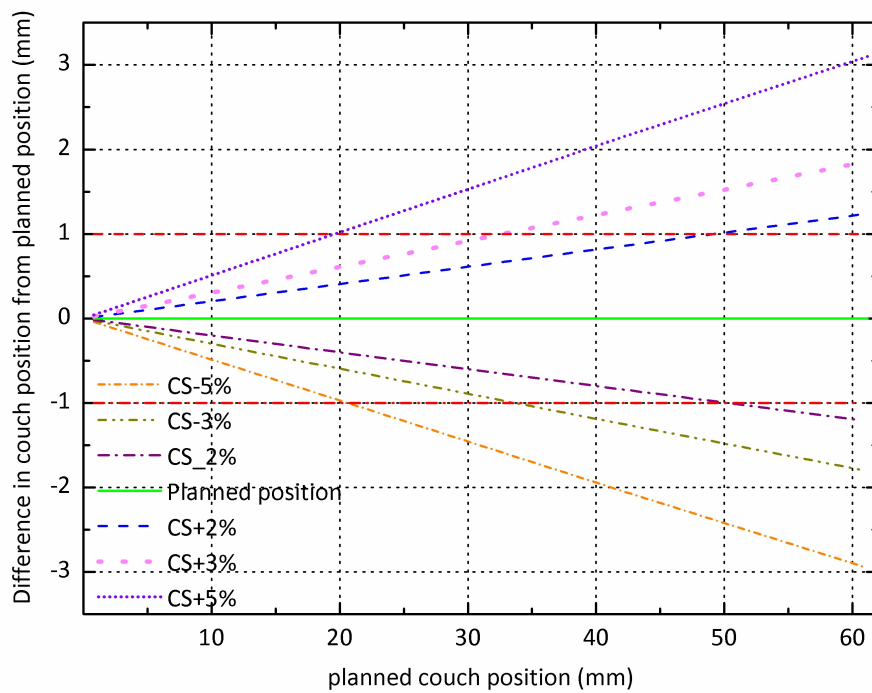


Figure 7.10: Comparing the expected couch position calculated based on planning parameter against the predicted couch position for simulated couch speed delivery error of $\pm 2\%$ cm per sec, $\pm 3\%$ cm per sec and $\pm 5\%$ cm per sec from planned value. The dotted red lines are the machine interlock threshold when the couch position is different from expected planned value (± 1 mm)

for c-arm linac based treatments such as RapidArc™[43] and IMRT delivery [133, 281] demonstrating GSP error is insensitive for linac based treatment as well. The JW and CS simulated errors were uniformly applied to all planned projections leading to a threading effect (refer to figure 7.8 coronal view), as both effectively change the pitch. The dose variation pattern that manifest as a ‘ripple’ (peak-to-trough relative to the average dose). This ripple in dose distribution is called threading effect. A detailed explanation about the threading effect can be found in previously reported studies [289, 290].

The threading effect has been shown to be dependent on the pitch value used, off-axis distance of the RT structures, and beam divergence [290]. The average off-axis distance of the farthest pixel in PTV56 was 11 cm. For GP and GSP errors the angles of radiation incidence are changed. This can lead to beams with high fluence through OARs or partially missing an off-axis located target e.g. PTV56 (figure 7.11). Because the spatial relationship of PTV to the parotid glands (i.e. overlap or clearance) varies from one patient to another (see figure 7.12), the effect of GP and GSP error is patient and plan specific and nonlinear. For GP errors, the angular offset in delivered projections from the planned position increases as a function of beam-on time. As demonstrated in figure 7.2, the gantry offset due to GP error had a major impact on an elongated and off-axis located PTV56. In (Appendix B), we studied the clinical impact of intentional HT delivery errors on lung SABR cases (i.e. long duration treatments) using the same framework proposed in this chapter and demonstrated that GP error have higher clinical impact on patient dosimetry compared to conventional fractionation treatment studied in this work. This suggest GP error will have a detrimental impact on long duration treatments such as total marrow/body irradiation (TMI/TBI) or located far off-axis structures or lung SABR cases (Appendix B). and therefore the impact from GP error could be much higher than what is presented here for these clinical scenarios.

One of the limitations of this work is the limited patient sample size. However, this framework can be used as an ongoing machine learning process. One approach would be for the process to be applied to an individual patient dataset to determine the plan specific delivery error threshold as well as validate plan robustness for a given machine QA tolerance. Another approach would be to evaluate the QA tolerance by considering the appropriate sample size for given treatment sites. There is growing interest to use the log file-based QA approach [291–293]. It is still not certain whether the log file-based QA approach offers the same confidence as real dosimetric measurements. Independent commissioning and robust routine QA of the sensors reported in the log files may be also required. Unfortunately, the

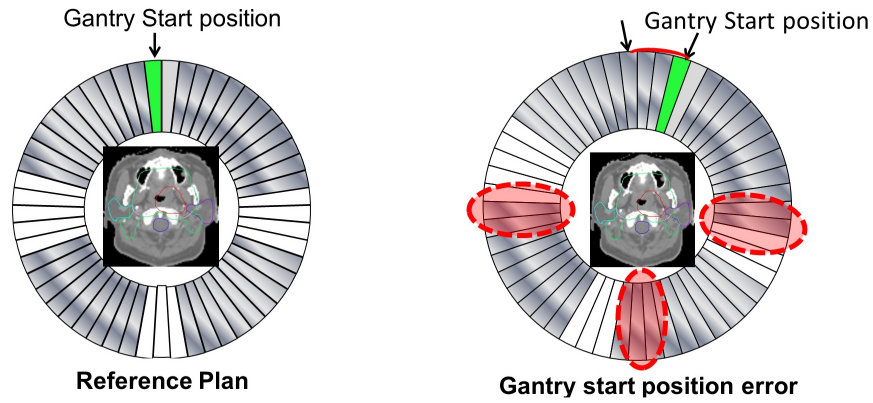


Figure 7.11: Illustration of dosimetric impact due to the gantry related delivery error i.e. gantry start position (GSP) and gantry period (GP). Error in GP or GSP will systematically offset the projection from the planned position (left) such that high fluence projections are rotated from their intended angles, affecting the delivered dose distribution



Figure 7.12: The transverse CT images for 3 different patients showing the spatial variation of the PTV70 contour (red colour) relative to parotid (cyan-right and purple-left side). The green contour is PTV56.

TomoTherapy log file is missing MLC information, which is one of the major uncertainties of treatment delivery. Instead, the log files report only the average error value between the planned and actual couch position. It should also be noted that we did not investigate the effect of combinations of errors. Therefore, our work has studied the clinical effects where only a single interlock might fail. That said the framework we have developed could be extended to study combinations of errors and is a potential topic of future work.

7.5 Conclusion

Dose variation in the considered nasopharynx dataset was within set tolerances for simulated errors in JW up to 0.5 mm, CS up to 1% cm per sec, GP up to 0.5 sec, GSP up to 2⁰ and MLC LOT random error up to 2% from the planned value for HT plans with jaw width of 2.5 cm, pitch of 0.287 or 0.403 and dose per fractionation of 2-2.4 Gy. Most of the clinically relevant errors are prevented by machine interlocks except the couch position and the secondary interlock for jaw position. Our study highlights that the system interlock thresholds for jaw position and couch position should be tighter and monitored with improved precision than monitored currently to avoid any clinically relevant delivery errors. This work has established a method to characterize HT machine delivery errors and estimate their clinical significance. We demonstrated that the effect of these delivery errors could be plan technique/site specific (particularly gantry speed errors). This work can be extended to additional error modes and other treatment techniques/anatomical sites in the future. Using this approach, a HT QA program can be strengthened by consideration of treatment sites, institution-specific planning methods, and clinical tolerances.

Chapter 8

Sensitivity evaluation of two commercial dosimeters in detecting helical Tomotherapy treatment delivery errors

Statement of joint authorship

S. Deshpande: Develop experimental design, performed experiments, analysed results, wrote manuscript

M. Geurts: Render advice on the experiment, interpreting results and write up

P. Vial: Render advice on the experiment, interpreting results and write up

P. Metcalfe: Assisted in interpreting results and writing, as supervisor he endorses the assessment

L. Holloway: Render advice on the experiment, interpreting results and write up

[‡]Part of this chapter has been submitted for publication:

S. Deshpande, M. Geurts, P. Vial, P. Metcalfe, L. Holloway Sensitivity evaluation of two commercial dosimeters in detecting helical Tomotherapy treatment delivery errors *Physica Medica*, (Accepted for publication)

8.1 Introduction

Inaccurate radiotherapy can result in ineffective treatment or serious harm to the patient [14]. Advanced radiotherapy technologies and methods such as intensity modulated radiotherapy (IMRT), volumetric modulated arc therapy (VMAT) and helical tomotherapy (HT) are complex and are less tolerant to poor implementation than are standard techniques [294]. HT is a dynamic delivery that relies on synchronisation of the gantry, treatment couch, and multileaf collimator (MLC) leaf movement with the radiation beam during treatment [49]. For these treatments, an optimised treatment plan (i.e. inverse planning) is tailored to each individual patient. The beam apertures generated during optimisation are highly complex and bear little resemblance to treatment beam fields used during TomoTherapy commissioning. Therefore, stringent delivery quality assurance (DQA) methods are recommended to ensure the correct treatment delivery for each patient [90], which should be conducted for each clinically approved plan prior to delivering the first treatment fraction to detect possible errors (both the dose calculation accuracy of the treatment planning system (TPS) and accuracy of treatment delivery). A wide variety of instrumentation and experimental methods are in clinical use for pre-treatment verification. Historically, HT DQA was performed with film or ion chamber point dose measurements [47]. The complexity and inefficiency of film dosimetry procedures has led to the development of systems that provide real-time measurements. In recent years a number of (2D, semi 3D and 3D) commercial detector arrays have become available including the Delta⁴ (ScandiDos AB, Uppsala, Sweden), ArcCHECK/MapCHECK (Sun Nuclear Corp., Melbourne, FL), MatriXX (IBA Dosimetry GmbH, Schwarzenbruck, Germany), and 2D-ARRAY seven29 (PTW, Freiburg, Germany) for pre-treatment verification that provides real-time measurements [51, 153, 156, 208, 295, 296]. Most clinics have now routinely adapted these commercially available dosimeters to perform HT DQA [297–301]. The gamma evaluation technique has become the current standard to provide a quantitative comparison [109]. However, there is limited evidence in the literature about the ability of such dosimetry systems to detect delivery errors for HT treatment deliveries.

Several studies (summarised in Table 8.1) have assessed the sensitivity of different detectors to IMRT and/or VMAT simulated errors. Fredh et al. [58] investigated a number of measuring devices and the response of these devices to MLC bank positional errors, dosimetric errors and collimator errors introduced into patient plans. Their study concluded that the different detectors were able to detect particular errors; however they did not quantify the sensitivities in detecting these errors. Arumugam et al [54] evaluated the sensitivity of Arc-

CHECK dosimeter to VMAT delivery associated with MLC and dose output errors. Their study inferred that ArcCHECK was able to detect a minimum of 3 mm MLC error, and 3% output errors. Detector sensitivity for error detection also depends on plan complexity.

Table 8.1: Summary of previous reported studies on detector sensitivity for commercial detectors.

Detector	Treatment type	Error type	Treatment sites (number of plans)	Key reference
Delta ⁴	VMAT	Translation error, Gantry rotation	Prostate,Spine,Intracranial Pancreas(50 plans)	Masi et al [52]
	Rapid Arc	MLC position and Dose error	Prostate (not specified)	Carver et al [302]
	Rapid Arc	MLC, dose and collimator error	Prostate,head and neck and brain(4 plans)	Fredh et al [58]
ArcCHECK	IMRT(SW)	Gantry rotation, MLC position	Head and Neck, prostate(3 plans)	Feliciano et al [53]
	VMAT	MLC position	TG-119 Mock plans (3 plans)	Feygelman et al [51]
	VMAT	Dose error, MLC error	Head and Neck, prostate (10 plans)	Arumugam et al [54]
	Helical Tomotherapy(HT)	Couch speed,MLC LOT,Gantry start position	Head and Neck,Prostate (9 plans)	Templeton et al [59]
MapCHECK	IMRT (S&S)	MLC error	Head and Neck(8 plans)	Yan et al [46]
	IMRT (S&S)	MLC error	Head and Neck(1 plan)	Le'tourneau et al [55]
MatriXX	IMRT(S&S)	MLC position and collimator error	Head and Neck, prostate(2 plans)	Bawazeer et al [56]
PTW 2D array	VMAT	Translation error, Gantry rotation	Prostate,Spine,Intracranial Pancreas(50 plans)	Masi et al [52]
	Rapid Arc	MLC, dose and collimator error	Prostate,head and neck and brain(4 plans)	Fredh et al [58]
	Rapid Arc and IMRT(SW)	MLC position and Collimator error	Head and Neck,prostate(12 plans) and test pattern(one)	Hussein et al [57]

SW=Sliding Window; S&S= Step and Shoot

Feygelman et al [51] have demonstrated that the larger gantry spacing between the CPs and narrow field width results in larger errors in dose calculation, especially in the ArcCHECK measurement plane compared to Delta⁴ detector [51]. This is mainly due to the discretisation

of the gantry angle aperture shapes in the TPS dose calculation. Masi et al [52] measured clinical VMAT plans using four different dosimetry systems. Authors reported slightly lower gamma pass-rate for plans from one of the considered planning systems which was attributed to a higher level of complexity of the optimised plans. The detector sensitivity to intentional 3 mm translation shifts and to gantry angle offset was shown to be strongly plan and partially detector dependent. Bawazeer et al [56] demonstrated the MatriXX^{Evolution} (IBA Dosimetry, Germany) 2D detector was able to detect MLC position errors of 1 mm and collimator rotation errors of 2° for step and shoot IMRT delivery. All of the above detector sensitivity studies focused on the MLC positional accuracy, collimator or gantry rotation and dose errors for C-arm linac based treatment and may therefore may not be relevant to the different delivery mechanism of HT machines.

The only study on detector sensitivity to detect HT delivery error using the ArcCHECK dosimeter was reported by Templeton et al [59]. They measured a total of nine clinical plans: three head and neck, three prostate with pelvis nodes, and three prostate only. The ArcCHECK sensitivity was assessed to detect intentionally introduced delivery errors in couch speed, gantry start position and MLC leaf open time. No specific details about planning parameters were provided for clinical plans used in their study. Author reported the error size required to degrade the gamma pass rate to 90% or below (using 3% and 3 mm gamma criteria) was on average a 3% change in couch speed, 5° change in gantry synchronisation (i.e. gantry start position), or a 5 ms change in leaf closing speed.

Our previous work [303, 304] (as described in chapter 7) evaluated the clinical impact of HT delivery error in couch speed, jaw width and MLC leaf open time errors for ten nasopharynx clinical plans. In this work, we have compared the sensitivity of two commercial dosimeters MatriXX^{Evolution} and ArcCHECK to detect clinically relevant errors in couch speed, jaw width and MLC leaf open time errors for the same sets of ten clinical nasopharynx HT plans considered in Chapter 7. The focus of the present work was to determine how the intentionally introduced delivery error would be manifested in QA dosimetry system measurements. The threshold was determined at which these dosimeters are sensitive to particular delivery errors. For each of the dosimeters, two parameters were evaluated i) the minimum error magnitude that the detector systems can detect (i.e. threshold) and ii) how the sensitivity to the errors varies between detector systems (i.e. sensitivity to a particular error).

In this work, we have compared the sensitivity of two commercially available dosimeters

MatriXX^{Evolution} and ArcCHECK to detect intentionally introduced delivery errors in jaw width, couch speed and MLC LOT using gamma criteria of 3% and 3 mm for ten clinical nasopharynx HT plans. The focus of the present work was to determine how the intentionally introduced delivery errors would be manifest in QA dosimetry system measurements, given the fact that there is marked deviation from patient geometry. The threshold was determined at which these dosimeters are sensitive to particular delivery errors. Two hypotheses were tested i) the minimum error magnitude that the detector systems can detect (i.e. threshold) and ii) that how the sensitivity to errors varies between detector systems (i.e. sensitivity to a particular error).

8.2 Methods and Materials

8.2.1 Patient selection and treatment planning

Ten retrospective clinical nasopharynx HT plans with varying complexity were selected for this study used in previous work [304] and previous chapter 7 . All ten clinical plans were optimised using a fixed 2.5 cm jaw width, 0.287 or 0.403 pitch and 2.2-2.4 modulation factor with the clinical TomoTherapy (Accuray Incorporated, Sunnyvale CA) TPS version 4.2.2, to meet planning goals outlined in the RTOG 0615 protocol [305].

8.2.2 Dosimetry system

Two commercial dosimetry systems were considered. The construction details and additional corrections required to convert the measured signal to dose for each dosimeter system are described in following sections

8.2.2.1 MatriXX^{Evolution} dosimetry system

The MatriXX^{Evolution} system consists of a MatriXX device (a two dimensional array of ionization chambers), a MULTICube Lite (IBA Dosimetry) phantom, and OmniPro-ImRT software (IBA Dosimetry, Germany). This array has 1020 air-vented plane parallel ionization chambers (with a volume of 0.08 cm³ each) arranged in a 32 × 32 grid providing a maximum field of view of 24 × 24 cm². The ionization chambers are spaced at 7.62 mm centre-to-centre. The MatriXX^{Evolution} measurements were made in the movie mode with a

sampling rate of 500 ms/snap (i.e. 500 ms/image). The MatriXX^{Evolution} device was inserted into the MULTICube Lite phantom. The MULTICube Lite is made of plastic water with dimensions 31.4 cm long, 22 cm high and 34 cm wide. The MULTICube Lite phantom is positioned on HT couch. The absolute dose calibration procedure recommended by the manufacturer was followed to calibrate the device. Only chamber sensitivity correction and calibration correction were applied to the measured signal. In the HT setting, the angular correction cannot be applied as the dosimetry system relies on inclinometer input for obtaining the instantaneous gantry position information and the inclinometer cannot be attached to a HT unit due to the gantry head access.

8.2.2.2 ArcCHECK dosimetry system

ArcCHECK is a cylindrical phantom that consists of 1386 diode detectors arranged in a helical grid pattern with 10 mm detector spacing. The helical grid detector array has dimensions of 20.8 cm diameter and 21 cm length with detectors at a depth of 2.9 cm from the surface of the phantom [51]. The dose measured by each detector is corrected for background, heterogeneity and diode angular response and field size sensitivity. The ArcCHECK dosimeter used in this study included the central cylindrical insert and all measurements were performed with the cylindrical insert in place. The absolute dose calibration procedure recommended by the manufacturer was followed to calibrate the device.

8.2.2.3 DQA Plans

DQA plans were recalculated by superimposing the clinical plan dose on phantom CT images. The scanned MatriXX^{Evolution} images were imported as a QA phantom for the MatriXX^{Evolution} dosimetry system. In the case of the ArcCHECK dosimetry system, a pseudo CT dataset (supplied by manufacturer) representing the ArcCHECK geometry was imported as a QA phantom. A uniform density of 1.15 g/cm³ was assigned to the ArcCHECK geometry as per manufacturer guidelines as well as used in previous work [63, 306]. The ArcCHECK was positioned such that the diodes passed through the high dose region of the plan, which resulted in an off-centred location of the QA phantom. The planned dose corresponding to the measured dose was extracted by the SNC Patient Dose Analysis software (version 6.6, Sun Nuclear Corporation, Melbourne, Florida, USA) from the DICOM 3D dose cubes calculated on the ArcCHECK phantom geometry [51]. In the case of the MatriXX^{Evolution}, the planar dose was directly extracted from the TPS at the detector plane.

8.2.2.4 Delivery errors and measurements

A HT delivery plan is defined by the following parameters; jaw width, gantry period, gantry start position and a sinogram (a matrix which defines the fraction of MLC LOT for each projection). In Chapter 7, we simulated all the above mentioned delivery errors to evaluate their clinical impact on patient dosimetry for a range of error magnitudes. In this work, we investigated the sensitivity of two detectors for delivery errors in jaw width, couch speed and MLC LOT only for error magnitude that was demonstrated to be clinically relevant i.e. compromise the patient dosimetry. For each patient, error plans were created by independently introducing systematic offsets in: a) jaw width error ± 1 , ± 1.5 and ± 2 mm, b) couch speed error $\pm 2\%$, ± 2.5 , $\pm 3\%$ and $\pm 4\%$, and c) MLC leaf open time (MLC LOT) errors. Three scenarios for MLC errors considered were: leaf 32 stuck open during delivery, leaf 42 stuck open during delivery (these leaves are commonly used to treat central and off-centered targets for head and neck cases) and 4% random reductions in MLC LOT from planned values. In the case of MLC LOT errors, the optimized clinical plan sinogram was edited using MATLAB (version: 7.10.0.499 (R2010a), Mathworks Inc., MA). The random error was simulated by using a normal distribution with a standard deviation of 4% and leaf open times greater than 100% are not possible to deliver, so were truncated. All intentional error plans along with the ‘no error’ plan for each patient were measured using both dosimetry systems in the same session to minimize any machine output or experimental variations. Prior to each measurement session, daily output and a cross plane profile were measured using TomoDOSE (Sun Nuclear Corporation, Melbourne, Florida, USA) as a constancy check to monitor machine behaviour. The gamma evaluation (global) technique (3%/3 mm) was applied to quantitatively compare the measured dose from the two dosimeters against the TPS. The 90% gamma pass rate is an action level at approximately the mean pass rate of previously treated plans for similar complexity in our clinic minus two standard deviations, as proposed in previous studies [59, 307]. The phantom set up accuracy was verified by on-board megavoltage CT (MVCT) image guidance prior to each measurement session.

8.2.3 Detector sensitivity

The sensitivity of both detectors to delivery errors was studied by calculating the gradient of the global γ pass rate (equation 8.1) for each error scenario.

$$\nabla\gamma = \frac{\Delta\gamma \text{ pass rate}}{\Delta \text{ introduced error}} \quad (8.1)$$

Where, ($\Delta\gamma$ pass rate) is the change in γ pass rate and (Δ introduced error) is the unit change in introduced error. The $\nabla\gamma$ for a given error scenario was calculated by fitting the γ pass rate for the studied error range using a linear least square fit. The gamma pass rate and Wilcoxon Signed–Rank significance ($P < 0.05$) test were used to decide whether an intentional introduced error can be detected by the dosimetry systems. The number of dose measurements points used for gamma computation are different for MatriXX and Arc-CHECK dosimeters due to difference in detector geometry and detector spacing. Therefore, the absolute gamma pass rate when measured for same clinical plan using both dosimeters would not be directly comparable. To compare sensitivity in detecting intentional errors for each dosimeter as a measure of change in gamma pass rate, first, the gamma pass rate with no error plan is normalised to 100% and then, the gamma pass rate for each intentional error plans were scaled to no error plan.

8.2.4 Criteria for minimum error detection

In the presence of varying complexity in clinical plans, the gamma pass rate for these plans are expected to exhibit a considerable spread for both intentional error and no error plans. In order to detect the error confidently in studied plans, a clear separation between the no error and intentional error delivery was defined by incorporating the standard deviation of the γ pass rate for both no error and intentional delivered error plans. As described in a previous study [54], an error in the simulated plan was considered detected when the criterion given in equation 8.2 is met.

$$\begin{aligned} &(\text{mean } \gamma \text{ pass rate} + \sigma \text{ of } \gamma \text{ pass rate}) \text{ for error delivery} < \\ &(\text{mean } \gamma \text{ pass rate} - \sigma \text{ of } \gamma \text{ pass rate}) \text{ for no delivery error} \end{aligned} \quad (8.2)$$

Where, σ is the standard deviation of the pass rate of the respective no-error and intentional delivery error plans.

The quantity on the right hand side of equation 8.2 represents the minimum pass rate (lower limit) observed in the no error delivery. Subtracting the σ of the no error plans from the mean pass rate of the no error plans allows the difference in level of complexity between plans to be considered. The quantity on the left hand side of the equation represents the maximum pass rate (upper limit) observed with the detected error. Adding the σ defines the upper limit of pass rate again considering plan complexity variation.

8.3 Results

8.3.1 Detector sensitivity

The mean (γ) global gamma pass rate for intentional error plans measured with both dosimeter systems is shown in figure 8.1. The global γ pass rate for the 3%/3 mm tolerance criteria decreased linearly with increase in error magnitude for both dosimeters. The error magnitude change required to degrade the gamma pass rate for each error type as well as the detector sensitivity determined using equation 8.1 for each error type is summarised in Table 8.2.

Table 8.2: Magnitude of change required to degrade mean gamma pass rate to below 90% with 3%/3mm gamma criteria and detector sensitivity as determined from equation 8.1 for both dosimeters. A linear fit of mean gamma pass rate versus error magnitude was used to obtain both error magnitude to degrade gamma pass rate below 90% and detector sensitivity

Error type	Error direction /details	Error magnitude to degrade the mean gamma pass rate $\leq 90\%$		Detector sensitivity $\nabla\gamma$	
		MatriXX	ArcCHECK	MatriXX	ArcCHECK
Jaw width	Negative	0.4 mm	0.8 mm	18.2	12.4
	Positive	0.2 mm	0.3 mm	32.9	30.3
Couch speed	Negative	0.7%	0.8%	10.3	9.8
	Positive	2.1%	2.2%	4.3	3.8

The gamma pass rate for intentional introduced errors in JW and CS are dependent on the error direction (see figure 8.1 and Table 8.3; -2% and +2% differ for couch speed and -1 mm

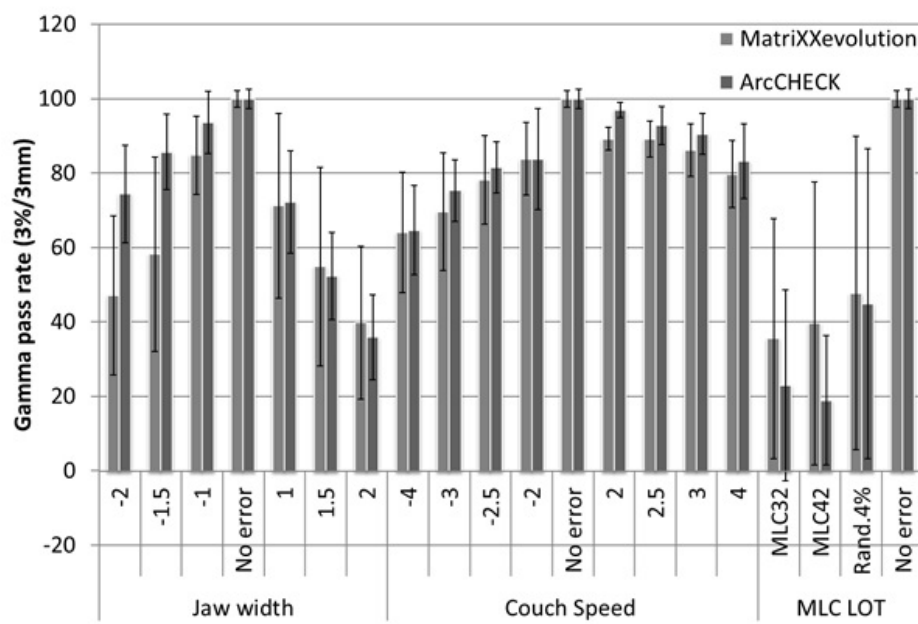


Figure 8.1: Comparison of mean gamma pass rate measured for intentional error plans in jaw width, couch speed and MLC LOT measured with ArcCHECK and MatriXX^{Evolution} dosimeters. The error bar shows maximum and minimum pass rate for a given error magnitude. The dotted red line represents 90% gamma pass rate used as an action level. The mean pass rate for no error plan for both dosimeter is normalised to 100% and gamma pass rate for each plan is then scaled to no error plan

and +1 mm for jaw width).

8.3.2 Error detection by dosimeter systems

Table 8.3 summarises the mean and mean- σ of γ pass rate for no error plans with 3% and 3 mm global gamma tolerance criteria along with mean+ σ of γ pass rate for couch speed and jaw width error plans. The Wilcoxon Signed-Rank test indicated a similarity in gamma pass rate metrics between the two dosimetry systems ($p > 0.05$). Although the overall mean gamma pass rates for both dosimeters is comparable, the error detection magnitude is slightly superior for MatriXX^{Evolution} compared to ArcCHECK (Table 8.3).

Table 8.3: Summary of gamma pass rate with 3%/3mm tolerance criteria and error detected. The statistical Wilcoxon Signed-Rank test was used to evaluate difference in sensitivity between two dosimetry systems for detecting the delivery error

Error type	Error magnitude	Mean of γ pass rate		(Mean- σ) of γ pass rate		(Mean+ σ) of γ pass rate		p-value (95% CI)
		AC	MAT	AC	MAT	AC	MAT	
No error	0	97.5	95.7	95.1	92.8			
Couch speed (%)	-4	58.7	62.5			72.1	78.5	0.374
	-2.5	73.5	74.1			86.7	87.1	0.678
	2.5	89.6	86.7			95.8	89.8	0.508
	4	80.7	75.5			88.7	87.6	0.173
Jaw width (mm)	-2	72.7	57.4			85.8	69.7	0.096
	-1.5	81.3	72.5			95.8	85.9	0.186
	1.5	63.9	59.9			64.2	71.7	0.441
	2.0	34.1	34			48.1	51.1	0.515
MLC	MLC 32 stuck	24.8	29.3			55.2	53.8	0.443
LOT	MLC 42 stuck	21.8	36.7			50.8	68.9	0.172
	Random 4%	36.3	46.7			71.1	80.3	0.612

AC=ArcCHECK; MAT= MatriXX^{Evolution}

8.4 Discussion

The approach we used in this work was to introduce errors that can occur based on machine malfunction or calibration errors. The effect on clinical dosimetry from the same intentional

introduced errors for the same sets of clinical plans in a patient geometry was quantified in our previous work [303, 304] and is presented in Chapter 7. All the errors introduced in this study to evaluate the detector sensitivity were demonstrated to be compromised the patient dosimetry and hence considered clinically relevant [303, 304]. We did not assess the detector sensitivity for gantry related errors. We demonstrated the gantry start position (GSP) error was least sensitive among all the delivery simulated in our previous work [303, 304]. Moreover, the sensitivity for GSP error for ArcCHECK was investigated in previous work [59] and hence did not consider the GSP error in this work. Regarding the other gantry related error i.e. gantry period (GP), there was a physical limitations on the machine to maintain the same treatment time to that of reference plan, when the GP from the patient calibration procedure is edited. Any change in gantry period error from the patient calibration procedure leads to change in treatment time which is proportional to the magnitude of change in gantry period. Therefore, we could not able to measure the GP delivery error. In this work, we have compared the sensitivity of two commercially available dosimeters MatriXX^{Evolution} and ArcCHECK to detect intentionally introduced clinically relevant delivery errors in jaw width, couch speed and MLC LOT for ten clinical nasopharynx HT treatment plans. The threshold was determined at which these dosimeters are sensitive to particular delivery errors.

Intentional delivery errors in couch speed or jaw width had an impact on overall dose distribution. The resultant dose discrepancy was spread uniformly over the entire treated volume but worse at the superior and inferior ends of the treatment volume. The MatriXX^{Evolution} shows slightly higher sensitivity to both these delivery errors compared to the ArcCHECK (Table 8.2 and 8.3). This could be due to the relatively coarse detector resolution of ArcCHECK (10 mm) compared to MatriXX^{Evolution} (7.62 mm) in the superior-inferior direction. Templeton et al [59] also studied the detector sensitivity of ArcCHECK for intentional delivery errors in couch speed and demonstrated an intentional error of 2.8% in couch speed led to a gamma pass rate $\leq 90\%$ for head and neck cases. Our work found this threshold to be -2.0% to +0.8% determined using linear interpolation from linear fit of the mean gamma pass rate vs error magnitude ($R^2 \geq 0.95$).

Templeton et al [59] did not provide details about complexity and planning parameters used for the head and neck plans used in their study. Therefore it is difficult to compare our results directly with Templeton et al [59]. Templeton et al [59] also reported the increase and decrease of a given parameter of the same magnitude yields similar passing rates. Our results for couch speed and jaw width introduced errors showed the increase and decrease

of a given parameter of the same magnitude yields different gamma pass rates (Table 8.3). Similar trends were observed in the relative change in dose volume histogram metrics in our previous dosimetric simulation work [303]. There were variations in plan complexity within the cohort of clinical plans used in this study even though they were from the same clinical site. This may have contributed to the large variations in gamma pass rates for the same error magnitude (figure 8.1). The factors that determine the clinical plan complexity are treatment plan length, targets off-centred from the machine rotational axis [58, 59], spatial separation between target and organ at risk, institute specific planning protocols. Therefore, it is important that each clinic should evaluate carefully detector sensitivity in detecting delivery errors and understand the limitations of dosimetry systems for their clinical applications and planning protocols. Table 8.4 compares the minimum magnitude of detected error (i.e. threshold) between the two dosimetry systems to the error magnitude that was demonstrated in Chapter 7 to be clinically relevant [303] and the set machine interlock tolerance.

Table 8.4: Comparison of minimum error detection by dosimeters, clinically relevant error magnitude based on dosimetric simulations and machine interlock

Error type	Minimum error detection criteria		Dosimetric based derived clinically relevant errors	Machine interlock tolerance
	MatriXX	ArcCHECK		
Jaw width	-1.5mm and 1mm	-2mm and 1mm	0.5mm	Primary interlock 500 microns and Secondary interlock 1.25mm
Couch speed	$\pm 2.5\%$	3% and 2.5%	2%	Couch position at any point of delivery is differing by 1mm from the planned value
MLC LOT	All errors	All errors	All error	i) Leaf does not begin to move in about 40ms from the time ii) when a leaf does not reach its destination in about 70 ms when a leaf moves past its intended destination

Both of the detectors show similar sensitivity to all the MLC LOT errors that were clinically relevant. A recent study by Fredh et al [58] measured the intentional delivery error plans for RapidArc (Varian Medical Systems, Palo Alto CA) plans. They demonstrated a wide variation of ability to detect the delivery errors when measured with the same error plans and different dosimetry systems. The variation in the ability to detect the delivery errors

between the two dosimetry systems for intentional errors simulated in this study could be associated with a number of factors, including the detector resolution, implementation of gamma reporting within different dosimetry systems, variation in data processing to convert the measured signal to dose, variation in plan complexity and the way the QA plan is prepared. Neilson [299] demonstrated a higher gamma pass rate (by about 3.3%) for the same clinical plan when measured by aligning the high dose volume with the detector plane compared to the QA plan with high dose situated at the centre of the phantom. In this work, we aligned the high dose with the detector plane for consistency while preparing a DQA plan with both dosimetry systems. We also monitored the machine behaviour prior to each measurement session, which was found to be stable and consistent (i.e. machine output was within 0.25% and profile shape measured with a TomoDose detector array was indistinguishable). As illustrated in Table 8.2 and figure 8.1, the sensitivity of error detection for given magnitude error was different when varied in opposite direction (e.g. JW +1mm and JW -1mm). Our previous work [304] had shown the resultant dosimetric impact from intentional JW and CS error for a given magnitude when varied in opposite direction was different for same clinical plans. This is reflected in sensitivity variation of error detection (Table 8.2 and figure 8.1). Typically, the phantom based QA measurements are performed by aligning the detector to high dose region (i.e. high dose PTV). As shown in our previous work [304], the impact on PTV dose variation is not of same magnitude when delivery error of similar magnitude introduced in opposite direction. Therefore, the gamma pass rate and hence the sensitivity of detector would not be similar to same error magnitude when varied in opposite direction.

An ideal dosimeter is one which can detect inconsistencies between planned and delivered dose distributions with a high level of confidence. The type of metric used for the dosimetry system sensitivity analysis has an important role [308]. In this study, the sensitivity of MatriXX^{Evolution} and ArcCHECK was assessed using the gamma analysis method which is widely used in clinical practice to compare the measured and planned dose distributions. In a real situation, the dose measured by a dosimetry system consists of inherent uncertainties from the treatment delivery as well as from inherent limitations of dosimeters [109, 309, 310] (i.e. detector spacing, angular response etc.). In addition to this, the dose calculated by the TPS has its own uncertainties due to limitations in the modelling of the treatment beam [311] and dose computation methods in complex treatment techniques. The combination of these uncertainties that are difficult to isolate. These uncertainties plays an important role in the minimum error that can be detected by the system with sufficient confidence in addition

to plan complexity and robustness to the delivery errors.

8.5 Conclusion

In this work the sensitivity of the MatriXX^{Evolution} and ArcCHECK dosimetry systems in detecting delivery errors that arise from jaw width, couch speed and MLC LOT for clinical nasopharynx plans has been systematically studied. No statistically significant differences ($p > 0.05$ 95% CI) were found in detecting the simulated delivery errors between the MatriXX^{Evolution} and ArcCheck dosimeter systems as indicated by the Wilcoxon Signed–Rank test. Both dosimeters used in the study were able to pick up clinically relevant delivery errors except the ArcCHECK with couch speed up to 2.5% and jaw width up to -1 mm. The evaluation of both detector’s sensitivity for different clinical sites will be studied in future work.

8.6 Acknowledgements and Disclosures

NSW cancer council grant project number 1067566. The authors also acknowledge Accuray Incorporated for providing the research TPS used for this work.

Chapter 9

Clinical implementation of an in-house Exit detector-based dose reconstruction tool for Helical Tomotherapy delivery quality assurance

Statement of joint authorship

S. Deshpande: Development of tool and experimental design, performed experiments, analysed results, wrote manuscript

A.Xing: Development of tool, interpreting results and write up

P. Metcalfe: Assisted in interpreting results and writing, as supervisor he endorses the assessment

L. Holloway and P. Vial: Render advice on the experiment, interpreting results and write up

M. Geurts: Development of tool, interpreting results and write up

[‡]Part of this chapter has been submitted for publication:

S. Deshpande, A.Xing, P.Metcalfe, L.Holloway, P. Vial, Clinical implementation of on board exit detector - a efficient pre-treatment quality assurance tool for Tomotherapy *Medical Physics*, (**Under Review**)

9.1 Introduction

Intensity Modulated Radiation Therapy (IMRT) patient-specific Quality Assurance (QA) is an important component of any IMRT clinical implementation [90], including helical tomotherapy (HT) (Accuray Incorporated, Sunnyvale, CA) [47]. Stringent QA methods are required now more than ever to be confident that the treatment is delivered accurately for each patient due the associated complexity in treatment delivery and dose distribution in modern radiotherapy treatments. Methods to perform IMRT patient-specific QA for HT, also referred to as Delivery Quality Assurance (DQA), commonly include film, ion chamber, and single planar/multi-planar/cylindrical ion chamber or diode arrays [53, 312–314]. The underlying limitations of phantom-based IMRT QA process are i) they are time consuming, ii) their measurement length is limited to approximately 27 cm or below to prevent the exposure of detector electronics, and iii) the phantoms are very heavy to handle. Also, all these detectors exhibit angular response. Some systems rely on inclinometer input for obtaining the instantaneous gantry position information to account the angular response; which cannot be attached to a HT unit due to the lack of gantry head access. This can cause additional measurement uncertainty since the angular response cannot be corrected. Phantom position can also cause measurement variability. Neilson [299] demonstrated a lower gamma pass (about 3.5%) rate reporting for the same clinical plan when measured by aligning the high dose volume with detector plane compared to the QA plan with high dose situated at centre of the phantom in case of ArcCHECK dosimetry system.

HT is a unique delivery method, often tasked with treating long or otherwise large fields such as cranio-spinal irradiation (CSI) [315–318] and total body/marrow/lymphatic irradiations [319, 320]. When performing DQA for long treatment fields using phantoms, the measurement device must be re-positioned multiple times to sample the entire treatment field. Alternatively, multiple films can be used with a custom large phantom [321]. As suggested by European Society for Radiotherapy and Oncology (ESTRO) [322], patient verification should be kept as simple as possible, because QA efforts are proportional to the number of patients. On the other hand, they should be extensive enough to be able to detect errors and problems.

Previous studies demonstrated the lack of correlation between conventional IMRT QA performance metrics (Gamma criteria) and dose errors in anatomic regions-of-interests [262, 323]. Hence, the interpretation of phantom-based QA results based on widely used gamma

criteria alone is difficult and challenging to link between QA results and their clinical significance. Now, few commercial dosimetry QA systems have implemented the dose reconstruction algorithm. These systems utilised the measured dose with conventional verification QA tool and reconstructs the dose inside patient to assess the clinical impact. However, the dose reconstruction algorithms contain significant approximations and their limitations have been demonstrated by recent studies [62, 63].

HT is a dedicated IMRT system with on-board MVCT imaging capability. The on board detector (OBD) consists of an arc-shaped CT xenon detector array located opposite the linear accelerator on a rotating slip-ring gantry. For the purpose of treatment planning dose calculation and optimisation, each rotation is divided into discrete 51 sections called projections. For each projection, each MLC leaf has a unique opening time. Each MLC event during each projection is stored as a sinogram (as delivery instruction). Sinogram is a binary file that contains the data for each projection (fluence or MLC data). The OBD measured fluence data is stored as binary file and can be extracted from the patient archive. Methods for the verification of Multi-Leaf Collimator Leaf Open Time (MLC LOTs) have been reported using the OBD to perform in vivo dose calculation based on dose reconstruction [215, 216, 218, 324]. Some researchers [64, 65] have proposed a DQA procedure that involves applying a simple method to verify the MLC performance as a pre-treatment verification tool using OBD. Pisaturo et al [64] developed a convolution based calculation model to link the leaf control sinogram from the TPS (treatment planning system) to the data acquired by the OBD during a static couch procedure. Dose reconstruction approach using OBD data was demonstrated by Handsfield et al [291] for in vivo dose verification, but used Monte Carlo (MC) based secondary dose calculations which required more computing resource or a longer calculation time as well as extensive validation/benchmarking of the MC model accuracy against previously proven dosimeters prior to implement clinically. Also, Chen et al [218] highlighted challenges with extracting the uncompressed raw projection data as it can take several minutes to transfer the raw data from the HT machine and requires proprietary knowledge of accessing the detector files. None of the previously reported studies, on HT pre-treatment verification [64, 65] utilising OBD did not implemented dose reconstruction.

This work reports on the development of an in-house exit detector based dose reconstruction DQA tool for HT pre-treatment plan verification which is simple, efficient and yet comprehensive to identify MLC LOT errors. Comprehensive validation of this tool for clinical

implementation purposes is presented. This includes: i) sensitivity to intentional MLC LOT error ii) dose reconstruction accuracy iii) Gamma analysis metrics comparison of the exit detector DQA tool versus clinical ArcCHEK DQA methods and iv) an efficiency assessment of the tool compared to the existing clinical DQA method.

9.2 Theory

The OBD response (R) for a given MLC leaf is modelled as a convolution of two components, namely the expected fluence (decomposed into the expected fluence (F) plus a leaf fluence error (E) resulting from the delivery error if any multiplied by an OBD sensitivity S (calibration factor) and a Leaf Spread Function (LSF), plus a background signal (B) as shown in equation 9.1:

$$R = S(F + E) \otimes LSF + B \quad (9.1)$$

The LSF is used to model the MLC penumbra. If the LSF is assumed to be independent of the MLC leaf, the convolution can be reduced to the multiplication of discrete Fourier transforms according to the convolution theorem, as shown in equation 9.2:

$$FT(R - B) = FT[S(F + E)] * FT(LSF) \quad (9.2)$$

The above equation can then be solved for the leaf fluence error E as shown in equation 9.3:

$$E = \left\{ FT^{-1} \left[\frac{FT(R - B)}{FT(LSF)} \right] * \frac{1}{S} \right\} - F \quad (9.3)$$

The parameters S , B and LSF can be determined using the vendor-supplied TomoTherapy Quality Assurance (TQA)[®] daily QA module. The advantage of using this procedure is that it is already delivered every day as part of morning QA. Figure 9.1 displays the measured OBD response for the TQA daily QA module.

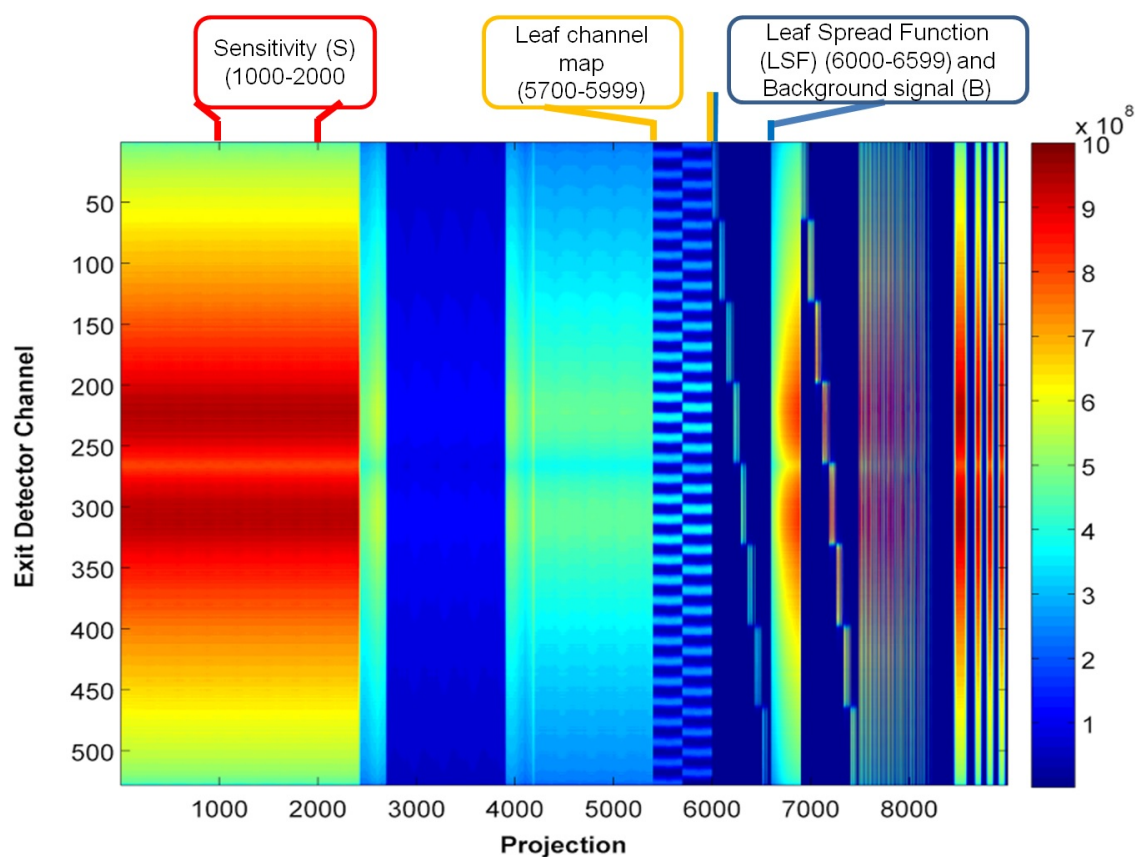


Figure 9.1: Exit detector response from TQA daily QA module. TQA daily QA module comprises of dynamic MLC procedure with varying MLC pattern. Each of the MLC pattern is sequenced to specific projection interval. The exit detector sensitivity (S), leaf to OBD channel, background signals (B), and leaf spread function (LSF) were determined from specific projections interval as shown.

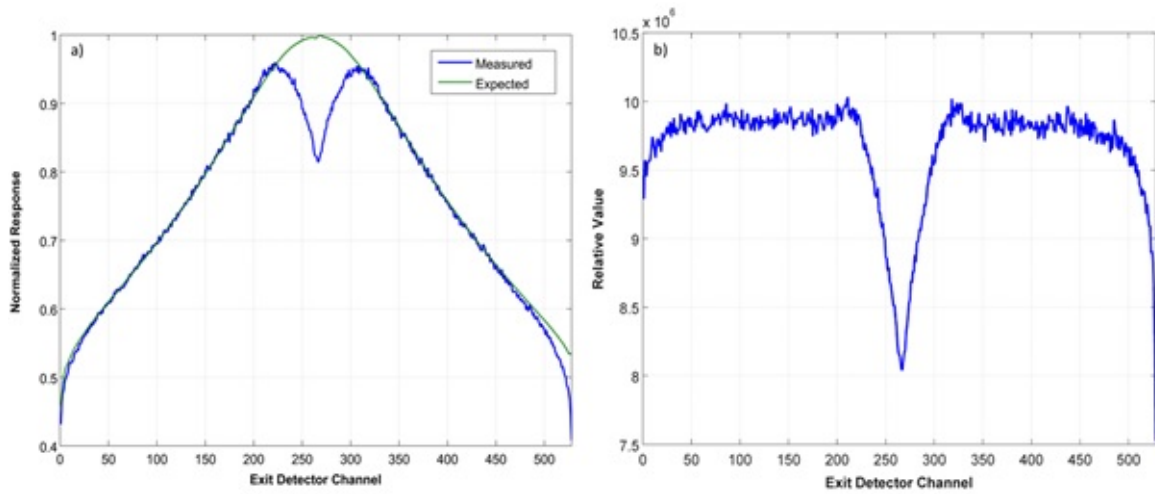


Figure 9.2: Resultant superimposed even and odd leaf detector response from Daily TQA module. For projections between 5400-5699 (only the odd MLC leaves are open) and between projections 5700-5999 (only even leaves are open). This data used to define a map of MLC leaf to the OBD channel that yields the maximum signal

Following sections described how each of these parameters (S, B and LSF) were determined using daily TQA procedure.

9.2.1 OBD Sensitivity (S)

Up through projection 2399 (Figure 9.1, all MLC leaves are open and the jaws are open (-2.4 cm, +2.4 cm), also referred to as J48. By extracting the exit detector channel response between projections 1000-2000 and dividing by the expected fluence distribution for the same field size, the OBD sensitivity (S) can be determined as shown in Figure 9.2

9.2.2 MLC leaf Map

The projections between 5400-5699, only the odd MLC leaves are open, and between projections 5700-5999, only even leaves are open. Figure 9.3a shows the superimposed even and odd leaf profiles as a function of OBD channel number. The maximum signal is used as it is the detector channel most closely aligned to the center the MLC leaf, therefore making its response most strongly correlated to leaf open and closing. Thus, by mapping the exit detector channel that yields the maximum signal i.e. profile peak which corresponds to known MLC leaf number which held open, a MLC leaf map to OBD channel can be established as

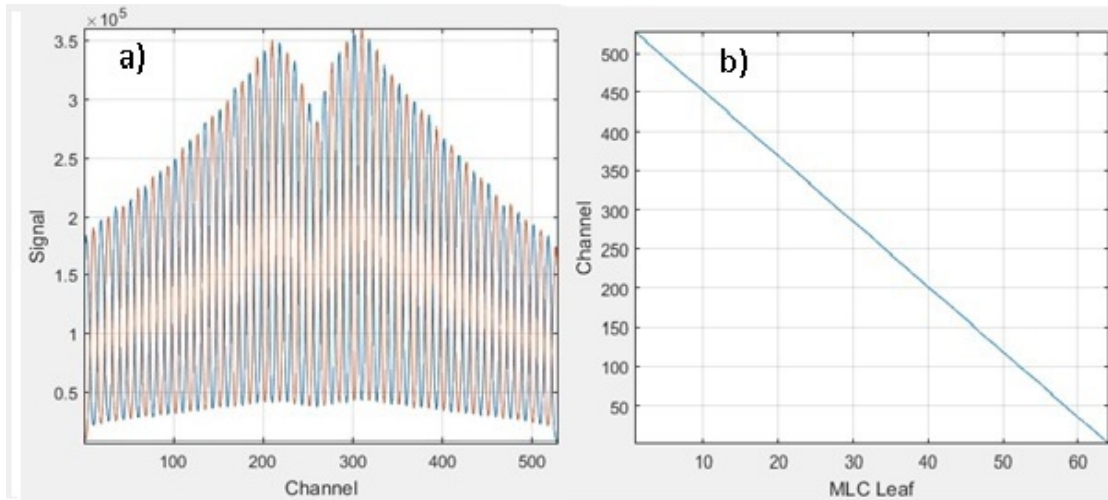


Figure 9.3: Resultant superimposed even and odd leaf detector response from Daily TQA module. For projections between 5400-5699 (only the odd MLC leaves are open) and between projections 5700-5999 (only even leaves are open). The MLC leaf map (b) was established by mapping the OBD channel that yields the maximum signal which corresponds to the known MLC leaf number(i.e. leaf held open).

shown in figure 9.3b. Because the Daily QA procedure includes gantry rotation, this mapping can also be determined as a function of gantry position. However, for simplicity only the mean channel is used in the proposed algorithm. Once a leaf channel map is determined, the signal for each leaf can be extracted from the exit-detector response R .

9.2.3 LSF and background signal (B)

The projection 6000 through 6599, banks are sequentially opened with different amounts of modulation. The modulation was achieved by changing the amount of time each binary leaf held open and the process is iterated for consecutive banks of eight leaves. The LSF is measured by recording the OBD signal for channel corresponding to leaf 26 (which is open), then the OBD signal for channels corresponding to adjacent leaves 10 through 25 (which are closed). The relative signal at each closed leaf is then computed by dividing the OBD signal for each closed leaf by the open leaf. Figure 9.4 shows the measured response for ten adjacent closed leaves. The LSF is considered to be symmetric. Therefore prior to calculating the discrete Fourier Transform, the LSF is mirrored and zero-padded to 64 leaves such that it is the same length as the number of MLC leaves in the measured exit-detector

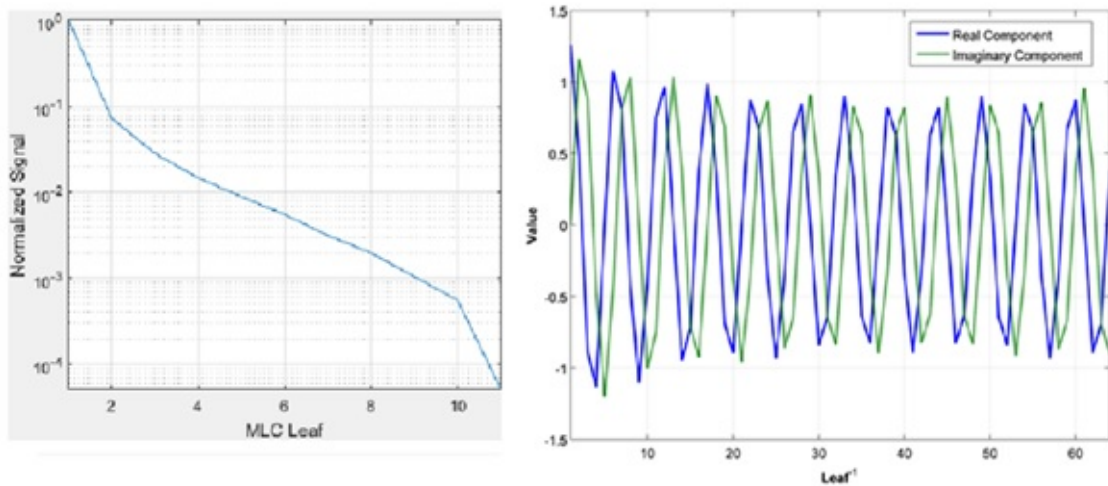


Figure 9.4: Leaf Spread Function (left) was derived using discrete Fourier Transform (right).

response R .

Finally, the background signal B can be determined using the same projections interval as used for LSF determination by measuring the exit detector signal under the closed leaves further away (i.e., greater than ten leaves) from an open leaf. The background signal is comprised of electronics leakage (dark current), radiation leakage through the MLC leaves, and scatter from other parts of the TomoTherapy system.

9.2.4 Planned Fluence Retrieval

Once the TQA Daily QA module exit-detector data has been parsed, the next step is to extract the expected fluence F for the patient plan from the patient archive. The patient archive uses eXtensible Markup Language (XML) to reference all treatment plan data and associated binaries. For each approved treatment plan, there are several variations of the MLC delivery pattern.

The machine agnostic and specific delivery plans are created when the optimized treatment plan is fractionated and approved for delivery on the destination treatment system. As its name suggests, the machine agnostic delivery plan represents the “ideal” fluence after the effects of fractionation, but before MLC-specific corrections are applied, such as leaf latency. The machine specific delivery plan, alternatively, is the set of delivery instructions for a TomoTherapy treatment system, which when delivered, would deliver the expected

fluence contained in the machine agnostic plan. Therefore, for purposes of this analysis the machine agnostic delivery plan is extracted.

The XPath Java™ API library (javax.xml.xpath) is leveraged to read the patient XML into MATLAB. The XPath expression `//fullDeliveryPlanDataArray/fullDeliveryPlanDataArray` is used to identify all delivery plans; subsequently, (Appendix C, Table C.4), lists the XPath sub-expressions and parameters extracted for each delivery plan. Using the above parameters, the binary file of leaf events can be read and converted into a 2D array of relative leaf open times for each MLC leaf and plan projection. The binary file stores each projection as a pair of leaf events; the first event is the time (in tau units, where one tau equals one projection) when the leaf opens, and the second is the time when the leaf closes. Subtracting these two values yields the fraction of a projection that the leaf is planned to be open, while the magnitude of the values (rounded down to an integer) is the projection that the event occurs in.

9.3 Methods and Materials

The TQA daily QA procedure and a static couch DQA of the patient's DQA plan were delivered on the treatment machine with the couch static and out of the bore. There is nothing in the beam path when delivering TQA and DQA. Based on these inputs, a simplified workflow was defined in few steps and illustrated in figure 9.5

The exit detector DQA tool was designed around two commonly available methods for exporting data from the HT system: patient archives and DICOM transit dose export. The latter data export method is not a default option and only available on licence purchase. The tool was developed in MATLAB (MathWorks Incorporated, Natick, MA) and was organized into four modules: i) extraction of OBD data from the static couch DQA procedure and TQA daily QA procedure to de-convolve the OBD signal into a 'measured sinogram' ii) extraction of the planned sinogram from the patient archive and comparison to the measured sinogram to determine differences in each leaf event (projection), iii) application of the differences from each leaf event to the optimized sinogram and recalculation of the dose using the TomoTherapy version 5.0 standalone dose calculator and finally, iv) 3D gamma dose evaluation and dose volume histogram comparison between planned and measured dose. This is discussed in details in following section.

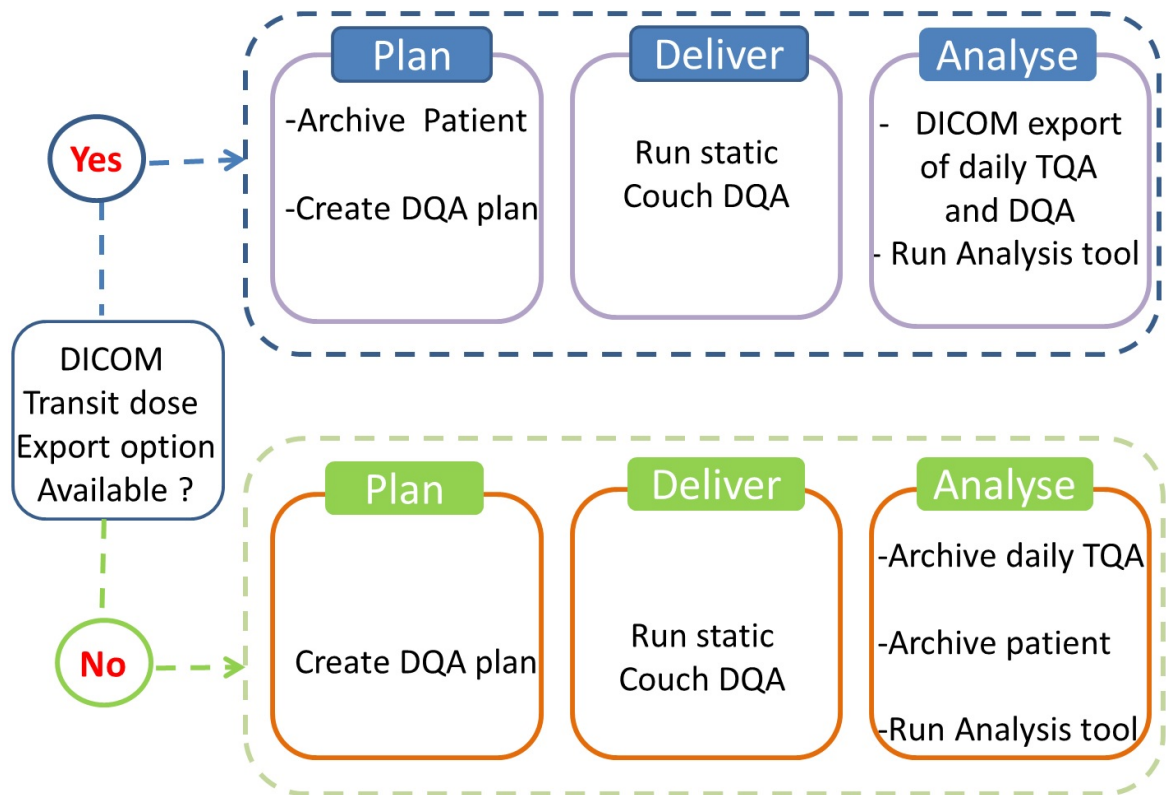


Figure 9.5: Illustration of clinical Workflow for performing exit detector DQA tool using two commonly available methods for exporting data from the HT system. The planned fluence for the analysis was machine agnostic delivery plan which was extracted from the patient archive. The static couch DQA procedure is standard clinical DQA plan executed on treatment machine with couch retracted outside bore and couch remains static while beam is on

9.3.1 Exit detector DQA tool

A brief description about each module's function is outlined in following sections.

9.3.1.1 Sinogram analysis

Once the TQA Daily QA module OBD data is parsed to the exit detector DQA tool, the next step is to retrieve the expected fluence (F) from the patient archive as described in section 9.2.4.

In order to calculate the de-convolved measured fluence, first, the OBD signal for each of the 64 leaves at a given projection is extracted from the sinogram. The OBD signal is then corrected by subtracting the background (B) and channel sensitivity (S). Finally, the de-convolution is calculated (as shown in equation 9.2) by computing the Fourier transform of the corrected OBD signal, dividing that by the Fourier transform of the LSF, then computing the inverse Fourier transform. This is repeated for each projection.

Following this, the fluence error E is computed using equation 9.3. As described in section 9.2.4, the binary file containing planned fluence information stores each projection as a pair of leaf events, by comparing the planned fluence with the measured fluence projection by projection, the difference from each leaf event can be determined.

9.3.1.2 Dose reconstruction

Following the sinogram analysis, the dose reconstruction step is performed using the TomoTherapy version 5.0 standalone dose calculator (Accuray Incorporated, Sunnyvale, CA). The beam model in clinical planning system is different from the beam model used in standalone dose calculator. To mitigate any potential systematic error in dose computation in measured plan from approved clinical plan, the dose calculation is actually performed twice, first without any changes made to the delivery plan leaf events, and subsequently with the fluence error (E) applied to the planned fluence. The former recalculated dose is referred as the 'original planned dose' while the latter is referred as 'adjusted planned dose'. A 3-D dose evaluation is then conducted using 2%/2 mm Gamma index (global) [240] criteria above a dose threshold of 10% for dose comparison. Dose volume histogram is calculated and evaluated from both original planned dose and adjusted planned dose to assess the clin-

ical impact.

9.3.2 Clinical validation

Comprehensive validation of this tool for clinical implementation purposes is presented. Several tests were designed to validate the accuracy and robustness of the exit detector DQA tool. The accuracy of each module of exit detector DQA tool was verified independently as described in following sections.

9.3.2.1 Sinogram analysis accuracy and sensitivity

The vendor supplied plans ('TomoPhant') designed to treat on-axis and off-axis cylindrical targets generated for each commissioned jaw width size on the 'cheese phantom' were used. The 'TomoPhant' treatment plans (1, 3, and 5) with no modification (unmodified) and with intentionally introduced MLC LOT error (modified) plans were used to assess the accuracy and sensitivity of this tool. Four MLC LOT intentional error scenarios were tested: (i) leaf 32 was 'stuck open' (modified to have a leaf open time of 100% for each projection), (ii) leaf 42 was 'stuck open', (iii) all leaves were randomly closed by 2%, and finally (iv) all leaves were randomly closed by 4%. The random MLC LOT errors are introduced using a normal distribution with a mean and standard deviation of -2% and then with a mean and standard deviation of -4%. The leaf open times greater than 100% are not possible to deliver, so were truncated. Each intentional error was introduced independently. A static couch DQA was then run five times, first with the original optimized delivery plan, then once with each intentional modification. The OBD data was extracted for each run and analysed by the tool. First, the original optimised delivery plan was compared with original machine agnostic delivery plan, and next the original optimised plans with the known modification applied (known intentional MLC LOT error) to compare with corresponding modified DQA plans. The original clinical plan recalculated for a given known plan modification (intentional MLC LOT errors) is referred as the '*a priori*' planned dose.

9.3.2.2 Reconstructed dose accuracy

Following the sinogram analysis (for both unmodified and modified 'TomoPhant' as described in section 9.3.2.1), the dose for original clinical plan, the original plan with each '*a priori*' modification and adjusted planned dose from measured static couch DQA was

recalculated using standalone Tomotherapy dose calculator as described in section 9.3.1.2). The accuracy of the adjusted planned dose calculations (dose reconstruction) on the cheese phantom for each plan were verified with ion chamber measurements (Standard Imaging A1SL, Middleton, WI) both in high and low gradient regions. This is equivalent to validate the reconstructed dose inside patient anatomy.

9.3.2.3 Clinical assessment of Exit detector DQA tool versus existing clinical ArcCHECK DQA method

Table 9.1: Summary of clinical plans with varying treatment characteristics for comparing two QA systems.

Clinical site	Number of clinical plans	Percentage MLC LOT time (Mean \pm SD)
Head and Neck	47	49.4 \pm 5.7
Brain	19	48.1 \pm 6.1
Pelvis	29	48.6 \pm 7.1
GI	14	48.1 \pm 4.8
Brain SRS	5	60.2 \pm 12.6
CSI	3	47.2 \pm 8.3
Lymphoma (Hypo-fractionated)	5	47.9 \pm 8.7

Prior to implementing the Exit detector DQA tool, ArcCHECK dosimetry system (Sun Nuclear Corp., Melbourne, FL) was pre-treatment DQA tool to verify clinical plan. Both the proposed exit detector DQA system and ArcCHECK dosimetry system used common 3D dose evaluation metrics (gamma criteria). To demonstrate both QA systems produce a comparable statistics, a similar analysis metrics (2%/2mm global gamma with dose threshold 10%) was used. Table 9.1 summarised the clinical plans having wide range of dosimetric and treatment characteristics were used for comparison. The treatment verification of three CSI plans was not possible with ArcCHECK dosimeter alone due to limited measurement length of dosimeter. In addition, the time taken to perform HT DQA for both methods was also compared to assess the efficiency. The similarity of Gamma pass rate and the efficiency between two DQA methods was tested using Wilcoxon Signed-Rank test.

9.3.2.4 DVH metrics calculation accuracy

To assess the accuracy of reported DVH metrics by exit detector DQA tool, five clinical plans were used. The clinically relevant DVH metrics for five different structures from each clinical plan were independently calculated using in-house Comp Plan tool and compared them to the reported DVH metrics by exit detector DQA tool. The DVH reconstruction code implemented in exit detector DQA tool was different from the in-house code Comp Plan [283] tool.

9.4 Results

9.4.1 Sinogram analysis sensitivity and accuracy

Table 9.2 summarises the sinogram analysis evaluation. The mean MLC LOT error across all leaf events (projection) for both unmodified and modified ‘TomoPhant’ plans are given. The smaller mean MLC LOT error in sinogram analysis evaluation for all unmodified plans validated the ability of the tool to measure the original plan. Similarly lower mean MLC LOT error for the sinogram analysis evaluation for modified plans validates the tool correctly identify the MLC LOT error. In addition, a graphical comparison for the leaf 42 staying open (intentional error) is provided in figure 9.6 demonstrating that the tool correctly identified that leaf was opened and pick up MLC LOT error.

Table 9.2: Mean MLC LOT error \pm standard deviation across all leaf events (projection) determined via sinogram analysis for both unmodified and modified ‘Tomophant’ plan. In the first column, the unmodified plan de-convolved fluence was compared to the planned sinogram. In each remaining column, the de-convolved fluence for each modification was compared to ‘*a priori*’ known modification to the planned fluence.

Plan	Unmodified	Leaf 32 Open	Leaf 42 Open	Random -2%	Random -4%
1	0.24% \pm 1.11	-0.09% \pm 1.03	0.07% \pm 1.64	0.36% \pm 2.46	-0.81% \pm 2.61%
2	-0.26% \pm 1.33	0.10% \pm 1.69	0.34% \pm 2.17	-0.59% \pm 3.31	-0.84% \pm 2.85%
3	-0.60% \pm 1.96	-0.51% \pm 1.45	-0.42% \pm 2.72	-0.60% \pm 2.61	-1.13% \pm 2.41%

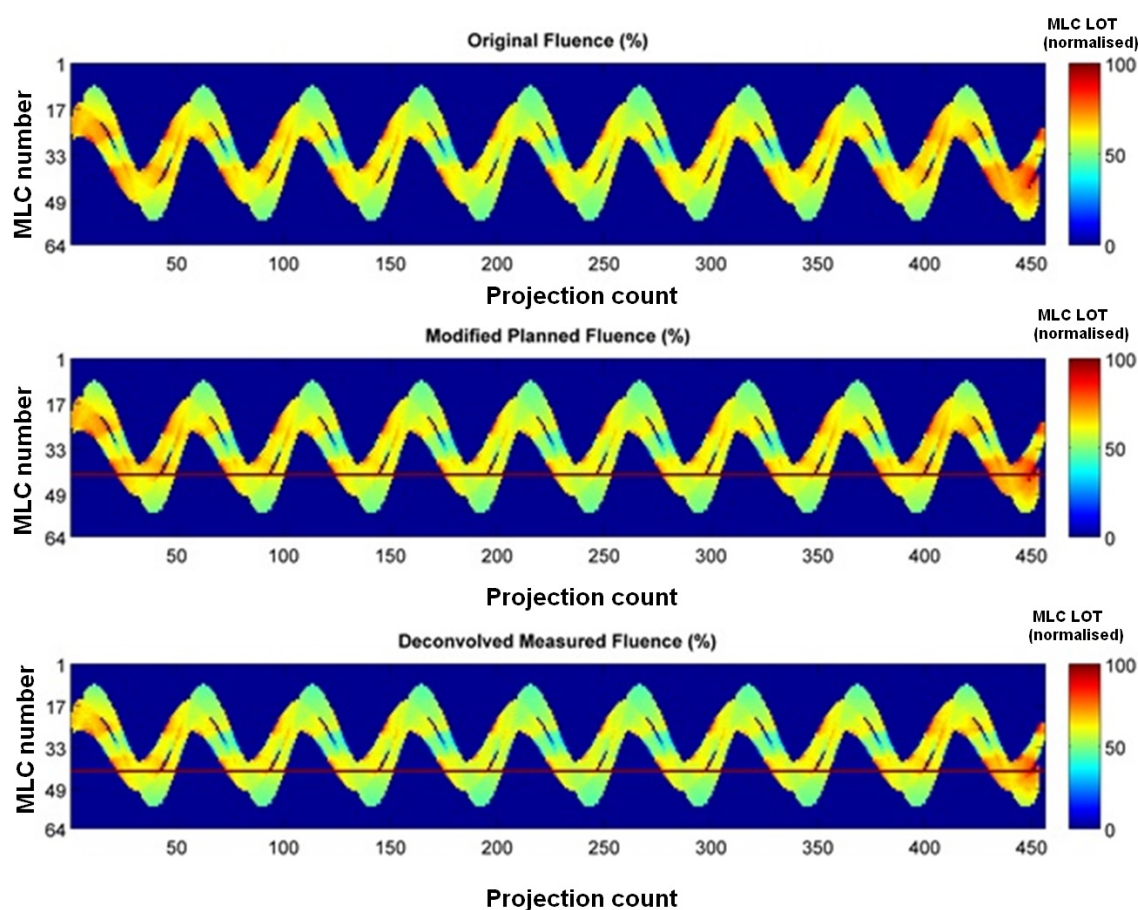


Figure 9.6: Graphical illustration of sinogram (top) extracted from original clinical plan, sinogram (middle) for the original optimised plans with ‘*a priori*’ known modification applied (leaf 42 stuck open) and static couch QA de-convolved measured fluence (bottom) of modified plan with leaf 42 stuck open.

9.4.2 Reconstructed dose accuracy

Table 9.3 presents the gamma pass rate for both unmodified (first column) and modified ‘TomoPhant’ plans (remaining columns). In case of modified plans (*a priori* planned dose versus measured) have shown high gamma pass rate (>95% with 2%/2 mm) indicating that this tool able to track the MLC LOT errors. Table 9.4 summarise the difference between the adjusted planned dose calculated by the exit detector DQA tool with ion chamber measurement for each unmodified ‘TomoPhant’ plan. The close agreement between the independent ion-chamber measured dose and dose calculated by the exit detector DQA tool (<2%) plus gamma pass rate > 95% (with stringent 2%/2mm gamma criteria) for all three unmodified ‘Tomophant’ demonstrates the accurate dose reconstruction of this tool inside patient anatomy.

Table 9.3: Gamma evaluation (2%/2mm) of original planned dose (planned) and adjusted planned dose (measured) computed from both unmodified and modified plans. In the first column, the unmodified adjusted planned dose is compared to the original planned dose. In each remaining column, the adjusted planned dose for each modification is compared to the original planned dose recalculated for the known plan modification (*‘a priori’* planned dose).

Plan	Unmodified	Leaf 32 Open	Leaf 42 Open	Random -2%	Random -4%
1	99.8%	99.1%	99.1	98.9%	97.3%
2	99.7%	98.7%	97.2	98.1%	96.6%
3	99.9%	99.2%	98.6	97.6%	96.8%

Table 9.4: Difference between the adjusted planned dose calculated by the tool and ion chamber measurement at various IEC-x positions along the cheese phantom. Measurement location X= -10.5 cm and X= -1.5 cm are in a low dose gradient region while other positions are in higher dose gradients. Each column represents different ion chamber measurement positions at different IEC-x positions along the mid-plane of the cheese phantom.

Plan	Dose difference between measured (ion chamber) and adjusted dose by tool at various IEC-x positions (cm)					
	X=-10.5 cm	X=-1.5 cm	X=2.0 cm	X=6 cm	X=10.5 cm	X=12 cm
1	-1.49%	0.61%	1.13%	0.16%	1.24%	1.90%
2	-1.50%	0.80%	1.83%	1.67%	1.20%	1.52%
3	-0.81%	1.49%	1.23%	1.26%	0.21%	0.41%

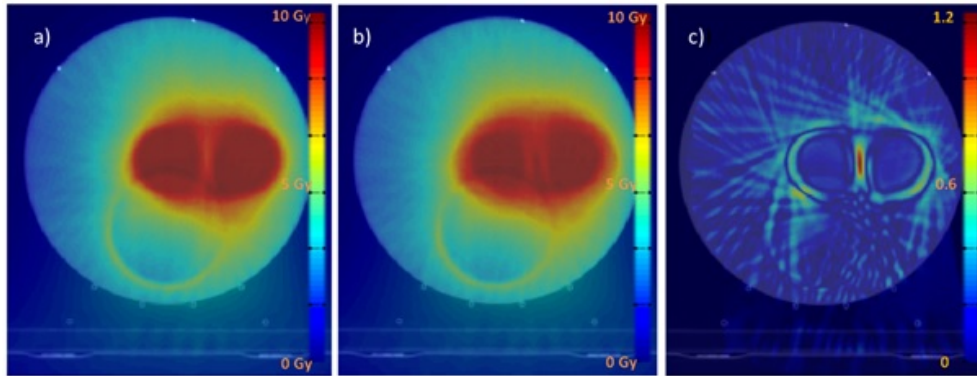


Figure 9.7: Transverse planar doses through the target for Tomophant (plan 1) with leaf 42 held open: a) original planned dose recalculated given known plan modification (*'a priori'* planned dose), b) modified OBD based adjusted dose (*'a posteriori'* adjusted dose) by tool and c) gamma map (2% and 2mm).

Figure 9.7 displays the transverse planar doses through the target for 'TomoPhant' (plan 1) with leaf 42 held open, and the corresponding gamma map. In comparing (a) to (b) in Figure 9.7, there is a slight increase in the penumbra around the target area. This causes the gamma index to be higher in this region between two targets as shown in figure 9.7(c).

9.4.3 Clinical assessment of Exit detector DQA tool versus ArcCHECK DQA method

The average gamma pass rate (2%/2mm) from 119 clinical plans DQA measurements was 94.9 ± 1.5 and 91.9 ± 3.3 for exit detector DQA tool and ArcCHECK phantom based measurements respectively. The Wilcoxon Signed-Rank test indicated a lack of significant difference in gamma pass rate metrics between the two DQA systems ($p=0.868$). It should be noted that the exit detector-based comparison is comparing all voxels greater than set dose threshold (10% of maximum dose), while the ArcCHECK is only comparing the difference at each diode. Therefore, although the differences are not directly comparable, both DQA methods yield similar QA results if a common analysis metrics is used demonstrated similar accuracy.

The time required for performing with exit detector QA tool for 119 conventional clinical plans was 24.7 ± 3.5 minutes compared to 39.5 ± 4.5 minutes (treatment length < 30 cm) for ArcCHECK phantom-based measurements. In particular, the time required to perform DQA with exit detector QA tool for the 3 CSI treatments was 35 ± 3.5 minutes compared to

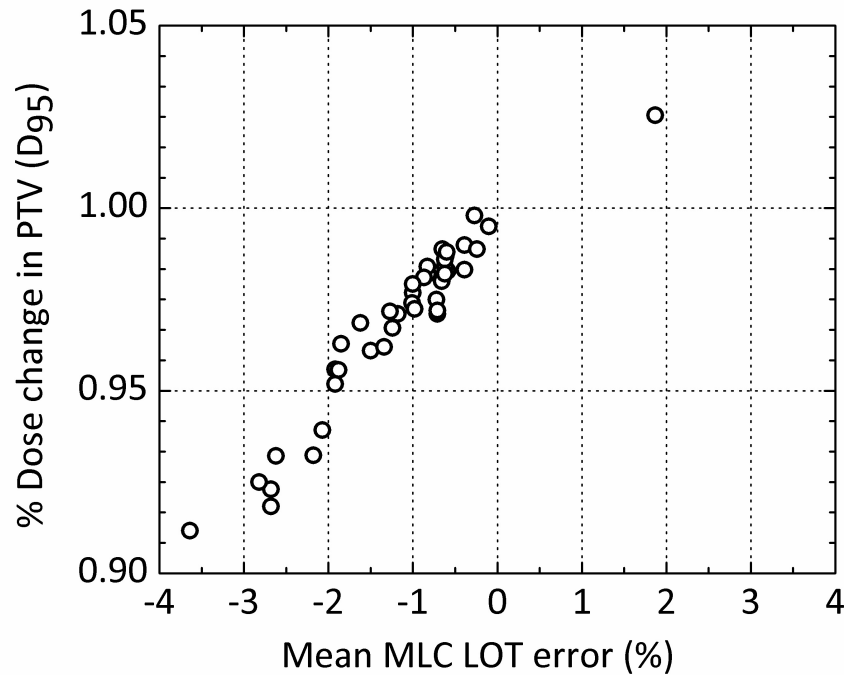


Figure 9.8: The planning target volume (PTV) D_{95} dose error as a function of the mean MLC LOT error (%).

90 ± 5.2 minutes for phantom (film and point dose measurement) based measurement. The exit detector DQA tool demonstrated a significant improvement in efficiency compared to the phantom based DQA method ($p=0.001$, 95% confidence level). The exit detector DQA tool showed significant efficiency gain for all three CSI treatment verification.

Out of 119 clinical plans measured, ArcCHECK phantom based measurements for seven clinical plans indicated a large drop in gamma pass rate when the gamma evaluation criteria was changed from 3%/3mm to 2%/2 mm ($92.4\% \pm 2.5\%$ to $75.5\% \pm 4.5\%$). Following the investigation using exit detector DQA tool sinogram analysis module indicated that larger mean LOT error with lower mean MLC LOT in all these clinical plans. Previous work [284] demonstrated the lower mean LOT yields larger point dose differences between planned and measured dose. The reconstructed dose with our tool also showed larger dose difference in terms of drop in D_{95} of PTV $> 5\%$ which is clinically relevant (figure 9.8) and consistent to previous work [284]. This demonstrates the sensitivity of the tool tracking the planning issues as well as MLC LOT errors that are clinically relevant in addition to time gain to perform patient treatment verification.

9.4.4 DVH metrics calculation accuracy

Table 9.5 illustrates the reported DVH metric accuracy reported by exit detector QA tool when compared with to those calculated independently in-house Comp Plan [283] tool from five clinical plans.

Table 9.5: Comparing the clinically relevant DVH parameter from five clinical reported by exit detector based DQA tool with in-house Comp plan tool. The difference is presented as mean \pm standard deviation (from five clinical plans)

Structure	DVH metrics	Difference in reported dose (Proposed tool vs in-house tool)
PTV	D ₉₅	0.84 ± 0.9
Spinal cord	D _{1cc}	1.1 ± 0.6
Parotid	Mean dosse	0.79 ± 0.9
Mandible	D _{1cc}	1.3 ± 0.9
Brainstem	D _{1cc}	1.1 ± 0.9

9.5 Discussion

This work presents a comprehensive clinical validation of an in-house exit detector-based dose reconstruction tool for HT DQA. We have demonstrated that the algorithm presented here is straightforward and comprehensive to identify the planning issues as well as MLC LOT errors. We also demonstrated that the exit detector based dose reconstruction offers powerful advantages over conventional QA methods to link the DQA results to their clinical significance, particularly for long treatments. In all tests, the tool was able to easily load in the measured data and patient archives and conduct the analysis including dose reconstructions without interruption of clinical workflow as shown in Figure 9.5. The relatively short time needed for this (5-7 minutes), demonstrates the tool is practical for routine clinical use. The static couch DQA is captured by the treatment staff and analysis is performed by physics. Both these tasks can be done in normal working hours, which reduces the physics staff burden of performing after hours pre-treatment QA measurements.

In addition, we demonstrated that the sinogram analysis module accurately identifies several types of MLC LOT errors (Table 9.2). The dose reconstruction accuracy of the algorithm was validated (Table 9.3 and 9.4) with direct measurement for baseline ‘TomoPhant’ plans

by independent ion chamber measurements (absolute dose) as well as 3D gamma criteria comparing planned versus measured (spatially). We noticed the higher gamma index (figure 9.7(c)) in the small gap between the targets, as the low dose in the gap disappears. The added penumbra is caused by the de-convolution's inability to completely remove the effect of leaf scatter. It is a limitation of the currently implemented LSF approximation evaluation method. This effect was exacerbated by the leaf remaining open for all projection, which is an extreme example and unlikely to be of clinical relevance. There is a scope to further improve accuracy in determining the LSF as a subject to future work.

Note that the exit detector DQA tool focuses mainly on MLC leaf differences and their effects on patient dose, and that there are numerous other mechanisms for plan delivery failure. For instance, couch motion and couch/gantry synchronicity are important during HT. However, the authors of TG-148 recommended checking these components quarterly with no expectation that IMRT QA would be sensitive enough to detect issues at the specifications reported in TG-148 for these tests. It is unclear that current DQA system with 3%/3mm gamma criteria, for routine clinical sites such as prostate, lung, or head and neck are sensitive enough to be considered an appropriate mitigation for these issues. The MLC LOT remains the most variable and patient-specific component of an HT treatment plan delivery [284, 324]. Moreover, MLC performance is not recommended as a routine test in AAPM TG-148 and other previous work HT QA [48, 50]. Many centres do not have an access to TQA packages to verify MLC performance hence is not performed routinely by most of the centres. We believe that the improved QA tools (i.e. TQA) available on modern TomoTherapy systems provide efficient and highly effective modules for measuring couch uniformity, jaw motion, and gantry speed, and synchronicity, making it feasible to increase the frequency of testing these components, rather than quarterly as recommended by TG-148.

The Exit detector DQA tool offers a great advantage for treatment verification, especially when the treatments lengths exceed the size of existing commercial QA dosimetry systems. Most phantom-based QA devices that are currently available measured dose to only a few points or on a finite 2D surface (flat or cylindrical) at a coarse resolution. If machine delivery errors result in dose errors beyond the measurement surface, those phantom-based QA methods may not be able to detect them. The OBD measured fluence with higher resolution and therefore increase detection sensitivity to MLC errors compared to external planar or cylindrical detectors arrays. This tool provides comprehensive MLC performance evaluation

of individual leaf differences on a per-plan basis and supplemented with dose distribution. As shown in figure 9.8, exit detector based DQA tool able to detect delivery issues related to MLC LOT and also helps to identify sources of errors such as planning issues (e.g. sub-optimal use of planning parameter). Unfortunately, there is no parameter that can be used during HT plan optimisation to restrict low MLC LOT. These errors or dose discrepancy (as shown in figure 9.8) would not have picked up by phantom-based measurements in case the commonly used 3%/3mm gamma criteria used. This demonstrated sensitivity of this tool over conventional QA methods. The performance of this tool was validated for all possible clinical scenario summarised in Table 9.1 by conducting the serial measurement with ArcCHECK (2%/2mm criteria). The similarity in gamma pass rate reported by these two QA systems indicates that the exit detector based DQA system maintains similar accuracy to that of phantom-based measurements.

There are several inputs that are obtained from a daily QA measurement. In addition to run the daily TQA procedure, an independent daily output measurement is performed using TomoDOSE[®](R) (Sun Nuclear Corp. of Melbourne, FL) which has been demonstrated to pick up machine performance degradation such as energy or output [325]. Also, as a safeguard, the exit detector QA is run on baseline ‘Tomophant’ immediately after the fortnight output constancy measurement with A1SL chamber is performed. This independent QA designed and implemented specifically to monitor the performance of the exit detector based QA tool on a fortnight basis. We also perform image guidance and registration tests as a part of the daily QA which checked the couch movement accuracy. Finally, we presented the clinical results for static jaw procedure only. The proposed tool is also capable for verifying the plans with dynamic jaw procedure; its validation is the subject of future work.

9.5.1 Conclusion

The exit detector tool demonstrated an improved efficiency and sensitivity relative to a conventional phantom-based QA method for HT treatment plan verification. This tool provides comprehensive MLC performance evaluation of individual leaf differences on a per-plan basis and provides an additional insight into the plan by showing the clinical impact of observed discrepancies. This functionality provides a better understanding to assess the DQA failure and the clinical relevance of QA results.

9.5.2 Acknowledgements

The author would like to thank Accuray Incorporated for providing the standalone dose calculator through a valuable research collaboration agreement. The authors have no relevant conflicts of interest to disclose.

Chapter 10

Discussion and Conclusion

10.1 General discussion

The recent rapid pace of development in radiotherapy techniques and the significant increase in the associated complexities, have introduced considerable new challenges to verify treatment accuracy and ensure patient safety. The development of novel detectors for treatment verification still remains an active area of research.

While the EPID's potential as a dosimeter has been well demonstrated [23], there are some technical challenges that still remain unresolved: e.g. i) inconsistent interpretations of standard EPID dose response from previous literature [28, 181–183] ii) challenges of clinical implementation of EPID based in vivo dosimetry in routine clinical practice.

The dose response linearity of standard a-Si EPIDs was evaluated for different combinations of linac, image acquisition settings and imaging data processing methods was investigated and a simple pixel-to-dose calibration method was described and validated in Chapter 3 for step and shoot IMRT delivery. This work contributes to a more consistent understanding and implementation of pixel-to-dose calibration methods for EPID-based IMRT dosimetry.

Ensuring patient safety and treatment accuracy for advanced techniques requires verifying both the target location (i.e. geometry) and the dose delivered to patient. Standard EPID design optimised for imaging applications is problematic for dosimetry due to non-linear energy dependence [25–27, 189, 248]. Previous work on novel EPID design was focused specifically to act as dosimeters rather than imagers [27, 37–39, 326]. In both cases, pro-

posed detectors have not been suitable for applications in both imaging and dosimetry.

Novel, dual-purpose prototypes developed to optimise the EPID detectors for radiotherapy applications were introduced and characterised in Chapters 4 and 5. The dual-purpose prototypes were designed to simultaneously verify both anatomical location and quantity the dose delivered during treatment on conventional linacs. These dual-purpose prototypes maintains water-equivalent dose response. A simple model for transit dosimetry based on a treatment planning system and a water equivalent EPID is presented in chapter 6. WE-EPID does not require a separate EPID model to correct for the complex dose response and hence, provides directly water-equivalent dose image transiting through patient. Clinical TPS provides a water-equivalent dose image at EPID plane (PDI) to compare against the measured transit dose image. Therefore, neither a separate EPID model to correct for the complex dose response nor an independent image prediction algorithm is necessary. The main advantage of this method is that PDI is calculated with the same beam model used for patient dose distribution calculation. Therefore, the model proposed in Chapter 6 provides a simpler and more direct method of performing accurate EPID-based in vivo dosimetry.

The HT system has a unique mechanism to deliver dose to patient. Therefore, a specific understanding is required of the effects of delivery uncertainties to enable the optimisation of methods for resilience to their presence (treatment robustness). Chapter 7 outlined a framework to characterize HT machine delivery errors and their clinical significance. This framework could be applied to any patient dataset to determine a given institution's plan specific delivery error threshold as well as validate plan robustness for a given machine QA tolerance or determine clinically relevant HT QA tolerances.

Treatment verification of HT clinical plans currently relies on phantom-based measurement QA. Different measurement systems have varying ability to reliably identify errors [58]. Chapter 8 outlined a systematic comparative assessment of commercial dosimetry systems sensitivity to detect clinically relevant HT delivery errors. This assessment provides a crucial understanding of the strengths and weaknesses of commercial dosimetry systems.

More efficient QA methods are needed to verify treatments to reduce the increased burden on physics resources due to the additional patient specific QA [60, 61]. The underlying limitations of phantom-based measurement QA are: i) Interpretations of QA results and their clinical relevance and ii) verification of treatment plans larger than the phantom physical

dimensions. Chapter 9 discussed the development and clinical implementation of exit detector DQA tool for HT pre-treatment verification. This tool offered an improved efficiency and sensitivity relative to a conventional phantom-based QA method for HT treatment plan verification. This tool also provides a comprehensive MLC performance evaluation of individual leaf differences on a per-plan basis and offers an advantage to assess the clinical impact of observed discrepancies. This functionality provides a better understanding to assess the DQA failure and the clinical relevance of QA results.

This thesis represents a body of work investigating two different components of treatment verification firstly for a conventional linac and secondly for HT based treatment delivery as outlined in chapter 1:

- (i). Dose characterisation and development of novel EPID based prototypes for treatment verification of a conventional linac system
- (ii). Assessment of current dosimetry systems and development of an on board exit detector based tool for efficient pre-treatment verification for HT delivery

10.1.1 Dose characterisation and development of novel prototype hybrid EPID based dosimeters for treatment verification for a conventional linac system

Research questions:

What are the underlying causes for EPID dose under response at smaller monitor units?

The key reviews [28, 181–185] regarding EPID dose response summarized in chapters 2 and 3, highlighted the inconsistent interpretation of EPID dose response characteristics. Chapter 3 investigated the EPID dose linearity under different combinations of linac, EPID design and acquisition system to understand the underlying causes of EPID under response to dose at small MU.

The measured EPID under response to dose showed good agreement between

static and segmented delivery and persists in both deliveries. This validates previously reported methods of applying the EPID under response to dose correction determined from open static beam exposures on a segment-by-segment basis for IMRT dosimetry [28, 181]. This work also demonstrated the gain ghosting as the dominant cause of EPID non-linear dose response, and how this effect impacts EPID dosimetry of segmental IMRT.

A method of simultaneous measurements with an ICA and EPID was demonstrated to reliably separate out the EPID dose response from beam delivery characteristics. This methodology demonstrated an irregularity in the Siemens acquisition readout scheme, which resulted in poor measurement reproducibility of IMRT fields at small MU per segment. Podesta et al. [221] modelled the discrepancies in Siemens clinical EPID dose response and confirmed that these variations are associated with a problem in the acquisition readout scheme (i.e. missing frames) consistent with the finding of work presented in Chapter 3.

Previous work [28, 181] implemented the ghosting/image lag correction on a pixel by pixel basis in their EPID dosimetry model. A pixel-to-dose calibration method described in Chapter 3 does not require this correction hence simplifying the EPID dosimetry model. This work (Chapter 3) resolves some of the inconsistencies in the literature regarding EPID dose response and proposes a simple yet accurate pixel-to-dose calibration method for EPID-based IMRT dosimetry. Dose linearity for dynamic MLC and VMAT delivery was not investigated, and further work is required to determine the applicability of these results to these dynamic deliveries.

Research questions:

Can the standard EPID design be improved on to provide a superior system for simultaneous geometric and dosimetric treatment verification?

Standard EPIDs are optimised for anatomical imaging but are suboptimal for dosimetry due to non-linear energy dependence [25–27, 189, 248]. Despite the potential, the clinical implementation of EPID dosimetry is still limited to a relatively small number of centres. Several groups have developed the methods

to account for energy response either with complex algorithms or Monte Carlo computations [25, 28–34] to utilise standard EPIDs as a dosimeter. Current research in EPID technology is focused on developing more efficient detectors for imaging using very high density scintillators [35, 247] which are likely to be even more problematic for dosimetry. The previously reported ‘direct EPID’ [27, 37–39, 326] designs demonstrated accurate patient dosimetry but suffered from decreased x-ray detection efficiency thus inhibiting their use for imaging and dosimetry.

Chapters 4 and 5 described development and characterisation of a novel dual detector configuration for treatment verification on a conventional linac. The novel dual detector configurations were modified with the specific goal of improving the dosimetry performance without compromising the imaging performance. Both dual detector configurations combined a conventional EPID (imager) and a 2D array dosimeter.

Excellent agreement in measured dose response ($<1.5\%$) and gamma pass rate ($>94\%$) for all clinical modulated fields was achieved for each of the prototype detectors compared to reference dosimeters in the transit geometry. The water equivalent dose response achieved with each novel prototype detector overcomes a limitation of implementing in vivo dosimetry with current EPIDs.

The imaging performance of both dual detector designs discussed in chapter 4 and 5 was approximately the same as the standard EPID. This demonstrates the dual detector configuration can be operated simultaneously as both imager and dosimeter without significant compromise in the performance of either device. The dual detector design decouples the imaging and dosimetry functions so that each can be optimized without significantly compromising the other, providing more flexibility for future improvements in radiotherapy treatment verification systems.

As a proof-of-concept, both novel prototypes demonstrated simultaneous geometric and dosimetric treatment verification. To utilise these prototypes as a clinical system requires additional engineering considerations, further optimisation, and therefore further research.

Research questions:

Can a water equivalent EPID overcome the current limitations of implementing a-Si EPID based dosimetry in the clinic?

The 2D dosimeter (chapter 4 and 5) within each novel prototype hybrid EPID based systems was demonstrated to maintain water equivalent dose response. Hence, no additional model is required to correct the complex dose response unlike a-Si EPID based dosimetry. A simple model for implementing comprehensive transit dosimetry as a means of in vivo dose verification with a novel prototypes and a conventional TPS was investigated in chapter 6. Excellent agreement was achieved in measured dose response when compared with TPS-calculated portal dose images.

This approach would overcome two complicated steps involved in standard EPID dosimetry models i) modeling the complex dose response [25–27, 189, 248] and ii) calculating the predicted dose image at the EPID plane [23]. The water equivalence of the novel prototype provides a means of directly comparing the measurement to the TPS calculated image dose, for individual patient treatment plans. No additional EPID modelling is required, thereby removing the uncertainty in modelling the complex dose response of standard EPIDs. This would simplify the implementation of EPID based dosimetry in the clinic.

Accurate dose in water algorithms implemented in other commercial TPSs (other than Pinnacle, the one studied here) are likely to have similar success, but would need comprehensive validation. Further development of a back-projection dose calculation method is warranted to facilitate in vivo dose verification in the future.

10.1.2 Assessment of current dosimetry systems and development of an on board exit detector based tool for efficient pre-treatment verification for HT delivery

Research questions:

What magnitude of changes to helical tomotherapy delivery parameters will have a clinical impact on the resulting dose distribution?

Many studies investigated the clinical impact due to changes in delivery parameters for conventional linacs as discussed in Chapter 7. However, the information from these studies cannot be directly translated to HT due to the different delivery mechanism of HT machines. Chapter 7 provides a framework to quantify clinically relevant HT delivery errors.

The work presented in Chapter 7 is the first study investigating the clinical impact due to changes in delivery parameters for HT delivery and provides a framework how clinically meaningful HT QA tolerances can be developed. The recommended AAPM Task Group 148 QA [47] tolerances and machine interlocks were also compared with clinically relevant errors. This framework was also tested on lung SABR plans (since they have different complexity compared to nasopharynx plans) and is presented in Appendix B. The dosimetric QA tolerance derived for both clinical sites were similar except for the gantry related delivery error. This demonstrates the effect of these delivery errors was technique/site specific (Table B.1). The recommended QA tolerances (AAPM Task Group 148) for HT machine were demonstrated to be adequate to prevent clinically relevant HT delivery errors for both lung SABR and nasopharynx plans. This validates the use of a generic HT QA tolerance table as outlined in AAPM Task Group 148 rather than separate plan complexity specific QA tolerance tables as the case for a conventional linac. Most of the clinically relevant errors are prevented by machine interlocks except the couch position and the secondary interlock for jaw position for nasopharynx clinical cases and should be monitored with improved precision.

This work has established a framework to characterize HT machine delivery errors and their clinical significance. This framework could be applied to any patient dataset to determine a given institutions plan specific delivery error threshold as well as validate plan robustness for a given machine QA tolerance or determine clinically relevant HT QA tolerances. This work can be extended to additional error modes and other treatment techniques/anatomical sites in the future.

Research questions:

Are the available commercial dosimeters sensitive to clinically relevant delivery errors for helical tomotherapy?

The systematic comparative assessment of sensitivity for MatriXX^{Evolution} and ArcCHECK to detect clinically relevant HT delivery errors were assessed and discussed in chapter 8. By altering the jaw width, couch speed and MLC LOT delivery parameters, failure modes were simulated and tested independently for the same ten nasopharynx clinical plans used for dosimetric simulation in chapter 7.

Templeton et al [59] also studied the detector sensitivity of ArcCHECK for intentional delivery errors in couch speed and demonstrated an intentional error up to 2.8% in couch speed led to a decrease in gamma pass rate to < 90% for head and neck cases. This threshold was -1.5% to +2.5% for couch speed error. However, Templeton et al [59] did not provide details about complexity and planning parameters used for the head and neck plans in their study, therefore it is difficult to compare our results directly.

Templeton et al [59] also reported that the increase or decrease of a given parameter by the same magnitude yields similar passing rates. On the contrary, our results for couch speed and jaw width introduced errors showed the increase or decrease of a given parameter by the same magnitude yields different gamma pass rates. Similar trends were observed in the relative change in dose volume histogram metrics reported in previous dosimetric simulation work [303] and discussed in Chapter 7, consistent with measurements for both dosimetry systems investigated here.

The Wilcoxon signed rank test indicated that no statistically significant differences were found in detecting the simulated delivery errors between these two dosimetry systems ($p \gg 0.05$, 95% confidence level). Both dosimeters were able to pick up clinically relevant delivery errors except the ArcCHECK with couch speed up to 2.5% and jaw width up to -1 mm. The MatriXX^{Evolution} showed slightly higher sensitivity to couch speed and jaw width delivery errors com-

pared to the ArcCHECK. This could be due to the relatively coarse detector resolution of ArcCHECK (10 mm) compared to MatriXX^{Evolution} (7.62 mm) in the superior-inferior direction.

This work evaluates the two commercial dosimetry system's sensitivity to detect clinically relevant delivery errors as well as their inherent limitations for a clinical site. This work provides a framework to evaluate the sensitivity of a detector to identify the delivery errors for HT treatment. The evaluation of the sensitivity of these commercial detectors for different clinical sites for HT treatments warrants future work.

Research questions:

Can the on board exit detector system achieve equivalent or improved sensitivity, robustness and efficiency compared to the current standard phantom based measurement for HT pre-treatment verification?

An in-house exit detector DQA tool was developed to analyse HT treatment plans and perform dose reconstruction to compare to the optimized patient dose. The comprehensive clinical implementation and validation of the tool is discussed in chapter 9. Excellent agreement was found in the gamma pass rate > 95% between the planned and reconstructed dose using this tool. The close agreement of measured ion chamber (<1.5%) to reconstructed dose computed by the exit detector DQA tool on the 'cheese phantom' validated the accuracy of dose reconstruction inside the patient. The mean time for performing DQA on the 119 clinical plans was 24.7 ± 3.5 minutes and 39.5 ± 4.5 minutes for the exit detector DQA tool demonstrated efficiency. The sensitivity to detect MLC errors was demonstrated.

The exit detector DQA tool offers a direct and comprehensive solution with the opportunity to visualize the clinical significance of MLC delivery errors. This tool offers powerful advantages for supplementing existing patient specific DQA with specific advantages for patient cases where the field delivery geometry exceed the size of the commercial dosimetry measurement systems. The development of this tool has addressed some of the limitations of phantom-

based measurement QA. The significant gain in efficiency of performing HT QA reduced the additional burden on physics resources in our local implementation.

10.2 Implementation of this work within a clinical environment

Some of the research presented in this dissertation has been adopted in local clinical practice. Positive clinical outcomes include:

(i) The pixel-to-dose calibration at 20 MU method discussed in chapter 3 has been implemented locally at the Liverpool Hospital-Cancer Therapy Centre as an EPID dosimetry model since 2013 [327].

(ii) The clinically relevant HT QA tolerance derived from framework discussed in Chapter 7 were adopted as clinical QA tolerances in department's QA protocol since June 2014.

(iii) The in-house exit DQA tool discussed in Chapter 9 for HT pre-treatment verification has been implemented locally at the Liverpool Hospital-Cancer Therapy Centre since August 2015.

To implement this work in routine clinical practice involves extensive documentation and staff training. Additional QA checks to assess the performance of this tool also requires additional QA time.

10.3 Future work

From the topics presented in this thesis there are a number of issues that justify further investigation, including:

(i) Further optimisation of novel prototype hybrid EPID based dosimeters

- (ii) Clinical implementation of the novel prototype hybrid EPID based dosimeters for in vivo dosimetry.
- (iii) Assessment of the clinical impact due to changes in HT delivery parameters for additional clinical sites and plan techniques
- (iv) Develop the HT exit detector DQA tool for generalised use

10.3.1 Optimisation of novel prototype hybrid EPID based dosimeters

Novel prototypes discussed in chapter 4 and 5 demonstrated their capability of performing two measures of treatment verification, imaging (geometric) and dosimetry (dosimetric) as a single system.

a) Novel prototype (EPID and ICA configuration)

For the dual detector design discussed in chapter 4, the following issues warrant further investigation

The engineering requirements of the mechanical support and the configuration of electronics and data readout schemes for both dual detector configuration discussed in chapter 4, the following issues warrant further investigation:

- (i) Develop a larger detection area ($40 \times 40 \text{ cm}^2$) and smaller detector spacing ($\leq 5\text{mm}$) for higher resolution dosimetry in modulated fields
- (ii) A higher signal to noise ratio for the ICA detector would also be desirable for use in the transit dosimetry setting
- (iii) Investigate the dose response characterisation of the next generation of MV imagers (when available)
- (iv) Optimisation of backscatter thickness

b) Novel prototype (EPID and MP configuration)

For the dual detector design discussed in Chapter 5, the following issues warrant further investigation

- (i) Develop a larger detection area ($40 \times 40 \text{ cm}^2$) and smaller detector spacing ($\leq 5\text{mm}$) on the dose detector (MP) for higher resolution dosimetry in modulated fields
- (ii) Investigate the optimal build up for dosimetry for beam energies $> 6 \text{ MV}$ without compromising the imaging performance.
- (iii) The use of novel prototypes under clinical applications such as moving target dosimetry, FFF beams; MLC/couch tracking needs further research.

10.3.2 Clinical implementation of EPID based prototype for in vivo dosimetry.

The framework for the clinical implementation of in vivo dose verification presented in chapter 6 utilising EPID based prototypes and a commercial TPS involves a number of steps. These steps should be integrated and automated to make this tool efficient and user friendly. The framework was validated for the Pinnacle treatment planning system only. The accuracy of the dose algorithm to calculate dose at the EPID plane for other planning systems needs further evaluation. The framework was validated with beams at orthogonal gantry angles only. Further work is therefore required to develop a process for extracting TPS-calculated doses at the EPID plane for beams and control points at all gantry angles similar to presented in previous work [264]. Similar to previously reported investigations [30, 198], the dose calculation algorithm should be implemented in order to calculate the dose inside the patient from the measured EPID dose on the planned CT data or treatment verification cone beam data. This approach provides the direct link between the treatment verification QA results and the clinical impact.

10.3.3 Assess the clinical impact due to changes in HT delivery parameter for additional clinical sites and planning techniques

The dosimetric simulation framework presented in chapter 8 can be extended to additional error modes and other treatment techniques/anatomical sites. To improve the efficiency for simulating the errors, all steps should be automated. The flexibility to incorporate the actual delivery parameter (such as actual delivery parameter from log files or from routine QA data base) needs further research to verify the robustness of the clinical plan or on newly implemented techniques. The sensitivity of all dosimetry systems to detect the clinically relevant delivery errors for specific treatment site/techniques should be assessed to gain confidence on pre-treatment QA. Such evaluation on sensitivity of different dosimetry systems provides an improved understanding of their strengths and limitations for individual clinical situations. Such an understanding also provides useful guidelines for the choice of the most appropriate dosimetry system to implement complex treatment techniques safer.

10.3.4 Develop the HT exit detector DQA tool for generalised use

The dose calculation on patient CT data requires a standalone tomotherapy research planning system. To generalise the utility of the tool, further development on a separate dose calculation engine [328] is warranted. Currently this tool calculates the dose on planned CT data. Further refinement of this tool is warranted to accommodate the dose calculations on MVCT images with other delivery parameters such as jaw width, couch speed etc (derived from log file) to assess overall impact on patient dosimetry.

10.4 Summary

This thesis dissertation investigated treatment verification for two different radiotherapy delivery systems. The first part of the thesis focused on improving EPID dosimetry on conventional linacs. This included improving the understanding of EPID dose response characteristics, and the development of novel prototypes that featured separate imaging systems for anatomical imaging and

dosimetric imaging.

The systematic investigation of standard EPID dose response demonstrated the gain ghosting as the dominant cause of EPID non-linear dose response, and how this effect impacts EPID dosimetry of segmental IMRT. The ghosting/image lag correction suggested in previous studies is complex to implement accurately on a pixel-by-pixel basis for EPID dosimetry. A much simpler pixel-to-dose calibration method was described and validated in chapter 3. This work also contributes to a more consistent understanding and implementation of pixel-to-dose calibration methods for EPID-based IMRT dosimetry.

Novel prototypes were introduced and characterised. These novel prototypes demonstrated for the first time the capability to simultaneously verify both location and quantity of the dose delivered during treatment on conventional linacs. No reduction in patient throughput is expected as the integration of EPIDs and daily imaging is already routine. The clinical implementation of the new prototypes promises to be highly cost-effective. The novel dual detector concept which decouples the imaging and dosimetry functions so that each can be optimised without significantly compromising the other, potentially provides more flexibility for future improvements in radiotherapy treatment verification systems (chapters 4 and 5). The water equivalent dose response of prototypes provides an accurate method to directly verify doses delivered during treatment without the additional uncertainties inherent in modelling the complex dose response of standard EPIDs. An approach to transit dose verification was presented in chapter 6 utilising a water equivalent EPID and a commercial TPS dose in water model. This approach would overcome two complicated steps involved in standard EPID dosimetry model i) modeling the complex dose response and ii) calculating the predicted dose image at the EPID plane and thereby simplify the implementation of EPID based dosimetry as routine practice across the wider community and clinics. The novel prototypes will benefit radiotherapy patients by reducing the risk of mistreatments and ensuring the accuracy of treatment with a new level of precision and confidence.

The second part of the thesis focused on treatment verification of the HT treatment delivery system. A framework to quantify clinically relevant HT delivery

errors was developed and described. Understanding the effect of delivery uncertainty enables the optimisation of planning protocols and validates planning protocol robustness for a given machine parameter QA tolerance.

The systematic comparative assessment of sensitivity for two commercial dosimeters to detect clinically relevant HT errors was presented. This assessment provides a crucial understanding of the strengths and weaknesses of commercial dosimetry systems and provides guidelines for choice of the most appropriate dosimeter for individual clinical situations. It will also inform future direction for improvement to next generation novel detector developments.

An in-house on board exit dosimetry DQA tool for HT pre-treatment QA was developed and demonstrated to be accurate and efficient. The ability of dose reconstructions provides an opportunity to understand the clinical relevance of QA results which helps the physicist and radiation oncologist to make well informed decisions. This tool significantly reduce the normally increased burden on physics resources for performing patient QA and overcomes limitations of current commercial dosimeters for verifying field delivery geometries exceeding the size of the commercial dosimetry measurement systems. This tool provides in depth analysis on a leaf-by-leaf basis which improves the understanding and interpretations of QA failure results for complex HT delivery.

It is hoped this project will benefit radiotherapy patients by reducing the risk of mistreatments and ensuring the accuracy of treatment with a new level of precision and confidence. The improved level of treatment verification will facilitate a safer and more efficient implementation of other new techniques.

Bibliography

- [1] J. Thariat, J.-M. Hannoun-Levi, A. S. Myint, T. Vuong, and J.-P. Gérard, “Past, present, and future of radiotherapy for the benefit of patients,” *Nature Reviews Clinical Oncology*, vol. 10, no. 1, pp. 52–60, 2013.
- [2] C. M. Nutting, J. P. Morden, K. J. Harrington, T. G. Urbano, S. A. Bhide, C. Clark, E. A. Miles, A. B. Miah, K. Newbold, and M. Tanay, “Parotid-sparing intensity modulated versus conventional radiotherapy in head and neck cancer (parsport): a phase 3 multicentre randomised controlled trial,” *The Lancet Oncology*, vol. 12, no. 2, pp. 127–136, 2011.
- [3] C. Haasbeek, D. Palma, O. Visser, F. Lagerwaard, B. Slotman, and S. Senan, “Early-stage lung cancer in elderly patients: a population-based study of changes in treatment patterns and survival in the netherlands,” *Annals of Oncology*, vol. 23, no. 10, pp. 2743–2747, 2012.
- [4] W. A. Hall, L. Colbert, D. Nickleach, J. Shelton, D. M. Marcus, J. Switchenko, P. J. Rossi, K. Godette, S. Cooper, and A. B. Jani, “Reduced acute toxicity associated with the use of volumetric modulated arc therapy for the treatment of adenocarcinoma of the prostate,” *Practical Radiation Oncology*, vol. 3, no. 4, pp. e157–e164, 2013.
- [5] M. Zelefsky, S. Leibel, P. Gaudin, G. Kutcher, N. Fleshner, E. Venkatramen, V. Reuter, W. Fair, C. C. Ling, and Z. Fuks, “Dose escalation with three-dimensional conformal radiation therapy affects the outcome in prostate cancer,” *International Journal of Radiation Oncology* Biology* Physics*, vol. 41, no. 3, pp. 491–500, 1998.
- [6] M. J. Zelefsky, X. Pei, J. F. Chou, M. Schechter, M. Kollmeier, B. Cox, Y. Yamada, A. Fidaleo, D. Sperling, L. Happersett, *et al.*, “Dose escalation for prostate cancer radiotherapy: predictors of long-term biochemical tumor control and distant metastases-free survival outcomes,” *European Urology*, vol. 60, no. 6, pp. 1133–1139, 2011.

- [7] Q. Wu, M. Manning, R. Schmidt-Ullrich, and R. Mohan, "The potential for sparing of parotids and escalation of biologically effective dose with intensity-modulated radiation treatments of head and neck cancers: a treatment design study," *International Journal of Radiation Oncology* Biology* Physics*, vol. 46, no. 1, pp. 195–205, 2000.
- [8] N. Anderson, C. Lawford, V. Khoo, M. Rolfo, D. L. Joon, and M. Wada, "Improved normal tissue sparing in head and neck radiotherapy using biological cost function based-imrt," *Technology in Cancer Research & Treatment*, vol. 10, no. 6, pp. 575–583, 2011.
- [9] S. Milker-Zabel, A. Zabel, C. Thilmann, W. Schlegel, M. Wannenmacher, and J. Debus, "Clinical results of retreatment of vertebral bone metastases by stereotactic conformal radiotherapy and intensity-modulated radiotherapy," *International Journal of Radiation Oncology* Biology* Physics*, vol. 55, no. 1, pp. 162–167, 2003.
- [10] T. Ebara, N. Tanio, T. Etoh, I. Shichi, A. Honda, and N. Nakajima, "Palliative re-irradiation for in-field recurrence after definitive radiotherapy in patients with primary lung cancer," *Anticancer Research*, vol. 27, no. 1B, pp. 531–534, 2007.
- [11] N. Lee, K. Chan, J. E. Bekelman, J. Zhung, J. Mechalakos, A. Narayana, S. Wolden, E. S. Venkatraman, D. Pfister, D. Kraus, *et al.*, "Salvage re-irradiation for recurrent head and neck cancer," *International Journal of Radiation Oncology* Biology* Physics*, vol. 68, no. 3, pp. 731–740, 2007.
- [12] S. Derreumaux, C. Etard, C. Huet, F. Trompier, I. Clairand, J.-F. Bottollier-Depois, B. Aubert, and P. Gourmelon, "Lessons from recent accidents in radiation therapy in france," *Radiation Protection Dosimetry*, vol. 131, no. 1, pp. 130–135, 2008.
- [13] *Prescribing, Recording, and Reporting Photon-Beam Intensity-Modulated Radiation Therapy (IMRT)*. ICRP, 2010.
- [14] L. Donaldson, "Radiotherapy risk profile, technical manual," *Geneva, Switzerland: World Health Organization*, 2008.
- [15] "The royal college of radiologists, society and college of radiographers, institute of physics and engineering in medicine, national patient safety agency, british institute of radiology 2008 Towards Safer Radiotherapy, London: The Royal College of Radiologists."

- [16] E. D. Yorke, *Dosimetric uncertainties and normal tissue tolerance*, book section 1. Uncertainties in External Beam Radiation Therapy, Madison, WI: Medical Physics Publishing, 2011.
- [17] C. K. Glide-Hurst and I. J. Chetty, “Improving radiotherapy planning, delivery accuracy, and normal tissue sparing using cutting edge technologies,” *Journal of Thoracic Disease*, vol. 6, no. 4, pp. 303–318, 2014.
- [18] H. Abbas, B. Chang, and Z. J. Chen, “Motion management in gastrointestinal cancers,” *Journal of Gastrointestinal Oncology*, vol. 5, no. 3, pp. 223–235, 2014.
- [19] P. R. Poulsen, B. Cho, A. Sawant, D. Ruan, and P. J. Keall, “Dynamic mlc tracking of moving targets with a single kv imager for 3d conformal and imrt treatments,” *Acta Oncologica*, vol. 49, no. 7, pp. 1092–1100, 2010.
- [20] W. D D’Souza, S. A. Naqvi, and X. Y. Cedric, “Real-time intra-fraction-motion tracking using the treatment couch: a feasibility study,” *Physics in Medicine and Biology*, vol. 50, no. 17, p. 4021, 2005.
- [21] P. J. Keall, J. A. Ng, R. O’Brien, E. Colvill, C.-Y. Huang, P. R. Poulsen, W. Fledelius, P. Juneja, E. Simpson, L. Bell, *et al.*, “The first clinical treatment with kilovoltage intrafraction monitoring (kim): A real-time image guidance method,” *Medical Physics*, vol. 42, no. 1, pp. 354–358, 2015.
- [22] S. Arumugam, M. Sidhom, A. Xing, and L. Holloway, “An online x-ray based position validation system for prostate hypofractionated radiotherapy,” *Medical Physics*, vol. 43, no. 2, pp. 961–974, 2016.
- [23] W. van Elmpt, L. McDermott, S. Nijsten, M. Wendling, P. Lambin, and B. Mijnheer, “A literature review of electronic portal imaging for radiotherapy dosimetry,” *Radiotherapy and Oncology*, vol. 88, no. 3, pp. 289–309, 2008.
- [24] F. Cremers, T. Frenzel, C. Kausch, D. Albers, T. Schönborn, and R. Schmidt, “Performance of electronic portal imaging devices (epids) used in radiotherapy: image quality and dose measurements,” *Medical Physics*, vol. 31, no. 5, pp. 985–996, 2004.
- [25] K. Luchka and S. Pistorius, “Dosimetric investigation and portal dose image prediction using an amorphous silicon electronic portal imaging device,” *Medical Physics*, vol. 28, no. 6, pp. 911–924, 2001.

- [26] C. Kirkby and R. Sloboda, "Consequences of the spectral response of an a-si epid and implications for dosimetric calibration," *Medical Physics*, vol. 32, no. 8, pp. 2649–2658, 2005.
- [27] M. Partridge, B.-M. Hesse, and L. Müller, "A performance comparison of direct-and indirect-detection flat-panel imagers," *Nuclear Instruments and Methods in Physics Research*, vol. 484, no. 1, pp. 351–363, 2002.
- [28] S. Nijsten, W. Van Elmpt, M. Jacobs, B. Mijnheer, A. Dekker, P. Lambin, and A. Minken, "A global calibration model for a-si epids used for transit dosimetry," *Medical Physics*, vol. 34, no. 10, pp. 3872–3884, 2007.
- [29] M. Wendling, R. J. Louwe, L. N. McDermott, J.-J. Sonke, M. van Herk, and B. J. Mijnheer, "Accurate two-dimensional imrt verification using a back-projection epid dosimetry method," *Medical Physics*, vol. 33, no. 2, pp. 259–273, 2006.
- [30] M. Wendling, L. N. McDermott, A. Mans, J.-J. Sonke, M. van Herk, and B. J. Mi-jnheer, "A simple backprojection algorithm for 3d in vivo epid dosimetry of imrt treatments," *Medical Physics*, vol. 36, no. 7, pp. 3310–3321, 2009.
- [31] P. B. Greer, P. Vial, L. Oliver, and C. Baldock, "Experimental investigation of the response of an amorphous silicon epid to intensity modulated radiotherapy beams," *Medical Physics*, vol. 34, no. 11, pp. 4389–4398, 2007.
- [32] B. Warkentin, S. Steciw, S. Rathee, and B. Fallone, "Dosimetric imrt verification with a flat-panel epid," *Medical Physics*, vol. 30, no. 12, pp. 3143–3155, 2003.
- [33] J. V. Siebers, J. O. Kim, L. Ko, P. J. Keall, and R. Mohan, "Monte carlo computation of dosimetric amorphous silicon electronic portal images," *Medical Physics*, vol. 31, no. 7, pp. 2135–2146, 2004.
- [34] P. Chin, E. Spezi, and D. Lewis, "Monte carlo simulation of portal dosimetry on a rectilinear voxel geometry: a variable gantry angle solution," *Physics in Medicine and Biology*, vol. 48, no. 16, p. N231, 2003.
- [35] A. Sawant, H. Zeman, S. Samant, G. Lovhoiden, B. Weinberg, and F. DiBianca, "Theoretical analysis and experimental evaluation of a csi (tl) based electronic portal imaging system," *Medical Physics*, vol. 29, no. 6, pp. 1042–1053, 2002.

- [36] A. Sawant, L. E. Antonuk, Y. El-Mohri, Q. Zhao, Y. Wang, Y. Li, H. Du, and L. Perna, "Segmented crystalline scintillators: Empirical and theoretical investigation of a high quantum efficiency epid based on an initial engineering prototype csi (tl) detector," *Medical Physics*, vol. 33, no. 4, pp. 1053–1066, 2006.
- [37] Y. Chen, J. M. Moran, D. A. Roberts, Y. El-Mohri, L. E. Antonuk, and B. A. Fraass, "Performance of a direct-detection active matrix flat panel dosimeter (amfpd) for imrt measurements," *Medical Physics*, vol. 34, no. 12, pp. 4911–4922, 2007.
- [38] P. Vial, P. B. Greer, L. Oliver, and C. Baldock, "Initial evaluation of a commercial epid modified to a novel direct-detection configuration for radiotherapy dosimetry," *Medical Physics*, vol. 35, no. 10, pp. 4362–4374, 2008.
- [39] M. Sabet, P. Rowshanfarzad, P. Vial, F. W. Menk, and P. B. Greer, "Transit dosimetry in imrt with an a-si epid in direct detection configuration," *Physics in Medicine and Biology*, vol. 57, no. 15, p. N295, 2012.
- [40] S. J. Blake, A. L. McNamara, S. Deshpande, L. Holloway, P. B. Greer, Z. Kuncic, and P. Vial, "Characterization of a novel epid designed for simultaneous imaging and dose verification in radiotherapy," *Medical Physics*, vol. 40, no. 9, pp. 091902(1–11), 2013.
- [41] G. Mu, E. Ludlum, and P. Xia, "Impact of mlc leaf position errors on simple and complex imrt plans for head and neck cancer," *Physics in Medicine and Biology*, vol. 53, no. 1, p. 77, 2007.
- [42] M. Oliver, K. Bush, S. Zavgorodni, W. Ansbacher, and W. A. Beckham, "Understanding the impact of rapidarc therapy delivery errors for prostate cancer," *Journal of Applied Clinical Medical Physics*, vol. 12, no. 3, 2011.
- [43] M. Oliver, I. Gagne, K. Bush, S. Zavgorodni, W. Ansbacher, and W. Beckham, "Clinical significance of multi-leaf collimator positional errors for volumetric modulated arc therapy," *Radiotherapy and Oncology*, vol. 97, no. 3, pp. 554–560, 2010.
- [44] H. Parsai, P. S. Cho, M. H. Phillips, R. S. Giansiracusa, and D. Axen, "Random and systematic beam modulator errors in dynamic intensity modulated radiotherapy," *Physics in Medicine and Biology*, vol. 48, no. 9, p. 1109, 2003.
- [45] A. Rangel and P. Dunscombe, "Tolerances on mlc leaf position accuracy for imrt delivery with a dynamic mlc," *Medical Physics*, vol. 36, no. 7, pp. 3304–3309, 2009.

- [46] G. Yan, C. Liu, T. Simon, L.-C. Peng, C. Fox, and J. Li, "On the sensitivity of patient-specific imrt qa to mlc positioning errors," *Journal of Applied Clinical Medical Physics*, vol. 10, no. 1, 2009.
- [47] K. M. Langen, N. Papanikolaou, J. Balog, R. Crilly, D. Followill, S. M. Goddu, W. Grant, G. Olivera, C. R. Ramsey, and C. Shi, "Qa for helical tomotherapy: Report of the aapm task group 148," *Medical Physics*, vol. 37, no. 9, pp. 4817–4853, 2010.
- [48] J. Balog, T. Holmes, and R. Vaden, "Helical tomotherapy dynamic quality assurance," *Medical Physics*, vol. 33, no. 10, pp. 3939–3950, 2006.
- [49] J. Balog and E. Soisson, "Helical tomotherapy quality assurance," *International Journal of Radiation Oncology* Biology* Physics*, vol. 71, no. 1, pp. S113–S117, 2008.
- [50] J. Fenwick, W. Tome, H. Jaradat, S. Hui, J. James, J. Balog, C. DeSouza, D. Lucas, G. Olivera, and T. Mackie, "Quality assurance of a helical tomotherapy machine," *Physics in Medicine and Biology*, vol. 49, no. 13, p. 2933, 2004.
- [51] V. Feygelman, G. Zhang, C. Stevens, and B. E. Nelms, "Evaluation of a new vmat qa device, or the "x" and "o" array geometries," *Journal of Applied Clinical Medical Physics*, vol. 12, no. 2, 2011.
- [52] L. Masi, F. Casamassima, R. Doro, and P. Francescon, "Quality assurance of volumetric modulated arc therapy: Evaluation and comparison of different dosimetric systems," *Medical Physics*, vol. 38, no. 2, pp. 612–621, 2011.
- [53] F. Garcia-Vicente, V. Fernandez, R. Bermudez, A. Gomez, L. Perez, A. Zapatero, and J. J. Torres, "Sensitivity of a helical diode array device to delivery errors in imrt treatment and establishment of tolerance level for pretreatment qa," *Journal of Applied Clinical Medical Physics*, vol. 13, no. 1, 2012.
- [54] S. Arumugam, A. Xing, T. Young, and L. Holloway, "Sensitivity of a helical diode array dosimeter to volumetric modulated arc therapy delivery errors," *Physica Medica*, vol. 31, no. 8, pp. 1043–1054, 2015.
- [55] D. Létourneau, M. Gulam, D. Yan, M. Oldham, and J. W. Wong, "Evaluation of a 2d diode array for imrt quality assurance," *Radiotherapy and Oncology*, vol. 70, no. 2, pp. 199–206, 2004.

- [56] O. Bawazeer, A. Gray, S. Arumugam, P. Vial, D. Thwaites, J. Descallar, and L. Holloway, "Evaluation of the ability of a 2d ionisation chamber array and an epid to detect systematic delivery errors in imrt plans," in *Journal of Physics: Conference Series*, vol. 489, p. 012071, IOP Publishing.
- [57] M. Hussein, E. J. Adams, T. J. Jordan, C. H. Clark, and A. Nisbet, "A critical evaluation of the ptw 2d-array seven29 and octavius ii phantom for imrt and vmat verification," *Journal of Applied Clinical Medical Physics*, vol. 14, no. 6, 2013.
- [58] A. Fredh, J. B. Scherman, L. S. Fog, and P. M. af Rosenschöld, "Patient qa systems for rotational radiation therapy: a comparative experimental study with intentional errors," *Medical Physics*, vol. 40, no. 3, p. 031716, 2013.
- [59] A. K. Templeton, J. C. Chu, and J. V. Turian, "The sensitivity of arccheck-based gamma analysis to manufactured errors in helical tomotherapy radiation delivery," *Journal of Applied Clinical Medical Physics*, vol. 16, no. 1, 2015.
- [60] J. M. Galvin, G. Ezzell, A. Eisbrauch, C. Yu, B. Butler, Y. Xiao, I. Rosen, J. Rosenman, M. Sharpe, and L. Xing, "Implementing imrt in clinical practice: a joint document of the american society for therapeutic radiology and oncology and the american association of physicists in medicine," *International Journal of Radiation Oncology* Biology* Physics*, vol. 58, no. 5, pp. 1616–1634, 2004.
- [61] B. Mijnheer, "State of the art of in vivo dosimetry," *Radiation Protection Dosimetry*, vol. 131, no. 1, pp. 117–122, 2008.
- [62] S. Arumugam, A. Xing, T. Young, D. Thwaites, and L. Holloway, "Validation of 3dvh estimated dvh metrics for prostate vmat plans," in *Journal of Physics: Conference Series*, vol. 573, p. 012053, IOP Publishing, 2015.
- [63] C. Stambaugh, B. Nelms, T. Wolf, R. Mueller, M. Geurts, D. Opp, E. Moros, G. Zhang, and V. Feygelman, "Measurement-guided volumetric dose reconstruction for helical tomotherapy," *Journal of Applied Clinical Medical Physics*, vol. 16, no. 2, 2015.
- [64] O. Pisaturo, F. Miéville, P. Tercier, and A. Allal, "An efficient procedure for tomotherapy treatment plan verification using the on-board detector," *Physics in Medicine and Biology*, vol. 60, no. 4, p. 1625, 2015.

- [65] D. Sevillano, C. Mínguez, A. Sánchez, and A. Sánchez-Reyes, "Measurement and correction of leaf open times in helical tomotherapy," *Medical Physics*, vol. 39, no. 11, pp. 6972–6980, 2012.
- [66] R. Siegel, D. Naishadham, and A. Jemal, "Cancer statistics, 2012," *CA: A Cancer Journal for Clinicians*, vol. 62, no. 1, pp. 10–29, 2012.
- [67] *Australia's Health 2012: In Brief*. AIHW, 2012.
- [68] G. Delaney, S. Jacob, C. Featherstone, and M. Barton, "The role of radiotherapy in cancer treatment," *Cancer*, vol. 104, no. 6, pp. 1129–1137, 2005.
- [69] M. B. Barton, S. Jacob, J. Shafiq, K. Wong, S. R. Thompson, T. P. Hanna, and G. P. Delaney, "Estimating the demand for radiotherapy from the evidence: a review of changes from 2003 to 2012," *Radiotherapy and Oncology*, vol. 112, no. 1, pp. 140–144, 2014.
- [70] S. Tyldesley, C. Boyd, K. Schulze, H. Walker, and W. J. Mackillop, "Estimating the need for radiotherapy for lung cancer: an evidence-based, epidemiologic approach," *International Journal of Radiation Oncology* Biology* Physics*, vol. 49, no. 4, pp. 973–985, 2001.
- [71] E. Curie, "Marie and pierre curie and the discovery of radium," *The British Journal of Radiology*, vol. 23, no. 271, pp. 409–412, 1950.
- [72] W. Schaefer and E. Witte, "Über eine neue körperhöhlenröntgenröhre zur bestrahlung von uterustumoren," *Strahlentherapie*, vol. 44, p. 283, 1932.
- [73] E. H. Grubbe, "Priority in the therapeutic use of x-rays," *Radiology*, vol. 21, no. 2, pp. 156–162, 1933.
- [74] V. Despeignes, "Observation concernant un cas de cancer de l'estomac traité par les rayons roentgen," *Lyon Med*, vol. 82, pp. 428–430, 1896.
- [75] R. F. Mould, *A century of X-rays and radioactivity in medicine: with emphasis on photographic records of the early years*. CRC Press, 1993.
- [76] R. Paterson, *The treatment of malignant disease by radium and X-rays*. 1948.
- [77] E. Leddy, "A study of the ionization method for measuring the intensity and absorption of roentgen rays and of the efficiency of different filters used in therapy," *Radiology*, vol. 19, no. 5, pp. 330–330, 1932.

- [78] J. Bergonie, "Interpretation de quelques resultats de la radiotherapie et ssai de fixation d'une technique rationnelle," *Compt Rend Acad Sci*, vol. 143, pp. 983–985, 1906.
- [79] C. Regaud and R. Ferroux, "Discordance des effects de rayons x, d'une part dans le testicule, par le peau, d'autre parts dans le fractionnement de la dose," *Compt Rend Soc Biol*, vol. 97, pp. 431–4, 1927.
- [80] H. Coutard, "Principles of x ray therapy of malignant diseases," *The Lancet*, vol. 224, no. 5784, pp. 1–8, 1934.
- [81] L. S. Taylor, "History of the international commission on radiological protection (icrp)," *Health Physics*, vol. 1, no. 2, pp. 97–104, 1958.
- [82] H. Johns, L. Bates, and T. Watson, "1000 curie cobalt 60 unit," *The British Journal of Radiology*, vol. 25, no. 294, pp. 296–302, 1952.
- [83] A. Laugier, "[the first century of radiotherapy in france]," *Bulletin De l'Academie Nationale De Medecine*, vol. 180, no. 1, pp. 143–160, 1996.
- [84] J. Le Bourgeois, J. Chavaudra, and F. Eschwege, "Cancers gynecologiques," *Radiotherapie Oncologique. Paris: Hermann Editeurs des Sciences et des Arts*, pp. 253–67, 1992.
- [85] D. I. Thwaites and J. B. Tuohy, "Back to the future: the history and development of the clinical linear accelerator," *Physics in Medicine and Biology*, vol. 51, no. 13, p. R343, 2006.
- [86] G. N. Hounsfield, "Computed medical imaging," *Journal of Computer Assisted Tomography*, vol. 4, no. 5, pp. 665–674, 1980.
- [87] P. Bey, C. Carrie, V. Beckendorf, C. Ginestet, P. Aletti, G. Madelis, E. Luporsi, P. Pommier, D. Cowen, L. Gonzague-Casabianca, *et al.*, "Dose escalation with 3d-crt in prostate cancer: French study of dose escalation with conformal 3d radiotherapy in prostate cancer—preliminary results," *International Journal of Radiation Oncology* Biology* Physics*, vol. 48, no. 2, pp. 513–517, 2000.
- [88] A. Brahme, "Optimization of stationary and moving beam radiation therapy techniques," *Radiotherapy and Oncology*, vol. 12, no. 2, pp. 129–140, 1988.
- [89] S. Webb, "Contemporary imrt: Developing physics and clinical applications," *Bristol, UK: Institute of Physics Publishing*, 2005.

- [90] G. A. Ezzell, J. M. Galvin, D. Low, J. R. Palta, I. Rosen, M. B. Sharpe, P. Xia, Y. Xiao, L. Xing, and X. Y. Cedric, "Guidance document on delivery, treatment planning, and clinical implementation of imrt: report of the imrt subcommittee of the aapm radiation therapy committee," *Medical Physics*, vol. 30, no. 8, pp. 2089–2115, 2003.
- [91] S. X. Chang, T. J. Cullip, K. M. Deschesne, E. P. Miller, and J. G. Rosenman, "Compensators: An alternative imrt delivery technique," *Journal of Applied Clinical Medical Physics*, vol. 5, no. 3, 2004.
- [92] D. Shepard, M. Earl, X. Li, S. Naqvi, and C. Yu, "Direct aperture optimization: a turnkey solution for step-and-shoot imrt," *Medical Physics*, vol. 29, no. 6, pp. 1007–1018, 2002.
- [93] T. LoSasso, C.-S. Chui, and C. C. Ling, "Physical and dosimetric aspects of a multi-leaf collimation system used in the dynamic mode for implementing intensity modulated radiotherapy," *Medical Physics*, vol. 25, no. 10, pp. 1919–1927, 1998.
- [94] B. J. Salter, "Nomos peacock imrt utilizing the beak™ post collimation device," *Medical Dosimetry*, vol. 26, no. 1, pp. 37–45, 2001.
- [95] T. R. Mackie, T. Holmes, S. Swerdloff, P. Reckwerdt, J. O. Deasy, J. Yang, B. Paliwal, and T. Kinsella, "Tomotherapy: a new concept for the delivery of dynamic conformal radiotherapy," *Medical Physics*, vol. 20, no. 6, pp. 1709–1719, 1993.
- [96] C. X. Yu, "Intensity-modulated arc therapy with dynamic multileaf collimation: an alternative to tomotherapy," *Physics in Medicine and Biology*, vol. 40, no. 9, p. 1435, 1995.
- [97] K. Otto, "Volumetric modulated arc therapy: Imrt in a single gantry arc," *Medical Physics*, vol. 35, no. 1, pp. 310–317, 2008.
- [98] J. K. Salama, J. P. Kirkpatrick, and F.-F. Yin, "Stereotactic body radiotherapy treatment of extracranial metastases," *Nature Reviews Clinical Oncology*, vol. 9, no. 11, pp. 654–665, 2012.
- [99] F. J. Lagerwaard, N. E. Versteegen, C. J. Haasbeek, B. J. Slotman, M. A. Paul, E. F. Smit, and S. Senan, "Outcomes of stereotactic ablative radiotherapy in patients with potentially operable stage i non-small cell lung cancer," *International Journal of Radiation Oncology* Biology* Physics*, vol. 83, no. 1, pp. 348–353, 2012.

- [100] M. T. Milano, A. W. Katz, H. Zhang, and P. Okunieff, "Oligometastases treated with stereotactic body radiotherapy: long-term follow-up of prospective study," *International Journal of Radiation Oncology* Biology* Physics*, vol. 83, no. 3, pp. 878–886, 2012.
- [101] J. De Los Santos, R. Popple, N. Agazaryan, J. E. Bayouth, J.-P. Bissonnette, M. K. Bucci, S. Dieterich, L. Dong, K. M. Forster, and D. Indelicato, "Image guided radiation therapy (igrt) technologies for radiation therapy localization and delivery," *International Journal of Radiation Oncology* Biology* Physics*, vol. 87, no. 1, pp. 33–45, 2013.
- [102] D. Verellen, M. De Ridder, N. Linthout, K. Tournel, G. Soete, and G. Storme, "Innovations in image-guided radiotherapy," *Nature Reviews Cancer*, vol. 7, no. 12, pp. 949–960, 2007.
- [103] T. Ackerly, C. Lancaster, M. Geso, and K. Roxby, "Clinical accuracy of exactrac intracranial frameless stereotactic system," *Medical Physics*, vol. 38, no. 9, pp. 5040–5048, 2011.
- [104] E. Weiss, H. Vorwerk, S. Richter, and C. F. Hess, "Interfractional and intrafractional accuracy during radiotherapy of gynecologic carcinomas: a comprehensive evaluation using the exactrac system," *International Journal of Radiation Oncology* Biology* Physics*, vol. 56, no. 1, pp. 69–79, 2003.
- [105] J. D. Fontenot, H. Alkhatib, J. A. Garrett, A. R. Jensen, S. P. McCullough, A. J. Olch, B. C. Parker, C.-C. J. Yang, L. A. Fairbent, and A. Staff, "Aapm medical physics practice guideline 2. a: Commissioning and quality assurance of x-ray–based image-guided radiotherapy systems," *Journal of Applied Clinical Medical Physics*, vol. 15, no. 1, 2014.
- [106] T. Willoughby, J. Lehmann, J. A. Bencomo, S. K. Jani, L. Santanam, A. Sethi, T. D. Solberg, W. A. Tomé, and T. J. Waldron, "Quality assurance for nonradiographic radiotherapy localization and positioning systems: Report of task group 147," *Medical Physics*, vol. 39, no. 4, pp. 1728–1747, 2012.
- [107] M. G. Herman, "Clinical use of electronic portal imaging," in *Seminars in Radiation Oncology*, vol. 15, pp. 157–167, Elsevier.

- [108] G. C. Sharp, S. B. Jiang, S. Shimizu, and H. Shirato, "Prediction of respiratory tumour motion for real-time image-guided radiotherapy," *Physics in Medicine and Biology*, vol. 49, no. 3, p. 425, 2004.
- [109] D. A. Low, J. M. Moran, J. F. Dempsey, L. Dong, and M. Oldham, "Dosimetry tools and techniques for imrt," *Medical Physics*, vol. 38, no. 3, pp. 1313–1338, 2011.
- [110] J. Shafiq, M. Barton, D. Noble, C. Lemer, and L. J. Donaldson, "An international review of patient safety measures in radiotherapy practice," *Radiotherapy and Oncology*, vol. 92, no. 1, pp. 15–21, 2009.
- [111] W. Bogdanich, "Radiation offers new cures, and ways to do harm," *The New York Times*, vol. 23, 2010.
- [112] M. Williams, "Radiotherapy near misses, incidents and errors: radiotherapy incident at glasgow," *Clinical Oncology*, vol. 19, no. 1, pp. 1–3, 2007.
- [113] G. S. Ibbott, A. Molineu, and D. S. Followill, "Independent evaluations of imrt through the use of an anthropomorphic phantom," *Technology in Cancer Research and Treatment*, vol. 5, no. 5, pp. 481–487, 2006.
- [114] J. Van Dyk, *The modern technology of radiation oncology: a compendium for medical physicists and radiation oncologists*. Medical Physics Pub Corp, 1999.
- [115] D. Thwaites, "Accuracy required and achievable in radiotherapy dosimetry: have modern technology and techniques changed our views?," in *Journal of Physics: Conference Series*, vol. 444, p. 012006, IOP Publishing.
- [116] B. Mijnheer, J. Battermann, and A. Wambersie, "What degree of accuracy is required and can be achieved in photon and neutron therapy?," *Radiotherapy and Oncology*, vol. 8, no. 3, pp. 237–252, 1987.
- [117] M. Essers and B. Mijnheer, "In vivo dosimetry during external photon beam radiotherapy," *International Journal of Radiation Oncology* Biology* Physics*, vol. 43, no. 2, pp. 245–259, 1999.
- [118] B. Mijnheer, S. Beddar, J. Izewska, and C. Reft, "In vivo dosimetry in external beam radiotherapy," *Medical Physics*, vol. 40, no. 7, 2013.

- [119] A. Mans, M. Wendling, L. McDermott, J.-J. Sonke, R. Tielenburg, R. Vijlbrief, B. Mijnheer, M. Van Herk, and J. Stroom, "Catching errors with in vivo epid dosimetry," *Medical Physics*, vol. 37, no. 6, pp. 2638–2644, 2010.
- [120] M. Williams, "Improving patient safety in radiotherapy by learning from near misses, incidents and errors," *The British Journal of Radiology*, 2014.
- [121] N. D'Souza, L. Holden, S. Robson, K. Mah, L. Di Prospero, C. S. Wong, E. Chow, and J. Spayne, "Modern palliative radiation treatment: Do complexity and workload contribute to medical errors?," *International Journal of Radiation Oncology* Biology* Physics*, vol. 84, no. 1, pp. e43–e48, 2012.
- [122] N. Ramakrishna, F. Rosca, S. Friesen, E. Tezcanli, P. Zygmanski, and F. Hacker, "A clinical comparison of patient setup and intra-fraction motion using frame-based radiosurgery versus a frameless image-guided radiosurgery system for intracranial lesions," *Radiotherapy and Oncology*, vol. 95, no. 1, pp. 109–115, 2010.
- [123] I. S. Grills, G. Hugo, L. L. Kestin, A. P. Galerani, K. K. Chao, J. Wloch, and D. Yan, "Image-guided radiotherapy via daily online cone-beam ct substantially reduces margin requirements for stereotactic lung radiotherapy," *International Journal of Radiation Oncology* Biology* Physics*, vol. 70, no. 4, pp. 1045–1056, 2008.
- [124] J.-P. Bissonnette, P. A. Balter, L. Dong, K. M. Langen, D. M. Lovelock, M. Miften, D. J. Moseley, J. Pouliot, J.-J. Sonke, and S. Yoo, "Quality assurance for image-guided radiation therapy utilizing ct-based technologies: a report of the aapm tg-179," *Medical Physics*, vol. 39, no. 4, pp. 1946–1963, 2012.
- [125] A. Bujold, T. Craig, D. Jaffray, and L. A. Dawson, "Image-guided radiotherapy: has it influenced patient outcomes?," in *Seminars in radiation oncology*, vol. 22, pp. 50–61, Elsevier.
- [126] P. Kupelian and J.-J. Sonke, "Magnetic resonance-guided adaptive radiotherapy: a solution to the future," in *Seminars in Radiation Oncology*, vol. 24, pp. 227–232, Elsevier.
- [127] M. J. Murphy, J. Balter, S. Balter, J. A. BenComo Jr, I. J. Das, S. B. Jiang, C.-M. Ma, G. H. Olivera, R. F. Rodebaugh, and K. J. Ruchala, "The management of imaging dose during image-guided radiotherapy: report of the aapm task group 75," *Medical Physics*, vol. 34, no. 10, pp. 4041–4063, 2007.

- [128] D. A. Low, "Quality assurance of intensity-modulated radiotherapy," in *Seminars in Radiation Oncology*, vol. 12, pp. 219–228, Elsevier.
- [129] A. J. Mundt and J. C. Roeske, *Intensity modulated radiation therapy: a clinical perspective*, vol. 1. PMPH-USA, 2005.
- [130] A. Van Esch, J. Bohsung, P. Sorvari, M. Tenhunen, M. Paiusco, M. Iori, P. Engström, H. Nyström, and D. P. Huyskens, "Acceptance tests and quality control (qc) procedures for the clinical implementation of intensity modulated radiotherapy (imrt) using inverse planning and the sliding window technique: experience from five radiotherapy departments," *Radiotherapy and Oncology*, vol. 65, no. 1, pp. 53–70, 2002.
- [131] J. R. Palta, C. Liu, and J. G. Li, "Quality assurance of intensity-modulated radiation therapy," *International Journal of Radiation Oncology* Biology* Physics*, vol. 71, no. 1, pp. S108–S112, 2008.
- [132] L. Dong, J. Antolak, M. Salehpour, K. Forster, L. O'Neill, R. Kendall, and I. Rosen, "Patient-specific point dose measurement for imrt monitor unit verification," *International Journal of Radiation Oncology* Biology* Physics*, vol. 56, no. 3, pp. 867–877, 2003.
- [133] G. T. Betzel, B. Y. Yi, Y. Niu, and X. Y. Cedric, "Is rapidarc more susceptible to delivery uncertainties than dynamic imrt?," *Medical Physics*, vol. 39, no. 10, pp. 5882–5890, 2012.
- [134] B. Mijnheer and D. Georg, "Guidelines for the verification of imrt, estro booklet 9," *ESTRO, Brussels*, 2008.
- [135] P. Xia and L. J. Verhey, "Intensity modulated radiation therapy," *The Modern Technology of Radiation Oncology: A Compendium for Medical Physicists and Radiation Oncologists. 2nd ed. Madison, WI: Medical Physics Publishing*, 2005.
- [136] J. VanDam and G. Marinello, *Methods for in vivo dosimetry in external radiotherapy*. Garant Publ., 1994.
- [137] A. B. Rosenfeld, A. Rosenfeld, T. Kron, F. d'Errico, and M. Moscovitch, "Advanced semiconductor dosimetry in radiation therapy," in *AIP Conference Proceedings*, vol. 1345, pp. 48–74, AIP, 2011.

- [138] T. Kron, "Thermoluminescence dosimetry and its applications in medicine—part 1: Physics, materials and equipment," *Australasian physical and engineering sciences in medicine/supported by the Australasian College of Physical Scientists in Medicine and the Australasian Association of Physical Sciences in Medicine*, vol. 17, no. 4, pp. 175–199, 1994.
- [139] Y. Horowitz, "The theoretical and microdosimetric basis of thermoluminescence and applications to dosimetry," *Physics in Medicine and Biology*, vol. 26, no. 5, p. 765, 1981.
- [140] D. P. Huyskens, R. Bogaerts, J. Verstraete, M. Lööf, H. Nyström, C. Fiorino, S. Broggi, N. Jornet, M. Ribas, and D. I. Thwaites, *Practical guidelines for the implementation of in vivo dosimetry with diodes in external radiotherapy with photon beams (entrance dose)*. ESTRO, 2001.
- [141] E. Yorke, R. Alecu, L. Ding, D. Fontenla, A. Kalend, D. Kaurin, M. Masterson-McGary, G. Marinello, T. Matzen, and A. Saini, "Diode in vivo dosimetry for patients receiving external beam radiation therapy," *Report of Task Group*, vol. 62, 2005.
- [142] A. B. Rosenfeld, D. Cutajar, M. Lerch, G. Takacs, I. Cornelius, M. Yudelev, and M. Zaider, "Miniature semiconductor detectors for in vivo dosimetry," *Radiation Protection Dosimetry*, vol. 120, no. 1-4, pp. 48–55, 2006.
- [143] C. Waldhäusl, A. Wambersie, R. Pötter, and D. Georg, "In-vivo dosimetry for gynaecological brachytherapy: Physical and clinical considerations," *Radiotherapy and Oncology*, vol. 77, no. 3, pp. 310–317, 2005.
- [144] E. L. Seymour, S. J. Downes, G. B. Fogarty, M. A. Izard, and P. Metcalfe, "In vivo real-time dosimetric verification in high dose rate prostate brachytherapy," *Medical Physics*, vol. 38, no. 8, pp. 4785–4794, 2011.
- [145] P. E. Metcalfe, "Experimental verification of cesium brachytherapy line source emission using a semiconductor detector," *Medical Physics*, vol. 15, no. 5, pp. 702–706, 1988.
- [146] K.-i. Sakata, H. Nagakura, A. Oouchi, M. Someya, K. Nakata, M. Shido, K. Koito, S. Sagae, R. Kudo, and M. Hareyama, "High-dose-rate intracavitary brachytherapy: results of analyses of late rectal complications," *International Journal of Radiation Oncology* Biology* Physics*, vol. 54, no. 5, pp. 1369–1376, 2002.

- [147] A. Hayton, *Investigation of MOSkin detectors for use in dosimetry of a HDR brachytherapy source*. PhD thesis, RMIT University, 2011.
- [148] A. Noel, P. Aletti, P. Bey, and L. Malissard, "Detection of errors in individual patients in radiotherapy by systematic in vivo dosimetry," *Radiotherapy and Oncology*, vol. 34, no. 2, pp. 144–151, 1995.
- [149] "Prevention of accidents to patients undergoing radiation therapy," *Ann ICRP*, vol. 30, no. 3, 2001.
- [150] P. E. Metcalfe, T. Kron, and P. Hoban, "The physics of radiotherapy x-rays and electrons," 2007.
- [151] V. C. Borca, M. Pasquino, G. Russo, P. Grosso, D. Cante, P. Sciacero, G. Girelli, M. R. La Porta, and S. Tofani, "Dosimetric characterization and use of gafchromic ebt3 film for imrt dose verification," *Journal of Applied Clinical Medical Physics*, vol. 14, no. 2, 2013.
- [152] A. L. Palmer, A. Dimitriadis, A. Nisbet, and C. H. Clark, "Evaluation of gafchromic ebt-xd film, with comparison to ebt3 film, and application in high dose radiotherapy verification," *Physics in Medicine and Biology*, vol. 60, no. 22, p. 8741, 2015.
- [153] A. M. Gloi, R. E. Buchana, C. L. Zuge, and A. M. Goettler, "Rapidarc quality assurance through mapcheck," *Journal of Applied Clinical Medical Physics*, vol. 12, no. 2, 2011.
- [154] B. Poppe, A. Blechschmidt, A. Djouguela, R. Kollhoff, A. Rubach, K. C. Willborn, and D. Harder, "Two-dimensional ionization chamber arrays for imrt plan verification," *Medical Physics*, vol. 33, no. 4, pp. 1005–1015, 2006.
- [155] J. Herzen, M. Todorovic, F. Cremers, V. Platz, D. Albers, A. Bartels, and R. Schmidt, "Dosimetric evaluation of a 2d pixel ionization chamber for implementation in clinical routine," *Physics in Medicine and Biology*, vol. 52, no. 4, p. 1197, 2007.
- [156] E. Spezi, A. Angelini, F. Romani, and A. Ferri, "Characterization of a 2d ion chamber array for the verification of radiotherapy treatments," *Physics in Medicine and Biology*, vol. 50, no. 14, p. 3361, 2005.
- [157] S. Cilla, L. Grimaldi, G. D'onofrio, P. Viola, M. Craus, L. Azario, A. Fidanzio, G. Stimato, C. Di Gesu, and G. Macchia, "Portal dose measurements by a 2d array," *Physica Medica*, vol. 23, no. 1, pp. 25–32, 2007.

- [158] B. Poppe, H. K. Looe, N. Chofor, A. Rühmann, D. Harder, and K. C. Willborn, "Clinical performance of a transmission detector array for the permanent supervision of imrt deliveries," *Radiotherapy and Oncology*, vol. 95, no. 2, pp. 158–165, 2010.
- [159] E. W. Korevaar, D. J. Wauben, P. C. van der Hulst, J. A. Langendijk, and A. A. van't Veld, "Clinical introduction of a linac head-mounted 2d detector array based quality assurance system in head and neck imrt," *Radiotherapy and Oncology*, vol. 100, no. 3, pp. 446–452, 2011.
- [160] D. Menichelli, M. Bruzzi, M. Bucciolini, C. Talamonti, M. Casati, L. Marrazzo, M. Tesi, C. Piemonte, A. Pozza, and N. Zorzi, "Design and development of a silicon-segmented detector for 2d dose measurements in radiotherapy," *Nuclear Instruments and Methods in Physics Research*, vol. 583, no. 1, pp. 109–113, 2007.
- [161] C. Talamonti, M. Bruzzi, M. Bucciolini, L. Marrazzo, and D. Menichelli, "Preliminary dosimetric characterization of a silicon segmented detector for 2d dose verifications in radiotherapy," *Nuclear Instruments and Methods in Physics Research*, vol. 583, no. 1, pp. 114–118, 2007.
- [162] A. S. Beddar, T. R. Mackie, and F. H. Attix, "Water-equivalent plastic scintillation detectors for high-energy beam dosimetry: Ii. properties and measurements," *Physics in Medicine and Biology*, vol. 37, no. 10, p. 1901, 1992.
- [163] A. Beddar, "Plastic scintillation dosimetry and its application to radiotherapy," *Radiation measurements*, vol. 41, pp. S124–S133, 2006.
- [164] L. Archambault, J. Arsenault, L. Gingras, A. S. Beddar, R. Roy, and L. Beaulieu, "Plastic scintillation dosimetry: Optimal selection of scintillating fibers and scintillators," *Medical Physics*, vol. 32, no. 7, pp. 2271–2278, 2005.
- [165] M. Clift, P. Johnston, and D. Webb, "A temporal method of avoiding the cerenkov radiation generated in organic scintillator dosimeters by pulsed mega-voltage electron and photon beams," *Physics in Medicine and Biology*, vol. 47, no. 8, p. 1421, 2002.
- [166] L. Archambault, A. S. Beddar, L. Gingras, F. Lacroix, R. Roy, and L. Beaulieu, "Water-equivalent dosimeter array for small-field external beam radiotherapy," *Medical Physics*, vol. 34, no. 5, pp. 1583–1592, 2007.

- [167] L. Archambault, A. S. Beddar, L. Gingras, R. Roy, and L. Beaulieu, "Measurement accuracy and cerenkov removal for high performance, high spatial resolution scintillation dosimetry," *Medical Physics*, vol. 33, no. 1, pp. 128–135, 2006.
- [168] L. L. Wang and S. Beddar, "Study of the response of plastic scintillation detectors in small-field 6 mv photon beams by monte carlo simulations," *Medical Physics*, vol. 38, no. 3, pp. 1596–1599, 2011.
- [169] M. Guillot, L. Beaulieu, L. Archambault, S. Beddar, and L. Gingras, "A new water-equivalent 2d plastic scintillation detectors array for the dosimetry of megavoltage energy photon beams in radiation therapy," *Medical Physics*, vol. 38, no. 12, pp. 6763–6774, 2011.
- [170] V. Collomb-Patton, P. Boher, T. Leroux, J.-M. Fontbonne, A. Vela, and A. Batalla, "The dosimap, a high spatial resolution tissue equivalent 2d dosimeter for linac qa and imrt verification," *Medical Physics*, vol. 36, no. 2, pp. 317–328, 2009.
- [171] M. Petric, J. Robar, and B. Clark, "Development and characterization of a tissue equivalent plastic scintillator based dosimetry system," *Medical Physics*, vol. 33, no. 1, pp. 96–105, 2006.
- [172] P. Metcalfe, A. Quinn, K. Loo, M. Lerch, M. Petasecca, J. Wong, N. Hardcastle, M. Carolan, J. McNamara, and D. Cutajar, "Review of four novel dosimeters developed for use in radiotherapy," in *Journal of Physics: Conference Series*, vol. 444, p. 012008, IOP Publishing.
- [173] R. Prabhakar, J. Cramb, and T. Kron, "A feasibility study of using couch-based real time dosimetric device in external beam radiotherapy," *Medical Physics*, vol. 38, no. 12, pp. 6539–6552, 2011.
- [174] H. Chung, J. Li, and S. Samant, "Feasibility of using two-dimensional array dosimeter for in vivo dose reconstruction via transit dosimetry," *Journal of Applied Clinical Medical Physics*, vol. 12, no. 3, 2011.
- [175] T. S. Baek, E. J. Chung, E. K. Koh, J. Seo, and M. Yoon, "Evaluation of the accuracy of dose delivery for imrt based on transit dosimetry," *Health Physics*, vol. 107, no. 3, pp. 200–205, 2014.

- [176] D. Jaffray, J. Bissonnette, and T. Craig, "X-ray imaging for verification and localization in radiation therapy," *The Modern Technology of Radiation Oncology*, vol. 2, pp. 259–284, 2005.
- [177] P. Munro, "Portal imaging technology: Past, present, and future," *Seminars in Radiation Oncology*, vol. 5, no. 2, pp. 115–33, 1995.
- [178] A. L. Boyer, L. Antonuk, A. Fenster, M. Van Herk, H. Meertens, P. Munro, L. E. Reinstein, and J. Wong, "A review of electronic portal imaging devices (epids)," *Medical Physics*, vol. 19, no. 1, pp. 1–16, 1992.
- [179] J. Leong, "Use of digital fluoroscopy as an online verification device in radiation therapy," *Physics in Medicine and Biology*, vol. 31, no. 9, p. 985, 1986.
- [180] L. E. Antonuk, "Electronic portal imaging devices: a review and historical perspective of contemporary technologies and research," *Physics in Medicine and Biology*, vol. 47, no. 6, p. R31, 2002.
- [181] L. McDermott, R. Louwe, J.-J. Sonke, M. Van Herk, and B. Mijnheer, "Dose–response and ghosting effects of an amorphous silicon electronic portal imaging device," *Medical Physics*, vol. 31, no. 2, pp. 285–295, 2004.
- [182] L. McDermott, S. Nijsten, J.-J. Sonke, M. Partridge, M. Van Herk, and B. Mijnheer, "Comparison of ghosting effects for three commercial a-si epids," *Medical Physics*, vol. 33, no. 7, pp. 2448–2451, 2006.
- [183] P. Winkler, A. Hefner, and D. Georg, "Dose-response characteristics of an amorphous silicon epid," *Medical Physics*, vol. 32, no. 10, pp. 3095–3105, 2005.
- [184] P. Winkler and D. Georg, "An intercomparison of 11 amorphous silicon epids of the same type: implications for portal dosimetry," *Physics in Medicine and Biology*, vol. 51, no. 17, p. 4189, 2006.
- [185] A. Kavuma, M. Glegg, G. Currie, and A. Elliott, "Assessment of dosimetrical performance in 11 varian a-si500 electronic portal imaging devices," *Physics in Medicine and Biology*, vol. 53, no. 23, p. 6893, 2008.
- [186] S. L. Berry, R.-D. Sheu, C. S. Polvorosa, and C.-S. Wu, "Implementation of epid transit dosimetry based on a through-air dosimetry algorithm," *Medical Physics*, vol. 39, no. 1, pp. 87–98, 2012.

- [187] S. L. Berry, C. Polvorosa, S. Cheng, I. Deutsch, K. C. Chao, and C.-S. Wu, "Initial clinical experience performing patient treatment verification with an electronic portal imaging device transit dosimeter," *International Journal of Radiation Oncology* Biology* Physics*, vol. 88, no. 1, pp. 204–209, 2014.
- [188] B. Heijmen, K. Pasma, M. Kroonwijk, V. Althof, J. De Boer, A. Visser, and H. Huizenga, "Portal dose measurement in radiotherapy using an electronic portal imaging device (epid)," *Physics in Medicine and Biology*, vol. 40, no. 11, p. 1943, 1995.
- [189] J. Chen, C. F. Chuang, O. Morin, M. Aubin, and J. Pouliot, "Calibration of an amorphous-silicon flat panel portal imager for exit-beam dosimetry," *Medical Physics*, vol. 33, no. 3, pp. 584–594, 2006.
- [190] R. Boellaard, M. Van Herk, and B. Mijnheer, "A convolution model to convert transmission dose images to exit dose distributions," *Medical Physics*, vol. 24, no. 2, pp. 189–199, 1997.
- [191] J. Chang, G. S. Mageras, C. S. Chui, C. C. Ling, and W. Lutz, "Relative profile and dose verification of intensity-modulated radiation therapy," *International Journal of Radiation Oncology* Biology* Physics*, vol. 47, no. 1, pp. 231–240, 2000.
- [192] A. Van Esch, T. Depuydt, and D. P. Huyskens, "The use of an a-si based epid for routine absolute dosimetric pre-treatment verification of dynamic imrt fields," *Radiotherapy and Oncology*, vol. 71, no. 2, pp. 223–234, 2004.
- [193] W. Li, J. V. Siebers, and J. A. Moore, "Using fluence separation to account for energy spectra dependence in computing dosimetric a-si epid images for imrt fields," *Medical Physics*, vol. 33, no. 12, pp. 4468–4480, 2006.
- [194] P. B. Greer, P. Cadman, C. Lee, and K. Bzdusek, "An energy fluence-convolution model for amorphous silicon epid dose prediction," *Medical Physics*, vol. 36, no. 2, pp. 547–555, 2009.
- [195] P. Reich, E. Bezak, M. Mohammadi, and L. Fog, "The prediction of transmitted dose distributions using a 3d treatment planning system," *Australasian Physics and Engineering Sciences in Medicine*, vol. 29, no. 1, pp. 18–29, 2006.
- [196] M. Mohammadi, E. Bezak, and P. Reich, "Verification of two-dimensional transmitted dose measurement in the presence of homogeneous/inhomogeneous phantoms,"

- Australasian Physical and Engineering Sciences in Medicine*, vol. 28, no. 4, p. 274, 2005.
- [197] T. S. Baek, E. J. Chung, J. Son, and M. Yoon, “Feasibility study on the verification of actual beam delivery in a treatment room using epid transit dosimetry,” *Radiation Oncology*, vol. 9, no. 1, p. 1, 2014.
- [198] T. R. McNutt, T. R. Mackie, P. Reckwerdt, and B. R. Paliwal, “Modeling dose distributions from portal dose images using the convolution/superposition method,” *Medical Physics*, vol. 23, no. 8, pp. 1381–1392, 1996.
- [199] T. R. McNutt, T. R. Mackie, P. Reckwerdt, N. Papanikolaou, and B. R. Paliwal, “Calculation of portal dose using the convolution/superposition method,” *Medical Physics*, vol. 23, no. 4, pp. 527–535, 1996.
- [200] C. Bojchko and E. Ford, “Quantifying the performance of in vivo portal dosimetry in detecting four types of treatment parameter variations,” *Medical Physics*, vol. 42, no. 12, pp. 6912–6918, 2015.
- [201] H. C. Woodruff, T. Fuangrod, P. Rowshanfarzad, B. M. McCurdy, and P. B. Greer, “Gantry-angle resolved vmat pretreatment verification using epid image prediction,” *Medical Physics*, vol. 40, no. 8, p. 081715, 2013.
- [202] H. C. Woodruff, T. Fuangrod, E. Van Uytven, B. M. McCurdy, T. van Beek, S. Bhatia, and P. B. Greer, “First experience with real-time epid-based delivery verification during imrt and vmat sessions,” *International Journal of Radiation Oncology* Biology* Physics*, vol. 93, no. 3, pp. 516–522, 2015.
- [203] P. Vial, H. Gustafsson, L. Oliver, C. Baldock, and P. B. Greer, “Direct-detection epid dosimetry: investigation of a potential clinical configuration for imrt verification,” *Physics in Medicine and Biology*, vol. 54, no. 23, p. 7151, 2009.
- [204] H. Gustafsson, P. Vial, Z. Kuncic, C. Baldock, and P. B. Greer, “Epid dosimetry: Effect of different layers of materials on absorbed dose response,” *Medical Physics*, vol. 36, no. 12, pp. 5665–5674, 2009.
- [205] H. Gustafsson, P. Vial, Z. Kuncic, C. Baldock, J. W. Denham, and P. B. Greer, “Direct dose to water dosimetry for pretreatment imrt verification using a modified epid,” *Medical Physics*, vol. 38, no. 11, pp. 6257–6264, 2011.

- [206] M. Sabet, F. W. Menk, and P. B. Greer, "Evaluation of an a-si epid in direct detection configuration as a water-equivalent dosimeter for transit dosimetry," *Medical Physics*, vol. 37, no. 4, pp. 1459–1467, 2010.
- [207] A. Teymurazyan and G. Pang, "Monte carlo simulation of a novel water-equivalent electronic portal imaging device using plastic scintillating fibers," *Medical Physics*, vol. 39, no. 3, pp. 1518–1529, 2012.
- [208] J. L. Bedford, Y. K. Lee, P. Wai, C. P. South, and A. P. Warrington, "Evaluation of the delta4 phantom for imrt and vmat verification," *Physics in Medicine and Biology*, vol. 54, no. 9, p. N167, 2009.
- [209] J. Gore and Y. Kang, "Measurement of radiation dose distributions by nuclear magnetic resonance (nmr) imaging," *Physics in Medicine and Biology*, vol. 29, no. 10, p. 1189, 1984.
- [210] K. Vergote, Y. De Deene, F. Claus, W. De Gersem, B. Van Duyse, L. Paelinck, E. Achten, W. De Neve, and C. De Wagter, "Application of monomer/polymer gel dosimetry to study the effects of tissue inhomogeneities on intensity-modulated radiation therapy (imrt) dose distributions," *Radiotherapy and Oncology*, vol. 67, no. 1, pp. 119–128, 2003.
- [211] K. Vergote, Y. De Deene, W. Duthoy, W. De Gersem, W. De Neve, E. Achten, and C. De Wagter, "Validation and application of polymer gel dosimetry for the dose verification of an intensity-modulated arc therapy (imat) treatment," *Physics in Medicine and Biology*, vol. 49, no. 2, p. 287, 2004.
- [212] P. Love, P. Evans, M. Leach, and S. Webb, "Polymer gel measurement of dose homogeneity in the breast: comparing mlc intensity modulation with standard wedged delivery," *Physics in Medicine and Biology*, vol. 48, no. 8, p. 1065, 2003.
- [213] H. Gustavsson, A. Karlsson, S. J. Bäck, L. E. Olsson, P. Haraldsson, P. Engström, and H. Nyström, "Magic-type polymer gel for three-dimensional dosimetry: Intensity-modulated radiation therapy verification," *Medical Physics*, vol. 30, no. 6, pp. 1264–1271, 2003.
- [214] C. Baldock, "Historical overview of the development of gel dosimetry: a personal perspective," in *Journal of Physics: Conference Series*, vol. 56, p. 14, IOP Publishing.

- [215] J. Kapatoes, G. Olivera, P. Reckwerdt, E. Fitchard, E. Schloesser, and T. Mackie, "Delivery verification in sequential and helical tomotherapy," *Physics in Medicine and Biology*, vol. 44, no. 7, p. 1815, 1999.
- [216] J. Kapatoes, G. Olivera, K. Ruchala, J. Smilowitz, P. Reckwerdt, and T. Mackie, "A feasible method for clinical delivery verification and dose reconstruction in tomotherapy," *Medical Physics*, vol. 28, no. 4, pp. 528–542, 2001.
- [217] M. Hashimoto, M. Uematsu, M. Ito, Y. Hama, T. Inomata, M. Fujii, T. Nishio, N. Nakamura, and K. Nakagawa, "Investigation of the feasibility of a simple method for verifying the motion of a binary multileaf collimator synchronized with the rotation of the gantry for helical tomotherapy," *Journal of Applied Clinical Medical Physics*, vol. 13, no. 1, 2012.
- [218] Q. Chen, D. Westerly, Z. Fang, K. Sheng, and Y. Chen, "Tomotherapy mlc verification using exit detector data," *Medical Physics*, vol. 39, no. 1, pp. 143–152, 2012.
- [219] P. B. Greer, "Off-axis dose response characteristics of an amorphous silicon electronic portal imaging device," *Medical Physics*, vol. 34, no. 10, pp. 3815–24, 2007.
- [220] J. Chang and C. Ling, "Using the frame averaging of as500 epid for imrt verification," *Journal of Applied Clinical Medical Physics*, vol. 4, no. 4, pp. 287–299, 2003.
- [221] M. Podesta, S. M. J. J. G. Nijsten, J. Snaith, M. Orlandini, T. Lustberg, and D. Emans, "Measured vs simulated portal images for low mu fields on three accelerator types: Possible consequences for 2d portal dosimetry," *Medical Physics*, vol. 39, no. 2, pp. 7470–79, 2012.
- [222] J. H. Siewerdsen and D. A. Jaffray, "A ghost story: Spatio-temporal response characteristics of an indirect-detection flat-panel imager," *Medical Physics*, vol. 26, no. 8, pp. 1624–41, 1999.
- [223] B. Warkentin, S. Rathee, and S. Steciw, "2d lag and signal nonlinearity correction in an amorphous silicon epid and their impact on pretreatment dosimetric verification," *Medical Physics*, vol. 39, no. 11, pp. 6597–6608, 2012.
- [224] G. J. Budgell, Q. Zhang, R. J. Troncner, and R. I. Mackay, "Improving imrt quality control efficiency using an amorphous silicon electronic portal imager," *Medical Physics*, vol. 32, no. 11, pp. 3267–78, 2005.

- [225] P. Vial, S. Deshpande, G. Goozee, and L. Holloway, "Dosimetric characteristics and potential applications of the i'mrt matrixx operating in movie mode," in *EPSM-ABEC 2009*, vol. 33, pp. 65–115, Australasian Physical and Engineering Sciences in Medicine.
- [226] S. Deshpande, L. Holloway, P. Metcalfe, and P. Vial, "An integrated 2-d dosimeter and electronic portal imaging device for in-vivo dosimetry: a feasibility study," *International Journal of Radiation Oncology* Biology* Physics*, vol. 84, no. 3, p. S764, 2012.
- [227] S. Deshpande, P. Vial, and L. Holloway, "2-d radiation therapy dosimetry using epids: Dose response variation between 3 siemens electronic portal imaging devices (epids)," *Radiation Measurements*, vol. 46, no. 12, pp. 1916–1919, 2011.
- [228] P. Vial, P. B. Greer, P. Hunt, L. Oliver, and C. Baldock, "The impact of mlc transmitted radiation on epid dosimetry for dynamic mlc beams," *Medical Physics*, vol. 35, no. 4, pp. 1267–1277, 2008.
- [229] P. Qi and P. Xia, "Relationship of segment area and monitor unit efficiency in aperture-based imrt optimization," *Journal of Applied Clinical Medical Physics*, vol. 14, no. 3, 2013.
- [230] S. Steciw, B. Warkentin, S. Rathee, and B. Fallone, "Three-dimensional imrt verification with a flat-panel epid," *Medical Physics*, vol. 32, no. 2, pp. 600–612, 2005.
- [231] Y. Wang, L. E. Antonuk, Q. Zhao, Y. El-Mohri, and L. Perna, "High-dqe epids based on thick, segmented bgo and csi: Tl scintillators: Performance evaluation at extremely low dose," *Medical Physics*, vol. 36, no. 12, pp. 5707–5718, 2009.
- [232] J. Qian, L. Lee, W. Liu, K. Chu, E. Mok, G. Luxton, Q.-T. Le, and L. Xing, "Dose reconstruction for volumetric modulated arc therapy (vmat) using cone-beam ct and dynamic log files," *Physics in Medicine and Biology*, vol. 55, no. 13, p. 3597, 2010.
- [233] J. D. Fontenot, "Feasibility of a remote, automated daily delivery verification of volumetric-modulated arc therapy treatments using a commercial record and verify system," *Journal of Applied Clinical Medical Physics*, vol. 13, no. 2, 2012.
- [234] B. Neal, M. Ahmed, K. Kathuria, T. Watkins, K. Wijesooriya, and J. Siebers, "A clinically observed discrepancy between image-based and log-based mlc positions," *Medical Physics*, vol. 43, no. 6, pp. 2933–2935, 2016.

- [235] P. Vial, "In-vivo dosimetry for imrt," *Proceedings of the SSD summer school Concept and trends in medical radiation dosimetry*, vol. 1345, pp. 165–180, 2011.
- [236] J. A. Moore and J. V. Siebers, "Verification of the optimal backscatter for an asi electronic portal imaging device," *Physics in Medicine and Biology*, vol. 50, p. 2341–2350, 2005.
- [237] D. M. Tucker, M. Souto, and G. T. Barnes, "Scatter in computed radiography," *Radiology*, vol. 188, pp. 271–274, 1993.
- [238] S. Saminathan, R. Manickam, V. Chandraraj, and S. S. Supe, "Dosimetric study of 2d ion chamber array matrix for the modern radiotherapy treatment verification," *Journal of Applied Clinical Medical Physics*, vol. 11, no. 2, 2010.
- [239] N. Papanikolaou, J. J. Battista, A. L. Boyer, C. Kappas, E. Klein, T. R. Mackie, M. Sharpe, and J. Van Dyk, "Tissue inhomogeneity corrections for megavoltage photon beams," *AAPM Task Group*, vol. 65, pp. 1–142, 2004.
- [240] D. A. Low, W. B. Harms, S. Mutic, and J. A. Purdy, "A technique for the quantitative evaluation of dose distributions," *Medical Physics*, vol. 25, no. 5, pp. 656–661, 1998.
- [241] A. Gopal and S. S. Samant, "Use of a line-pair resolution phantom for comprehensive quality assurance of electronic portal imaging devices based on fundamental imaging metrics," *Medical Physics*, vol. 6, no. 36, pp. 2006–2015, 2009.
- [242] P. Munro, J. Rawlinson, and A. Fenster, "Therapy imaging a signal to noise analysis of metal plate film detectors," *Medical Physics*, vol. 14, no. 6, pp. 975–984, 1987.
- [243] R.T.Droege, "A megavoltage mtf measurement technique for metal screen film detectors," *Medical Physics*, vol. 6, no. 4, pp. 272–279, 1979.
- [244] A. Sawant, L. E. Antonuk, and Y. El-Mohri, "Slit design for efficient and accurate mtf measurement at megavoltage x-ray energies," *Medical Physics*, vol. 34, no. 5, pp. 1535–1545, 2007.
- [245] H. Fujita, D.-Y. Tsai, T. Itoh, K. Doi, J. Morishita, K. Ueda, and A. Ohtsuka, "A simple method for determining the modulation transfer function in digital radiography," *IEEE Transactions on Medical Imaging*, vol. 11, pp. 34–39, 1992.

- [246] T. Fuangrod, H. C. Woodruff, E. v. Uytven, B. M. C. McCurdy, Z. Kuncic, D. J. O'Connor, and P. B. Greer, "A system for epid-based real-time treatment delivery verification during dynamic imrt treatment," *Medical Physics*, vol. 40, no. 9, pp. 091907 (1–11), 2013.
- [247] A. Sawant, L. E. Antonuk, Y. El-Mohri, Q. Zhao, Y. Li, Z. Su, Y. Wang, J. Yamamoto, H. Du, and I. Cunningham, "Segmented crystalline scintillators: An initial investigation of high quantum efficiency detectors for megavoltage x-ray imaging," *Medical Physics*, vol. 32, no. 10, pp. 3067–3083, 2005.
- [248] P. B. Greer, "Correction of pixel sensitivity variation and off-axis response for amorphous silicon epid dosimetry," *Medical Physics*, vol. 32, no. 12, pp. 3558–3568, 2005.
- [249] S. Deshpande, A. L. McNamara, L. Holloway, P. Metcalfe, and P. Vial, "Feasibility study of a dual detector configuration concept for simultaneous megavoltage imaging and dose verification in radiotherapy," *Medical Physics*, vol. 42, no. 4, pp. 1753–1764, 2015.
- [250] J. Wong, I. Fuduli, M. Carolan, M. Petasecca, M. Lerch, V. Perevertaylo, P. Metcalfe, and A. B. Rosenfeld, "Characterization of a novel two dimensional diode array the "magic plate" as a radiation detector for radiation therapy treatment," *Medical Physics*, vol. 39, no. 5, pp. 2544–2558, 2012.
- [251] Z. A. Alrowaili, M. L. Lerch, M. Petasecca, M. G. Carolan, P. E. Metcalfe, and A. B. Rosenfeld, "Beam perturbation characteristics of a 2d transmission silicon diode array, magic plate," *Journal of Applied Clinical Medical Physics*, vol. 17, no. 2, 2016.
- [252] Z. Alrowaili, M. L. Lerch, M. Carolan, I. Fuduli, C. Porumb, M. Petasecca, P. Metcalfe, and A. B. Rosenfeld, "2d mapping of the mv photon fluence and 3d dose reconstruction in real time for quality assurance during radiotherapy treatment," *Journal of Instrumentation*, vol. 10, no. 09, p. P09019, 2015.
- [253] A. L. Kwan, J. A. Seibert, and J. M. Boone, "An improved method for flat-field correction of flat panel x-ray detector," *Medical Physics*, vol. 33, no. 2, pp. 391–393, 2006.
- [254] J. Shen, J. Metz, T. Zhu, J. Panetta, J. Finlay, M. Xu-Welliver, J. Plastaras, A. V. Bar, and S. Both, "Dosimetric consequences of pancreatic tumor motion when predetermined treatment margins are employed during intensity-modulated radiation ther-

- apy,” *Journal of BU ON.: official Journal of the Balkan Union of Oncology*, vol. 17, no. 3, pp. 526–532, 2011.
- [255] B. Zhao, Y. Yang, T. Li, X. Li, D. E. Heron, and M. S. Huq, “Dosimetric effect of intrafraction tumor motion in phase gated lung stereotactic body radiotherapy,” *Medical Physics*, vol. 39, no. 11, pp. 6629–6637, 2012.
- [256] M. Woo and A. Nico, “Impact of multileaf collimator leaf positioning accuracy on intensity modulation radiation therapy quality assurance ion chamber measurements,” *Medical Physics*, vol. 32, no. 5, pp. 1440–1445, 2005.
- [257] W. Luo, J. Li, R. A. Price Jr, L. Chen, J. Yang, J. Fan, Z. Chen, S. McNeeley, X. Xu, and C.-M. Ma, “Monte carlo based imrt dose verification using mlc log files and r/v outputs,” *Medical Physics*, vol. 33, no. 7, pp. 2557–2564, 2006.
- [258] T. Knoos, A. Ahnesjö, P. Nilsson, and L. Weber, “Limitations of a pencil beam approach to photon dose calculations in lung tissue,” *Physics in Medicine and Biology*, vol. 40, no. 9, p. 1411, 1995.
- [259] D. W. Bailey, L. Kumaraswamy, M. Bakhtiari, H. K. Malhotra, and M. B. Podgorsak, “Epid dosimetry for pretreatment quality assurance with two commercial systems,” *Journal of Applied Clinical Medical Physics*, vol. 13, no. 4, 2012.
- [260] J. Gimeno, M. Pujades, T. García, V. Carmona, F. Lliso, R. Palomo, C. Candela-Juan, J. Richart, and J. Perez-Calatayud, “Commissioning and initial experience with a commercial software for in vivo volumetric dosimetry,” *Physica Medica*, vol. 30, no. 8, pp. 954–959, 2014.
- [261] J. Liebich, J. Licher, C. Scherf, E. Kara, N. Koch, C. Rödel, and U. Ramm, “Simple proposal for dosimetry with an Elekta iViewGT™ electronic portal imaging device (epid) using commercial software modules,” *Strahlentherapie und Onkologie*, vol. 187, no. 5, pp. 316–321, 2011.
- [262] B. E. Nelms, K. H. Rasmussen, and W. A. Tome, “Evaluation of a fast method of epid-based dosimetry for intensity modulated radiation therapy,” *Journal of Applied Clinical Medical Physics*, vol. 11, no. 2, p. 3185, 2010.
- [263] J. Martínez Ortega, N. Gómez González, P. Castro Tejero, M. Pinto Monedero, N. Tolani, L. Núñez Martín, and R. Sánchez Montero, “A portal dosimetry dose pre-

- diction method based on collapsed-cone algorithm using the clinical beam model,” *Medical Physics*, 2016.
- [264] I. Yohannes, H. Prasetyo, and C. Bert, “Noncoplanar verification: a feasibility study using philips’ pinnacle3 treatment planning system,” *Journal of Applied Clinical Medical Physics*, vol. 16, no. 6, 2015.
- [265] A. E. Millin, R. S. Windle, and D. G. Lewis, “A comparison of electronic portal dosimetry verification methods for use in stereotactic radiotherapy,” *Physica Medica*, 2015.
- [266] P. Vial, S. J. Blake, A. L. McNamara, L. Holloway, P. B. Greer, and Z. Kuncic, “A new concept in detector design for radiation therapy: simultaneous imaging and dosimetry for comprehensive treatment verification,” in *Nuclear Science Symposium and Medical Imaging Conference (NSS/MIC), 2013 IEEE*, pp. 1–6, IEEE.
- [267] S. J. Blake, A. L. McNamara, P. Vial, L. Holloway, and Z. Kuncic, “Optimisation of the imaging and dosimetric characteristics of an electronic portal imaging device employing plastic scintillating fibres using monte carlo simulations,” *Physics in Medicine and Biology*, vol. 59, no. 22, p. 6827, 2014.
- [268] S. J. Blake, Z. Cheng, S. Atakaramians, S. Meikle, M. Lu, P. Vial, and Z. Kuncic, “In silico investigation of factors affecting the mv imaging performance of a novel water-equivalent epid,” *Physica Medica*, vol. 32, no. 12, pp. 1819–1826, 2016.
- [269] A. Ahnesjö and M. M. Aspradakis, “Dose calculations for external photon beams in radiotherapy,” *Physics in Medicine and Biology*, vol. 44, no. 11, p. R99, 1999.
- [270] L. Parent, J. Seco, P. M. Evans, A. Fielding, and D. R. Dance, “Monte carlo modelling of a-si epid response: the effect of spectral variations with field size and position,” *Medical Physics*, vol. 33, no. 12, pp. 4527–4540, 2006.
- [271] “Pinnacle physics reference guide, version 8.0 document number 9201-5135a-eng,” A. Amsterdam: Philips Medical Systems, 2006.
- [272] G. Starkschall, R. E. Steadham, R. A. Popple, S. Ahmad, and I. I. Rosen, “Beam-commissioning methodology for a three-dimensional convolution/superposition photon dose algorithm,” *Journal of Applied Clinical Medical Physics*, vol. 1, no. 1, pp. 8–27, 2000.

- [273] M. Podesta, S. M. J. J. G. Nijsten, L. C. G. G. Persoon, S. G. Scheib, C. Baltes, and F. Verhaegen, "Time dependent pre-treatment epid dosimetry for standard and fff vmat," *Physics in Medicine and Biology*, vol. 59, no. 16, p. 4749, 2014.
- [274] P. Andreo, J. Cramb, B. Fraass, F. Ionescu-Farca, J. Izewska, V. Levin, B. Mijnheer, J. Rosenwald, P. Scalliet, K. Shortt, *et al.*, "Commissioning and quality assurance of computerized planning systems for radiation treatment of cancer," *International Atomic Energy Agency technical report series*, no. 430, 2004.
- [275] H. Schiefer, A. Fogliata, G. Nicolini, L. Cozzi, W. Seelentag, E. Born, F. Hasenbalg, J. Roth, B. Schnekenburger, K. Münch-Berndl, *et al.*, "The swiss imrt dosimetry intercomparison using a thorax phantom," *Medical physics*, vol. 37, no. 8, pp. 4424–4431, 2010.
- [276] T. Knöös, E. Wieslander, L. Cozzi, C. Brink, A. Fogliata, D. Albers, H. Nyström, and S. Lassen, "Comparison of dose calculation algorithms for treatment planning in external photon beam therapy for clinical situations," *Physics in medicine and biology*, vol. 51, no. 22, p. 5785, 2006.
- [277] X. Y. Cedric, C. J. Amies, and M. Svatos, "Planning and delivery of intensity-modulated radiation therapy," *Medical Physics*, vol. 35, no. 12, pp. 5233–5241, 2008.
- [278] D. N. Margalit, Y.-H. Chen, P. J. Catalano, K. Heckman, T. Vivenzio, K. Nissan, L. D. Wolfsberger, R. A. Cormack, P. Mauch, and A. K. Ng, "Technological advancement and error rates in radiation therapy delivery," *International Journal of Radiation Oncology* Biology* Physics*, vol. 81, no. 4, pp. e673–e679, 2011.
- [279] D. Tatsumi, M. Hosono, R. Nakada, K. Ishii, S. Tsutsumi, M. Inoue, T. Ichida, and Y. Miki, "Direct impact analysis of multi-leaf collimator leaf position errors on dose distributions in volumetric modulated arc therapy: a pass rate calculation between measured planar doses with and without the position errors," *Physics in Medicine and Biology*, vol. 56, no. 20, p. N237, 2011.
- [280] D. A. Low, X. R. Zhu, J. A. Purdy, and S. Söderström, "The influence of angular misalignment on fixed-portal intensity modulated radiation therapy," *Medical Physics*, vol. 24, no. 7, pp. 1123–1139, 1997.
- [281] L. Xing, Z.-X. Lin, S. S. Donaldson, Q. T. Le, D. Tate, D. R. Goffinet, S. Wolden, L. Ma, and A. L. Boyer, "Dosimetric effects of patient displacement and collimator

- and gantry angle misalignment on intensity modulated radiation therapy,” *Radiotherapy and Oncology*, vol. 56, no. 1, pp. 97–108, 2000.
- [282] J. D. Fenwick, W. A. Tomé, M. W. Kissick, and T. R. Mackie, “Modelling simple helically delivered dose distributions,” *Physics in Medicine and Biology*, vol. 50, no. 7, p. 1505, 2005.
- [283] L. C. Holloway, J. A. Miller, S. Kumar, B. M. Whelan, and S. K. Vinod, “Comp plan: A computer program to generate dose and radiobiological metrics from dose-volume histogram files,” *Medical Dosimetry*, vol. 37, no. 3, pp. 305–319, 2012.
- [284] D. C. Westerly, E. Soisson, Q. Chen, K. Woch, L. Schubert, G. Olivera, and T. R. Mackie, “Treatment planning to improve delivery accuracy and patient throughput in helical tomotherapy,” *International Journal of Radiation Oncology* Biology* Physics*, vol. 74, no. 4, pp. 1290–1297, 2009.
- [285] G. Mu, E. Ludlum, and P. Xia, “Impact of mlc leaf position errors on simple and complex imrt plans for head and neck cancer,” *Physics in Medicine and Biology*, vol. 53, no. 1, p. 77, 2007.
- [286] J. V. Siebers, P. J. Keall, Q. Wu, J. F. Williamson, and R. K. Schmidt-Ullrich, “Effect of patient setup errors on simultaneously integrated boost head and neck imrt treatment plans,” *International Journal of Radiation Oncology* Biology* Physics*, vol. 63, no. 2, pp. 422–433, 2005.
- [287] J. Dutreix, M. Tubiana, and A. Dutreix, “An approach to the interpretation of clinical data on the tumour control probability-dose relationship,” *Radiotherapy and Oncology*, vol. 11, no. 3, pp. 239–248, 1988.
- [288] K. U. Hunter, L. L. Fernandes, K. A. Vineberg, D. McShan, A. E. Antonuk, C. Cornwall, M. Feng, M. J. Schipper, J. M. Balter, and A. Eisbruch, “Parotid glands dose–effect relationships based on their actually delivered doses: implications for adaptive replanning in radiation therapy of head-and-neck cancer,” *International Journal of Radiation Oncology* Biology* Physics*, vol. 87, no. 4, pp. 676–682, 2013.
- [289] M. W. Kissick, J. Fenwick, J. A. James, R. Jeraj, J. M. Kapatoes, H. Keller, T. R. Mackie, G. Olivera, and E. T. Soisson, “The helical tomotherapy thread effect,” *Medical Physics*, vol. 32, no. 5, pp. 1414–1423, 2005.

- [290] M. Chen, Y. Chen, Q. Chen, and W. Lu, "Theoretical analysis of the thread effect in helical tomotherapy," *Medical Physics*, vol. 38, no. 11, pp. 5945–5960, 2011.
- [291] L. L. Handsfield, R. Jones, D. D. Wilson, J. V. Siebers, P. W. Read, and Q. Chen, "Phantomless patient-specific tomotherapy qa via delivery performance monitoring and a secondary monte carlo dose calculation," *Medical Physics*, vol. 41, no. 10, p. 101703, 2014.
- [292] D. W. Litzenberg, J. M. Moran, and B. A. Fraass, "Verification of dynamic and segmental imrt delivery by dynamic log file analysis," *Journal of Applied Clinical Medical Physics*, vol. 3, no. 2, pp. 63–72, 2002.
- [293] N. Tyagi, K. Yang, D. Gersten, and D. Yan, "A real time dose monitoring and dose reconstruction tool for patient specific vmat qa and delivery," *Medical Physics*, vol. 39, no. 12, pp. 7194–7204, 2012.
- [294] B. Paliwal and D. Tewatia, "Advances in radiation therapy dosimetry," *Journal of Medical Physics*, vol. 34, no. 3, p. 108, 2009.
- [295] S. Syamkumar, S. Padmanabhan, P. Sukumar, and V. Nagarajan, "Characterization of responses of 2d array seven29 detector and its combined use with octavius phantom for the patient-specific quality assurance in rapidarc treatment delivery," *Medical Dosimetry*, vol. 37, no. 1, pp. 53–60, 2012.
- [296] V. Chandraraj, S. Stathakis, R. Manickam, C. Esquivel, S. S. Supe, and N. Papanikolaou, "Comparison of four commercial devices for rapidarc and sliding window imrt qa," *Journal of Applied Clinical Medical Physics*, vol. 12, no. 2, 2011.
- [297] S. Xu, C. Xie, Z. Ju, X. Dai, H. Gong, L. Wang, and J. Yang, "Dose verification of helical tomotherapy intensity modulated radiation therapy planning using 2d-array ion chambers," *Biomed Imaging Interv J*, vol. 6, no. 2, p. e24, 2010.
- [298] X. Chuanbin, X. Shouping, J. Zhongjian, D. Xiangkun, G. Ruigang, and G. Han-shun, "A comparison between two-dimensional ion chamber array and edr2 film for intensity modulated planning of helical tomotherapy," *Chinese Journal of Radiation Oncology*, vol. 20, no. 4, pp. 330–333, 2011.
- [299] C. Neilson, M. Klein, R. Barnett, and S. Yartsev, "Delivery quality assurance with arccheck," *Medical Dosimetry*, vol. 38, no. 1, pp. 77–80, 2013.

- [300] M. Geurts, J. Gonzalez, and P. Serrano-Ojeda, “Longitudinal study using a diode phantom for helical tomotherapy imrt qa,” *Medical Physics*, vol. 36, no. 11, pp. 4977–4983, 2009.
- [301] P. Myers, S. Stathakis, A. N. Gutiérrez, C. Esquivel, P. Mavroidis, and N. Papanikolaou, “Evaluation of ptw seven29 for tomotherapy patient-specific quality assurance and comparison with scandidos delta4,” *Journal of medical physics*, vol. 37, no. 2, p. 72, 2012.
- [302] A. Carver, M. Gilmore, S. Riley, J. Uzan, and P. Mayles, “An analytical approach to acceptance criteria for quality assurance of intensity modulated radiotherapy,” *Radiotherapy and Oncology*, vol. 100, no. 3, pp. 453–455, 2011.
- [303] S. Deshpande, A. Xing, A. George, L. Holloway, P. Vial, P. Metcalfe, D. Thwaites, M. Lee, and M. Geurts, “Clinical significance of treatment delivery errors for tomotherapy treatment – a dosimetric simulation study,” *Journal of Medical Radiation Sciences*, vol. 61, no. Supplement S1, p. 57, 2014.
- [304] S. Deshpande, M. Geurts, P. Vial, P. Metcalfe, M. Lee, and L. Holloway, “Clinical significance of treatment delivery errors for helical tomotherapy nasopharyngeal plans—a dosimetric simulation study,” *Physica Medica*, vol. 33, pp. 159–169, 2017.
- [305] N. Y. Lee, Q. Zhang, D. G. Pfister, J. Kim, A. S. Garden, J. Mechalakos, K. Hu, Q. T. Le, A. D. Colevas, and B. S. Glisson, “Addition of bevacizumab to standard chemoradiation for locoregionally advanced nasopharyngeal carcinoma (rtog 0615): a phase 2 multi-institutional trial,” *The Lancet Oncology*, vol. 13, no. 2, pp. 172–180, 2012.
- [306] M. Aristophanous, Y. Suh, P. C. Chi, L. J. Whittlesey, S. LaNeave, and M. K. Martel, “Initial clinical experience with arccheck for imrt/vmat qa,” *Journal of Applied Clinical Medical Physics*, vol. 17, no. 5, 2016.
- [307] S. Bresciani, A. Di Dia, A. Maggio, C. Cutaia, A. Miranti, E. Infusino, and M. Stasi, “Tomotherapy treatment plan quality assurance: the impact of applied criteria on passing rate in gamma index method,” *Medical Physics*, vol. 40, no. 12, p. 121711, 2013.
- [308] S. J. Thomas and I. R. Cowley, “A comparison of four indices for combining distance and dose differences,” *International Journal of Radiation Oncology* Biology* Physics*, vol. 82, no. 5, pp. e717–e723, 2012.

- [309] Y. Shimohigashi, F. Araki, H. Tominaga, J. Sakata, K. Kawasaki, N. Kanetake, Y. Iwashita, S. Yoshimura, T. Kawakami, T. Ishihara, *et al.*, “Angular dependence correction of matrix and its application to composite dose verification,” *Journal of Applied Clinical Medical Physics*, vol. 13, no. 5, 2012.
- [310] V. Chaswal, M. Weldon, N. Gupta, A. Chakravarti, and Y. Rong, “Commissioning and comprehensive evaluation of the arccheck cylindrical diode array for vmat pre-treatment delivery qa,” *Journal of Applied Clinical Medical Physics*, vol. 15, no. 4, 2014.
- [311] T. Craig, J. Battista, and J. Van Dyk, “Limitations of a convolution method for modeling geometric uncertainties in radiation therapy. ii. the effect of a finite number of fractions,” *Medical Physics*, vol. 30, no. 8, pp. 2012–2020, 2003.
- [312] J. Balog, G. Olivera, and J. Kapatoes, “Clinical helical tomotherapy commissioning dosimetry,” *Medical Physics*, vol. 30, no. 12, pp. 3097–3106, 2003.
- [313] M. Geurts, J. Gonzalez, and P. Serrano-Ojeda, “Longitudinal study using a diode phantom for helical tomotherapy imrt qa,” *Medical Physics*, vol. 36, no. 11, pp. 4977–4983, 2009.
- [314] A. Van Esch, C. Clermont, M. Devillers, M. Iori, and D. P. Huyskens, “On-line quality assurance of rotational radiotherapy treatment delivery by means of a 2d ion chamber array and the octavius phantom,” *Medical Physics*, vol. 34, no. 10, pp. 3825–3837, 2007.
- [315] G. Bauman, S. Yartsev, T. Coad, B. Fisher, and T. Kron, “Helical tomotherapy for craniospinal radiation,” *The British Journal of Radiology*, 2014.
- [316] S. K. Hui, J. Kapatoes, J. Fowler, D. Henderson, G. Olivera, R. R. Manon, B. Gerbi, T. R. Mackie, and J. S. Welsh, “Feasibility study of helical tomotherapy for total body or total marrow irradiation),” *Medical Physics*, vol. 32, no. 10, pp. 3214–3224, 2005.
- [317] W. Parker, M. Brodeur, D. Roberge, and C. Freeman, “Standard and nonstandard craniospinal radiotherapy using helical tomotherapy,” *International Journal of Radiation Oncology* Biology* Physics*, vol. 77, no. 3, pp. 926–931, 2010.
- [318] J. A. Peñagaricano, N. Papanikolaou, Y. Yan, E. Youssef, and V. Ratanatharathorn, “Feasibility of cranio-spinal axis radiation with the hi-art tomotherapy system,” *Radiotherapy and Oncology*, vol. 76, no. 1, pp. 72–78, 2005.

- [319] T. E. Schultheiss, J. Wong, A. Liu, G. Olivera, and G. Somlo, "Image-guided total marrow and total lymphatic irradiation using helical tomotherapy," *International Journal of Radiation Oncology* Biology* Physics*, vol. 67, no. 4, pp. 1259–1267, 2007.
- [320] J. Y. Wong, J. Rosenthal, A. Liu, T. Schultheiss, S. Forman, and G. Somlo, "Image-guided total-marrow irradiation using helical tomotherapy in patients with multiple myeloma and acute leukemia undergoing hematopoietic cell transplantation," *International Journal of Radiation Oncology* Biology* Physics*, vol. 73, no. 1, pp. 273–279, 2009.
- [321] Y. Takahashi and S. K. Hui, "Fast, simple, and informative patient-specific dose verification method for intensity modulated total marrow irradiation with helical tomotherapy," *Radiation Oncology*, vol. 9, no. 1, p. 1, 2014.
- [322] M. Alber, B. Mijnheer, and D. Georg, *Guidelines for the verification of IMRT*. Estro Brussels, Belgium, 2008.
- [323] M. Stasi, S. Bresciani, A. Miranti, A. Maggio, V. Sapino, and P. Gabriele, "Pretreatment patient-specific imrt quality assurance: A correlation study between gamma index and patient clinical dose volume histogram," *Medical Physics*, vol. 39, no. 12, pp. 7626–7634, 2012.
- [324] K. Sheng, R. Jones, W. Yang, S. Saraiya, B. Schneider, Q. Chen, G. Sobering, G. Olivera, and P. Read, "3d dose verification using tomotherapy ct detector array," *International Journal of Radiation Oncology* Biology* Physics*, vol. 82, no. 2, pp. 1013–1020, 2012.
- [325] K. Langen, S. Meeks, D. Poole, T. Wagner, T. Willoughby, O. Zeidan, P. Kupelian, K. Ruchala, and G. Olivera, "Evaluation of a diode array for qa measurements on a helical tomotherapy unit," *Medical Physics*, vol. 32, no. 11, pp. 3424–3430, 2005.
- [326] Y. El-Mohri, L. E. Antonuk, J. Yorkston, K.-W. Jee, M. Maolinbay, K. L. Lam, and J. Siewerdsen, "Relative dosimetry using active matrix flat-panel imager (amfpi) technology," *Medical Physics*, vol. 26, no. 8, pp. 1530–1541, 1999.
- [327] A. Xing, S. Arumugam, S. Deshpande, G. Armia, L. Holloway, G. Goozee, A. Gray, and P. Vial, "Streamlining epid-based imrt quality assurance: auto-analysis and auto-report generation," in *Journal of Physics: Conference Series*, vol. 489, p. 012084, IOP Publishing, 2014.

- [328] S. J. Thomas, K. R. Eyre, G. S. J. Tudor, and J. Fairfoul, “Dose calculation software for helical tomotherapy, utilizing patient ct data to calculate an independent three-dimensional dose cube,” *Medical Physics*, vol. 39, no. 1, pp. 160–167, 2012.
- [329] R. B. Barriger, J. A. Forquer, J. G. Brabham, D. L. Andolino, R. H. Shapiro, M. A. Henderson, P. A. Johnstone, and A. J. Fakiris, “A dose–volume analysis of radiation pneumonitis in non–small cell lung cancer patients treated with stereotactic body radiation therapy,” *International Journal of Radiation Oncology* Biology* Physics*, vol. 82, no. 1, pp. 457–462, 2012.
- [330] G. M. Videtic, C. Hu, A. K. Singh, J. Y. Chang, W. Parker, K. R. Olivier, S. E. Schild, R. Komaki, J. J. Urbanic, and H. Choy, “A randomized phase 2 study comparing 2 stereotactic body radiation therapy schedules for medically inoperable patients with stage i peripheral non-small cell lung cancer: Nrg oncology rtog 0915 (ncctg n0927),” *International Journal of Radiation Oncology* Biology* Physics*, vol. 93, no. 4, pp. 757–764, 2015.

Appendix A

LSF and MTF measurement

To assess the impact on imaging performance due to the presence of 2D dosimeter in dual detector configuration, the MTF was determined using an angled slit technique as described in chapter 4. A purpose built LSF apparatus with slit angle set to 4^0 was used for MV image quality experiments. Two 2D dosimeter (ICA and MP) were used. Three different configurations of dual detector were investigated i) MP placed beneath the EPID ii) MP placed above the EPID and iii) ICA placed above the EPID. EPID images of the slit for both reference imaging configuration i.e. standard EPID and dual detector configuration were acquired. The calculated MTF and LSF for reference imaging configuration was compared with dual detector configuration as shown in figure (Figure A.1) and (Figure A.2)

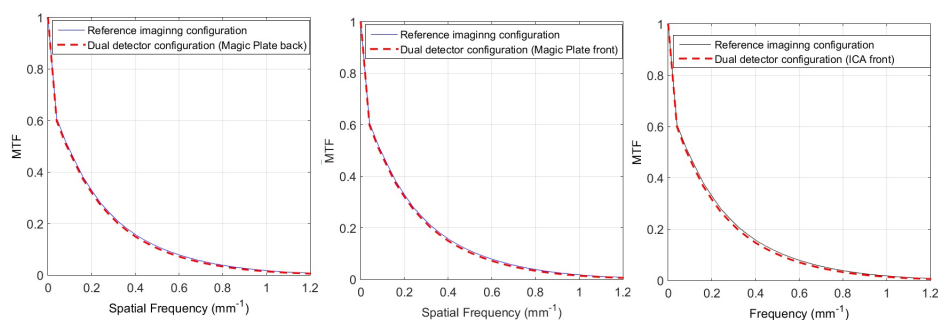


Figure A.1: Comparison of measured modulation transfer function (MTF) for the reference imaging configuration versus dual detector configuration (MP placed beneath EPID) on left, reference imaging configuration versus dual detector configuration (MP placed above EPID) in middle and reference imaging configuration versus dual detector configuration (ICA placed above EPID) on right.

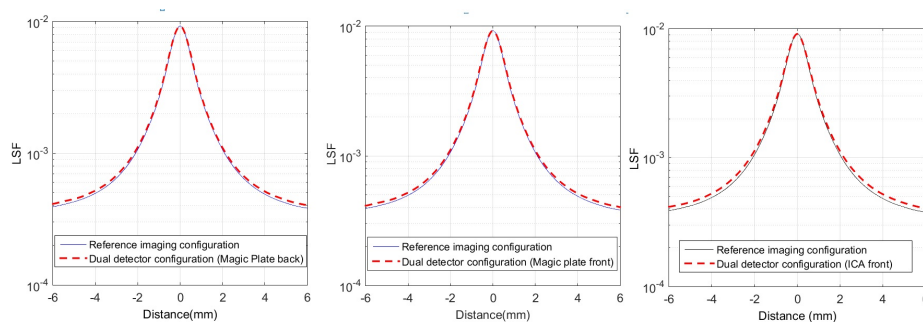


Figure A.2: Comparison of measured line spread function (LSF) for the reference imaging configuration versus dual detector configuration (MP placed beneath EPID) on left, reference imaging configuration versus dual detector configuration (MP placed above EPID) in middle and reference imaging configuration versus dual detector configuration (ICA placed above EPID) on right.

Appendix B

Tomotherapy error simulation for lung SABR

The clinical impact due to changes in delivery parameter for lung SABR plans was assessed via dosimetric simulation. We used same framework and similar delivery errors discussed in chapter 7. Ten clinical lung SABR (HT) plans were selected for this study. All clinical plans were optimised using a fixed 2.5 cm jaw width, 0.286 pitch and 1.6-1.8 modulation factor with the clinical HT planning system. Each plan was edited using the TomoTherapy version 5.0 standalone GPU dose calculator (Research planning system) to introduce systematic errors in jaw width (JW), couch speed (CS), gantry period (GP), gantry start position (GSP), multi leaf collimator leaf open time (MLC LOT) errors with an individual MLC leaf (either 32, 42 or 52) stuck open. For the case of MLC LOT, the random errors in MLC LOT with standard deviation of 1-10% with a mean MLC LOT error of zero were investigated. Each error type was simulated independently for a range of magnitudes. Dose metrics and associate clinical thresholds were assessed for the following structures: (D98% = prescription dose and D99% \geq 90% of prescription dose and conformity index), (lung-PTV) mean dose < 4Gy), heart ($D_{1cc} < 27\text{Gy}$) and oesophagus ($D_{1cc} < 28.5\text{Gy}$) and maximum point dose to spinal cord < 25 Gy and great vessels < 45Gy) were assessed [329, 330]. The magnitude for each of the errors where the clinical tolerance values was exceeded for any treatment plan was determined. The errors where the clinical tolerance was exceeded were compared against both the current machine interlock thresholds and quality assurance (QA) tolerance values

[‡]Part of work presented in ICCR 2016 conference, London UK

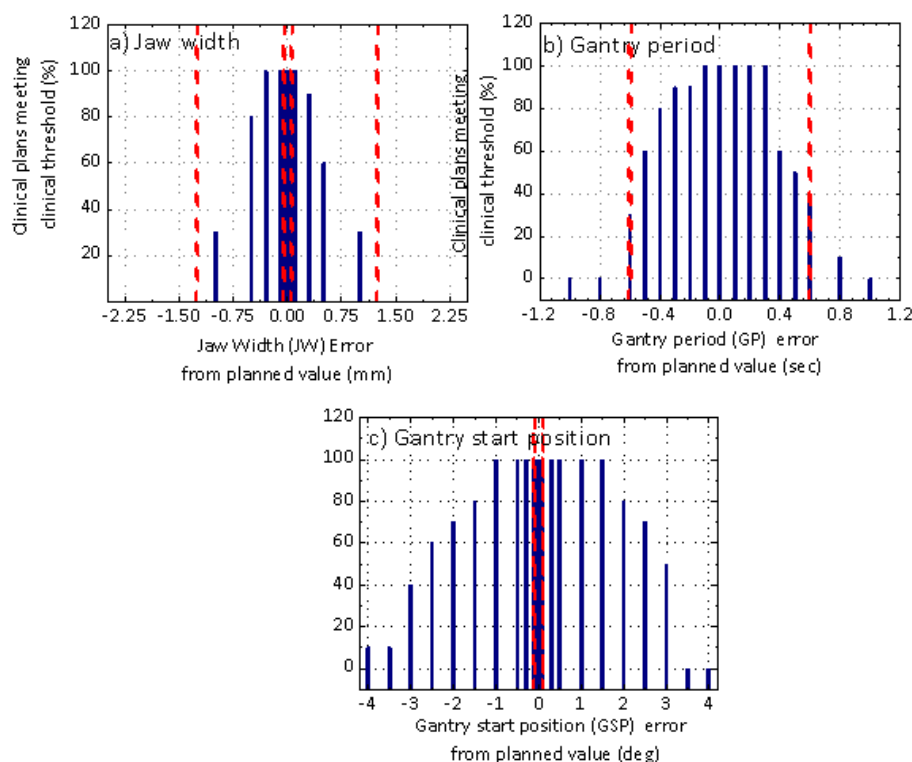


Figure B.1: Histogram distribution of the treatment plans meeting the set clinical tolerances (both PTV and OAR) for varying magnitude of errors in a) jaw width (JW) b) couch speed (CS) c) gantry period (GP) and d) gantry start position (GSP). The red dashed bar shown above represents the machine interlock threshold for each error type. The green line shown above represents the machine QA thresholds as specified by TG-148 report.

as outlined in AAPM report 148 [47]. The dosimetric QA tolerance derived for nasopharynx cases were compared to assess whether generic QA tolerance can be used for all HT plan techniques.

Most of the clinically relevant errors are prevented by machine interlocks except the couch position and the secondary interlock for jaw position and gantry period. This work highlights that the interlock thresholds for jaw position, gantry period and couch position should be monitored more precisely than monitored currently to avoid any clinically relevant delivery errors. Clinically significant machine tolerances were similar between lung SABR and previous Head and Neck clinical cases (7) for JW and CS and different for gantry related error. However, If the clinical HT machine QA tolerance are maintained within the specifications outlined in AAPM TG 148 recommendation, all the clinically relevant errors derived for both clinical cases having varying complexity would

be prevented. This validates the AAPM TG-148 recommendations to have a generic QA tolerance table irrespective to the complexity of treatment techniques unlike for conventional C-arm Linac (TG-142).

Table B.1: Comparing the dosimetrically derived QA tolerances for lung SABR, nasopharynx cases with AAPM TG-148 recommended machine QA tolerance. The nasopharynx data is taken from chapter 7.

Machine parameter	Clinically relevant errors (from planned value) Lung SABR	Clinically relevant errors (from planned value) Nasopharynx plans	AAPM TG-148 QA tolerance
Jaw width	> 0.5mm	> 0.5mm	1% of JW (0.25 mm for 2.5cm JW)
Couch speed	> 1.5%	> 1.5%	< 2%
Gantry period	> 0.6 sec	1.5 sec	No specific tolerance
Gantry start position	>1 ⁰	>2 ⁰	1 ⁰
MLC LOT	Relatively insensitive for both systematic error and random error	MLC LOT systematic error (MLC stuck open)	No specific tolerance and test

Appendix C

Description of values retrieved from the patient XML in exit dosimetry DQA tool

The XPath Java TM API library (javax.xml.xpath) is leveraged to read the patient XML into MATLAB. The XPath expression //fullDeliveryPlanDataArray/fullDeliveryPlanDataArray is used to identify all delivery plans; Table C.4 lists the XPath sub-expressions and parameters extracted for each delivery plan.

Table C.1: Values retrieved from the patient XML for determination of the planned fluence

XPath Expression	Description
deliveryPlan/purpose	Delivery plan purpose (fluence, machine specific/agnostic)
deliveryPlan/dbInfo/databaseParent	Delivery plan parent Unique Identifier (UID)
deliveryPlan/dbInfo/creationTimestamp/date	Creation Date
deliveryPlan/dbInfo/creationTimestamp/time	Creation Time
deliveryPlan/scale	Plan scale
deliveryPlan/totalTau	Number of leaf events
deliveryPlan/states/states/lowerLeafIndex	Leaf number of the first leaf in the delivery plan binary array
deliveryPlan/states/states/numberOfProjections	Number of projections in binary array
deliveryPlan/states/states/numberOfLeaves	Number of leaves in binary array
deliveryPlan/states/states/synchronizeActions/synchronizeActions/jawVelocity/	List of front and back jaw velocity changes during plan
binaryFileNameArray/binaryFileNameArray	File name of binary array containing leaf events

Dose re-calculation is performed using the TomoTherapy version 5.0 standalone

dose calculator, provided with a research treatment planning workstation through a collaboration agreement with Accuray Incorporated. The standalone dose calculator accepts a series of input files listed in Table C.2.

Table C.2: Files required for execution of the standalone dose calculator

Input File	Description
dcom.header	Text file containing beam model information specific to the commissioned TomoTherapy Treatment System. Additional binary files (below) are referenced by this file.
cone.img	Binary file containing the transverse profile. Also used to determine the expected open field fluence
penumbra.img	Binary file containing the longitudinal/jaw profiles for various field sizes.
lft.img	Binary file containing the MLC leaf penumbra profiles.
fat.img	Binary file containing the Collapsed Cone Fluence Attenuation Table.
kernel.img	Binary file containing the Collapsed Cone Convolution kernel.
ct.header	Text file containing information about the size, location, and dimensions of the CT image, as well as the CT to density table.
ct_0.img	Binary file containing the CT image.
plan.header	Text file containing information about the treatment plan, including all synchronized and unsynchronized events (jaw velocities, gantry velocity, start angle, starting jaw positions, etc.), as well as the number of MLC leaf events stored in the plan.img binary file.
plan.img	Binary file containing the timing of each MLC leaf open and close event during plan delivery.
dose.cfg	Text file containing information about the size, location, and dimensions of the resulting dose calculation image.

The CT files (ct.header and ct_0.img) are generated by searching the patient XML using the XPath expression `//fullPlanDataArray/fullPlanDataArray` to load all delivery plans in the patient XML, then `plan/briefPlan/approvedPlanTrialUID` to find which approved plan is associated with the selected machine agnostic delivery plan (using the plan trial UID), then searching for the associated KVCT image using the expression `fullImageDataArray/fullImageDataArray/image`. Under this node, Table C.3 lists the XPath expressions used to extract the necessary CT specifications.

Next, the expression `plan/fullDoseIVDT` is used to determine the CT to density table associated with the fluence delivery plan identified above. A copy of the

imaging equipment archives are stored within each patient archive; by searching through the imaging equipment XML files, the CT to density table referenced by plan/fullDoseIVDT can be determined, and the table extracted.

Table C.3: Values retrieved from the patient XML for determination of the planning CT

XPath Expression	Description
imageType	Type of fullImageData. Should be KVCT.
arrayHeader/binaryFileName	File name of binary data containing the CT image.
arrayHeader/dimensions	Dimensions (x,y,z) of the CT image.
arrayHeader/start	Starting coordinate (x,y,z) of the first voxel.
arrayHeader/elementSize	Size (x,y,z) of each voxel.

This data, along with the CT data, is then written to the text file ct.header. The binary file of the CT image is written to ct_0.img. The same dimensions, coordinates, and voxel sizes are used to define the dose.cfg text file, such that dose is calculated for each CT voxel (also referred to as Fine calculation).

The plan.header file is generated by searching the patient XML for all treatment delivery parameters of the fluence delivery plan associated with the machine agnostic plan. This is accomplished by using the XPath expression //fullPlan-DataArray/fullPlanDataArray to load all delivery plans in the patient XML, then deliveryPlan/dbInfo/databaseParent to find which fluence delivery plan is associated with the selected machine agnostic delivery plan (using the parent UID). Table C.3 lists the sub-expressions used to extract each delivery parameter required.

Table C.4: Values retrieved from the patient XML for determination of the delivery parameters

XPath Expression	Description
deliveryPlan/purpose	Delivery plan purpose (fluence, machine specific/agnostic)
deliveryPlan/dbInfo/databaseParent	Delivery plan parent Unique Identifier (UID)
deliveryPlan/dbInfo/creationTimestamp/date	Creation Date
deliveryPlan/dbInfo/creationTimestamp/time	Creation Time
deliveryPlan/scale	Plan scale
deliveryPlan/totalTau	Number of leaf events
deliveryPlan/states/states/lowerLeafIndex	Leaf number of the first leaf in the delivery plan binary array
deliveryPlan/states/states/numberOfProjections	Number of projections in binary array
deliveryPlan/states/states/numberOfLeaves	Number of leaves in binary array
deliveryPlan/states/states/unsynchronizeActions/unsynchronizeActions/gantryPosition	Starting gantry position/angle
deliveryPlan/states/states/unsynchronizeActions/unsynchronizeActions/jawPosition/	Front and back starting jaw position
deliveryPlan/states/states/unsynchronizeActions/unsynchronizeActions/isocenterPosition	Isocenter position (x,y,z)
deliveryPlan/states/states/synchronizeActions/synchronizeActions/gantryVelocity	Gantry velocity
deliveryPlan/states/states/synchronizeActions/synchronizeActions/jawVelocity/	List of front and back jaw velocity changes during plan
deliveryPlan/states/states/synchronizeActions/synchronizeActions/isocenterVelocity	Isocenter velocity/couch speed
binaryFileNameArray/binaryFileNameArray	File name of binary array containing leaf events

Appendix D

Matlab Script

D.1 Codes for gamma comparison

```
A1=image1;
```

```
A2=image2;
```

```
dosed=0.03;
```

```
DTA=3;
```

```
size1=size (A1) ;
```

```
size2=size (A2) ;
```

```
dosed = dosed * max(A1 ( : ) ) ; %scale dosed as a percent of the maximum  
dose
```

```
G=zeros ( size1 ) ; %this will be the output
```

```
Ga=zeros ( size1 ) ;
```

```
if size1 == size2
```

```

for i = 1 : size1( 1 )

for j = 1 : size1( 2 )

for k = 1 : size1( 1 )

for l = 1 : size1( 2 )

r2 = ( i - k )2 + ( j - l )2; %distance (radius) squared

d2 = ( A1( i , j ) - A2( k , l ) )2 ; %difference squared

Ga( k , l ) = sqrt(r2 / (DTA)2 + d2/ (dosed)2);

end

end

G( i , j )=min(min(Ga)) ;

end

end

else

fprintf('matrices A1 and A2 are do not share the same dimensions')

end

numWithinField = nnz(G);

numpass = nnz(G<1)./numWithinField;

avg = sum(G(:))./numWithinField;

```

```

numWithinField = nnz(G);

numpass = nnz(G<1)./numWithinField;

avg = sum(G(:))./numWithinField;

figure, imagesc(G,[0 1.2]), axis('image'), colorbar;

```

D.2 Codes for MTF and LSF calculations

To calculate MTF for an angled slit image, need 2 images: one with the open slit measurement, and another with the slit shielded to give you a background reading, which we subtract from the open slit image.

Read the open-slit .his image file and shielded-slit image using following codes.

```

function image = readHISfile_Sam()

% First need to load the data...

[FileName, PathName, FilterIndex] = uigetfile('/*.his','Select .his file to analyze','MultiSelect','off');

numFiles = 1;

% Create an empty array to store the integrated image

image = double(zeros(1024,1024,numFiles));

file_id = fopen(FileName);

if file_id == -1

warning('File could not be opened');

```

```
image = -1;

else

FileType = fread(file_id,1,'uint16'); %2 bytes

HeaderSize = fread(file_id,1,'uint16'); %2 bytes

HeaderVersion = fread(file_id,1,'uint16'); %2 bytes

FileSize = fread(file_id,1,'uint32'); %4 bytes

ImageHeaderSize = fread(file_id,1,'uint16'); %2 bytes

ULX = fread(file_id,1,'uint16'); %2 bytes

ULY = fread(file_id,1,'uint16'); %2 bytes

BRX = fread(file_id,1,'uint16'); %2 bytes

BRY = fread(file_id,1,'uint16'); %2 bytes

NumFrames = fread(file_id,1,'uint16'); %2 bytes

Correction = fread(file_id,1,'uint16'); %2 bytes

IntTime_us = fread(file_id,1,'double'); %8 bytes

Extra = fread(file_id,18,'uint16'); %36 bytes - = 68 bytes

ImageHeader = fread(file_id,16,'uint16'); %32 bytes - = 32 bytes

Header = struct('FileType',FileType, ...

'HeaderSize',HeaderSize, ...
```

```
'HeaderVersion',HeaderVersion, ...
```

```
'FileSize', FileSize, ...
```

```
'ImageHeaderSize', ImageHeaderSize, ...
```

```
'UpperLeftX', ULX, ...
```

```
'UpperLeftY', ULY, ...
```

```
'BottomRightX', BRX, ...
```

```
'BottomRightY', BRY, ...
```

```
'NumFrames', NumFrames, ...
```

```
'Correction', Correction, ...
```

```
'IntegrationTime_us', IntTime_us, ...
```

```
'Extra', Extra, ...
```

```
'ImageHeader', ImageHeader);
```

Or, if one wishes to simply read the header as a single data type of uint16, comment out the above, uncomment the next 3 lines, and comment out the following lines 90 and 93: % Header = fread(file_id,50,'uint16'); % dim = Header(9:10); % numFrames = Header(11);

% Parse the header for data (the image dimensions - 1024x1024)

```
dim = [Header.BottomRightX Header.BottomRightY];
```

% Parse the header for data (the number of frames)

```
numFrames = Header.NumFrames;

% Write a for-loop to read through all frames, 1 at a time, to create an integrated
(summed) image.

for i = 1:numFrames image = double(fread(file_id,dim(1)*dim(2),'uint16'));

image = reshape(image,dim)';

end

fclose(file_id);

end
```

Run the same code to read in the shielded-slit image.

Open the script ConstructLSF.m and edit the filenames at the beginning of the function (lines 21 and 22) to match the names of the files you saved above

```
function LSF = ConstructLSF()

raw = load('filename_open.2Dlslf');

bg = load('filename_shielded.2Dlslf');

cor = raw - bg;

cor(cor<0) = 0;

% Make all dead pixels away from the slit 0:

%bins = -74.8:0.4:74.8; % For simulated data (375 x 0.4mm bins)

bins = -204.8:0.4:204.8; % For simulated data (1025 x 0.4mm bins)
```

```

x = bins(:); y = bins(:);

%cor = cor';

%%%%%%%%%%%%%%%%%%%%%%%%%%%%%%%%%%%%%%%%%%%%%%%%%%%%%%%%%%%%%%%% ROI %%%%%%%%%%

figure

logzplot(cor,'image','colorbar');

set(gcf,'units','normalized','outerposition',[0 0 1 1])

drawnow

hBox = imrect;

roiPosition = wait(hBox);

roiPositionIndexX = round(roiPosition(1)):round(roiPosition(1)+roiPosition(3));

roiPositionIndexY = round(roiPosition(2)):round(roiPosition(2)+roiPosition(4));

close

corRoi = cor(roiPositionIndexY,roiPositionIndexX);

% To re-align the offset source position for each point along the slit to the CAX,
must shift the

% x-values. To do this, we first need to know the angle of the slit wrt vertical.

% Now let's find the peaks - start with the max value in each column and save
them in the vector "PEAKS"

maxValue = max(max(corRoi));

```

```
n = 1;

for i = 1:size(corRoi,2)

for j = 1:size(corRoi,1)

if ((corRoi(j,i) == max(corRoi(j,:))) && (corRoi(j,i) > 0.5*maxValue))

peaks(n,1) = bins(roiPositionIndexX(i));

peaks(n,2) = bins(roiPositionIndexY(j));

peaks(n,3) = corRoi(j,i);

n = n+1;

end

end

end

% Plot the defined region of the slit with the peaks superimposed:

figure2 = figure('Position',[10 100 600 600]);

% Create axes

axes2 = axes('Parent',figure2,'Layer','top','FontName','helvetica');

set(gca,'XGrid','on');

set(gca,'YGrid','on');

box(axes2,'on');
```

```
axis square;

hold(axes2,'all');

colormap(jet(64));

logzplot(bins(roiPositionIndexX),bins(roiPositionIndexY),corRoi,'image','colorbar');

scatter(peaks(:,1),peaks(:,2),40,'k','MarkerFaceColor','k','linewidth',1);

% Now we need to take the (x,y) values from PEAKS to determine the slit

% angle. Perhaps find the line of best fit, then calculate the

% angle from the fit's endpoints:

p = polyfit(peaks(:,1),peaks(:,2),1);

% p returns 2 coefficients fitting  $r = a_1 * x + a_2$ 

r = p(1) .* peaks(:,1) + p(2); % compute a new vector r that has matching data-
points in x

scatter(peaks(:,1),r,40,'+b','MarkerFaceColor','b');

delta_x = peaks(length(peaks),1) - peaks(1,1);

delta_y = r(length(r)) - r(1);

theta = atan(delta_x / delta_y); %angle in radians

radtodeg(theta)

% OK, now that we know the slit angle, we can begin to reconstruct the sub-
sampled LSF. %Each row of the SLIT image should be shifted by an amount
```

```
ShiftedX = Ytan(theta):
```

```
for i = 1:length(roiPositionIndexY)
```

```
ShiftedX(i,:) = bins(roiPositionIndexX(:)) - (bins(roiPositionIndexY(i))*tan(theta));
```

```
end
```

```
% Now we need to combine each of the above LSFs to create a single, sub-sampled LSF.
```

```
% Concatenate and sort the combined LSF and the central LSF according to x-values:
```

```
LSF_at(:,1) = ShiftedX(1,:);
```

```
LSF_cat(:,2) = corRoi(1,:);
```

```
for i=2:length(roiPositionIndexY)
```

```
TEMP_cat(:,1) = ShiftedX(i,:);
```

```
TEMP_cat(:,2) = corRoi(i,:);
```

```
LSF_cat = cat(1, LSF_cat, TEMP_cat);
```

```
end
```

```
[~,P] = sort(LSF_cat(:,1),1);
```

```
LSF_cat = LSF_cat(P,:);
```

```
%Combined LSF
```

```
% Now we just need to average together those bins that have the same x value
```

```
TEMP_x = LSF_cat(1,1);

TEMP_y = LSF_cat(1,2);

n_y = 1;

j = 0;

for i = 2:length(LSF_cat)

    if LSF_cat(i,1) == LSF_cat(i-1,1)

        % if this x-value is (almost) the same as the one before it

        TEMP_x = LSF_cat(i,1);

        TEMP_y = TEMP_y + LSF_cat(i,2);

        n_y = n_y + 1;

        % index for calculating average y-value

    else

        % if this is a new x-value

        j = j + 1;

        % index for adding newly average entries to final LSF

        LSF(j,1) = TEMP_x;

        LSF(j,2) = TEMP_y/n_y;

        % reset the variables
```

```

n_y = 1;

TEMP_x = LSF_cat(i,1);

TEMP_y = LSF_cat(i,2);

end

end

LSF(:,2) = medfilt1(LSF(:,2),5);

% Try instead to normalize to the area under the LSF

LSF(:,2) = LSF(:,2) ./ sum(LSF(:,2));

```

Now, simply run the command » [lsf, mtf] = ConstructMTF(); and you will be shown the open-slit image in colorscale. To calculate the MTF, you need to use the mouse to select a rectangular region encompassing part of the slit. Feel free to experiment with which region you choose and see if/how it affects the final MTF.

```

function [LSF, MTF] = ConstructMTF()

% First need to construct the LSF:

LSF = ConstructLSF();

%T = LSF(2,1) - LSF(1,1) % Sample spacing (distance in mm between neighbouring x-values)

SPACING = diff(LSF(:,1));

T = mean(SPACING);

```

```
Fs = 1/T; % Sampling frequency (in mm-1)

x = LSF(:,1);

y = LSF(:,2);

L = length(x); % number of elements in the LSF

% Plot the central LSF before performing the DFT:

figure;

semilogy(x,y);

set(gca,'fontsize',20)

title('LSF','fontsize',20);

xlabel('position (mm)','fontsize',20);

Y = nudft(x,y,0:mean(SPACING):3);

MTF(:,1) = 0:mean(SPACING):3;

MTF(:,2) = abs(Y);

% To speed up FFT algorithm, specify the transform length as a power of 2.

%NFFT = 2*nextpow2(L); % Next power of 2 from length of x (equals 512) %Y
= fft(y,NFFT); %Y = fftshift(y)/L;

%Create a vector of linearly spaced numbers from 0 to 1:

%Z = linspace(0,1,NFFT/2+1);
```

```

% Now make the vector run from 0 to 1.25 mm-1

%X = Fs/2*Z;

%MTF(:,1) = X; %MTF(:,2) = abs(Y(1:NFFT/2+1)); % example does 2*abs(...)

% Plot the newly-calculated MTF:

figure(11);

plot(MTF(:,1),MTF(:,2),'-');

grid on

ylim([0 1]);

title('MTF','fontsize',20);

xlabel('Spatial Frequency (mm-1)','fontsize',20)

set(gca,'fontsize',20)

%semilogx(MTF(:,1),MTF(:,2));

xlim([0.01 1.25]);

```

D.3 Codes for CT FOV manipulation

```

function image = readDICOMImages(path)

% Description: readDICOMImages read all CT images from a given directory

% into a matlab structure called image.

```

```
% Input: path-the directory where all patient CT images sit.

% Output: image- matlab structure with following field. % image.data-the 3D
matrix containing the CT data. % image.patientID % .....other head informa-
tion.

% usage:

% Below is an example of how this function is used:

% path = '/path/to/files/';

% image = LoadDICOMImages(path);

% Author: Dr.Aitang Xing and Shrikant Deshpande

% list all the dicom file in director into cell array

file_list=getFileList(path);

names=listDicomFile(file_list);

% Execute in try/catch statement try

% If a valid screen size is returned (MATLAB was run without -nodisplay)

if usejava('jvm') && feature('ShowFigureWindows')

% Start waitbar

progress = waitbar(0, 'Loading DICOM images'); end

% Initialize empty variables for the UIDs, patient demographics, and image %
dimensions image.classUID = '';
```

```
image.studyUID = "";

image.seriesUID = "";

image.frameRefUID = "";

image.instanceUIDs = cell(0);

image.patientName = "";

image.patientID = "";

image.patientBirthDate = "";

image.patientSex = "";

image.patientAge = "";

image.width(3) = 0;

% Initialize empty 3D array for images and vector of slice locations % (the data
may not be loaded in correct order; these will be used to % re-sort the slices
later)

images = [];

sliceLocations = [];

% Loop through each file in names list

for i = 1:length(names)

% Update waitbar

if exist('progress', 'var') && ishandle(progress)
```

```
waitbar(i/(length(names)+2), progress);

end

% Attempt to load each file using dicominfo

try

% If dicominfo is successful, store the header information % info = dicom-
info(fullfile(path, namesi));

info=dicominfo(namesi);

catch

continue end

% If this is the first DICOM image (and the class UID % have not yet been set

if strcmp(image.classUID,'')

% Store the UIDs, patient demographics, and slice thickness (in cm)

image.classUID = info.SOPClassUID;

image.studyUID = info.StudyInstanceUID;

image.seriesUID = info.SeriesInstanceUID;

image.frameRefUID = info.FrameOfReferenceUID;

if isfield(info, 'PatientName')

image.patientName = info.PatientName;
```

```
end

if isfield(info, 'PatientID')

    image.patientID = info.PatientID;

end

if isfield(info, 'PatientBirthDate')

    image.patientBirthDate = info.PatientBirthDate;

end

if isfield(info, 'PatientSex')

    image.patientSex = info.PatientSex;

end

if isfield(info, 'PatientAge')

    image.patientAge = info.PatientAge;

end

image.width(3) = info.SliceThickness / 10;

% Otherwise, if this file's study UID does not match the others, % multiple
% DICOM studies may be present in the same folder (not % currently supported)

elseif strcmp(image.studyUID, info.StudyInstanceUID)

% Otherwise, if this file's series UID does not match the others, % multiple
% DICOM series may be present in the same folder (not % currently supported)
```

```
elseif strcmp(image.seriesUID,info.SeriesInstanceUID)

% Otherwise, if this file's slice thickness in cm is different than % the others,
throw an error (variable slice thickness is not % currently supported)

elseif image.width(3) ~= info.SliceThickness / 10

end

% Append this slice's instance UID image.instanceUIDslength(image.instanceUIDs)+1
= info.SOPInstanceUID;

% Append this slice's location to the sliceLocations vector sliceLocations(length(sliceLocations)+
= ... info.ImagePositionPatient(3);

% Append this slice's image data to the images array images(size(images,1)+1,,:,:)
= dicomread(info);

end

% Update waitbar if exist('progress', 'var') && ishandle(progress)

waitbar((length(names)+1)/(length(names)+2), progress, ...

'Processing images');

end

% Set image type based on series description (for MVCTs) or DICOM

% header modality tag (for everything else)

if strcmp(info.SeriesDescription, 'CTTrue Image Set')

image.type = 'MVCT';
```

```
else

image.type = info.Modality;

end

% Retrieve start voxel coordinate from DICOM header, in cm image.start(1) =
info.ImagePositionPatient(1) / 10;

% Adjust IEC-Y to inverted value, in cm image.start(2) = -(info.ImagePositionPatient(2)
+ info.PixelSpacing(2) * ... (size(images, 2) - 1)) / 10;

% Retrieve x/y voxel widths from DICOM header, in cm

image.width(1) = info.PixelSpacing(1) / 10;

image.width(2) = info.PixelSpacing(2) / 10;

% If patient is Head First

if isequal(info.ImageOrientationPatient, [1;0;0;0;1;0]) || ... isequal(info.ImageOrientationPatient,
[-1;0;0;0;-1;0])

if info.ImageOrientationPatient(5) == 1 image.position = 'HFS';

elseif info.ImageOrientationPatient(5) == -1 image.position = 'HFP';

end

[~, indices] = sort(sliceLocations, 'descend');

image.start(3) = -max(sliceLocations) / 10;

elseif isequal(info.ImageOrientationPatient, [-1;0;0;0;1;0]) | ... isequal(info.ImageOrientationPatient,
[1;0;0;0;-1;0])
```

```
if info.ImageOrientationPatient(5) == 1 image.position = 'FFS';

elseif info.ImageOrientationPatient(5) == -1 image.position = 'FFP';

end

[~,indices] = sort(sliceLocations, 'ascend');

image.start(3) = min(sliceLocations) / 10; end

image.data = single(zeros(size(images, 3), size(images, 2), ... size(images, 1)));

if exist('Event', 'file') == 2 Event('Sorting DICOM images'); end

for i = 1:length(sliceLocations)

image.data(:, :, i) = ... single(rot90(permute(images(indices(i), :, :), [2 3 1])));
end

image.data = max(image.data, 0);

image.data = flip(image.data, 1);

image.dimensions = size(image.data);

if exist('progress', 'var') && ishandle(progress) waitbar(1.0, progress, 'Image
loading completed'); end

if exist('progress', 'var') && ishandle(progress) close(progress); end

clear i images info sliceLocations indices progress;

catch err

if exist('progress', 'var') && ishandle(progress), delete(progress); end
```

```
end

end

% run this script for changing FOV and rewrite dicom

path2='define path';

file_list=getFileList(path2);

cell=listDicomFile(file_list);

for k=1:length(cell)

    tmp1=cell{k};

    I3=dicomread(tmp1);

    info3=dicominfo(tmp1);

    X3=padarray(I3,[256 256],0);

    tmp5=strcat(num2str(k),'.dcm')

    X4=dicomwrite(X3,tmp5,info3,'CreateMode','copy');

end
```